MEK-PHD 2009-07

# Characterization of Vortex Generator Induced Flow

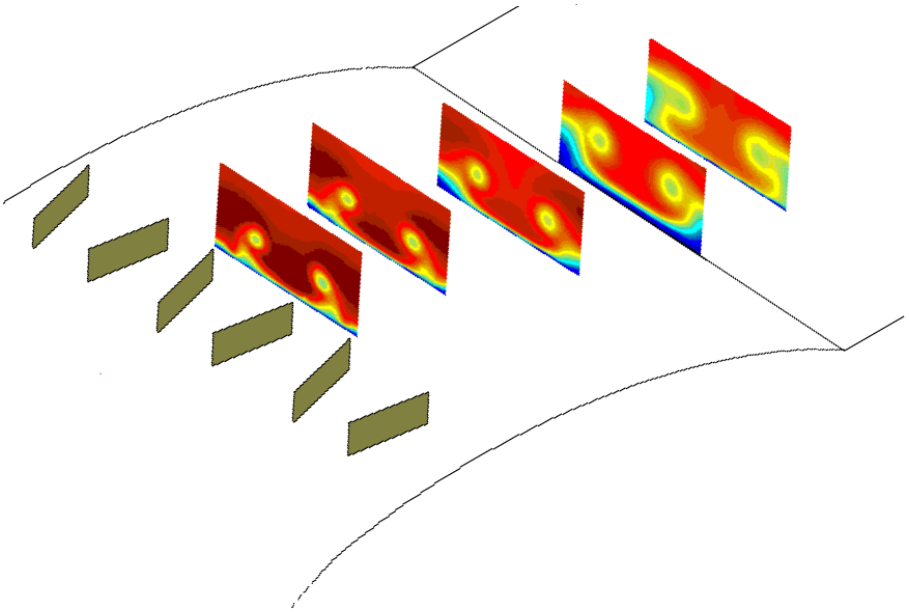

by

**Clara Marika Velte**

Dissertation submitted to the Technical University of Denmark
in partial fulfillment of the requirements for the degree of
Doctor of Philosophy in Mechanical Engineering

**Fluid Mechanics**
**Department of Mechanical Engineering**
**Technical University of Denmark**
**July, 2009**

Fluid Mechanics
Department of Mechanical Engineering
Nils Koppels Allé, Building 403
Technical University of Denmark
DK-2800 Lyngby, Denmark



MEK-PHD 2009-07 / ISBN 978-87-90416-37-9

DCAMM Special Repport No. S118

This thesis has been typeset using LaTeX2e.

"When theoretical results are presented,
no one seems to believe in them,
except the one who did the analysis.

When experimental results are presented,
everyone seems to believe in them,
except the one who did the experiments."

- Unknown

# Abstract

The aim of this thesis is the characterization and modeling of the longitudinal structures actuated by vortex generators. Results from generic studies performed at low Reynolds numbers have shown that the device induced vortices possess helical structure of the vortex core. Further, their ability to control separation and downstream evolution across the chord of a circular sector have been studied. Similar flow structures to the ones found in the generic experiments have been found in a higher Reynolds number setting, more applicable to realistic cases common to, e.g., aeronautical applications. The helical structure of the vortices can, however, not be confirmed by the results of these experiments due to practical concerns of obtaining a measuring signal with high enough quality and resolution.

Furthermore, in order to study the dynamics of the device induced structures, power spectra from LDA time series have been constructed from the burst-mode LDA theory developed mainly by Buchhave and George [19, 46]. In the process of applying this theory to the LDA time series, a technique has been developed correcting for the effect of random noise in spectra and correlations. The power spectra obtained from the flow behind the actuating devices did not display any distinct periodicity of the flow, but rather a random, or at best quasi-periodic, behavior. In addition, commonly employed interpolation and resampling methods for estimating power spectra from LDA data were compared to the corresponding spectra derived from hot-wire data. When the flow was well resolved, these methods showed acceptable results at high LDA data rates at all frequencies except at the highest ones. However, they failed miserably at low data rates, essentially burying the entire spectrum in frequency dependent noise beyond recognition.

# Resumé

Formålet med den forelæggende afhandling er karakterisering og modellering af de longitudinale strukturer som dannes af hvirvelgeneratorerne. Resultater fra fundamentale studier udført ved lave Reynoldstal har vist at de genererede hvirvler har en hvirvelkerne med helisk struktur. Endvidere har deres dygtighed til at kontrollere separation og deres udvikling langs med strømningsretningen over korden på en cirkulær sektor blevet undersøgt. Lignende strømningsstrukturer er observeret ved højere Reynoldstal, mere karakteristiske for de fleste applikationer. Hvirvlernes heliske struktur kan dog ikke blive verificeret ved hjælp af resultaterne af disse målinger på grund af praktiske problemer med at opnå et målesignal med tilfredsstillende kvalitet og opløsning.

For at studere de passivt dannede strukturers dynamik, er frekvens-spektre fra LDA-tidsserier blevet beregnet udfra burst-mode LDA-teori som er udviklet hovedsageligt af Buchhave og George [19, 46]. Ved at applicere denne teori på LDA-tidsserier udvikledes en teknik som korrigerer for effekten af hvidt støj i frekvensspektre og korrelationer. De frekvensspektre der beregnedes udfra målinger lavet bagved hvirvelgeneratorerne fremviste ikke nogle spor af distinkte periodiske bevægelser i den betragtede strømning. Det virker udfra resultaterne, som at bevægelserne optræder enten kvasiperiodiskt eller måske helt tilfældigt. Desuden er nogle af de mest anvendte interpolations- og resamplingmetoder, for at vurdere spektre ved LDA-data, blevet sammenlignet med tilsvarende spektre lavet med hot-wire-data. Ved god opløsning af strømningen gav disse metoder tilfredsstillende resultater over næsten alle frekvenser, uden de allerhøjeste. Dog mislykkes metoderne fuldstændigt ved lave data rates, hvor den frekvensafhængige støj mere eller mindre begraver hele det beregnede spektre, og al væsentlig information er fortabt.

# Contents

# Preface

This dissertation is submitted in partial fulfillment of the requirements for obtaining the degree of Doctor of Philosophy (Ph.D.) in Mechanical Engineering. The dissertation is based on research work conducted during the period from December 2005 to June 2009 at the Department of Mechanical Engineering (MEK), Fluid Mechanics Section at the Technical University of Denmark (DTU) and the Turbulence Research Laboratory (TRL) at Chalmers University of Technology. The work has been supported by the Danish Research Council, DSF, which is acknowledged for their financial support of the project under Grant 2104-04-0020. The work was carried out under guidance of my supervisors, Associate Professor, Ph.D. Martin Otto Lavér Hansen, Professor, Ph.D. William Kenneth George and Associate Professor, Ph.D. Knud Erik Meyer, to whom I wish to express my deepest and sincere gratitude. As my principal supervisor, Martin Hansen has been of great support and guidance as well as being patient and encouraging, both directly to me and my external collaborations. Further, he has helped me find a good balance between my work and private life, for which I am most grateful. I could not have wished for a better principal supervisor. I would also like to express additional gratitude to Bill George for making me his student and giving me so much of his time to answer all of my questions. Working with him has been intense, rewarding and a whole lot of fun. Further, I am deeply grateful to Professor, Ph.D. Valery L. Okulov for sharing his knowledge on helical symmetry of vortices.

I would also like to thank my office room mates Wei, Niels, Jimmy and Jacob and the rest of the staff at the Fluid Mechanics Section at DTU for great support and friendship. I would like to direct special thanks to the Turbulence Research Laboratory group at Chalmers University of Technology for accepting me as a guest for such a long time and for making my stay so fruitful and pleasant. Gunnar Johansson, Peter Johansson and Murat Tutkun are acknowledged for their support and discussions and Bettina Frohnapfel and Holger Nobach are acknowledged for providing me their measurement data. Thanks to Maja Wänström for being someone to share and discuss ideas with and to Ulrik Ullum for the support on PIV. Thanks to Kasper Jønck for the simulations, discussions and moral support during the Easter vacation in the lab and to Dalibor Cavar for carrying out the LES simulations. I would also like to thank the staff at LM Glasfiber for lending me their wind tunnel for two weeks and for providing me with computational results. Further, Petter Dahlander at the Combustion group at Chalmers is kindly acknowledged for letting me use the DaVis software. Thanks to Benny Edelsten for excellent IT support and running coaching as well as to Ebbe and Morten for the help with practical problem solving.

Finally, I would like to express my deepest gratitude to my close family and friends for their support. In particular my husband Andreas, who has been extremely understanding, loving and caring during the term of this PhD project. When I'm feeling blue all I have to do is take a look at you.

Lyngby, June 16, 2009
Clara Marika Velte

# Part I

# Introduction

# Chapter 1

# Importance of Work

One of the most prominent causes of drag on bodies in motion through a viscous fluid is flow separation near the rear of the body and at abrupt changes in its geometry (such as sharp edges and protrusions). Separation occurs when the flow in the boundary layer is retarded to a point where it can no longer counteract the pressure gradient and separates from the surface. This results in reversed flow and thickening of the boundary layer downstream of the separation point. Prandtl [110] showed that separation like that over a uniform infinite cylinder is caused by excessive momentum loss near the wall in a boundary layer trying to move downstream against increasing pressure, $dp/dx > 0$. This adverse pressure gradient appears in the rear of the cylinder, whereas a favorable pressure gradient, $dp/dx < 0$, appears in the front of the body. If the adverse pressure gradient declines after separation, reattachment can sometimes occur downstream of the separation point, resulting in a region with fluid recirculation. If reattachment does not occur, the separation will result in a low velocity wake downstream of the body where the pressure on the downstream side of the cylinder is essentially constant, and equal to the low pressure on the top and bottom points of the cylinder just downstream of where separation occurs. The pressure in the recirculating and wake regions is much lower than the large pressure which occurs at the stagnation point on the upstream side of the cylinder, leading to a pressure imbalance and, consequently, a large pressure drag on the cylinder, see, e.g., White [153]. If the boundary layer flow remains attached, only a relatively small drag due to the skin friction will remain.

Methods commonly employed for flow control today provide promising means to increase the performance of aerodynamic systems when the boundary layer is separated, or at least close to separated. This is done by re-distributing the momentum in the boundary layer in such a way as to yield a fuller velocity profile (see figure 1.1) and thereby effectively moving the separation point further aft, delaying or even obstructing separation. Both active (e.g., blowing, synthetic jets, pulsed jets, suction, plasma actuators and Micro Electro-Mechanical Systems (MEMS)) and passive (e.g., turbulators, surface roughness, riblets, dimples, bumps and vortex generators) devices have been employed in aerodynamic research as well as in commercial applications. Different devices can trigger different mechanisms in the flow, hopefully ultimately resulting in higher streamwise momentum in the separated region and an elimination of the recirculating flow. For passive momentum addition to a boundary layer, two

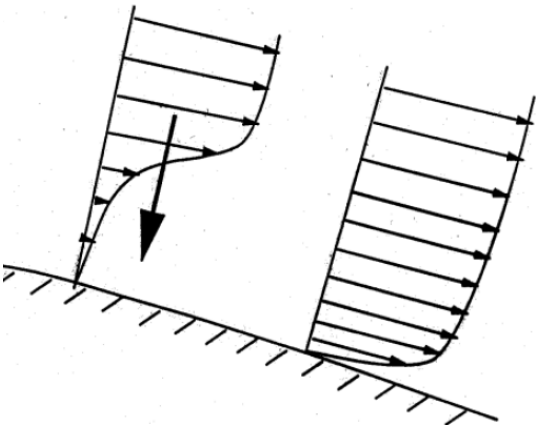

Figure 1.1: Sketch of the redistribution of the streamwise momentum in the boundary layer.

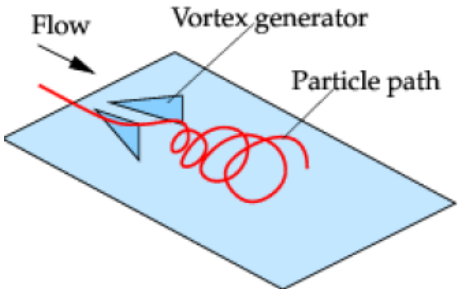


Figure 1.2: Sketch of a vortex generator pair in a flow, displaying a conceivable particle path actuated by one of the vortex generators (from [115]).

general methods are commonly applied:

- The use of fixed lifting surfaces, commonly referred to as vortex generators, for the generation of embedded streamwise vortices that cause macro overturning of the mean flow.
- Reynolds stress amplification, which can be accomplished by a range of methods and devices, yielding increased cross-stream momentum transfer.

The investigations in the current work are limited to the former alternative. Vortex generators were, to the best knowledge of the author, formally introduced by Taylor [131, 132, 133, 134] and are series of small winglets that are mounted perpendicularly on a surface at an angle of attack to the oncoming flow. These aerodynamic devices generate longitudinal vortices, causing overturning of the near wall flow via macro motions [108]. Figure 1.2 displays a sketch of a vortex generator pair on a wall with an oncoming flow and an interpretation of a conceivable particle path actuated by one of the devices. Vortex generators are believed to re-energize the boundary layer by inducing momentum transfer between the free-stream and the near wall region through

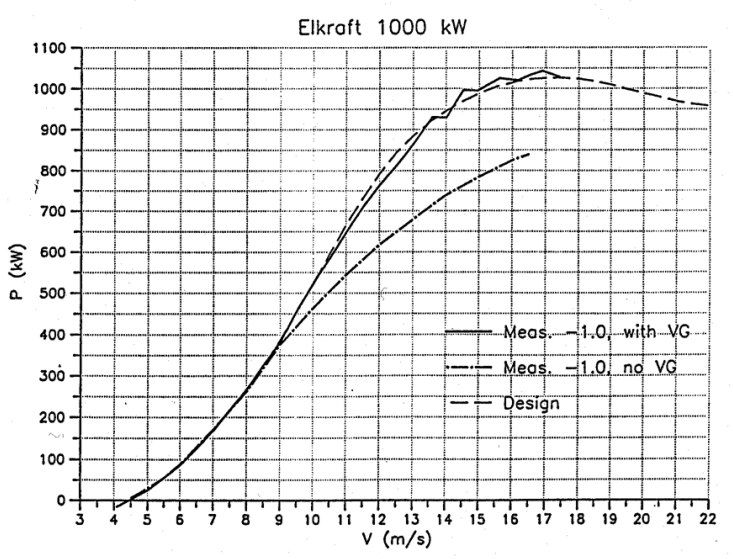


Figure 1.3: Power curve of the ELKRAFT 1000 kW wind turbine measured with and without vortex generators [103].

advection of high momentum fluid towards the near wall region and retarded fluid out into the outer layer or free stream. These processes are described by Rao *et al.* [114], Betterton *et al.* [11], Pauley and Eaton [106], Lin *et al.* [72, 73, 74, 75] and Jenkins *et al.* [60]. Experimental studies with passive devices performed by Lin *et al.* [72, 73, 74, 75] concluded that the most efficient mechanism to reduce flow separation is based on the exchange of momentum between the near wall region and the outer flow. These studies also confirm that the effect of streamwise vortices is to transfer high momentum fluid toward the wall and thereby increase the skin friction, which is done most efficiently by vortex generators producing longitudinal counter-rotating vortices. In [147], it is stated that studies conducted within the AIDA project have suggested that vortex generators are the most promising means of passive flow control in intermediate turbine ducts. Generic studies describing the physics of vortex generator actuated vortices can be found, e.g., in [124, 39, 71, 26, 27, 89]. Thus, being a passive method that can delay or even obstruct separation and that requires no auxiliary power, vortex generators can be employed to increase the lift on, e.g., an airfoil. However, they suffer a parasitic drag penalty when applied. It is therefore of importance to know how the lift/drag ratio is affected at all stages of usage. In an empirical study optimizing the aerodynamic performance of the ELKRAFT 1000 kW wind turbine Øye [103] showed that vortex generators can be applied successfully, increasing the output power for nearly all wind speeds, see figure 1.3. They have also successfully yielded a 100% increase in the lift/drag ratio for a high-lift airfoil and significant reductions of the pressure loss in a diffusor [76].

These passive devices have a range of engineering applications, but are most commonly employed in separation control, mixing and heat transfer appli-

cations. For separation control, they are commonly found on external surfaces such as airfoils [107, 95, 16], in aviation application and on various turbines as well as on road vehicles and boat keels. They are also likely to be found on internal surfaces such as ducts, diffusers [56, 32, 18] and compressor blades [129]. In mixing applications, vortex generators can be used, e.g., to mix toxic, acid or in other respects hazardous chemicals. Vane-type vortex generators can enhance the turbulence mixing, which is generally very efficient [38]. In heat transfer applications, their main function is to advect low temperature fluid towards a hot surface in order to cool the surface down and to transport the hot fluid away from the wall. In this way, cool fluid will continuously be supplied to the heated wall, keeping the surface temperature under control. This application might, e.g., be of interest in heat exchangers.

Vortex generators have the advantage of being effective, cost-effective and simple to set up and manufacture, which is why they are generally the primary option in trying to control flow separation. Even though vortex generators are commonly employed, their effect on the flow is not yet fully understood. The common practice in engineering applications is to find one configuration of vortex generators that works optimally, or at least well, in the most critical stages of application, without knowing or dealing with their effect on the flow in all of the remaining phases. Vortex generators have many degrees of freedom in the form of geometrical parameters such as general shape, height, length and angle to the main flow direction as well as the chord wise position and span wise spacing. It can therefore be tedious and costly to find the optimal device configuration for every new product empirically and therefore manufacturers tend to be conservative in their choice of products and aerodynamic devices. If one can better understand the physics of how vortex generators mix high momentum fluid into the boundary layer, it could be possible to optimize the effect of the devices in a faster and less expensive manner.

The scope of the present work is to investigate the physics of the flow actuated by vortex generators, due to their common application on wind turbine blades and other aerodynamic applications. Vortex generators can have virtually any shape, but are most commonly rectangular or triangular vanes. In this thesis, only these two device geometries are therefore considered. The device height can also vary substantially, usually ranging from the boundary layer thickness or even beyond, to a fraction of it. The effects of actuators of various heights have been investigated with emphasis on devices of boundary layer height due to their common application and modest interaction with the wall bounded flow, facilitating the study of their physics.

# Chapter 2

# Previous Work

The theory of vortex dynamics can be traced back to Helmholtz [55], who developed the theory for straight parallel vortex filaments in the midst of the $19^{\text{th}}$ century. The vortices treated in this thesis have a finite core with a non-uniform vorticity distribution across. They can be formally treated as wing tip vortices emerged in wall-bounded flow. In accordance with [109], one must account for the possible disturbance of the mirror vortex resulting from the presence of the wall. Let us start by discussing free vortices and then approach the case of vortices submerged in wall-bounded flow.

For three-dimensional uniform vortex pairs without axial flow, there exist two commonly observed outcomes. If the vortices are counter-rotating, the vortices can be subject to long-wave Crow instability or short-wave elliptic instabilities. The Crow instability is an inviscid long-wave co-operative line-vortex instability [25, 121]. This is most commonly observed behind large aircraft in operation when the wingtip vortices interact with the wakes of the engines. This instability typically undergoes the following stages, see figure 2.1. The vortices interact by amplifying initial (sinusoidal) perturbations in each other. These perturbations grow through interaction from one vortex on another and self induction. Eventually, this instability leads to the formation of vortex loops. Analysis similar to that of Crow was developed for vortices in liquid Helium II by Raja Gopal [112, 113] and attempts to calculate the three-dimensional instability of the von Karman vortex street (a staggered double row of vortices) were made by Schlayer [122] and Rosenhead [119]. Short-wavelength elliptic instabilities are usually found in vortex pairs of high characteristic ratio at low and high Reynolds numbers. In an experimental study, Leweke and Williamson [70] studied the cooperative short-wavelength elliptic instability of a freely developing counter-rotating vortex pair. Some pictures from this paper illustrating visualizations of these short-wavelength instabilities in a vortex pair evolution coupled with long-wavelength Crow instabilities are displayed in figure 2.2.

On the other hand, if the vortices are co-rotating the vortices will either rotate about their common center of mass or, if the characteristic size of the vortex core exceeds a certain fraction of their separation distance, the two vortices do not remain separated, but merge into one single vortex. Previous work has mainly comprised constant vorticity patches [28, 29, 102, 120, 149]. However, experimentally observed vortices usually have a non-uniform vorticity distribution across the vortex core. This has, e.g., been observed in two-dimensional

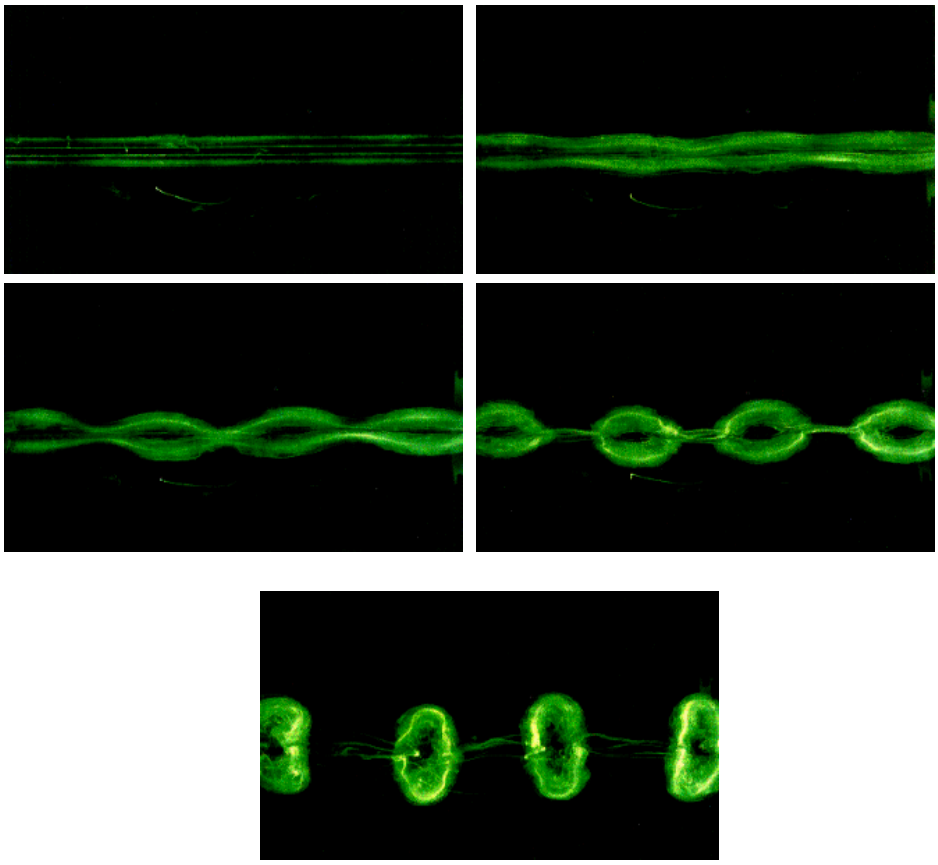

Figure 2.1: Visualization of long-wavelength instabilities in vortex pair evolution. The pictures were obtained from the official web-page of Cornell University *www.mae.cornell.edu/fdrl/research/long_wave.jpg*.

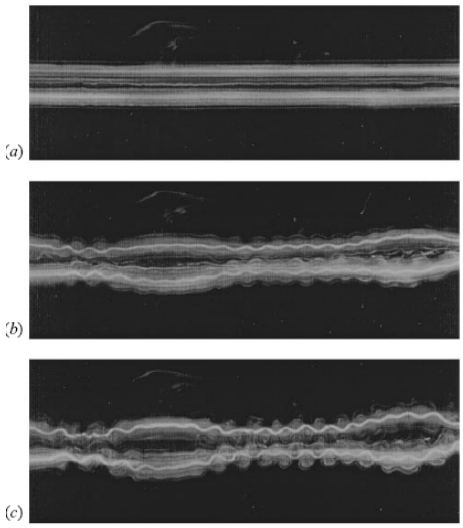


Figure 2.2: Visualization of combined long- and short-wavelength instabilities in vortex pair evolution The figure was obtained from Leweke and Williamson [70].

turbulence, where the vorticity distribution is better approximated by Lamb-Oseen vortices having a Gaussian vorticity profile [61]. A merging criterion for a pair of equal two-dimensional co-rotating vortices was found theoretically by [120], where critical values for the onset of merging were found from a stability analysis. This theoretical study was later supported experimentally and numerically by Meunier *et al.* [91]. The highly nonlinear process of merging of a vortex pair has been analyzed numerically [90] and analytically [3]. Dritschel [28] posed that the process of merging can be perceived as an instability of a pair of vortices.

Lamb [67] studied the two-dimensional dynamics of point vortices in ground effect. Much experimental work has since been carried out describing embedded vortices in wall-bounded flow using single point measurements; see, e.g., [89, 106, 124, 125]. For a deeper understanding and the optimization of the effect of vortex generators, three-dimensional instantaneous realizations of the flow structures can provide valuable information. Particle Image Velocimetry (PIV) and Stereoscopic PIV (SPIV) have become increasingly popular due to their abilities to provide instantaneous realizations of all three velocity components in a plane [52, 143, 144, 146]. It has also recently become possible to carry out experimental studies using more complex techniques such as time-resolved tomographic PIV, which has also been applied to vortex generator induced flow [42].

Many studies have presented nominal guidelines for optimizing the effect of forced mixing for vortex generators of varying geometries under different flow conditions, [52, 56, 107, 124, 133, 150]. Further, the contribution of Lin [76] and Rao and Kariya [114] provide nice reviews on experimental and computational studies of low-profile, a.k.a. submerged, vortex generators. Some of the studies

showed that such devices, much smaller than the boundary layer thickness ($\sim 0.1\delta$), still can be fairly efficient, while reducing the parasitic drag. However, such devices must be placed fairly close to the location of separation. Therefore, larger devices might be more suitable in many applications such as over curved surfaces without protrusions (e.g., airfoils), where one typically does not have a fixed position of separation.

Streamwise vortices embedded in turbulent boundary layers is a common phenomenon and is seen, e.g., in the treatment of free organized structures (see, e.g., [117, 101, 62, 2] and references therein), Görtler vortices in boundary layers over walls of streamwise concave curvature (see [53]), corner vortices with an axial velocity component, vortex rings near walls and as roll-up or horseshoe vortices folding around objects attached to a wall [2]. Longitudinal vortices imposed using passive devices such as vortex generators might act as to enhance and interact with these pre-existing naturally occurring longitudinal vortex structures in the boundary layer, thus aiding in the exchange of momentum between the boundary layer and the outer flow. How the actuating devices interact with the coherent structures of the boundary layer, if at all, is not fully understood at this point.

Attempts have been made to correctly characterize vortex generator actuated vortices for device heights comparable to the boundary layer thickness [77, 127, 157]. Some take into account or observe the Lamb-Oseen vortex structure of the secondary velocities. However, the non-uniform axial velocity component $u_z$ commonly observed across the vortex core has previously never been properly explained except as a velocity deficit. In the present work, the flow structures downstream of vortex generators have been analyzed in order to gain insight into the physical processes of the flow to increase the predictability and simplify the optimization of their effect (cf., [143, 144, 146]). Generic experiments at low Reynolds numbers have shown that the vortices possess helical symmetry of the vorticity and therefore can be modeled by relatively simple equations provided that the helical pitch and convection velocities of the vortices are known [146]. Since the velocity formulation used to determine helical symmetry of the vortex is linear, one can apply averaging in both space and time; $< u_z >=< u_0 > \pm < u_\theta r/l >$, where $<>$ indicates averaging. $u_z$ and $u_\theta$ are the axial and azimuthal velocities, respectively and $u_0$ is the convection velocity of the vortex. r is the radial coordinate and l is the helical pitch. This enables the neglection of, e.g., turbulent pulsations, positional variations of the vortex in time or variations across the azimuthal coordinate $\theta$. If the averaged data can fulfill the averaged velocity formulation, then one has found helical symmetry of the vortex in that averaged sense.

# Chapter 3

# Current Investigations

## 3.1 Objective

The objective of this PhD project is to design and perform suitable experiments to investigate the flow structures actuated by vortex generators as well as investigating their effect on separation. Stereoscopic Particle Image Velocimetry (SPIV), Hot-Wire Anemometry (HWA) and Laser Doppler Anemometry (LDA) flow measurements have been analyzed in terms of time averaged statistics and dynamical analysis. In order to evaluate the induced effect of the vortex generators, both incident and actuated flow have been measured. A two-dimensional model for the mean induced effect of the vortices has been produced and the investigation of the three-dimensional downstream evolution is planned, for which measurements and some analysis have already been carried out. Important all-embracing and intermediate goals in the project have been:

- Design and construction of the experimental facility. In particular the test section, to obtain better optical access. Further, vibrations from the fan have been isolated so that they do not reach the test section and the fan has been replaced and relocated from the second to the third bend upstream of the test section.
- Detailed PIV measurements of the incident flow and with several configurations of actuated flow in generic experiments at low Reynolds numbers, involving the following intermediate goals:
  - Experimental investigation of a single vortex generator on a plane wall, with a variable angle of attack to the oncoming flow. In an analysis of the data and characterization of the vortices from ensemble averaged statistics, the vortices have been found to possess helical symmetry, enabling the construction of a two-dimensional model for the vortex structures.
  - Experimental investigation of the induced effect of a cascade of vortex generators situated in a fashion producing counter-rotating vortices on a circular sector (bump). The impact of the actuators on separation has been investigated as well as the downstream evolution of the helical parameters of the actuator induced vortices, showing an abrupt transition at the trailing edge of the bump.

  - The results have been collected and will eventually be published in a database.

- Measuring the effect of vortex generators at higher Reynolds numbers in a setting more realistic to most applications in the newly built LM Glasfiber wind tunnel using SPIV.

  - Detection of the characteristic macro mixing flow patterns as seen in the generic experiments performed on the actuator cascade on the bump, indicating that the same type of flow process is active at these high Reynolds numbers. This also suggests that it is plausible that helical symmetry of the vortex generator actuated vortices persists at higher Reynolds numbers that are more common to many engineering applications, however, this can not be confirmed from the measurements.

- HWA and LDA measurements have been performed in the generic experimental setup. The inlet has been characterized using both HWA and LDA. However, for practical purposes, the HWA results are the ones primarily presented. Further, some dynamical analysis of the flow has been conducted with the aid of power spectra. Some intermediate steps in this work comprise:

  - Application of an existing theory for the correct representation of an unbiased and unaliased power spectral estimator for LDA data, see George [46] and Buchhave [19].
  - As a consequence of the work of evaluating power spectra from LDA data, a method for noise removal in spectra and correlations has been developed.
  - Further, spectra obtained using commonly applied interpolation and resampling methods have been analyzed. The results show that these methods perform poorly when the average data rate of the LDA is low compared to the smallest scales of the flow. At high average data rates, the methods perform better, but can still not resolve the spectrum at the highest frequencies of the bandwidth.

## 3.2 Method and delimitations

SPIV was chosen for measuring the flow in all of the experimental setups, primarily due to its ability to capture instantaneous realizations of the flow in a plane. The measurement planes were always chosen perpendicular to the main flow direction, due to the assumption of symmetry of the vortices in these planes. By varying the downstream position of the measurement plane, it is possible to study the streamwise evolution of the vortices.

SPIV is an expansion of the PIV measurement technique, employing two cameras at different viewing angles to the measurement plane to capture the velocity component directed out of the plane, which otherwise would have been projected onto the in-plane components. In order for the two cameras to recognize a common coordinate system in the object plane, which should ideally coincide with the laser sheets, a calibration procedure is performed. A target

with a well defined pattern with an origin and coordinate axes is placed in the center of the laser sheet and traversed throughout its whole depth. For a number of well-defined positions, images of the target is recorded by both cameras. This information is incorporated to construct a mapping function between the image and object planes, enabling reconstruction of the 3 component velocity field from the planar images obtained for each camera.

In recent years, it has been shown that the systematic errors that arise from the calibration target not coinciding with the center of the laser sheet can potentially have tremendous impact on the velocity vectors obtained after reconstructing the three-component velocity field [24, 111, 154, 155]. Figure 3.1 displays a sketch showing how these disparities arise for a simple translation of the light sheet relative to the calibration target. If the position of the calibration target is not identical with that of the center of the light sheet, the imaged areas of the cameras will not concur. An illustrative and highly relevant example is when performing measurements on a wing tip vortex; For significant disparity, the vortex centers seen by each camera will appear at different positions in the coordinate system provided by the calibration, yielding a distorted vortex or maybe even two separate vortices after reconstruction of the three-component velocity vector map [111]. The misalignment between the calibration target and the laser sheet can be estimated by the construction of so-called disparity maps [155]; Two simultaneously recorded single-exposure PIV images from each camera are mapped onto the object plane using the mapping function obtained through the calibration images. Cross-correlating these images, a vector field will result, providing a measure of the misalignment residual across the measurement plane [24].

Due to the finite thickness of the laser sheet and the viewing angles of the cameras to it, the particle pattern in an interrogation area will not look the same to both cameras. This is due to the particle distribution throughout the thickness of the light sheet, which yields different views from different viewing angles, see figure 3.2. If the laser sheet is thick, this effect might result in weak correlations, in particular if two or more particles reside on an axis symmetrical to the optical axis to one of the camera lenses. This will cause the particles to be visible to one camera, while the other one portrays them as one single particle since the other particles are imaged in the same position. It is therefore advantageous to study an ensemble average of the disparities to quantify and remove the effect of these ambiguities. Averaging the correlation planes obtained from cross-correlating the images of the two cameras obtained from the same laser pulse will yield an average correlation peak with the shape of an elliptic ridge, from which the disparity can be found. This correlation peak further provides information about the thickness of the light sheet of the pulse under consideration. Conducting this for both laser pulses, one can from the correlation peaks obtain information about the relative positions of the two laser sheets [154]. By simple triangulation, the corresponding point at the center of the light sheet can be deduced. The position of the center of the light sheet is found by fitting a plane through the points obtained for all interrogation areas. Thereby, one can find the mapping functions to correct the calibration to the actual positions of each laser plane. It might be necessary to iterate the procedure a few times to reach convergence. This method is well described in [154]. One should therefore, if possible, perform the correction by averaging the correlation functions of each interrogation area instead of the disparity vector maps. This procedure

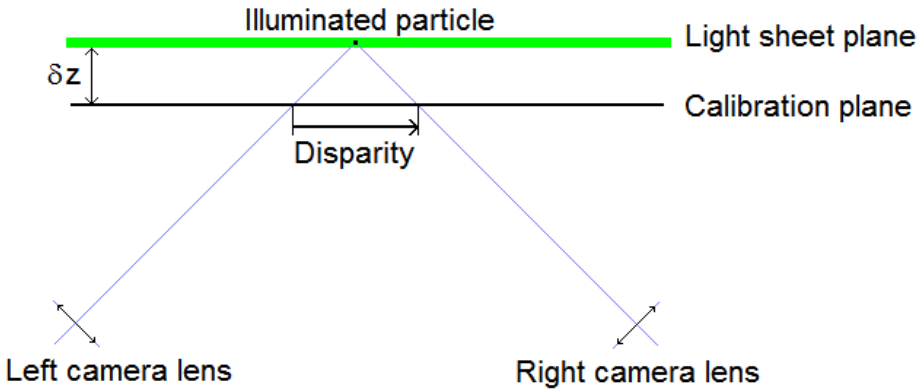


Figure 3.1: Sketch showing the effect of having non-overlapping laser sheet and calibration target by a translation $\delta z$. The misalignment results in a disparity between the imaged areas.

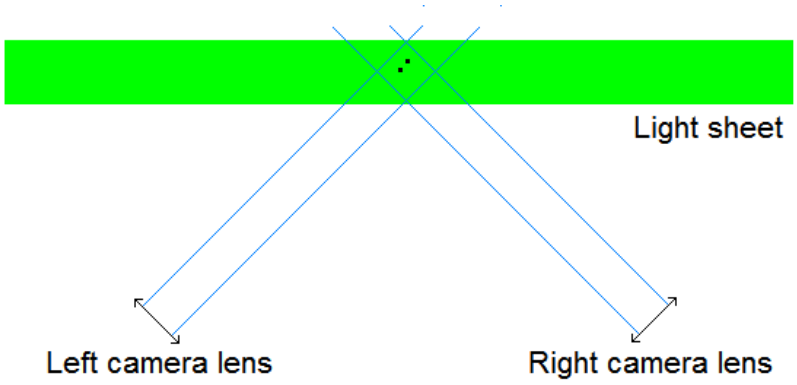


Figure 3.2: A light sheet of finite thickness with particles dispersed throughout its depth will result in different particle patterns for the same interrogation area as seen by cameras viewing the same area from different directions. In the example above, two particles clearly distinguished from one angle will appear as a single particle to the other camera.

provides more information, since it retains all of the necessary information in the measurements, and removes the ambiguity of the particle position throughout the depth of the laser sheet [111, 154].

It has also been shown that misalignment errors can influence measured turbulence statistics unless the interrogation area is small compared to the local Taylor microscale [148]. The increase in the apparent turbulence mean square of the velocity is proportional to the mean square of the misalignment and inversely proportional to the square of the Taylor microscale. Hence, it is beneficial if the Taylor microscale exceeds the misalignment and it can be devastating if the misalignment is larger.

In all investigations presented in this work, it has been strived to fulfill the guidelines of Keane and Adrian [65] to obtain optimal accuracy of the SPIV measurements, yielding a measurement accuracy of optimally about 0.1 pixel.

- Image density, $N_I \geq 15$
- Out-of-plane displacements, $|w|\Delta t/\Delta z_0 < 0.25$
- Spatial gradients, $M|\Delta \mathbf{u}|\Delta t/d_I < 0.05$

Here $d_I$ denotes the interrogation area (IA) side length, $\Delta z_0$ the laser sheet thickness and $M$ the magnification factor. For more detailed descriptions and guides to both the theoretical and practical aspects of PIV, please consult Raffel *et al.* [111] and Westerweel [151].

### 3.2.1 Generic experiments

For the generic experiments, a low Reynolds number wind tunnel was provided with a test section of cross sectional area $0.6\times0.3$ m$^2$. The optimal operating velocity of the wind tunnel was about 1 m/s. The flow at the inlet of the test section and the flow over a circular sector (bump) in this wind tunnel before its reconstruction was previously characterized by Schmidt [123].

Testing of vortex generators on real airfoils is expensive and difficult. It requires large flow facilities and/or high flow speeds to obtain high Reynolds numbers to generate turbulent boundary layers on the airfoil. Furthermore, transition to turbulence in the boundary layer is a complicated process that introduces additional uncertainty to the experiment and the spatial resolution of the available measurement techniques is very poor at these small flow scales. For these reasons and due to the limitations in equipment and wind tunnel facilities, an experiment is proposed that creates similar flow conditions for the vortex generators as they experience on a real airfoil. A turbulent boundary layer is formed on the test section walls, tripped by a turbulent free stream created at the inlet by a turbulence generating grid. This provides a relatively thick turbulent boundary layer, which makes it easier to resolve the vortex generator actuated flow structures. One should be aware that at this low Reynolds number ($\mathrm{Re}_h \approx 1\,700$ based on a vortex generator height of $\mathrm{h} = 25$ mm), the log-law region does not appear in the boundary layer. This has been confirmed from investigations of the data of Schmidt [123]. The incident and actuated flow will scale with the boundary layer and can therefore advantageously be measured and resolved, however, in a not very realistic flow.

For the investigation of the structure of the vortices, a single vortex generator with a variable angle of attack to the incoming flow was placed on the plane test section wall. In the investigations of the separation control abilities of the vortex generators, a bump was mounted on the test section wall, creating a pressure distribution leading to flow separation similar to the conditions of a real airfoil. In this study a cascade of actuators were positioned on the bump, generating counter-rotating vortices.

A turbulent boundary layer was deliberately chosen because of the applicability and in order to obtain a fuller velocity profile. This facilitates the study of the vortices, since it yields an almost uniform velocity profile in the area of interest and hence, the boundary layer velocity gradient does not impose as much on the flow in the region where the vortex resides. Further, the current investigations have shown that the vortices are stable despite the turbulent pulsations. Laminar boundary layers are sensitive and can be subjected to transition, especially when encountering the vortex generators which are renown to trigger transition. Also, there are to the knowledge of the author none, or at least not many, interesting applications using vortex generators in laminar boundary layer flows. One should also stress that it is plausible that the results regarding helical symmetry of the vortices also hold for laminar flow, since they display this behavior for turbulent flow which contains more and stronger perturbations.

High intensity laser light reflections, harmful to the sensitive CCD camera sensors, is a fundamental problem for most PIV applications near walls and other surfaces. The light budget of these reflections is typically high compared to the sought for signal (i.e., scattering of seeding particles). Hence, the presence of surfaces often leads to aggravation of the particle images, i.e., signal quality, since one has to reduce the amount of light from the laser sufficiently for the reflections not to damage the sensors of the cameras. In order to avoid these harmful reflections from reaching the CCD sensors of the cameras, Rhodamine 6G mixed with mat varnish was applied to all reflecting surfaces. Rhodamine 6G is a fluorescent dye, which shifts the wavelength of the laser light through absorption and re-emission. The cameras were equipped with bandpass filters admitting wavelengths corresponding to about that of the laser light. In this way, the detection of the scattering of the particles was virtually unaffected, while harmful reflections were substantially reduced. This technique facilitated measurements close to the test section walls as well as very close up onto the vortex generators.

The disparity due to misalignment between the center of the light sheet and the calibration target found in these investigations, typically around 0.05 pixels, were always smaller than the optimal measurement accuracy of the PIV system (0.1 pixels). No calibration correction was therefore applied for these measurements. The Taylor microscale was estimated to $\lambda_f \approx 9\,\mathrm{mm}$ from LDA measurements of time series at a position 270 mm downstream if the inlet at the center of the cross-section of the test section [123]. It was thus possible to align the calibration target to the laser sheet with an accuracy significantly smaller than the measured Taylor microscale. The Taylor microscale can, for purposes of resolving gradients in the flow, be compared to the PIV interrogation area size, which was approximately 1-2 mm for all measurements under consideration. The Taylor microscale will, of course, vary with distance from walls, but the above numbers can nevertheless serve as a guide.

HWA and LDA measurements were employed to study the dynamics of the vortices. The power spectra are mainly of interest for the detection of dominant frequencies from large scale fluctuations (not constituting turbulence) such as the oscillations of the device induced vortices, which would appear as relatively distinct peaks in the spectra if the oscillations are periodic. The spectra obtained from measurements taken downstream of the vortex generators were compared to corresponding spectra from data acquired in the incident (uncontrolled) flow in the same position as a reference. No distinct peaks were found, but rather a smooth redistribution of the energy across most of the band width. This is an indication of complex quasi-periodic or purely non-periodic oscillations. This can be expected based on the discussion on long- and short-wavelength instabilities in Chapter 2. Pre-existing characteristic spatial structures in the incident flow might also have an effect on the dynamics of the vortices, which is why these results should not be considered general. In previous work by Ullum *et al.* [142] in the same wind tunnel prior to its redesign, it was found from measurements that structures stemming from the grid produced an array of interacting jets still detectable 562 mm downstream of the inlet grid at a free stream velocity of 1.2 m/s. Because of these ambiguities, the dynamics of the structures were not studied further.

Numerical simulations were not conducted by the author due to shortage of time and the conditions under which the flow is constrained. Due to the absence of the inertial subrange, it is not feasible to model turbulent wall-bounded flow at low Reynolds numbers [135]. This range is characterized by a constant spectral flux which is equal to the dissipation and only appears at fairly high Reynolds numbers. In LES, it is assumed that the flow exhibits an inertial subrange, independently of Reynolds number, in order to obtain closure. The one-dimensional spectra obtained by Mydlarski and Warhaft [94] from measurements in a wind tunnel using an active grid showed strong Reynolds number dependency. The most interesting feature of the results, however, was that in spite of the relatively high Reynolds numbers, the spectra did not display a $k^{-5/3}$ range. In wall bounded flows, the implementation of LES becomes even more difficult. Recent experiments performed using hot-wire rakes in a boundary layer in a wind tunnel at a Reynolds number based on momentum thickness of 20 000 have detected the inertial subrange [141]. However, even at these high Reynolds numbers, the inertial subrange did not appear inside $y^+ = yu_\tau/\nu \leq 445$, but develops rapidly when exceeding about $y^+ \geq 890$. Therefore, it is silly to implement LES in the near wall region inside of $y^+$ of at least a couple of hundred in the generic experiments considered in this thesis. A more thorough discussion on the need for an inertial subrange and in particular the implications of wall-bounded flows in LES can be found in [48]. Further, most current turbulence models as such are designed to simulate turbulence and therefore cannot capture large scale motions like overturning of the boundary layer as produced by vortex generators. Examples of this from applications can be found in Chapter 6 and [143, 144]. Further, in order to be able to compare the results of the measurements and computations, it is important to have spatially and temporally coherent inlet boundary conditions for the simulations that correspond to the ones in the experimental setup [47]. This can be achieved in a quite realistic way using Proper Orthogonal Decomposition (POD) and Linear Stochastic Estimation (LSE) based on measurement data, which was demonstrated on measurements of a plane turbulent mixing layer [30]. This was not

done in the current work, but should however be employed if flow simulations are attempted in future studies.

The reason why the boundary layer thickness has been used as a measure of the height of the vortex generators instead of, e.g., the momentum thickness is not merely by convention; see, e.g., [52, 76]. Only one vortex generator size was investigated in the generic experiments presented in this thesis. The uncontrolled boundary layer was tripped by a turbulent free stream, yielding a very sharp streamwise average velocity gradient close to the wall. The vortex generator height was of the order of the boundary layer thickness, hence the incident average velocity profile in the region of the vortex displayed only small gradients. The vortices thus operated in a region of the oncoming average velocity field which was fairly constant across the wall normal coordinate. Therefore, even though the determination of the boundary layer thickness is sensitive, the effect of an inaccurate prediction is not very critical in this case.

### 3.2.2 Applied experiments (LM wind tunnel)

These measurements were performed in order to investigate the structure of the device induced vortices in a more applied and realistic setting. The primary objective was to check whether the vortices displayed the same characteristics as the ones seen at low Reynolds numbers. Further, the study is an example of how a vortex generator geometry can be optimized empirically.

Though the actuators were submerged, i.e., the device height is only a fraction of the boundary layer thickness, very similar structures to those observed in the generic experiments were found at all measured positions and Reynolds numbers at an angle of attack corresponding to the maximum gliding ratio. This indicates the presence of the same flow process, suggesting that it is plausible that the vortices even under these conditions possess helical symmetry. This could, however, not be confirmed or dismissed mainly for two reasons: First, since the distances of the cameras to the measurement volume by necessity were relatively large ($\sim$1.5 m) and the induced flow structures were of the order of centimeters, it was difficult to obtain a good resolution of the measurements. Teleconverters doubling the magnification were used, however, at the expense of decreased light intensity from the scattering particles. Further, the depth of focus was reduced substantially, providing tough conditions for obtaining satisfactory focus across the CCD sensors of the cameras. Second, due to strong reflections from the actuators, measurements could not be performed very close upstream where the vortices are generated. This decreases the probability for detecting this kind of process, if present, due to the increased impact of turbulent pulsations and viscous effects.

Due to the occurrence of vibrations in the wind tunnel test section at higher free stream velocities, probably caused mainly by shedding from the airfoil, the experiments were performed at Reynolds numbers well below the threshold for noticeable vibrations. However, concerns still existed for transitional effects in the boundary layer flow due to vibrations. The investigations were nevertheless performed with the intention of detecting larger scale structures generated by the device induced vortices.

These experiments posed much tougher conditions for the calibration accuracy than the generic ones. Measurements were performed in spanwise planes perpendicular to the airfoil surface. For dynamic range considerations due to

the cross-flow arrangement, the laser sheets of the two pulses were deliberately shifted relative to each other so that the second pulse was situated about 25% of the laser sheet thickness farther downstream than the first one. It was therefore impossible to place the calibration target at the center of both light sheets at the same time, which is hard enough to do even if the laser sheets are overlapping and identical to begin with. As a consequence, calibrations computed directly using the Soloff method [128], without correcting for the laser sheet and calibration target not being parallel, will inevitably suffer so-called disparity error [154]. The calibrations were performed as to span the entire light sheet thickness at low laser intensities well with margin. The resulting disparity maps displayed vectors corresponding to a domination of error due to a translational shift of the calibration target in relation to the center of the laser light sheet, which is expected since the calibration is performed for both light sheets which are deliberately shifted. For precaution during the experiments, several calibrations were performed spanning larger depths than were seemingly necessary at the moment.

Calibration corrections for shifted pulses could not be performed by the Dantec software, which only allowed for the correction of one laser pulse at a time. This software thus requires perfect overlap of the light sheets, which should also ideally be identical for the correction to be valid. If the beams of the two laser cavities are not very carefully aligned and have similar intensity distributions, the correction will only be valid for the laser pulse that is chosen in the correction process. Since the laser pulses were deliberately shifted relative to one another in order to increase the dynamic range, this option is far from optimal for these measurements. In addition, performing this procedure manually is not possible using the software at hand, since it does not allow the performance of average correlation on images from separate cameras manually and does not provide any numerical values associated with the correlation planes.

Instead, the DaVis 7.2 software was used to compute the disparity maps by averaging the correlation planes as was described above. This software allowed for the calibration correction to be applied to both laser pulses. Disparity maps were constructed by cross-correlating simultaneously acquired images mapped onto the object plane as described earlier. The disparity maps again displayed vectors corresponding to a domination of error due to a translational shift of the calibration target in relation to the center of the laser light sheet, as expected. The disparity errors associated with the calibration are sometimes quite large in the current measurements, typically of the order of 50% of the free stream velocity.

# Chapter 4

# Outline of Thesis

The thesis is divided into five main parts;

- Introduction
- Helicity of Vortex Structures
- Separation Control
- Dynamics of Embedded Vortices
- Summary and Future Work

"Helicity of Vortex Structures" mainly deals with the characterization of the device generated vortices. A 2D model was constructed based on helical symmetry of the vortex and all helical parameters were found to vary linearly with the device angle of attack to the oncoming flow.

In "Separation Control", investigations of the ability of separation control of the vortex generators was studied. This was done in a generic study as well as in a more applied one. The generic study also confirmed the helical symmetry of the vortices for a cascade of actuators. This could not be done in the applied measurements due to limitations in resolution and problems with strong reflections. However, both studies displayed the same basic flow patterns of the actuated flow, suggesting that helical symmetry persists also at high Reynolds numbers.

"Dynamics of Embedded Vortices" describes an investigation of the dynamics of the vortices. Time-series measurements were performed using HWA at various positions downstream of one single actuator as well as a cascade of vortex generators with corresponding measurements for the uncontrolled incident flow. Power spectra were estimated from these time-series, expecting a distinct peak if the vortices oscillate periodically. None of the power spectra of the controlled flows displayed this kind of peak, but rather imposed smooth distributions of energy across the high energies. It was therefore concluded that the dynamics of the vortices is random or, at best, quasi-periodic. Further, the inlet was characterized using both LDA and HWA measurements, though the HWA measurements are mainly analyzed and shown due to practical reasons related to computational time of producing power spectra from LDA measurements and the high noise levels associated with them, see George [46] and Buchhave [19].

Profiles were measured across the height of the wind tunnel test section and time series were recorded to detect large scale periodic structures. In computing power spectra from the LDA data, a burst-mode LDA spectral estimator, derived by George [46] and Buchhave [19], is applied. As a spin-off, this project led to the identification of the random noise component in spectra and correlations, which is contained in the self-products and contains both noise and the signal carrier variance. If the noise is white (frequency independent), it can easily be identified and removed from spectra and correlations. In addition, interpolation and resampling techniques applied to LDA data to obtain spectral estimates were tested against power spectra from HWA data, showing that these techniques can be applied only under very strict conditions of high data rates. However, they still fail to resolve the highest frequencies of the flow. For low data rates, the spectrum is buried in frequency dependent noise. This has been predicted theoretically, see Adrian and Yao [1].

"Summary and Future Work" provides a summary of the work comprised in this thesis and describes the continuation of the work being done. The downstream evolution of the vortices is investigated in an attempt to create a 3D model of the vortices. In addition, suggestions are given for further work.

Most of the presented work has been conducted in collaboration with other researchers. The respondent is the first author of all of the papers that are published or will be submitted for publication based on the material contained in the thesis. In the short presentation of the chapters below, the division of the work has been clarified.

**Chapter 5** This chapter comprises the foundation of the thesis and shows that the structure of the device induced vortices is helical. This is a generic experiment, performed at low Reynolds number ($Re = 2600$ based on the inlet grid mesh size $L = 0.039$ m and free stream velocity $U_\infty = 1.0\ \mathrm{m\,s^{-1}}$). All of the experimental work and analysis presented was performed by the respondent. The interpretation of the data and the development of the 2D vortex model was performed in conjunction with both Martin O. L. Hansen and Valery L. Okulov.

**Chapter 6** This chapter treats the effect of the vortex generators in terms of separation control. A cascade of rectangular and triangular vortex generators mounted as to produce counter-rotating vortices were tested on a cylindrical sector. The downstream development of these vortices was studied, showing that the actuators are successful in delaying separation. This particular analysis has been simplified in the sense that the flow is analyzed in a spanwise averaged sense, even though the flow is highly three-dimensional. The LES flow simulations were able to capture the vortical motions to some extent, but could not be used for direct comparison with the measurements due to the deviating inlet conditions from the true one, the slight difference in configurations and shortcomings of the method in low Reynolds number wall-bounded flow; see, e.g., George and Tutkun [48]. Further, the downstream evolution of the helical parameters of the vortices was studied, displaying an abrupt transition at the trailing edge of the bump to a different state. All of the experimental work was performed by the respondent. The planning of the experiments and the analysis was performed by the respondent and Martin O. L. Hansen with emphasis on the respondent. The simulations were performed by Dalibor Cavar.

**Chapter 7** In this chapter, it is shown that the basic structure of the actuated flow observed in Chapter 6 persists at higher Reynolds numbers more common to most vortex generator applications, suggesting that the helical structure prevails also under these conditions. Further, the vortex generators displayed a large effect on the axial velocity profile on an airfoil in stall, efficiently counteracting separation. The experimental planning was done by the respondent, Martin O. L. Hansen and Knud Erik Meyer, with emphasis on the respondent who also mainly conducted the experiments. The analysis and interpretation of the data was done by the respondent and Martin O. L. Hansen, with emphasis on the respondent.

**Chapter 8** This chapter describes the experimental studies performed to investigate the dynamics of the vortex generator induced vortices as well as characterization of the inlet of the wind tunnel used in the studies in Chapters 5 and 6. Time series of two-component hot-wire measurements were performed. Initially, LDA measurements had been performed for this purpose, but were abandoned due to the supremacy of the HW measurements in terms of processability of data both time- and computerpowerwise as well as the substantially lower spectral noise floor. The spectra of the measurements conducted behind the vortex generators showed no distinct peak, suggesting that the vortices have at best quasi-periodic dynamics. All of the work in this chapter was conducted by the respondent.

**Chapter 9** A method was developed for the removal of the effect of the random noise component in autospectra and autocorrelations. The total effect of the random noise is always contained in the self-products. In autocorrelations, the random noise is confined to the origin, since it is uncorrelated with itself for all time lags except zero, where it is fully correlated. This noise spike at the origin is transformed into white, band-width limited noise in the corresponding autospectrum. The noise can be removed by excluding the self-products in the spectral estimator and offsetting the spectrum so that the high frequency asymptote is zero, compensating for the subtracted energy corresponding to the signal carrier variance lost in the process of subtracting the trace. The analogous action for the autocorrelation is to make a parabolic fitting around the origin to obtain the signal carrier variance. The development of the novel theory was mainly performed by the respondent, but to some extent in collaboration with William K. George and Murat Tutkun. The experimental data was provided by Murat Tutkun.

**Chapter 10** This chapter contains an overview of some basic and advanced signal processing aspects needed to continue the discussion on burst-mode LDA spectra. In particular, the section treating random sampling is of interest for the continuation. Further, concepts like variability and random noise impact on random sampling spectral estimators are addressed. The effects of windowing and aliasing on randomly sampled data are briefly discussed.

**Chapter 11** A correct, unbiased and unaliased spectral estimator, derived by [46], is applied for the first time and is for two different data sets compared to corresponding hot-wire spectra. These burst-mode LDA spectra show good

concurrency with the corresponding HWA spectra. Despite the random sampling provided by the LDA measurements, aliasing peaks were detected in the data sets used, found to be related to the precision of the stored measurement data and the limitations in temporal resolution due to the finite size of the measuring volume, respectively. The analysis was conducted by the respondent and William K. George, with emphasis on the respondent. The experimental data was provided by Bettina Frohnapfel and Holger Nobach.

**Chapter 12** Commonly employed techniques for spectral estimation of LDA data by interpolation and uniform resampling are investigated and compared to power spectra based on HWA data. The effects of applying two kinds of techniques are evaluated in this chapter; sample-and-hold and linear interpolation and resampling. The effectiveness of the techniques strongly depends on the average data rate of the LDA measurements at acquisition. At low data rates, the sample-and-hold spectrum will be dominated by noise that falls of as $f^{-2}$, burying the true signal. For the linear interpolation and resampling technique, the spectrum falls off even faster. If the data rates are high enough to resolve the smallest scales, which is rarely satisfied due to practical reasons, the resulting spectral estimates from both methods will predict the power spectrum correctly across most of the bandwidth, with the exception of the very highest frequencies. The analysis was conducted by the respondent and William K. George, with emphasis on the respondent. The experimental data was provided by Bettina Frohnapfel and Holger Nobach.

# Part II

# Helicity of Vortex Structures

# Chapter 5

# Helical Structure of Longitudinal Embedded Vortex

Embedded vortices in turbulent wall-bounded flow over a flat plate, generated by a passive rectangular vane-type vortex generator with variable angle $\beta$ to the incoming flow in a low-Reynolds-number flow ($\mathrm{Re} = 2\,600$ based on the inlet grid mesh size $\mathrm{L} = 0.039$ m and free stream velocity $\mathrm{U}_\infty = 1.0\,\mathrm{m\,s^{-1}}$), have been studied with respect to helical symmetry. The studies were carried out in a low-speed closed-circuit wind tunnel utilizing Stereoscopic Particle Image Velocimetry (SPIV). The vortices have been shown to possess helical symmetry, allowing the flow to be described in a simple fashion. Iso-contour maps of axial vorticity revealed a dominant primary vortex and a weaker secondary one for $20° \leq \beta \leq 40°$. For angles outside this range, the helical symmetry was impaired due to the emergence of additional flow effects. A model describing the flow has been utilized, showing strong concurrence with the measurements, even though the model is decoupled from external flow processes that could perturb the helical symmetry. The pitch, the vortex core size, the circulation and the advection velocity of the vortex all vary linearly with the device angle $\beta$. This is important for flow control, since one thereby can determine the axial velocity induced by the helical vortex as well as the swirl redistributing the axial velocity component for a given device angle $\beta$. This also simplifies theoretical studies, e.g., to understand and predict the stability of the vortex and to model the flow numerically.

## 5.1 Introduction

Longitudinal vortices are often generated for the purpose of separation control and mixing using passive devices called vortex generators. A vortex generator is similar to a wing with a small aspect ratio mounted normally to a surface with an angle of incidence to the oncoming flow. It is designed to overturn the boundary layer flow via large-scale motions, thereby redistributing the streamwise momentum in the boundary layer, which aids in preventing sepa-

ration. Vortex generators were formally introduced by Taylor [131] as an aid in suppressing separation in diffusers. Many studies have presented (nominal) guidelines for optimizing the effect of forced mixing for these passive devices for varying geometries and flow conditions (see, e.g., [52], [107], [124]). Further, a review on low-profile vortex generators was written by Lin [76]. The applicability of controlled near-wall vortices in engineering is vast, since vortices can transport both heat and momentum, aiding in cooling or re-energizing the lowest part of the boundary layer. Being able to control/optimize parameters such as the strength and size of the longitudinal vortices to the existing flow setting is highly desired and it is therefore of interest to develop theories and models which can predict and describe these. Some models have been proposed in order to describe the flow, both theoretically (see, e.g., [127]) as well as computationally (see, e.g., [77, 157]). The model of [127] predicts the flow field induced by low-profile triangular vanes (extending approximately to the logarithmic region of the boundary layer) in a zero pressure gradient boundary layer. The method modifies the governing equations based on the scales of the geometry and the oncoming flow. Good agreement is found with experiments; however, this model only treats low-profile devices extending to a fraction of the boundary layer height. Having a similar geometric configuration, Liu *et al.* [77] introduced vortices numerically using body forces and utilized the fact that the azimuthal velocity distribution of the device-induced vortices is similar to that of Lamb-Oseen vortices. The non-uniform axial component was obtained by introducing a Gaussian distributed streamwise force component. However, this was merely introduced and never motivated more than on a purely empirical basis to compensate for the momentum deficit in the wake of the device.

The main objective of this work is the experimental investigation of device-generated vortices to define helical vortex structures in wall-bounded flow and to create a new model which more correctly can describe the vortex flow. Previously, a lot of experimental work was conducted describing embedded vortices in boundary layer flows using single point measurement techniques; see, e.g., [124, 125]. However, the development of Stereoscopic Particle Image Velocimetry (SPIV) allows non-intrusive instantaneous measurement realizations of the flow in a plane and is the predominating measurement technique for these investigations today; see, e.g., [52, 144]. SPIV measurements in spanwise planes downstream of a single rectangular vortex generator on a flat plate have been conducted and investigated. This configuration is subject to a parametric study, investigating the effect on the helical vortex when varying the angle of the actuating device to the oncoming flow. A turbulent boundary layer profile was considered suitable due to a fuller velocity profile. This also makes the results applicable to flows at more realistic Reynolds numbers. The turbulence level was generated using an inlet grid to yield a high enough turbulence intensity to obtain a turbulent boundary layer profile. Results show that the vortex generator gives rise to longitudinal vortices that possess helical symmetry. A simple theoretical flow model is put forward based on the hypothesis of helical symmetry of the generated vortices and the Gaussian distribution of the vorticity field. The axial and azimuthal vorticity components are coupled according to the definition for helical symmetry of vorticity fields; $\omega_r = 0$ and $\omega_\theta/\omega_z = r/l$, where $l$ represents the helical pitch (see figure 5.1*b*). $u_z$ and $u_\theta$ are the axial and azimuthal velocities, respectively. $u_0$ is the convection velocity of the vortex and r is the radial coordinate. Even though the vortex generators operated in a

turbulent boundary layer, yielding relatively large perturbations, the vortex was observed to be stable in the experiments. Since the velocity formulation used to determine helical symmetry of the vortex is linear, one can apply averaging in both space and time; $< u_z >=< u_0 > \pm < u_\theta r/l >$, where $<>$ indicates averaging. This enables the neglection of, e.g., turbulent pulsations, positional variations of the vortex in time or variations across the azimuthal coordinate $\theta$. If the averaged data can fulfill the averaged velocity formulation, then one has found helical symmetry of the vortex in that averaged sense. None of the previous work has dealt with the helical symmetry of embedded longitudinal vortices and specifically, the longitudinal vortices generated by vortex generators have not previously been known to possess helical symmetry.

## 5.2 Experimental setup and arrangement

Consider the test section setup in figure 5.2. The measurements were carried out in a closed-circuit wind tunnel with an 8:1 contraction ratio and a test section of cross-sectional area $300 \times 600$ mm with length 2 m. At the inlet of the test section, a turbulence-generating grid with mesh length 39 mm was situated. The test section had optical access through the top and bottom walls as well as through the sidewall opposite to the wall with the attached vortex generator. The coordinate system is defined in figure 5.2. $z$ is the axial flow direction, $y$ is the wall-normal direction and $x$ is the spanwise direction.

The experiments were conducted at free stream velocity $\mathrm{U}_\infty = 1.0$ m s$^{-1}$. The wind tunnel speed was obtained by measuring the pressure drop across an orifice plate. The turbulence intensity at the inlet from laser doppler anemometry (LDA) measurements has been found to be 13 %. The boundary layer thickness at the position of the vortex generator has been estimated from LDA measurements to be approximately $\delta_{VG} = 25$ mm. The actuator, as seen in figure 5.2 and in a schematic with a view from above in figure 5.3, is a rectangular vane of the same height as the local boundary layer thickness, $h = \delta_{VG}$, with a length of $2h$. The vortex generator was positioned on a vertical wall in the center of the test section with its trailing edge 750 mm downstream of the inlet grid when it is at zero angle to the mean flow. In order to easily and accurately alter the device angle, the vortex generator was attached to a pin which could be accessed from outside the test section through a hole in the test section wall. This pin was in turn attached to a pointer arm placed over a protractor indicating the relative angle of the actuator to the mean flow direction. The protractor had a radius of 200 mm and grading for integer values of each degree. The device angle of incidence $\beta$ could therefore be determined with a relatively high accuracy. The measurements were conducted in a spanwise plane, with plane normal parallel to the test section walls, positioned five device heights downstream of the vortex generator. The measurement plane has been indicated by a dashed line in figure 5.2. Measurements were conducted for $5^\circ \leq \beta \leq 85^\circ$ with $5^\circ$ angle spacings.

The SPIV equipment was mounted on a rigid stand and included a double cavity NewWave Solo 120XT Nd-YAG laser (wavelength 532 nm) capable of delivering light pulses of 120 mJ. The pulse width, i.e., the duration of each illumination pulse, was 10 ns. The light-sheet thickness at the measurement position was 2 mm and was created using a combination of a spherical convex

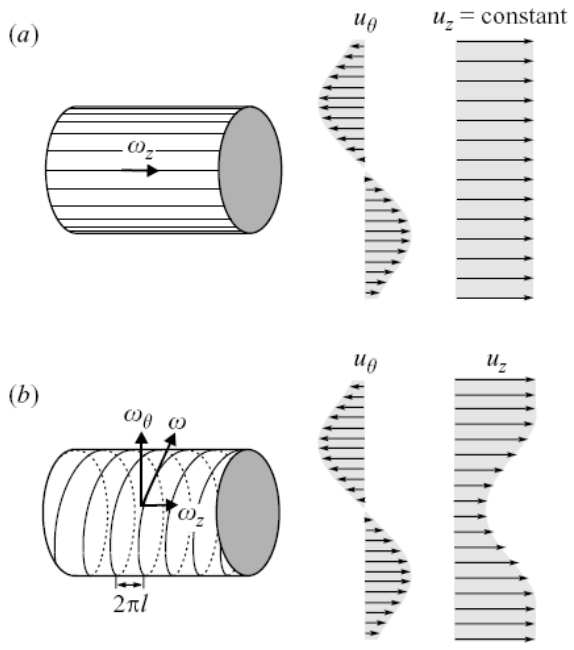


Figure 5.1: Sketch of vorticity field and induced velocity profile by Lamb-Oseen vortex with rectilinear vortex lines (a) and Batchelor vortex with helical structure of vortex lines (b).

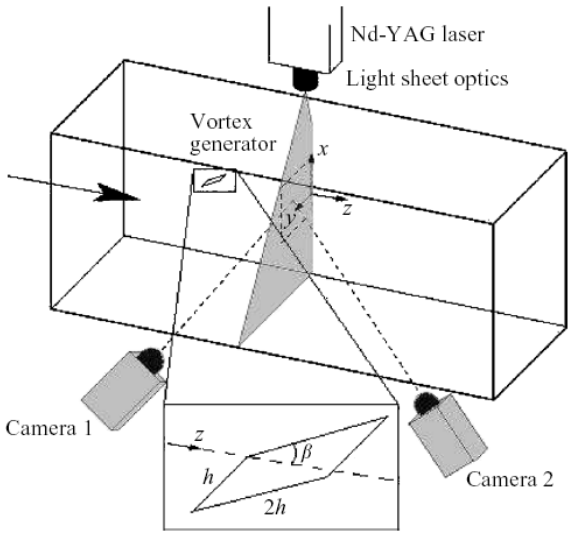


Figure 5.2: Schematic illustration of the experimental set-up and device geometry. The large arrow to the left indicates the main flow direction and $\beta$ the device angle. The measurement plane in the laser sheet has been indicated by dashed lines.

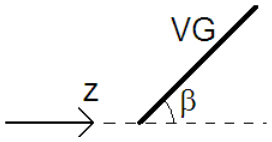


Figure 5.3: Schematic illustration of the vortex generator as seen from above. The variable angle $\beta$ of the vortex generator to the oncoming flow (z-direction) is indicated in the figure.

and a cylindrical concave lens. The equipment also included two Dantec Dynamics HiSense MkII cameras ($1344 \times 1024$ pixels) equipped with 60 mm lenses and filters designed to only pass light with wavelengths close to that of the laser light. Both cameras were mounted on Scheimpflug angle adjustable mountings. The seeding, consisting of DEHS (di-ethyl-hexyl-sebacin-esther) droplets with a diameter of 2–3 $\mu$m, was added to the flow downstream of the test section in the closed-circuit wind tunnel in order to facilitate a homogeneous distribution of the particles before they enter the test section. The laser was placed above the test section, illuminating a plane normal to the test section walls (see figure 5.2). The two cameras were placed in the forward scattering direction. The angle of each respective camera to the laser sheet was 45°. The $f$-numbers of the cameras were set to 2.8, yielding a depth of field which is small but sufficient to cover the thickness of the laser sheet and keeping all illuminated particles in focus while still attaining sufficient scattered light from the tracer particles. In order to avoid reflections from the wall and the vortex generator within the wavelength band of the camera filters, these areas were treated with a fluorescent dye, Rhodamine 6G, mixed with matt varnish to obtain a smooth surface and to ensure that the dye stayed attached. This technique is further described in [144] and section 6.2.7 in Chapter 6.

A calibration target was aligned with the laser sheet. This target had a well-defined pattern, which could be registered by the two cameras to obtain the geometrical information required for reconstructing the velocity vectors received from each camera to obtain a full description of all three velocity components in the plane. Calibration images were recorded with both cameras at five well-defined streamwise positions throughout the depth of the laser sheet in order to capture the out-of-plane component in the reconstructed coordinate system of the measurement plane under consideration [128]. A linear transform was applied to these images for each camera to perform the reconstruction. This procedure was executed both previous to and after the conduction of the measurements to ensure that no drift had occurred. The images were processed using Dantec DynamicStudio software version 2.0. Adaptive correlation was applied using refinement with an interrogation area size of $32 \times 32$ pixels. Local median validation was used in the immediate vicinity of each interrogation area to remove spurious vectors between each refinement step. The overlap between interrogation areas was 50%. For each measurement position, 500 realizations were acquired. The recording of image maps was done with an acquisition rate of 1.0 Hz, ensuring statistically independent realizations based on the convection velocity $U_\infty = 1.0\ \mathrm{m\,s^{-1}}$ and the mesh size $d = 0.039$ m, yielding a time scale of $t = d/U_\infty = 0.039$ s. The velocity vector maps contain $73 \times 61$ vectors. The

linear dimensions of the interrogation areas $(x,y) = (1.55,1.04)$ mm can be compared to the Taylor microscale and the Kolmogorov length scale estimated to $\lambda_f \approx 9$ mm and $\eta \approx 0.5$ mm from LDA measurements [123]. A characterization study of the inlet flow can be found in Chapter 8.

## 5.3 Modeling of the longitudinal vortex

The existence of Lamb-Oseen reminiscent vortex structures embedded in wall-bounded flow has been reported in various experiments and numerical simulations (see, e.g., Liu *et al.* [77]). For the Lamb-Oseen vortex, the vorticity is non-zero only for the axial component as (see figure 5.1*a*)

$$\omega_r = 0; \quad \omega_\theta = 0; \quad \omega_z = \frac{\Gamma}{\pi\varepsilon^2} \exp\left(-\frac{r^2}{\varepsilon^2}\right). \tag{5.1 a–c}$$

A more general model is the Batchelor vortex [6], which includes the non-uniform axisymmetrical axial velocity distribution $u_z$ which approaches the Lamb-Oseen vortex in the extreme. This vortex model is commonly used in instability studies of swirling flows (see [54] and references therein). To describe experimental swirl flows [5, 31, 68] the Batchelor vortex model is usually referred to in the form

$$u_\theta = \frac{K}{r}\Big(1 - \exp\left(-\alpha r^2\right)\Big); \quad u_z = W_1 + W_2 \exp\left(-\alpha r^2\right) \tag{5.2 a,b}$$

where $K$, $W_1$, $W_2$ and $\alpha$ are empirical constants with simple physical interpretations as identified by [98]

$$\Gamma = 2\pi K; \quad l = K/W_2; \quad u_0 = W_1 + W_2 \quad \text{and} \quad \varepsilon = 1/\sqrt{\alpha} \tag{5.3 a–d}$$

where $\Gamma$ is the vortex strength (circulation), $l$ is the pitch of the helical vortex lines, $u_0$ is the advection velocity of the vortex and $\varepsilon$ is the effective size of the vortex core with Gaussian axial vorticity distribution (see figure 5.1*b*). The profiles given in (5.2) can reproduce experimentally determined swirl flow with high accuracy. One possible approach is to test if the empirical model (5.2) can describe the longitudinal vortex in the present case. However, in accordance with [109] one needs to account for the possible disturbance of the mirror vortex, resulting from the presence of the wall. Another more suitable approach is therefore to extend the Batchelor vortex model to model the flow by helical symmetry of the vorticity, leaving no restrictions on the shape of the vortex core. Flows with helical vorticity can be described by correlation between the axial and circumferential vorticity vector components

$$\omega_r = 0; \quad \omega_\theta = r\omega_z/l; \quad \omega_z = \frac{\Gamma}{\pi\varepsilon^2} \exp\left(-\frac{r^2}{\varepsilon^2}\right) \tag{5.4 a–c}$$

with the vorticity vector always directed along the tangent of the helical lines $x = r\cos\theta$; $y = r\sin\theta$; $z = l\theta$. Flows with helical vorticity can in addition be characterized by the following condition for the velocity field $\vec{u} = \{u_r, u_\theta, u_z\}$:

$$u_z + \frac{r}{l}u_\theta = u_0 \equiv \text{constant} \quad \text{or} \quad u_z = u_0 - \frac{r}{l}u_\theta \tag{5.5 a,b}$$

It can be shown that conditions (5.4*a,b*) and (5.5) are equivalent (cf., [99]). For a flow fulfilling the requirement of (5.5), the main flow parameters are $u_0$ and $l$. Sometimes $u_0$, $u_z$ and $u_\theta$ are found directly from measurements. The pitch $l$ can then be deduced from (5.5), but this approach might lead to an estimate of high relative error if $u_z - u_0$ is small. Multiplying (5.5) by $u_z$ and integrating over the cross-section of the flow one can obtain the pitch through the swirl number $S$ (see Alekseenko *et al.* [5])

$$l = -F_{mm}/(F_m - u_0 G), \tag{5.6}$$

where $F_{mm} = \int_\Sigma \rho u_\theta u_z r \, \mathrm{d}\Sigma$ is the angular momentum flux in the axial direction, $F_m = \int_\Sigma \rho u_z^2 \, \mathrm{d}\Sigma$ the momentum flux in the axial direction, $G$ the flow rate, $\rho$ the fluid density and $\Sigma$ the cross-section area. All parameters can now be determined: $u_0$ is found directly from the measurements, $l$ is found through (5.6) and the circulation $\Gamma$ and the vortex size $\varepsilon$ can be extracted from (5.4*c*). Based on the experimental observation the simple Batchelor vortex model is chosen as

$$u_\theta = \frac{\Gamma}{2\pi r}\left[1 - \exp\left(-\frac{r^2}{\varepsilon^2}\right)\right]; \quad u_z = u_0 - \frac{\Gamma}{2\pi l}\left[1 - \exp\left(-\frac{r^2}{\varepsilon^2}\right)\right]. \tag{5.7a,b}$$

The only requirements of this simple model are the size of the vortex core, the circulation, the helical pitch and the vortex advection velocity.

## 5.4 Testing of helical symmetry and embedded columnar vortex flow

The analysis of the embedded vortices was done based on the ensemble averaged complete cross-plane velocity field from the SPIV measurements and the therefrom derived axial vorticity component (see figure 5.4*a–c*). The iso-contour maps of axial vorticity reveal the presence of a secondary vortex, which can be seen next to the main vortex at $x/h \approx 3$ in the iso-contour map for $\beta = 35°$ in figure 5.4(*b*). Figure 5.4(*d*) displays a sketch of the primary and the secondary vortices in the upper half and the mirrored velocity field in the lower half.

Figure 5.5 shows the measured axial $u_z$ (upper) and azimuthal $u_\theta$ (lower) velocity profiles (+) for various values of the device angle $\beta$ extracted along a line parallel to the wall through the center of the primary vortex. Verification of the hypothesis of helical symmetry was done by comparing the left- (+) and right-hand side (∘) of (5.5*b*) calculated from the measured values of $u_z$ and $u_\theta$. The helical pitch $l$ was found by minimizing the sum of the residuals of the right- and left-hand sides of (5.5*b*) in a least squares sense for a limited set of points in the radial direction. The values computed from the right-hand side (∘) are only displayed on the left side of the primary vortex center, since the flow on the right side is perturbed by the secondary vortex. The two data sets overlap quite well, which is why the difference between the calculated and measured values is hardly visible for some angles.

The axial vorticity fields of the vortices derived from the measurement data have Gaussian distributions and one can therefore use (5.4*c*) to find an estimate of the circulation $\Gamma$ and vortex size $\varepsilon$ of both the main and the secondary vortices. The local flow characteristic $u_0$ was found directly from the measurements and

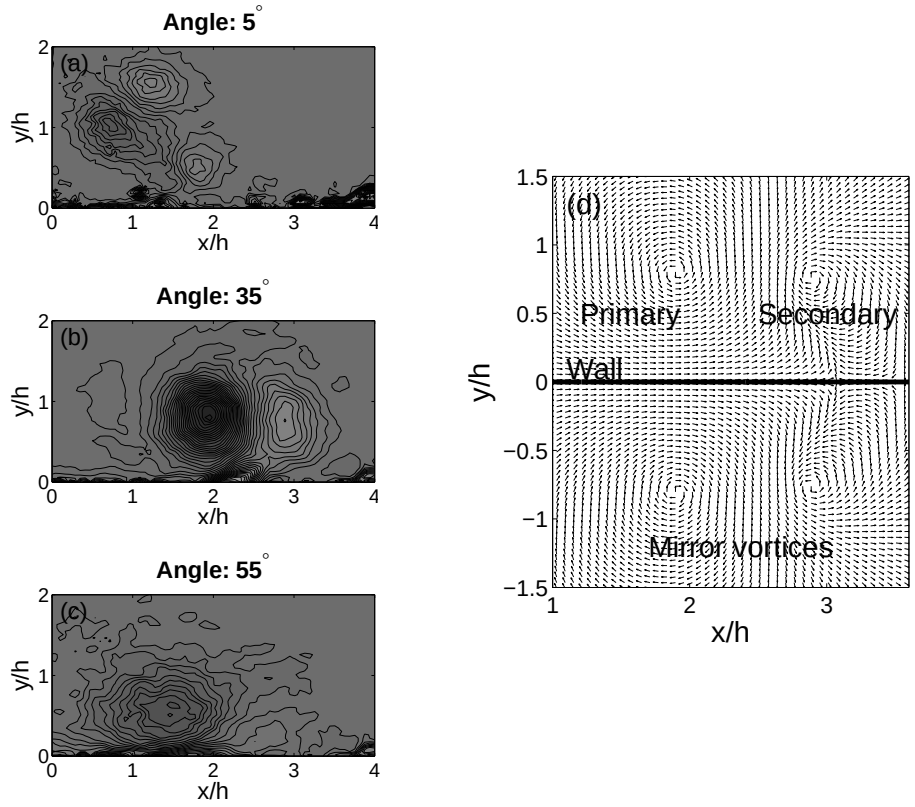


Figure 5.4: Iso-contour maps of axial vorticity for device angles $(a)$ $\beta = 5°$, $(b)$ $\beta = 35°$ and $(c)$ $\beta = 55°$. In $(d)$ a sketch showing a sample velocity distribution of the primary and secondary (upper half) and mirror vortices (lower half) in the range $20° \leq \beta \leq 40°$ is presented. The wall is illustrated by a thick line at $y/h = 0$.

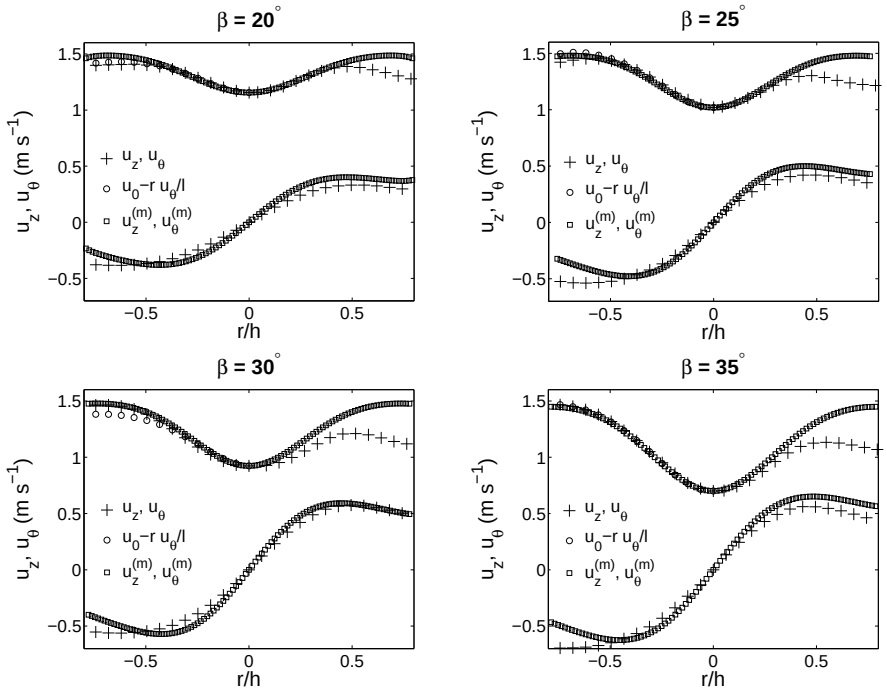


Figure 5.5: Testing of helical symmetry of embedded vortices generated by a vortex generator for various device angles $\beta$. The measured axial ($u_z$, upper) and azimuthal ($u_\theta$, lower) velocity profiles (+) are plotted. The measured values $u_z$ are compared to the right-hand side of (5.5$b$) calculated using the measured values $u_\theta$ ($\circ$). These computed values are only displayed on the left side, since the flow on the right side is perturbed by the secondary vortex. The two data sets overlap quite well and the difference between the calculated and measured values is hardly visible for some angles. Also the azimuthal and axial velocity profiles of the utilized vortex model (5.7$a$,$b$) are displayed ($\square$).

the helical pitch $l$ was obtained from (5.6), yielding a result which agreed well with the values obtained by minimizing the sum of residuals of (5.5$b$) in a least squares sense. The azimuthal ($u_\theta^{(m)}$) and axial ($u_z^{(m)}$) velocities induced by the main vortex were modeled using (5.7$a$,$b$) ($\Box$) and should be compared to the measurements (+) (see figure 5.5). This simple model is decoupled from all additional flow effects such as the secondary and mirror vortices and the non-uniform flow due to the presence of the wall. In spite of this, the model describes the primary vortex flow well in the regime under consideration.

The secondary vortex is present with varying strength at all considered device angles, introducing a disturbance in the flow field of the main vortex and thereby causing asymmetry. The mirror vortices will have the same effect on the symmetry of the main vortex. For angles smaller than 15°, an additional vortex was observed, increasing the complexity of the flow by yielding a three-vortex system perturbing the vorticity distribution and the velocity field considerably (see figure 5.4$a$). For small values of $\beta$, the vortex system becomes more complicated and (5.4$c$) is not representative for the actual flow. For angles larger than 40°, the fit again becomes worse due to the instabilities for high values of circulation at large device angles (see figure 5.4$c$). For increasing values of $\beta$, the vorticity component will surpass from streamwise to more and more spanwise, eventually resulting in pure shedding in the extreme $\beta = 90°$. Due to the decreasing longitudinal vorticity component for large values of $\beta$, the helical symmetry is destroyed. The deviations arise because we have a simple model with linear interactions, which is being compared to measured values originating from a more complex representation of the flow. Nonlinearities are not captured by the linear model and become increasingly dominant outside the range $20° \leq \beta \leq 40°$.

Figure 5.6 shows the device angle dependency of the parameters of the problem in the range $20° \leq \beta \leq 40°$. The device angle dependency of the vortex radius $\varepsilon$ and circulation estimate $\Gamma$, obtained from the Gaussian fit (5.4$c$) of the vorticity, are shown in figures 5.6($a$) and 5.6($b$), respectively. The data sets have been fitted with a linear approximation in a least squares sense, with corresponding error estimates. For the estimate of the circulation, the fitting has been extrapolated to zero device angle. As expected, the extrapolated circulation is approximately zero at $\beta = 0°$, since a device with no angle to the flow ideally will not give rise to any circulation. One can see that the vortex size and the magnitude of the circulation increase linearly with the device angle. The device angle dependency of the helical flow characteristics $l$ and $u_0$ with linear fitting and error bars are shown in figures 5.6($c$) and 5.6($d$), respectively. In figure 5.6($c$), the values of the helical pitch $l$ obtained from minimizing the residual of (5.5$b$) in a least squares sense ($\circ$) are compared to the helical pitch of the swirling flow (5.6) ($\Box$) obtained using the axial and azimuthal velocities of the model (5.7$a$,$b$). These two data sets are strongly correlated and it is also seen that the pitch only varies marginally with device angle $\beta$. The advection velocity of the vortex $u_0$ decreases linearly with device angle.

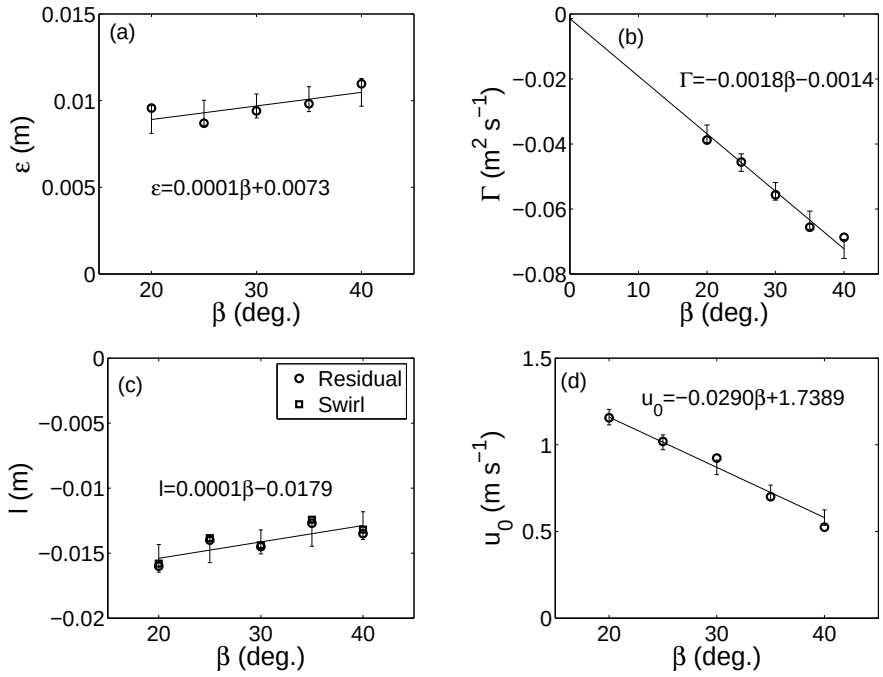


Figure 5.6: Device angle $\beta$ dependency of (a) the vortex radius $\varepsilon$, (b) the circulation $\Gamma$, (c) the helical pitch $l$ and (d) the advection velocity of the vortex $u_0$. The data sets are provided with a linear fit in a least squares sense with corresponding error bars. In (c), the helical pitch $l$ has been obtained from minimizing the residual of (5.5$b$) in a least squares sense ($\circ$) and is compared to the helical pitch of the swirling flow (5.6) ($\square$) obtained using (5.7$a$,$b$).

## 5.5 Conclusions

Vortices generated by a passive rectangular vane-type vortex generator of the same height as the boundary layer thickness in a flat plate wall-bounded flow have been studied experimentally. It has been shown that the embedded vortices possess helical symmetry in the device angle range $20° \leq \beta \leq 40°$. Despite that the vortex generators operated in a turbulent boundary layer with relatively large perturbations, the vortex was observed to be stable in the experiments. The velocity formulation for helical symmetry of the vortex is linear, hence one can apply averaging in both space and time; $< u_z >=< u_0 > \pm < u_\theta r/l >$, where $<>$ indicates averaging. One can therefore neglect, e.g., turbulent pulsations, positional variations of the vortex in time or variations across the azimuthal coordinate $\theta$. If the averaged data can fulfill the averaged velocity formulation, then one has found helical symmetry of the vortex in that averaged sense.

The flow field in the considered regime consists of two vortices, the primary one and the secondary one. Outside of this range additional flow effects influence the helical vortex in a destructive way, deterring the helical symmetry to persist. The vorticity distribution across the vortices is Gaussian, yielding estimates of the vortex radius $\varepsilon$ and circulation $\Gamma$ through (5.4*c*). This rendered the possibility to describe the flow in a realistic and simple fashion, utilizing a model for the azimuthal and axial velocity components (5.7*a,b*). Comparison of these modeled velocities to the measured data showed to concur well in the device angle regime under consideration. Being the main flow characteristics of a vortex with helical symmetry, the determination of the helical pitch $l$ and the axial velocity at the vortex center $u_0$ is of great importance to characterize the vortex (5.5*a,b*). $u_0$ was obtained directly from the measurements, whereas the pitch was determined by minimization of the sum of the residuals of (5.5*b*) in a least squares sense or alternatively from (5.6). The results of these two methods for pitch evaluation showed a high degree of concurrence.

The vortex radius $\varepsilon$, the circulation $\Gamma$, the helical pitch $l$ and the advection motion of the vortex (or axial velocity at the vortex center) $u_0$ all showed linear dependency with the device angle $\beta$. These simple relations render it possible to predict these parameter values for device angles in the range $20° \leq \beta \leq 40°$ well and thereby determine vortex strength, size and axial flow distribution. They also facilitate theoretical studies analyzing, e.g., stability and aid in modeling, the flow within this range. The vortex radius showed a weak increase with increased device angle $\beta$, while the circulation $\Gamma$ showed a large increase in magnitude. The vortex advection velocity $u_0$ decreased with increased device angle while the helical pitch did not change notably and can, for the purpose of the model, be considered close to constant.

# Part III

# Separation Control

# Chapter 6

# Generic Experiment - Low Re Wind Tunnel

Stereoscopic Particle Image Velocimetry measurements have been executed in a low-speed wind tunnel in spanwise planes in the flow past a row of vortex generators, mounted on a bump in a fashion producing counter-rotating vortices. The measurement technique is a powerful tool, providing all three velocity components in the entire measurement plane. The objective of this study is to investigate the effect of vortex generators in a turbulent, separating, low Reynolds number ($Re = 20\,000$ based on the bump chord $c = 0.3$ m and free stream velocity $U_\infty = 1.0$ m s$^{-1}$) boundary layer over a geometry which is generating an adverse pressure gradient similar to the flow past a wind turbine blade. The low Reynolds number is chosen on the basis that this is a fundamental investigation of the structures of the flow induced by vortex generators and the fact that one obtains a thicker boundary layer and larger structures evoked by the actuating devices, which are easier to measure and resolve. The flow behaves as expected, in the sense that the vortices advect high momentum fluid into the boundary layer, making it thinner and more resistant to the adverse pressure gradient with respect to separation. The amount of reversed flow is significantly reduced when vortex generators are applied. The idea behind the experiments is that the results will be offered for validation of modeling of the effect of vortex generators using various numerical codes. Initial LES computations have been performed that show the same qualitative behavior as in the experiments. Results show that mounting the actuators in a cascade, producing counter-rotating vortices, can eliminate the perturbing secondary vortex generated for each actuator, see Chapter 5. Further, the downstream development of the device induced vortices, which possess helical symmetry (see Chapter 5 or [146]), is studied. Since rectangular actuators provide a more symmetric flow around the vortex core, these actuators were chosen for this investigation. The downstream evolution of characteristic parameters of helical vortices is studied, displaying a linear variation of the helical parameters up to the trailing edge of the bump where the vortices experience an abrupt transition in structure.

## 6.1 Introduction

Vortex generators, as described by Taylor [131, 132, 133, 134], have been used for more than fifty years in applied aerodynamics on airplane wings. Vortex generators belong in the category boundary layer manipulators. Their function is to re-energize an adverse pressure gradient boundary layer that is about to separate by advecting high momentum fluid from the outer part of the boundary layer down to the low momentum zone closer to the wall. A vortex generator is commonly a small triangular or rectangular plate that is mounted on a surface at an angle to the incoming flow, see figure 6.1. A vortex generator acts like a small wing with a low aspect ratio and the flow past the tip creates a longitudinal vortex that transports high momentum fluid down into the near wall region of the boundary layer. The positive effect of vortex generators on an airplane wing is to delay separation to higher angles of attack and thus increasing the maximum lift coefficient so that an airplane can land at a lower speed. However, this increased maximum lift is paid for by a so-called drag penalty, where the drag for small angles of attack is increased. Vortex generators are also used to increase the maximum speed of commercial jets flying at approximately Mach 0.8. Locally on the wing, the flow is accelerated and can exceed the speed of sound, Mach 1, which can cause so-called shock induced separation even for very low angles of attack. This is easily felt by the pilot and determines the speed limit on many subsonic passenger airplanes. However, vortex generators can also be used to delay this type of separation to allow the airplane to fly slightly faster. Since commercial jets have no problems in increasing the lift coefficient at, e.g., landing configuration by using flaps and slats, the main reason that they often are equipped with vortex generators is shock induced separation.

For small airplanes and wind turbines, the flow is far from reaching Mach 1 and there is thus no problem with shock induced separation. However, sometimes a high lift coefficient is needed to decrease the landing speed for STOL airplanes (Short Take of and Landing). A classical solution has been to use so-called slots in front of the leading edge. The slot is a small, stationary list in front of the edge of the main wing that for large angles of attack allows high momentum flow from the pressure side to be accelerated in the slot between the list and the main wing creating a high momentum flow to the suction side of the wing and thus makes the flow more resistant to the adverse pressure gradient. Vortex generators have the same effect on the flow in the sense that they also delay separation and increase the maximum lift coefficient. Because they can be mounted/glued directly to the pressure side of a bare wing, a less complicated wing can be built and therefore they are often used on modern sport planes instead of slots. Vortex generators are sometimes used to prevent separation of the flow past the rudder or ailerons to improve the controlling of the airplane, which could otherwise be drastically worsened. Vortex generators are used on wind turbine blades for two reasons. One is to decrease separation and increase lift at high angles of attack and the other is to attempt to increase the maximum ratio between the lift and the drag coefficients, which directly influences the aerodynamic efficiency of the turbine. The relative wind seen by a wind turbine blade is composed by the incoming wind speed and the rotational velocity of the blade. There exists an optimum value for the tip speed ratio, $\lambda_{opt} = \omega \mathrm{R}/\mathrm{V}_o$, where the wind turbine operates most efficiently. To run the turbine at this optimum value, it is necessary to increase the angular velocity

of the rotor, $\omega$, proportionally to an increasing wind speed, $V_o$. However, there is for noise reasons a limit on the speed of the tip of approximately 70 m/s, that gives a limit on the rotational speed of $\omega_{max} = 70/\mathrm{R}$, where R is the rotor radius. The rotational speed of approximately 70 m/s at the tip decreases linearly further inboard with the decreasing radius. Thus, the flow at the tip will mainly be in the rotor plane and near the hub the flow seen by the blade will almost be perpendicular to the rotor plane. This twisting of the relative wind speed could in principle be compensated for by twisting the blades, but there is, for structural reasons, a limit of the extent to which this can be done. Since the relative wind speed increases when approaching the tip, the highest aerodynamic loads are also situated here, giving large bending moments at the root of the blades. To be able to carry these loads, the blade must be very thick close to the root and eventually it often ends with a cylindrical cross section. The last real airfoil (i.e., with cross section with a sharp trailing edge) often has a thickness to chord ratio of more than 30%. This is very bad from an aerodynamic point of view in the sense that the flow may separate even for very small angles of attack. This, in combination with the fact that the angles of attack for these inboard sections, for the reasons given above, are large, almost guarantees a separated flow for all wind speeds even for pitch regulated machines. Since vortex generators are known to delay and to some extent suppress separation, it is natural to apply vortex generators on the inner part of wind turbine blades. Because vortex generators give some drag penalty also for low angles of attack, they are normally not used on the outer part of wind turbine blades. The fact that vortex generators can have quite a dramatic effect on the performance of wind turbines is shown in [103], where a comparison between the measured power curve on the 1 MW experimental Avedøre wind turbine is shown with and without vortex generators on the inner part of the blades, see figure 1.3 Chapter 1. At a wind speed of 15 m/s, the gain in power output due to the usage of vortex generators is 25%. The maximum power occurring at a wind speed of around 17 m/s for a pitch of -1 degree for the wind turbine running in stall regulation is approximately 850 kW for the clean configuration and 1050 kW when using vortex generators. However, this extreme increase in power output can be explained by over-optimistic values for the lift coefficient for the innermost part of the blade during the design of the wind turbine and should not be expected for all wind turbines.

To have an effect over a section of a blade, vortex generators are mounted in arrays and often in pairs that can produce either co- or counter-rotating vortices. Further, the size, geometry, aspect ratio, angle of incidence to the flow, chordwise position in relation to the separation line, configuration of co- or counter-rotating vortices etc. are parameters that must be optimized in order to use vortex generators in a most efficient manner. To answer these questions, one needs to do experiments. In [76], a review by Lin *et al.* on experimental research on vortex generators is given. In a recent paper by Godard and Stanislas [52], a parametric study of the effect of vortex generators was conducted in which the devices were placed on a bump designed to keep the boundary layer flow on the verge of separation. An optimum vortex generator geometry was sought using hot film sensor skin friction measurements and thereafter characterized using Stereoscopic Particle Image Velocimetry (SPIV). The main conclusions were that triangular vanes in a counter-rotating configuration give the best effect on skin friction increment. The optimal device configuration showed good

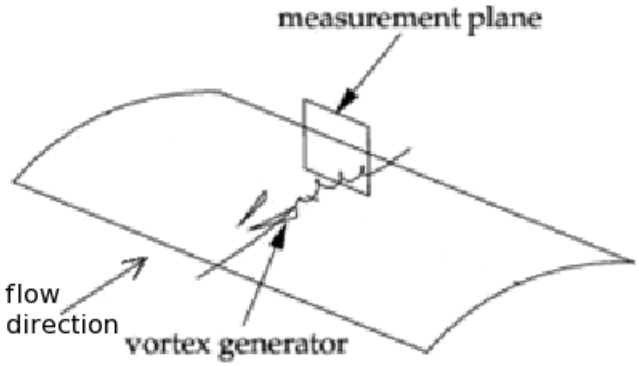


Figure 6.1: Triangularly shaped vortex generators. The figure is originally from [115].

concurrence with results found in the literature for all parameters except for the device height, which appeared to behave differently from results found in the literature. The characterization study done on the most optimal case showed counter-rotating vortices, stable in their downstream development, transferring momentum from the outer flow and in towards the near wall region.

As a starting point, this optimal configuration was employed in the present study as well, even though the conditions are different. Results showed similar overall behavior in the flow to that found by Godard and Stanislas [52]. Results of the current study also show that the rectangular vortex generator induced vortices possess helical symmetry, which was also shown in Chapter 5 and in [146]. Further, mounting the vortex generators in a cascade in a fashion generating counter-rotating vortices cancels out the perturbing secondary vortex present in the previous study. The helical parameters display a linear variation across the bump chord up to the trailing edge of the bump, where the vortices experience an abrupt transition to a different state, obtaining a new structure.

## 6.2 Experimental setup

### 6.2.1 Wind tunnel

The measurements were carried out in a closed-circuit wind tunnel with an 8:1 contraction ratio and a test section of cross sectional area 300×600 mm with length 2 m. The suction side of a wind turbine wing is represented by a bump mounted vertically on one of the test section walls with the leading edge positioned 600 mm downstream of the inlet grid. The bump is a circular sector, extended in the spanwise direction, creating a cylindrical sector with radius 390 mm. The bump height is 30 mm and the chord length and bump width are 300 mm and 600 mm respectively. The presence of this model in the flow induces an adverse pressure gradient strong enough to generate separation. The experiments were conducted at a free stream velocity of $U_\infty = 1$ m/s, corresponding to Re = 20 000 based on the bump chord length. The turbulent inflow is assured by a turbulence generating inlet grid with mesh length M = 39 mm situated at

the beginning of the test section. In [123], the turbulence intensity at the inlet has been estimated to 12% and the boundary layer thickness at the streamwise position of the actuators has been estimated from LDA measurements to 25 mm. These values were found prior to the redesign of the wind tunnel. A characterization study of the inlet flow, measured after the amendments to the wind tunnel, is presented in Chapter 8.

The boundary layer is here defined as the part of the flow contained by vorticity derived from the presence of the wall. The principle of determining the boundary layer thickness is to determine where the vorticity is reduced to a value much smaller than the maximum value ($\omega_z = 0.01\omega_{z\,max}$). This is here defined as the boundary where the viscous effects cease to influence the flow. When calculating the vorticity, it is tedious to do measurements that give you the data to calculate both terms. In the potential flow free stream, the first and the second term must cancel out since there is no vorticity. In the boundary layer, however, vorticity is present, which means that the terms must be unequal. An order of magnitude analysis gives that if U and x are of order 1, then V and y are of order $\delta$. Therefore the second term is quadratically larger than the first term.

$$\omega_z = \frac{1}{2}\left( \underbrace{\frac{\partial V}{\partial x}}_{\frac{\delta}{1}} - \underbrace{\frac{\partial U}{\partial y}}_{\frac{1}{\delta}} \right) \tag{6.1}$$

Therefore one can argue that the second term should be sufficient in determining the vorticity. The boundary layer thickness was therefore extracted from a velocity profile measured by LDA at the position of the trailing edges of the vortex generators with no actuators present. $\partial U/\partial y$ was obtained from the velocity profile and thereby also the estimate of the vorticity.

### 6.2.2 Actuators

Vanes of the same height as the boundary layer thickness, $\delta_{VG}$, were applied. $\delta_{VG}$ represents the boundary layer thickness at the position of the trailing edges of the devices. Due to their frequent use in applications such as on wind turbine blades, the effect of triangular vanes was studied in the sense of separation control. However, rectangular vanes were used in the study of the downstream development of the vortices since they generate vortices with a more symmetric core as observed in the azimuthal direction. The vortex generators were positioned with their trailing edges at 50% bump chord. The resulting parameters from the optimal vortex generator configuration found as a result of the optimization study performed by Godard and Stanislas [52] have been used and can be found in figure 6.2, where $h$ is the device height, $l$ is the device length, $s$ is the distance between the trailing edges of two vortex generators within one pair, $z$ is the distance between two vortex generator pairs and $\beta$ is the device angle of incidence. This geometry was chosen only as a starting point. The optimum geometry will, of course, depend on the application and is therefore most likely not universal, but has nevertheless also been used in this experiment. The distance between the devices and the separation line showed a weak dependency on the wall shear stress and was therefore not considered in this study.

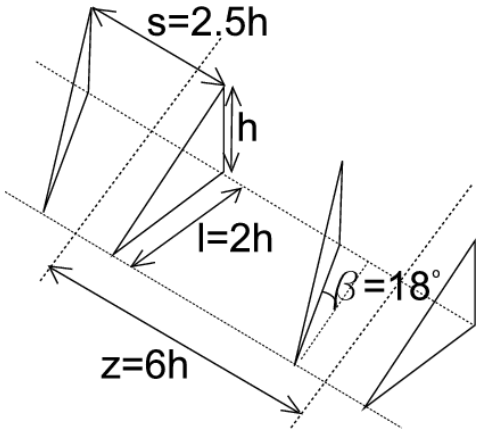


Figure 6.2: Sketch of vortex generator geometry.

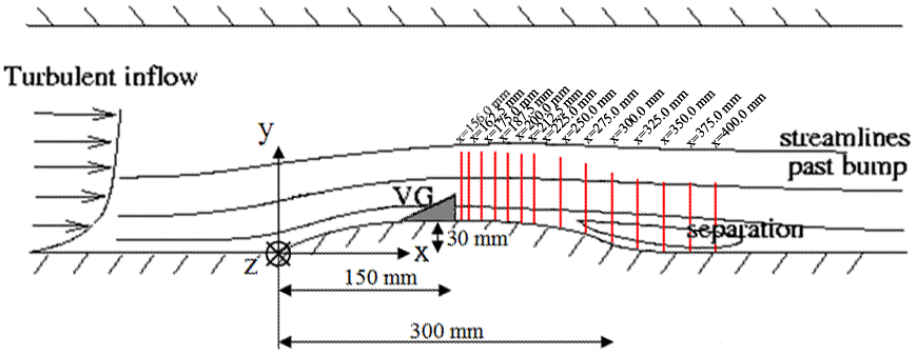


Figure 6.3: Sketch of the wind tunnel test section, the positioning of measurement planes and definition of coordinate system.

### 6.2.3 Measurement planes

The measurements were conducted in spanwise planes at various positions downstream of the vortex generators. A sketch of the wind tunnel test section and the positioning of measurement planes is shown in figure 6.3, where also the coordinate system is defined. The equipment was mounted on a rigid traverse, traversing in the axial and normal directions. This configuration enables one to calibrate only once and perform measurements accurately at the different streamwise positions using the same calibrated configuration. All measurement planes are parallel to each other and their normal component is parallel to the test section walls.

### 6.2.4 Setup of SPIV equipment

The experimental setup is illustrated by a sketch in figure 6.4. A laser was placed above the test section, illuminating the vertically mounted bump from the side. Two cameras were placed on the same side of the light sheet, resulting in one

camera placed in the forward scattering direction and one in the backward scattering one. The angle of each respective camera to the laser sheet was 45°. The f-numbers were set to between 8 and 16 for the camera in the forward scattering direction and 4 or 5.6 for the camera in the backward scattering one, depending on the light budget of the particle scattering and reflections from surfaces at each individual plane position. The stereoscopic PIV equipment included a double cavity NewWave Solo 120XT Nd-YAG laser (wavelength 532 nm), capable of delivering light pulses of 120 mJ. The pulse width, i.e., the duration of each illumination pulse, was 10 ns. The light sheet thickness at the measurement position was 2 mm and was created using a combination of a spherical convex and a cylindrical concave lens. The equipment also included two Dantec Dynamics HiSense MkII cameras ($1344 \times 1024$ pixels) equipped with 60 mm lenses and filters designed to only pass light with wavelengths close to that of the laser light. Both cameras were mounted on Scheimpflug angle adjustable mountings. The seeding, consisting of glycerol droplets with a diameter of 2-3 $\mu$m, was added to the flow downstream of the test section. The seed particles were added at this position in order to obtain a more homogeneous distribution of the tracers throughout the measurement volume without significantly disturbing the flow. This kind of global seeding of the complete tunnel is possible since the tunnel is a closed-circuit wind tunnel. The size of the seed particles has been measured by an APS TSI 3320 time-of-flight spectrometer. The droplets are produced by blowing pressurized air over a thin-walled pipe with diameter of 0.5 mm. The other end of the pipe is submerged in glycerol.

A calibration target was aligned with the laser sheet. This target has a well defined pattern, which can be registered by the two cameras to obtain the geometrical information required for reconstructing the velocity vectors received from each camera to obtain a full description of all three velocity components in the plane. Calibration images were recorded with both cameras at five well defined streamwise positions throughout the laser sheet according to Soloff *et al.* [128]. A linear transform was applied to these images for each camera respectively to perform the reconstruction. This procedure was executed both previous to and after the measurements to assure that no drift had occurred.

### 6.2.5 Data processing

The images were processed using Dantec FlowManager software version 4.7. Adaptive correlation was applied using refinement with an interrogation area size of $32 \times 32$ pixels. Local median validation was used in the immediate vicinity of each interrogation area to remove spurious vectors between each refinement step. The overlap between interrogation areas was 50%. For each measurement position, 500 realizations were acquired. The recording of image maps was done with an acquisition rate of 1.0 Hz.

The disparity was typically around 0.05 pixels, i.e., smaller than the optimal measurement accuracy of the PIV system (0.1 pixels). No calibration correction was therefore applied. The Taylor microscale was estimated to $\lambda_f \approx 9$ mm from LDA measurements of time series at a position 270 mm downstream of the inlet at the center of the cross-section of the test section [123]. This should be compared to the PIV interrogation area size, which was approximately 1-2 mm for all measurements under consideration. With the prerequisites of the measurement setup, it was possible to align the calibration target to the laser sheet

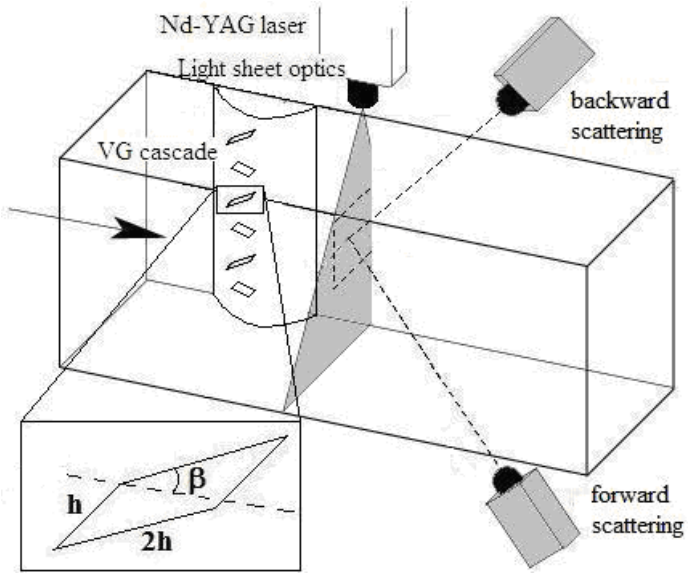


Figure 6.4: Sketch of the SPIV setup at the test section with rectangular actuators mounted.

with an accuracy significantly smaller than the measured Taylor microscale at that position.

### 6.2.6 Mean fields, spatial resolution and accuracy

The velocity vector maps contain 73 by 63 vectors. The interrogation areas have linear dimensions 1.15 mm in the y-direction and 1.73 mm in the z-direction. In the PhD thesis by Schmidt [123], the Taylor microscale was estimated from LDA measurements of time series to be in the order of $\lambda_f \approx 9$ mm at a position 330 mm upstream of the bump leading edge at mid-channel. The estimate of the Kolmogorov length scale was in the order of $\eta \approx 0.5$ mm. LDA velocity profile measurements had also been used to obtain the wall shear stress at the same downstream position. From this, an estimate of the viscous length scale is obtained, $\delta_\nu = \nu(\rho/\tau_w)^{1/2} = 0.2$ mm. The spatial resolution of the velocity vector fields is defined by the size of the interrogation area, which also limits the spatial resolution of the estimation of velocity gradients and hence vorticity. In order to resolve the smallest scales in the flow, one needs to fulfill the Nyquist criterion. Therefore, scales smaller that half of the size of the interrogation area can not be resolved. Streamwise vorticity was calculated using central differencing, which gives second order accuracy of the velocity derivative estimate and half the uncertainty of, e.g., forward or backward difference. The scheme cancels out the effect of oversampling from the 50% overlap between interrogation areas, in the estimation of the velocity gradient, since neighboring data is not correlated (cf., Raffel *et al.* [111]).

Since the PIV velocity measurement points are local averages over the area of interrogation, one can never obtain measurements closer to the wall than half of the height of the interrogation area size. And even then, because of the

Table 6.1: Control parameters for evaluation of correlation noise.

| Control parameters | |
|---|---|
| $N_I \geq 10 - 20$ | Particle image density<br>$N_I$ - mean number of particle images in an interrogation area |
| $F_O \geq 0.75$ | Loss of particles due to out-of-plane motion<br>$F_O$ - fraction of particles present inside the interrogation area in both images |
| $M\|\Delta U\|\Delta t/d_\tau \leq 0.5$ | Velocity gradients<br>$M$ (pix/m) - image magnification<br>$\Delta U$ (m/s) - difference in velocity across the interrogation area<br>$\Delta t$ (s) - time between acquired PIV images<br>$d_\tau$ - mean particle image diameter |

high velocity gradients in this region that are averaged out across the interrogation window, one needs to be careful in interpreting the measurements at these points. Therefore, the position of the wall was determined by extrapolating the mean velocity profiles towards the wall using the no-slip condition.

Keane and Adrian [65] used an analytical model and Monte Carlo simulations to investigate the effects of experimental parameters to optimize PIV performance. They showed that double-pulsed systems were optimal when the interrogation area particle image density exceeded 10-20. They also showed that velocity gradients reduce the valid data rate and introduce velocity bias. The primary source of error in 2-component PIV measurements is correlation noise. Westerweel [152] and Foucaut *et al.* [34] have shown that if the values of the control parameters in table 6.1 are satisfied, then the RMS of the measured particle image displacements $\sigma_{corr} \approx 0.1$ pixel.

The dominating factor from table 6.1 is the effect of velocity gradients, which was only altered by changing the image magnification and the time between pulses. If there are large velocity gradients in the flow, variations of particle displacement across the interrogation areas will lead to a broadening of the correlation peak. This will in turn lead to deterioration in the precision of the estimate of the position of the correlation peak. If one lets the time separation between acquired images be relatively large, this precision error will be small in relation to the displacement. However, if velocity gradients are present, this strategy will also lead to a broadening of the correlation peak, since the variation in displacement will increase as the time separation increases. The choice of experimental design will therefore by necessity have to be a trade-off between precision and relative displacement error. If the velocity gradients vary across the measurement plane, one cannot design the experiment so that it is optimized over the entire measurement volume. The number of spurious vectors was always less than 5%, which shows that the effect of large velocity gradients in the flow on accuracy was not unwieldy.

Since the main flow component is perpendicular to the measurement plane, the finite thickness of the laser sheet will be critical in limiting the dynamic velocity range, i.e., the ratio of the maximum velocity to the minimum resolvable velocity. Maximizing the dynamic velocity range is of importance for accuracy

issues, originating from the difficulties of determining the position of the particle image. A larger dynamic range will minimize the effect of this uncertainty. Therefore, the measurements need to be a trade-off between the laser sheet thickness and the time between laser pulses.

Another source of error, which is not commonly considered, is the ability of the particles to follow the flow. This might be an issue, especially in regions of accelerating flow such as in a large scale rotation. An example of this is the longitudinal vortices behind vortex generators. Due to the excess density of the particles in relation to the surrounding medium, there is a centrifugal force acting on them, forcing them to move outwards from the vortex center. This is however discarded from having any significant effect in the flow under consideration because of two reasons; the velocities are very low and the distribution of particles in the PIV images is homogeneous. At higher velocities, a reduced particle concentration in the vortex core is commonly observed (see, e.g., Stanislas *et al.* [130]).

### 6.2.7 Reflection reduction

Reflections from the vortex generators and bump surface entering the CCD cameras constituted a problem for two reasons. The reflections appeared in the most interesting part of the measurement region, corrupting the signal in this area. The high power of the laser light also creates reflections harmful for the CCD chip. If these high power reflections reach the CCD chip, one risks damage to the cameras in the form of dead pixel elements. Reflections were removed by painting the reflecting surfaces with a mixture of Rhodamine 6G and varnish. Rhodamine 6G is a fluorescent dye, absorbing light with the wavelength of the laser and reflecting light which has a wavelength slightly shifted from the absorbed one. The cameras were equipped with green-pass filters, which only permit the wavelengths of the laser to pass, allowing the scattering from the particles to pass through and preventing strong reflections from surfaces to reach the CCD chip. Rhodamine 6G has its absorption peak at around 530 nm and its emission peak at about 552 nm. This method was successful in reducing most of the unwanted reflections. An additional approach applied in some of the measurement positions was to acquire images with no particles present in the flow at the same position as the measurements were taken. These images were subtracted from the images used for measurements prior to processing, removing unwanted reflections and retaining the particle scattering.

Before applying Rhodamine 6G, acquiring images including the wall and receiving a good quality measurement signal was not possible since, even at relatively low laser intensity, the reflections from the wall were too strong, risking damage to the CCD chip. The effect of applying Rhodamine 6G to the bump surface made measurements with maximum laser power close to the surface possible for all measurement positions. The largest reflection reducing effect is, however, obtained by utilizing the reflection subtraction technique, removing almost all of the reflections from the wall and in particular the reflections from the vortex generators as close up as 6 mm from the device trailing edges. Prior to applying this technique, reflections from the vortex generators obstructing the signal were detected as far as up to 100 mm downstream of the devices.

### 6.2.8 LES computations

The method of the LES simulations, which were not performed by the respondent, can be found in [144].

## 6.3 Results and discussion

### 6.3.1 Downstream development of vortices

#### 6.3.1.1 Triangular actuators

In order to be able to quantify the induced effect of the vortex generators on the flow, both the controlled and uncontrolled flow have been measured for all positions. In figure 6.5, for four positions downstream of the streamwise placement of the vortex generators, the arithmetic averages of the velocity vector maps obtained from SPIV measurements of the uncontrolled (left column) and controlled (middle column) flows are displayed. The estimator of the mean is based on 500 recorded independent velocity field realizations. The rightmost column shows the projected longitudinal vorticity of each corresponding mean velocity vector map for the controlled case. In the left and middle columns, the secondary velocities are illustrated as arrows, whereas the primary velocities are plotted as color contours. For the sake of clarity, only every fourth vector is displayed in these plots, but the data in the contour plots has not been reduced. The positions of the planes are given in absolute coordinates, referring to the coordinate system given in figure 6.3, as well as in coordinates relative to the vortex generators; The y-coordinate is defined to always be zero at the wall surface. The four downstream positions of the measurement planes are $x_{VG}/h = 1$, 2, 4 and 8, where $x_{VG}$ has the same direction as the x-component, with its origin at mid chord of the bump (at the trailing edges of the devices), i.e., $x_{VG} = 0$ at $x = 150\,\mathrm{mm}$.

It can be seen in the velocity fields in figure 6.5 that the uncontrolled flow displays a 2D boundary layer, experiencing separation in the area around the bump trailing edge. One can also see that the vortex generators have a quite substantial impact on the boundary layer. The presence of the vortex generators causes the flow to rotate, creating counter-rotating longitudinal vortices distorting the flow so that the high momentum fluid is transported from the outer flow into the near wall region in the downwash region (in the vicinity of z= 0). The boundary layer becomes significantly thinner in this zone, whereas the low momentum fluid is transported upwards in the upwash region between two vortices as seen on the sides in the velocity plots. One can also see the downstream development of the flow field, where the vortices start off more or less isolated from effects due to the wall. The vortices are then gradually integrated with the remaining part of the boundary layer flow, eventually submerging into the boundary layer. The vorticity plots reveal that the vortex generators on average give rise to primary vortices, which in turn generate shear layers due to the presence of the wall. One can also see that throughout the downstream development of the longitudinal vortices, the mean distance between the vortices is almost constant. This distance is close to the distance between the trailing edges of two vortex generators within one pair. The mean of the longitudinal vortices therefore does not move substantially in the spanwise direction. One

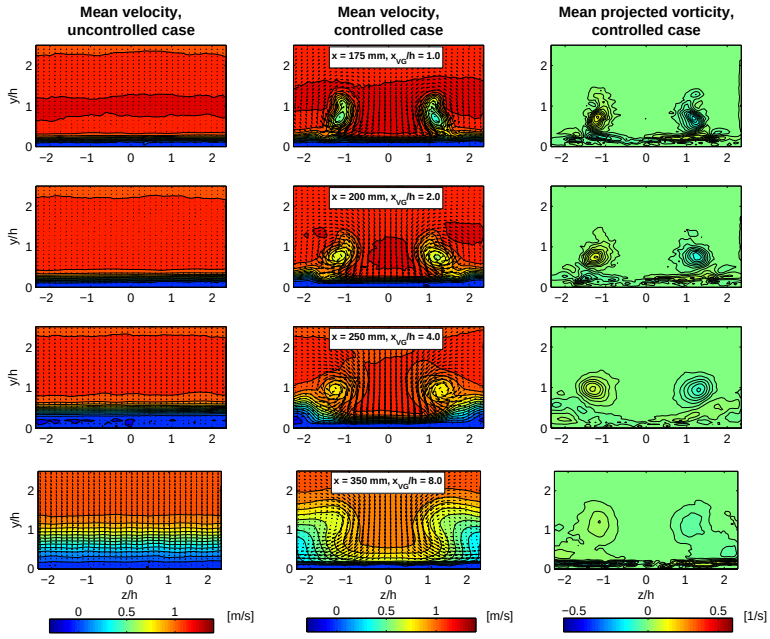


Figure 6.5: Plots of averaged velocity and vorticity fields. The left column displays the mean velocity for the uncontrolled case, the middle column shows the corresponding mean velocity for the controlled case and the right column displays the corresponding projected longitudinal vorticity for the controlled case, represented by contours. In the velocity vector plots, the in-plane components are represented by vectors and the out-of-plane component is represented by contours. These quantities are displayed for four positions downstream of the vortex generators ((a) $x_{VG}/h = 1$, (b) $x_{VG}/h = 2$, (c) $x_{VG}/h = 4$ and (d) $x_{VG}/h = 8$), $h/\delta = 1$, showing the streamwise development of the flow field. The largest secondary velocities are of the order of 0.5 m/s, which can be compared to the free stream velocity of approximately $U_\infty = 1$ m/s.

can also see a progression of the vortices away from the wall as one moves along the downstream direction, which is expected from inviscid theory.

The induced effect of the vortex generators on the boundary layer can also be seen in figure 6.6, which shows the estimated mean of the measured axial and normal velocity profiles at different streamwise positions in the controlled and uncontrolled configuration in the symmetry plane, situated in the downwash region (z= 0 mm). It is clearly seen that the transfer of high momentum into the boundary layer from the vortex generators decreases the separation behind the bump at this spanwise position. The increase in downwash due to the vortex generators can be seen in the normal velocity profiles in figure 6.6(b) and the effect on the reduction of recirculating flow can accordingly be traced in figure 6.6(a).

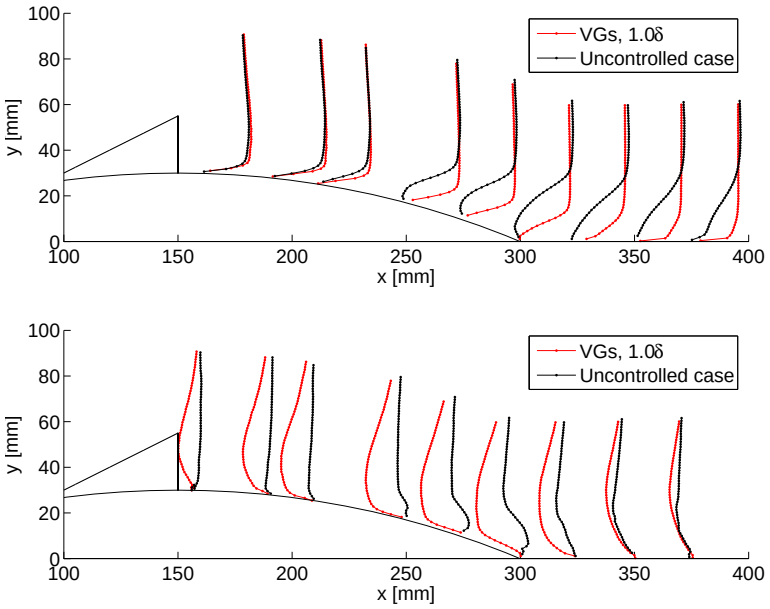


Figure 6.6: Streamwise (a) and normal (b) velocities in the downwash region ($z = 0$). The normal velocity has been scaled with a factor of four compared to the streamwise one.

#### 6.3.1.2 Rectangular actuators

As an overview of the development of the vortices, figure 6.7 displays the longitudinal velocity field obtained for some of the measurement planes in their approximate positions of acquisition along the bump and wind tunnel test section wall. The wind tunnel velocity direction is from the lower left corner to the upper right one.

Figure 6.8 shows the testing of helical symmetry of one of the embedded vortices at various downstream positions. In the same manner as in Chapter 5, the measured axial ($u_\xi$) and azimuthal ($u_\theta$) velocities are plotted along with the result of computing the right-hand side of (5.5$b$) using the measured values $u_\theta$. The convection velocity $u_0$, being the axial velocity at the center of the vortex core, was obtained directly from the measurement data. The helical pitch was obtained through the swirl number S,

$$l = -\frac{F_{mm}}{F_m - u_0 G} \tag{6.2}$$

where $F_{mm}$ and $F_m$ are the angular and axial momentum flux in the axial direction, respectively. G is the flow rate, $\rho$ is the fluid density and $\Sigma$ is the cross-section area.

Due to the perturbing impact of the neighboring vortex, which increases as the upwashing vortices approach each other as one moves downstream, these computed values are only displayed on the left side. As can be seen in the

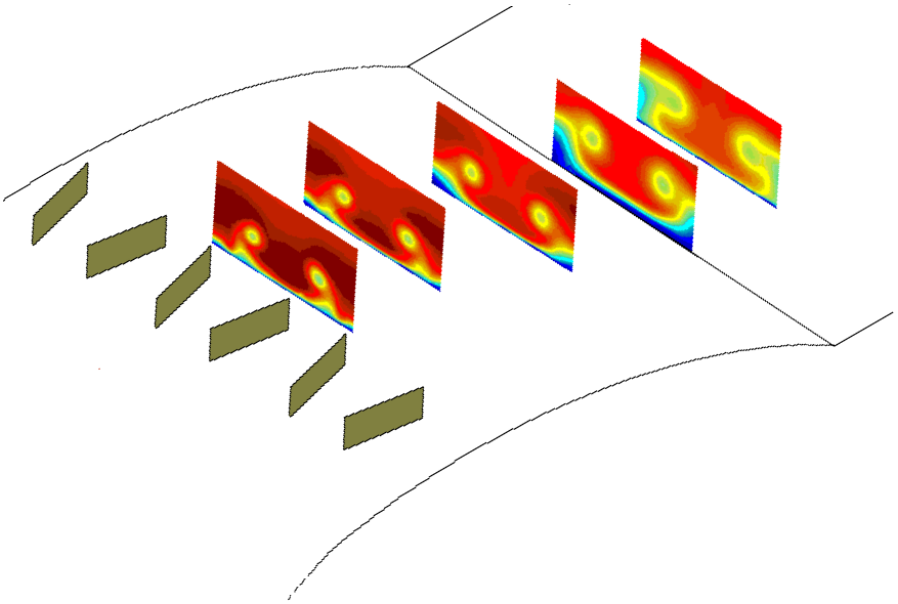

Figure 6.7: Sketch of bump and rectangular vortex generator cascade with longitudinal velocity component displayed by contour plots in some measurement planes placed approximately in their positions of acquisition. The velocity direction is from the lower left corner to the upper right one.

figure, the two data sets overlap quite well in the range $3 \leq x/h \leq 7$. For lower values, the vortex has not yet developed properly and therefore does not display a collapse of the data sets. For higher values, the vortex has transferred to a different state and therefore the pitch is not predicted correctly.

Figures 6.9(*a-d*) show the helical parameters of one of the measured vortices as a function of the downstream distance to the actuator cascade. The quantities are non-dimensionalized by the vortex generator height h and free stream velocity $U_\infty$. $\varepsilon$ and $\Gamma$ were obtained from the expression for the vorticity distribution (see equation (5.1*c*)).

The circulation has a high variability, most probably as a result of inadequacy in the method of estimating the quantity. From the other parameters, it is apparent that the vortex develops through 3 stages throughout the span of the measurements; Initially, the vortex is formed from the generated vortex sheet within a distance of approximately one vortex generator height. The vortex then reaches a stable region where the helical parameters can be approximated to vary linearly in the downstream direction approximately up to the position of the bump trailing edge ($x^* = 6$). This is seen by fitting the data by a linear approximation in a least squares sense and applying corresponding error bars, as has been done in figures 6.9(*a-d*). At the trailing edge of the bump, where the geometry experiences a sudden change, the pressure gradient will change accordingly, triggering an abrupt transition to another stage of the vortex to a helical symmetry with a different set of helical parameters, which begin to digress from the previous trend. The convection velocity is not substantially affected, while the vortex core radius grows rapidly after passing the trailing edge

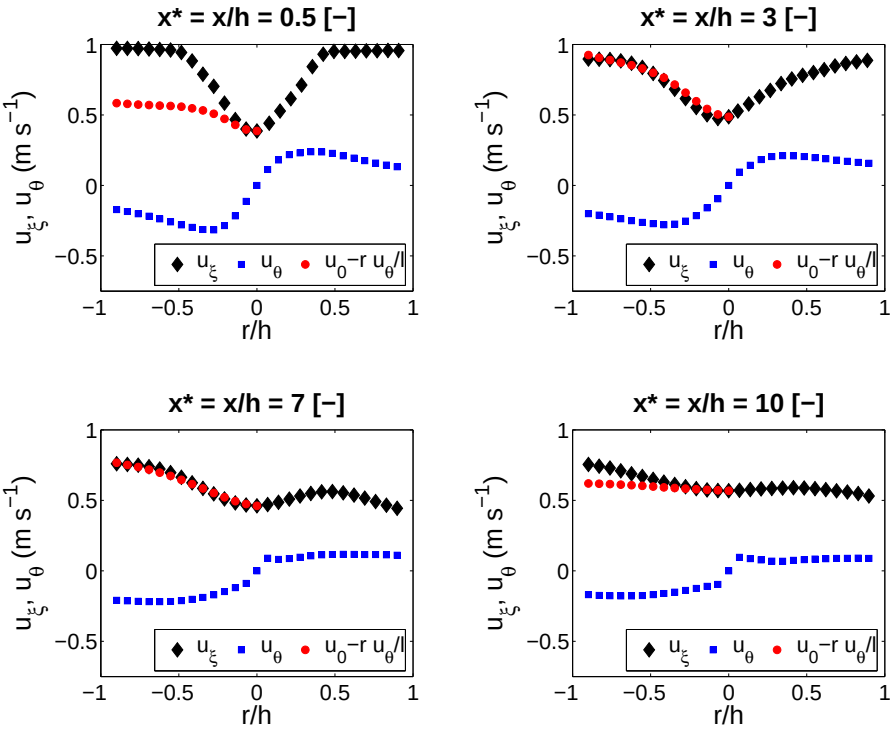


Figure 6.8: Testing of helical symmetry at various downstream positions of one of the embedded vortices in a cascade of counter-rotating vortices. The measured axial ($u_\xi$) and azimuthal ($u_\theta$) velocities are plotted along with the result of computing the right-hand side of (5.5$b$) using the measured values $u_\theta$ and the pitch l obtained from the swirl (6.2). These computed values are only displayed on the left side, since the flow on the right side is perturbed by the neighboring vortex. The two data sets overlap quite well in the range $3 \leq x/h \leq 7$. For lower values, the vortex has not yet developed properly. For higher values, the vortex has transferred to a different state and therefore the pitch cannot be predicted correctly.

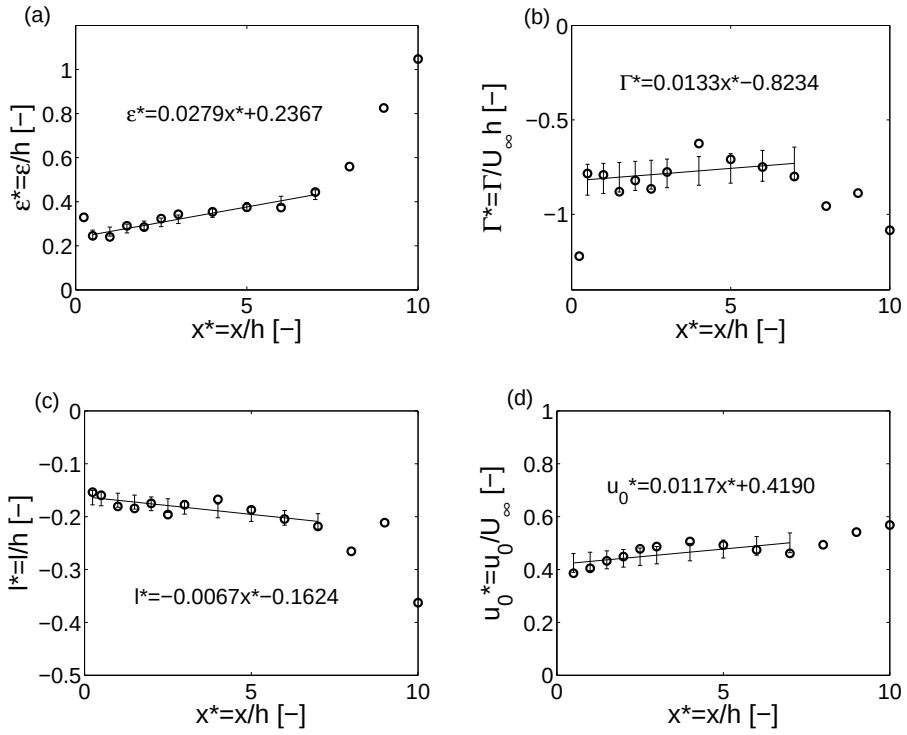


Figure 6.9: Helical parameters of the actuator induced vortex. The parameters have been non-dimensionalized by the vortex generator height h and free stream velocity $U_\infty$ respectively. The parameters presented in each subfigure are the (a) vortex core radius, (b) estimate of the circulation, (c) helical pitch and (d) vortex convection velocity.

of the bump. The increasing growth of the vortex core can also be seen in the downstream development of the vortices depicted in figure 6.7. The unstable behavior of the helical pitch above $x^* = 6$ indicates that it cannot be predicted above this limit, which provides even further support for the hypothesis that the vortex has abruptly transferred to a new state.

The possibility of transition of a helical vortex to a different state without changing the sign of the helical pitch was predicted theoretically and supported by computations by Martemianov and Okulov [81]. This was shown by solving the energy equations and comparing the solutions obtained when the integral parameters (flow rate, circulation, axial flux of angular and axial momentum) were conserved. Several solutions could be obtained, depending on the initial vorticity distribution, rendering it possible to transfer between two solutions of equal sign of the helical pitch. Further, contrary to the common conception, Okulov *et al.* [100] showed theoretically and numerically that vortex breakdown can occur even if there is no change in flow topology.

### 6.3.2 Volumetric flow rate

As a rough measure, the volumetric flow rate has been calculated by integrating the streamwise velocity component U for each vector over its respective interrogation area and summing all of these values up for each respective measurement plane. By performing this calculation for all axial vector components that are negative in the streamwise direction, one obtains an estimate of the reversed flow rate. Figure 6.10 shows the magnitude of the reversed volumetric flow rate calculated from the estimator of the mean for the controlled and the uncontrolled case. This flow rate has been non-dimensionalized with the total flow rate through each respective measurement plane, i.e., the volumetric flow rate for both the negative and the positive streamwise vectors have been included. The plot thus shows the streamwise development of the separation for the two cases with and without devices. One can clearly see that the vortex generators reduce the amount of reversed volumetric flow rate substantially. However, they do not completely eliminate the backflow. The largest backflow in the clean case is found at measurement position $x = 300\,\text{mm}$, which can be explained from the discontinuity in the geometry in the model at the border between the trailing edge of the bump and the test section wall. At $x = 300\,\text{mm}$, the reduction in the normalized reversed flow rate is about 90% to the case without vortex generators. The unsteady point of separation, which on average is located at a streamwise position of approximately $x = 210\,\text{mm}$ (previously known from Schmidt [123]), is not substantially affected by the vortex generators, however, it is evident that the reattachment point at $x = 350\,\text{mm}$ (also known from [123]) is significantly affected by the vortex generators. This is a rough two-dimensional simplification of a complex three-dimensional flow. Therefore the results serve only as an indication of the flow behavior.

### 6.3.3 Vortex generator modeling

Figure 6.11 shows the time averaged velocity fields of the SPIV measurements (left column) and the LES simulations (right column) for four planes ($x = 175$, 200, 250 and $350\,\text{mm}$) for triangular vanes of height $h/\delta = 1.0$. The planes correspond to positions within and in the vicinity of the separation region in

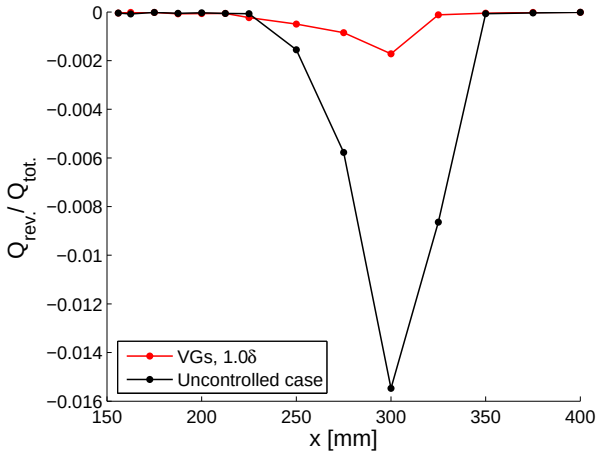


Figure 6.10: Reversed volumetric flow rate for every measurement position normalized by the total flow rate in each respective measurement plane.

the clean configuration. One can see that the longitudinal vortices have the same qualitative structure and downstream development in the measurements and the computations. It is seen that LES has the ability of capturing similar large scale structures in the flow due to the effect of the vortex generators as observed from the PIV measurements. The vortices start out as isolated vortices and gradually submerge into and unite with the boundary layer further downstream. However, one can see that the agreement is not perfect and it is not possible to make a direct comparison since the geometry and inlet conditions used in the experiments are not exactly identical to the ones used in the computations. Still, the concurrence between the measurements and the computations shows that the sensitivity in modeling to geometry of this flow by LES is not high for this particular case. Beyond these matters, a perfect agreement is still not expected. Inherent assumptions in the computations also give rise to non-correspondence between measurements and modeling. LES assumes that the boundary layer flow obeys the log-law and that there exists an inertial subrange, independently of Reynolds number. It has been shown from experiments, see Gad-el-Hak and Bandyopadhyay [37], that the Reynolds-stress profiles in the overlap region depend on the Reynolds number. Therefore the turbulent processes can not be completely independent of Reynolds number and the boundary layer flow predicted by LES will never concur completely with experiments because of the low Reynolds numbers.

## 6.4 Conclusions

It has been shown that it is possible to measure and resolve the flow created by a cascade of vortex generators inducing counter-rotating vortices and their effect on the boundary layer using SPIV. It is apparent from the results that the vortex generators have the expected effect on the flow in the sense that

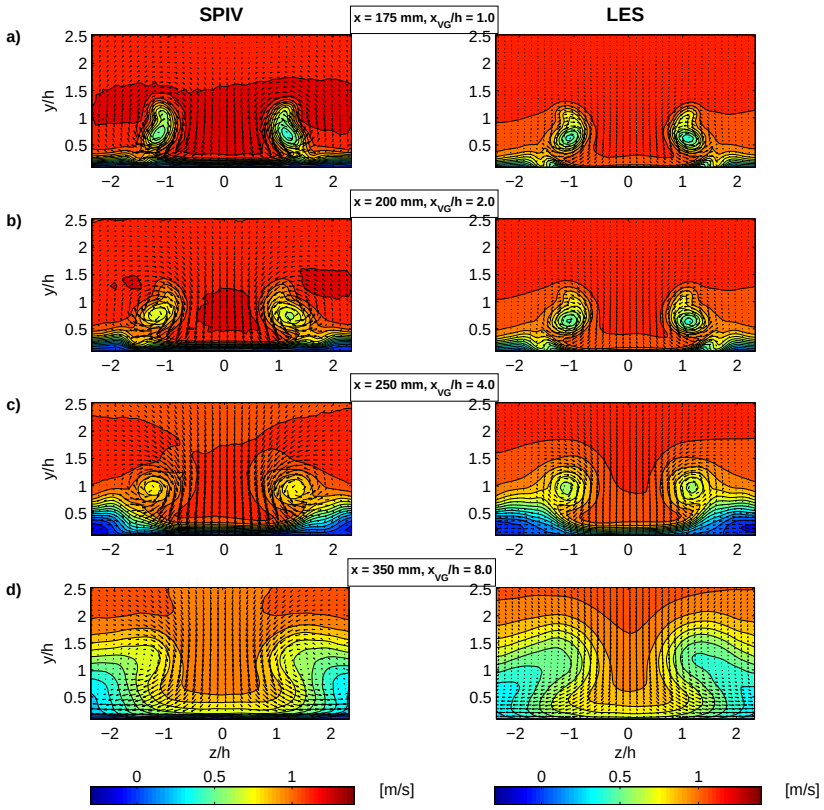


Figure 6.11: Plots of averaged velocity fields with in-plane components represented by vectors and out-of-plane component represented by contours for four positions downstream of the vortex generators ((a) $x_{VG}/h = 1$, (b) $x_{VG}/h = 2$, (c) $x_{VG}/h = 4$ and (d) $x_{VG}/h = 8$), $h/\delta = 1$. The left column shows results from SPIV measurements and the right column shows corresponding results from Large Eddy Simulation (LES). The largest secondary velocities are of the order of 0.5 m/s, which can be compared to the free stream velocity of approximately $U_\infty = 1$ m/s.

they create large scale mixing near the wall. The measurements clearly show a structured vortex behind each vortex generator, whose development can be traced throughout the downstream planes. The effect of the vortex generators on the amount of reversed flow is significant and shows a clear reduction in the amount of recirculated flow. The separation point seems not to be substantially affected whereas the re-attachment point is influenced, curtailing the extent of the separated region. It is stressed that this is a rough simplification of a complex highly three-dimensional flow and that the results serve only as a rough indication of the behavior of the flow. Further, the expected behavior of the streamwise and normal velocities in the downwash region was observed.

A quite qualitative comparison with LES simulations of a slightly different case of the flow behind vortex generators shows that LES is, to some extent, capable of capturing the large scale motions of the longitudinal vortices and reproducing the overall flow structure. Previous tests with RANS-models (cf., Velte *et al.* 2007 [143]) have shown not to possess this capability for the case under consideration.

For the rectangular actuators, the helical parameters displayed a smooth, linear variation along the bump surface except for the estimate of the circulation, which was not accurate using this method. After passing the trailing edge of the bump, the trend deviated from the previous one and the helical vortex experienced an abrupt transition from one state to another without changing sign of the helical pitch. It has previously been shown, both theoretically and computationally, that this kind of transition is possible [81].

# Chapter 7

# Applied Experiments - LM Wind Tunnel Tests

Stereoscopic Particle Image Velocimetry (SPIV) measurements investigating the effect of vortex generators on the flow near stall and at best aerodynamic glide ratio performance have been carried out in the LM Glasfiber wind tunnel on a DU 91-W2-250 profile. Measurements at two Reynolds numbers were analyzed; $Re = 0.9 \cdot 10^6$ and $2.4 \cdot 10^6$, corresponding to free stream velocities $U_\infty = 15$ m/s and $U_\infty = 40$ m/s, respectively. The experimental results show longitudinal vortex structures generated by the devices and mixing close to the wall, transferring high momentum fluid into the near wall region, which is shown to delay separation in the near stall configuration. The vortex structures display similar behavior to those found in the low Reynolds number experiments described in Chapter 6, suggesting that the same flow process is active. Therefore, it is plausible that the helical structure of the vortices persists at these high Reynolds numbers.

## 7.1 Introduction

Vortex generators have many degrees of freedom in the form of geometrical parameters such as general shape, height, length and angle to the main flow direction. Further, it is necessary to specify their chordwise position in relation to the location of the separation line and spanwise spacing on the blade. In industry, some experience exists for particular blade or product designs. But when new products are manufactured, such as new airfoils for wind turbine blades, the optimum geometry of the vortex generators might change. This is associated with some uncertainty and therefore blade manufacturers for wind turbines are often conservative in their choice of airfoils and in their use of aerodynamic devices. A potential exists to increase the aerodynamic efficiency of wind turbine blades and to decrease unwanted loads. By better understanding the physics of how vortex generators mix high momentum fluid into the boundary layer, it could be possible to optimize the effect of the devices and thus reduce the production price for electricity.

On wind turbine blades, vortex generators are used to solve flow separation problems on the inner part of the blade where the airfoil is thick and

the flow angles are high. Wind turbine blades must withstand a high out-of-the-rotor-plane-loading and to absorb the corresponding bending moments, a certain thickness is required. It is not uncommon that the innermost airfoils for this reason have a thickness of up to 40% of the chord. Further, there is a limit on how much a real wind turbine blade is twisted to adapt to the direction of the oncoming local flow velocity. For these reasons, there is always separated flow on the innermost wind turbine blade. A severe inboard separation may also influence the flow further outboard, which is important for the generation of rotor torque. The vanes can increase the lift, but also yield an increased drag. Vortex generators are sometimes integrated in the blade design, but are also used to change unexpected flow separation on already manufactured clean blades. To improve the aerodynamic performance of the part of the blades closest to the hub, vortex generators have successfully been used [103].

Many studies have presented nominal guidelines for optimizing the effect of forced mixing for vortex generators of varying geometries under different flow conditions, [52, 56, 107, 124, 133, 150]. Previously, a lot of experimental work was done describing embedded vortices in wall-bounded flow using single point measurements; see, e.g., [89, 106, 124, 125]. More recent investigations utilize Particle Image Velocimetry (PIV) or Stereoscopic PIV (SPIV) to investigate the flow structures [52, 143, 144, 145, 146], providing instantaneous realizations of all three velocity components in a plane. Further, a review on experimental and computational studies of low-profile vortex generators was written by Lin [76]. In Liu *et al.* [77] it is reported from measurements that the vortex generator induced secondary velocities have a Lamb-Oseen-like structure. In a cylindrical coordinate system for Lamb-Oseen vortices, the vorticity component is purely axial $\omega_z$, yielding a non-uniform azimuthal velocity distribution $u_\theta$ and leaving the axial velocity component $u_z$ unaffected. Computational models have been constructed attempting to describe the effect of the devices on the flow; see, e.g., [77, 127, 157]. Some take into account or observe the Lamb-Oseen vortex structure of the secondary velocities. However, the non-uniform axial velocity component $u_z$ commonly observed has previously never been properly explained except as a velocity deficit. The work presented in Chapter 5 describes the analysis of the flow structures downstream of one vortex generator in order to gain insight into the physical processes of the flow to increase the predictability and simplify the optimization of their effect. Among other results, generic experiments at low Reynolds numbers have shown that the vortices possess helical symmetry of the vorticity and therefore can be modeled by relatively simple equations provided that the helical pitch and convection velocities of the vortices are known [146]. In this study, the negative axial velocity deficit commonly observed was first recognized to be the result of induction due to the helical structure of the vortex core. In addition to the axial vorticity component, vortices with helical symmetry of the vorticity have an azimuthal vorticity component $\omega_\theta$, giving rise to the non-uniform induced axial velocity $u_z$. Lamb-Oseen vortices constitute a special case, where the helical pitch approaches infinity, reducing the azimuthal vorticity component to zero and thereby yielding a rectilinear vortex.

In the present work, it is shown from Stereoscopic PIV measurements that the vortices at higher, more applicable Reynolds numbers have the same basic behavior as the ones at substantially lower Reynolds numbers, see Chapter 6. This suggests that the same type of flow process is active, and thus it is plausible that the vortices possess helical symmetry also at these more applicable

conditions. The knowledge that the vortices might be understood from helical symmetry of the vorticity may lead to better theoretical and numerical models that can simulate and optimize the effect of vortex generators also for other geometries.

## 7.2 Experimental setup and arrangement

### 7.2.1 Wind tunnel

The wind tunnel situated at LM Glasfiber in Lunderskov, Denmark, is a closed return system, with a contraction ratio of 10:1. The maximum speed is 105 m/s (Mach 0.3), yielding a Reynolds number of $Re = 6.3 \cdot 10^6$ based on a profile of chord 900 mm. The test section (see figure 7.1) has a width of 1.35 m, a height of 2.70 m and a length of 7 m. A turn table, designed for holding profiles, is located with its center 2.915 m downstream of the test section inlet at its mid-height. The fan is located at the opposite end of the tunnel to the test section and has a maximum power of 1 MW. The tunnel is equipped with a cooling system to keep the temperature at a constant level. A wake rake is mounted on a traverse, which can move in a plane perpendicular to the flow downstream of the turn tables. The test section is equipped with a differential pressure measurement system, which measures 256 pressures: The pressure distribution on the airfoil model, the pressures on floor and ceiling along the test section as well as static and total pressures on the wake rake. Finally, both turn tables have a balance system. The pressure distributions and load balance signals can be used to derive airfoil force coefficients, see [36]. The tunnel is designed to have low turbulence intensity in the test section. Measurements at the cross-section of the turntable center reveal a turbulence intensity of about Tu = 0.09% in the lengthwise component at Reynolds numbers within the range $Re = 3\text{-}4.8 \cdot 10^6$ [105].

### 7.2.2 DU 91-W2-250 profile

The tests were conducted on the DU 91-W2-250 profile, which is a wind turbine dedicated airfoil developed at Delft University of Technology [118, 136]. The chord length of the profile is 900 mm and the span is 1 350 mm, which is the same as the width of the test section. Pressure taps were integrated in the profile across the entire chord.

### 7.2.3 Vortex generators

Triangular vanes of height h = 4.5 mm and length l = 2h were positioned with an angle of $\beta = 18°$ to the mean flow in a counter-rotating fashion with a distance between the trailing edges of the devices of s = 3h within one pair and z = 5h between each pair, see figure 7.2. The vortex generator configurations were found empirically from polar measurements made by LM Glasfiber, maximizing $C_L$ and $C_L/C_D$ in a parametric study.

The Stereoscopic PIV measurements were conducted at two angles of attack; $\alpha = 6.5°$, corresponding to maximum $C_L/C_D$ (maximum gliding ratio) with vortex generators attached at 50% chord and $\alpha = 18.0°$, corresponding to maximum $C_L$ with vortex generators attached at 20% chord. These angles were

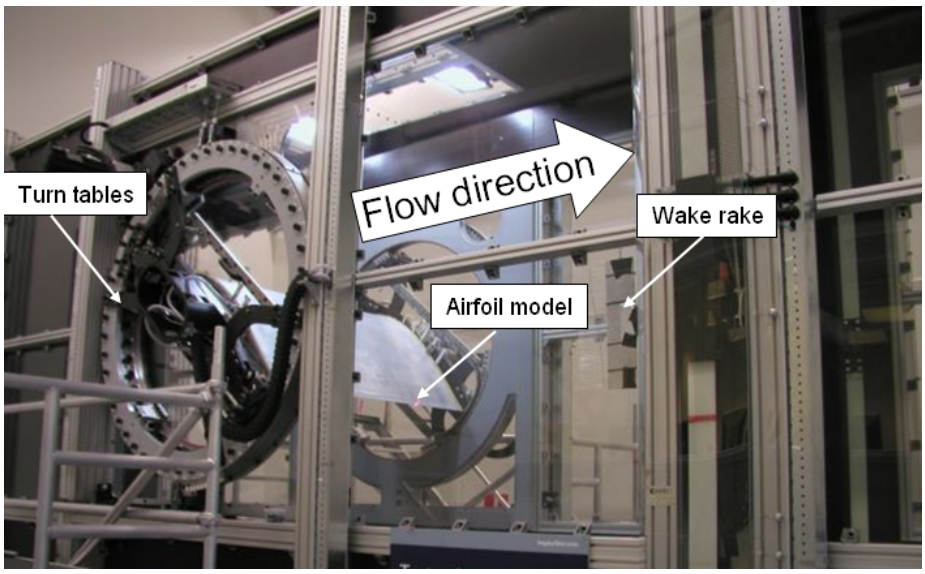


Figure 7.1: LM Glasfiber wind tunnel test section.

chosen based on polar measurements performed by LM Glasfiber, maximizing $C_L/C_D$ and $C_L$ for each respective case. The chordwise positioning of the vortex generators was chosen based on the distance to the separation line. Xfoil simulations for $Re = 3.0{\cdot}10^6$ show that separation occurs at about 35% chord for an angle of attack of $\alpha = 18.0°$ with no vortex generators present, whereas separation only occurs at the trailing edge for an angle of attack of $\alpha = 6.5°$.

The boundary layer thickness for $Re = 3.0{\cdot}10^6$, corresponding to a free stream velocity of $U_\infty$= 50.0 m/s, at the position of the vortex generators has previously been estimated using two-dimensional RANS-simulations to be about $\delta = 11$ mm at $x/c = 50\%$ for $\alpha = 6°$. For $\alpha = 18°$ at $x/c = 20\%$ and the same Reynolds number, the boundary layer thickness is estimated to be about $\delta = 6$ mm.

### 7.2.4 Stereoscopic PIV setup and data processing

The stereoscopic PIV equipment included a double cavity NewWave Solo 120XT Nd-YAG laser (wavelength 532 nm) delivering light pulses of 120 mJ. This laser was placed at the side of the test section on the turn table, illuminating a sheet along the span of the profile, see figure 7.3. The light sheet thickness at the measurement position was 1.5 mm and was created using a combination of a spherical convex and a cylindrical concave lens. The convex lens focuses the light and creates a beam waist at the measurement position. The concave lens was used to spread the laser beam in one of the directions to create the light sheet. Due to the cross-flow arrangement, the second pulse of the laser was shifted downstream by approximately 25% in order to further increase the dynamic range of the out-of-plane component. The equipment also included two Dantec Dynamics HiSense MkII cameras (1344×1024 pixels) equipped with 60 mm lenses and filters designed to only pass light with wavelengths close to that of

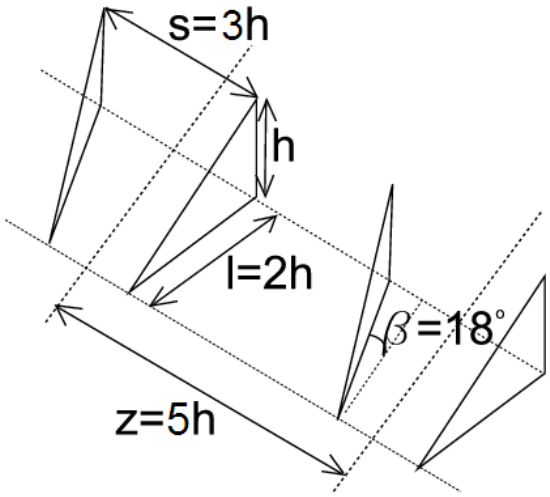


Figure 7.2: Vortex generator geometry.

the laser light, allowing for the scattering from the particles to pass through and partially preventing ambient light and unwanted reflections to reach the CCD chip. Both cameras were mounted on Scheimpflug angle adjustable mountings. In order to obtain a smaller measurement area and therefore better spatial resolution, the cameras were equipped with teleconverters, doubling the effective focal length of the camera lenses. The two cameras were placed downstream of the airfoil on either side of the wind tunnel, i.e., on the same side of the light sheet, resulting in one camera being placed in the forward scattering direction and one in the backward scattering one, see figure 7.3. Since the cameras were mounted in fixed positions, the angle of each respective camera to the laser sheet varied between 32.0°-42.5° depending on the streamwise light sheet position. The $f$-numbers were set to between 4.0 and 5.6 for the camera in the forward scattering direction and was always set to 2.8 for the camera in the backward scattering one, depending on the light budget of scattering from the particles and reflections from the profile surface and the devices at each plane position. The seeding consisted of DEHS (di-ethyl-hexyl-sebacin-esther) droplets with a diameter of approximately 1–2 $\mu$m and was added to the flow downstream of the test section.

Calibration was performed using a calibration target with a well defined pattern placed in the light sheet and acquiring images of it with both cameras at five distinct positions throughout the depth of the laser sheet according to Soloff *et al.* [128]. A mapping function was computed from these calibration images using the camera pinhole model, mapping the object space onto the image plane (the CCD sensor). However, unless the calibration target is perfectly aligned with both laser sheets, the mapping function will not provide coordinate systems that coincide with the measurement planes. Due to the deliberate shift in the downstream direction of the second laser pulse to increase the dynamic range of the measurements, it was impossible to place the calibration target at the center of both light sheets. In practice, it is usually very difficult to achieve satisfactory overlap for the disparity not to affect the measurements significantly even if the

light sheets overlap perfectly. As a consequence, the calibrations associated with the measurements suffer a systematic error that is commonly referred to as disparity. The misalignment between the calibration target and the laser sheet can be estimated from so-called disparity maps [155]; Two simultaneously recorded single-exposure PIV images from each camera are mapped onto the object plane using mapping algorithm obtained through the calibration images. Cross-correlating these, a vector field commonly referred to as disparity map will result, providing a measure of the misalignment residual across the measurement plane [24]. One should, if possible, perform the correction by averaging the correlation planes in stead of the disparity maps. This procedure provides more information, since it retains all of the necessary information in the measurements and, for well converged statistics, removes the ambiguity of the particle position throughout the depth of the laser sheet [111, 154]. Due to the finite thickness of the laser sheet and the viewing angles of the cameras to it, the average correlation peak obtained in this manner will have the shape of an elliptic ridge. This elongated peak provides, among other things, information on the light sheet thickness and its relative position as well as the disparity vector [154].

The DaVis 7.2 software was used to compute the disparity maps as described above, displaying vectors corresponding to a domination of error due to a translational shift of the calibration target in relation to the center of the laser light sheet. This is expected, since the calibration is performed for both light sheets simultaneously, which are deliberately shifted to one another. The errors associated with the calibration are sometimes quite large in the current measurements, typically of the order of 50% of the free stream velocity. For precaution during the experiments, several calibrations were performed spanning larger depths than were seemingly necessary in order to be able to correct the calibrations during the data processing. The DaVis 7.2 software supports self-calibration (cf., [154]), providing the possibility to adjust the coordinate system and the camera calibration so that the calibration target is mapped to the center of the light sheet, thus eliminating the misalignment errors. Further, the images were processed with DaVis 7.2 using cross-correlation over two refinement passes with a final interrogation area size of 32×32 pixels. Local median validation was used in the immediate vicinity of each interrogation area to remove spurious vectors between each refinement step. The overlap between interrogation areas was set to 50%. The number of recorded velocity fields for the different measurements varied between 1500 and 1800. The recording of image maps was done with an acquisition rate of 2.0 Hz to ensure statistical independency of the samples. For a free stream velocity of 15 m/s and tunnel dimension 2.7 m, the time scale of the largest eddies can be approximated to $t = 2.7/15 = 0.18$ s. For a free stream velocity of 40 m/s, the approximated time scale is $t = 2.7/40 = 0.07$ s. The size of the interrogation area varied, but was typically 1.0-1.5 mm in both the spanwise (z) and the wall normal (y) direction. The measurement volume typically had a width of 120 mm, a height of 65 mm and a thickness of 1.5 mm restricted to the thickness of the laser sheet.

### 7.2.5 Reflection reduction

Reflections from the vortex generators and bump surface entering the CCD cameras constituted a problem for two reasons. The reflections often appeared in the most interesting parts of the measurement region, corrupting the signal

Table 7.1: Measurement planes for $\alpha = 6.5°$, corresponding to maximum gliding ratio with vortex generators applied.

| $U_\infty$ (m/s) | $X_{VG}/h$ 20 | 40 |
|---|---|---|
| 15.4 | VGs | VGs/no VGs |
| 40.0 | VGs | VGs/no VGs |

Table 7.2: Measurement planes for $\alpha = 18.0°$, corresponding to maximum lift with vortex generators applied.

| $U_\infty$ (m/s) | $X_{VG}/h$ 20 | 48 |
|---|---|---|
| 15.1 | VGs | VGs/no VGs |

in this area and making the sought for particle scattering hard to detect. The reflections can also be harmful to the CCD chip due to the high power of the laser light. Since we were not allowed to apply Rhodamine 6G in this setting, reflections were suppressed by painting the reflecting surfaces with dull black paint. This significantly reduced the reflections as seen by the camera, however not completely. Further, images acquired with no particles present in the flow at the same position as the measurements were subtracted from the measurement images prior to processing, almost completely removing all unwanted reflections.

### 7.2.6 Measurement planes

The SPIV measurements were conducted in planes parallel to the span of the wing and normal to the surface of the profile, see figure 7.3. The measurement positions were primarily chosen based on results from numerical simulations, suggesting the location of the separation line. The experiments were conducted at two free stream velocities, $U_\infty = 15$ m/s and 40 m/s, corresponding to Reynolds numbers based on profile chord $Re = 0.9{\cdot}10^6$ and $2.4{\cdot}10^6$, respectively. The measurement planes with configurations for each angle of attack (maximum gliding ratio and lift) are listed in tables 7.1 and 7.2. $U_\infty$ is the free stream velocity and $X_{VG}/h$ is the distance between the vortex generators and the measurement plane normalized by the device height h. "VGs" indicates controlled flow and "no VGs" means uncontrolled flow.

### 7.2.7 Combined 3D stall and end effects

At high angles of attack, flow visualizations by oil paint suggest that the flow over the airfoil surface is not two-dimensional even when vortex generators are applied, see figure 7.4. This three-dimensional pattern arises due to a combination of separation and end wall influence effect. Similar three-dimensional large-scale structures or "stall cells" in two-dimensional geometries at high angles of attack have previously been observed [15, 17]. The results of these tests display marked three-dimensional patterns even for airfoils with relatively high aspect ratios. In the current study, effects of this three-dimensionality of the flow are displayed in all of the SPIV measurements. However, these effects are very small when there is no separation as for $\alpha = 6.5°$.

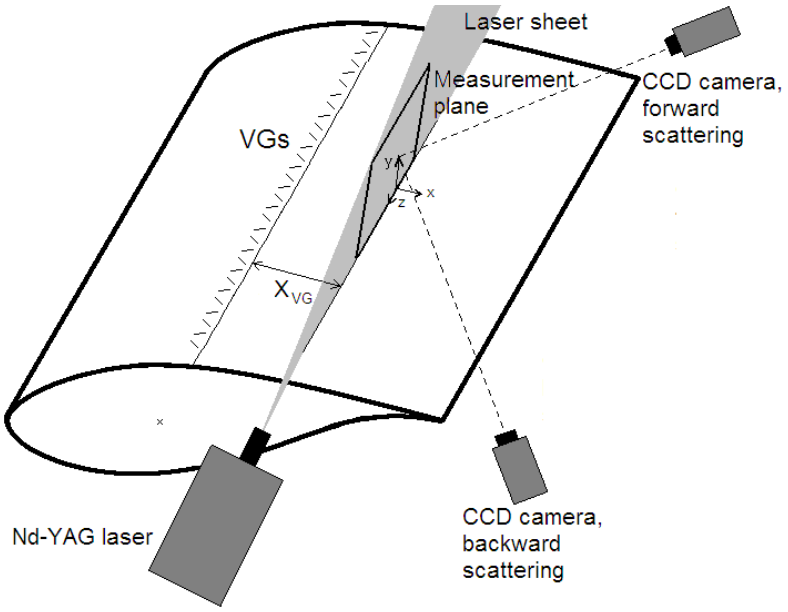


Figure 7.3: Sketch of the experimental setup and the airfoil with vortex generators applied. The Nd-YAG laser illuminates a sheet along the span of the profile. Within this laser sheet, a measurement plane is displayed along with its local coordinate system and the distance $X_{VG}$ between the trailing edge of the vortex generators and the measurement plane. In addition, the positions of both CCD cameras are indicated.

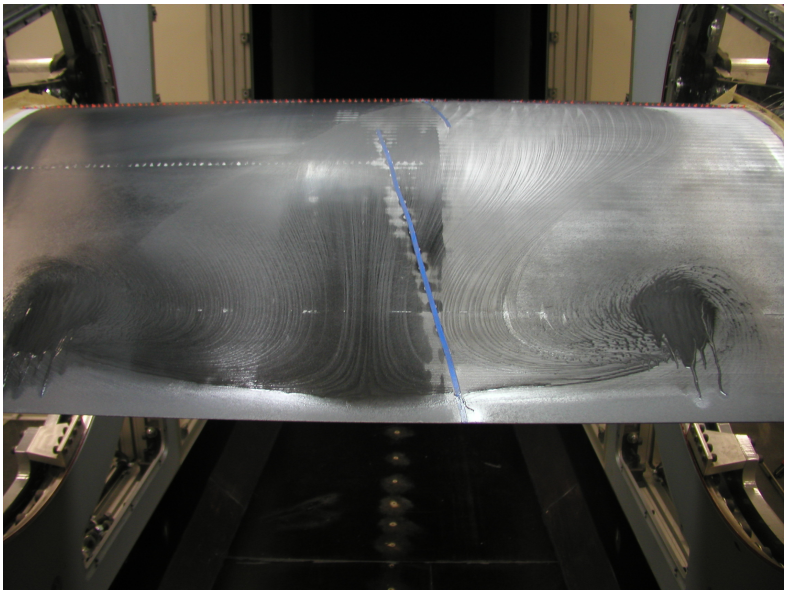

Figure 7.4: Flow visualizations by oil paint at angle of attack $\alpha = 18.0°$ and $U_\infty = 40.0$ m/s. Vortex generators are applied at $x/c = 0.2$.

## 7.3 Results

### 7.3.1 Flow at maximum gliding ratio; $\alpha = 6.5°$

When vortex generators are attached to the blade at 50% chord, polar measurements made by LM Glasfiber have shown that the gliding ratio $C_L/C_D$ is maximized around an angle of attack of $\alpha = 6.5°$. As described in section 7.2.6, measurements have been carried out at two positions along the chord; $X_{VG}/h = 20$ and 40. Further, two velocities were considered; 15.4 and 40.0 m/s corresponding to Reynolds numbers $Re = 0.9{\cdot}10^6$ and $2.4{\cdot}10^6$, respectively. Due to time restrictions for usage of the wind tunnel, only the controlled flow was considered in the most upstream plane whereas both the controlled and uncontrolled flow was measured in the most downstream measurement position. In the following, the measurements performed at free stream speed $U_\infty = 15.4$ m/s will be considered first and thereafter a similar analysis will be conducted for the measurements performed at free stream speed $U_\infty = 40.0$ m/s.

#### 7.3.1.1 Low Reynolds number case

Figures 7.5 and 7.6 show zoom-ins of averaged velocity vector maps for measurements performed with vortex generators applied for free stream velocities $U_\infty = 15.4$ m/s at $X_{VG}/h = 20$ and 40, respectively. Since the pattern seen in the figures repeats itself throughout the measurement area, only a small portion is shown in order to obtain a closer view of the average structures. The axial velocity component is represented by color contours and the secondary velocities are displayed by vectors. The axial velocity component has been normalized by the free stream velocity $U_\infty = 15.4$ m/s. The boundary layer thickness of the uncontrolled flow at $X_{VG}/h = 40$ was determined from the measurements, taking the spanwise average of the mean velocity field, and is indicated by a white horizontal line in figure 7.6. Since the uncontrolled flow was not measured at the more upstream position, no such line is shown in figure 7.5.

In all cases without devices, a three-dimensional boundary layer varying across the span is observed as described in section 7.2.7, displaying a small deviation from zero in the spanwise velocity W, in contrast to what is expected in a two-dimensional boundary layer. This deviation is, however, never larger than 3.5% of the free stream velocity and is usually smaller than 2%. It is therefore remarked that the spanwise median velocity profile has been subtracted from the mean field in order to better reveal the structures of the longitudinal vortices generated by the devices.

Effects of reflections can be detected in figure 7.5 in the span $9 < z/h < 10$, where the 3C velocity vector map is distorted by reflections from one of the vortex generators. In addition, the measurements are subject to strong reflections from the airfoil surface and therefore, one cannot obtain valid vectors close to the wall due to the low signal-to-noise ratio. This in turn obstructs the positioning of the wall. Further, the flow closest to the wall is most presumably not resolved due to the high velocity gradients in this region compared to the relatively large size of the interrogation areas. A high velocity gradient across the interrogation area will be filtered across the spatial extent of the interrogation window, yielding a clearly erroneous measuring value. This makes it further difficult to approximate the position of the wall from the measurements. In

addition, due to the limitations in spatial resolution of the measurements, the velocities in the vortex cores are hard to resolve and detect.

This might in part explain why one cannot always clearly distinguish the expected spanwise velocities entering into the vortical motion close to the wall. Another plausible hypothesis, assuming that the flow is well resolved, is that the flow pattern is a mixture of the motions of longitudinal vortices and a streak-like behavior which is amplified by the forcing of the flow from the vortex generators. The thought is that the vortical motions interact with turbulent streaks in the boundary layer further upstreams, enhancing and ordering their effect and thereby making their momentum redistribution effect persist farther downstream. However, one can evidently observe the resolved vortical macro-motions in the average induced effects of the actuators in figure 7.5, centered at positions y/h = 1, z/h = 1, 4, 6 and 9 as well as in figure 7.6 in the same positions, with the full vortical motion reconnecting even close to the wall at some positions despite the strong wall reflections.

It is therefore more likely that the vortices obey the same flow patterns as have been observed in similar measurement results at very low Reynolds numbers with higher resolution, see Chapters 5 and 6 or [143, 144]. These secondary macro-motions of the flow, overturning the boundary layer in a way that is at least similar to the expected longitudinal vortices observed in the previous studies, are clearly seen and accordingly the axial velocity close to the wall is redistributed. A schematic of the mixing structures generated by longitudinal vortices is displayed in figure 7.7, where figure 7.7*a* shows a counter-rotating configuration as applied in the current experiment. Two dominant momentum redistribution processes can be identified; the downwash at z/h = 0, 5, and 10 in the velocity vector maps in figures 7.5 and 7.6, where high momentum fluid is transported towards the wall and the upwash at z/h = 2.5 and 7.5 in the same figures, where the retarded fluid is advected away from the wall. Arrows in figure 7.7*a* indicate the direction of the advection for both processes. Figure 7.7*b* displays a case in which the vortices are co-rotating, leading to simultaneous upwash and downwash in each spacing between vortices.

A representative snapshot of the velocity vector field of the uncontrolled flow at $X_{VG}/h = 40$ is displayed in figure 7.8. To improve the clarity of the figures, the velocity vectors have been scaled down by a factor of 2/3 in the snapshots compared to the average velocity fields throughout the chapter. A turbulent boundary layer is seen with seemingly disordered structures interacting. Figures 7.9 and 7.10 show typical snapshots of instantaneous realizations of the controlled flow at free stream velocity $U_\infty = 15.4$ m/s and $X_{VG}/h = 20$ and 40, respectively. In the snapshot of the more upstream position, the complete vortical motion is well captured instantaneously and can be seen, e.g., at z/h = -10, -7, 0, 3 and 8. This can also be seen to some extent in the more downstream position, but the structures are far less organized here. Further, comparing the instantaneous structures with and without actuators, one can conclude that they are somewhat similar. However, the more organized device induced structures are more ordered and structured, supposedly enhancing already existing structures in the boundary layer to counteract separation. Though subject to strong turbulent pulsations, the structures seem to remain distinct and intact at both positions.

Further, figures 7.11 and 7.12 show the normalized spanwise averaged axial velocity profile from the mean controlled velocity field along with normalized

axial velocity profiles extracted from the mean velocity field in the upwash and downwash regions at $X_{VG}/h = 20$. Figure 7.12 shows all these profiles for $X_{VG}/h = 40$, with the addition of the normalized spanwise averaged axial velocity profile from the mean velocity field for the uncontrolled flow. Similar behavior is seen in the up- and downwash regions compared to the spanwise averaged profile of the contolled flow, indicating that the basic structure persists when moving downstream. This is also reflected in the previous average as well as the instantaneous velocity vector plots.

Comparing to the uncontrolled case, it seems that the negative effect in the upwash region is larger than the positive effect in the downwash region, which is also reflected in the controlled spanwise averaged velocity profile. This deficit is potentially the remainings of the negative induction in axial velocity caused by the helical symmetry of the vortices, see Chapter 5. Then one can explain the lost streamwise energy by an exchange between the primary and secondary velocities, boosting the tangential velocity component that redistributes the axial momentum in the boundary layer. It is also noted that the actuator induced effect is quite local, not substantially affecting the average axial flow in the boundary layer beyond $y/h \approx 5$.

#### 7.3.1.2 High Reynolds number case

A similar analysis for the higher Reynolds number case, acquired at a free stream velocity of $U_\infty = 40.0$ m/s, shows the same basic results as for the lower Reynolds number case. Figures 7.13 and 7.14 show zoom-ins of averaged velocity vector maps for measurements performed with vortex generators applied for free stream velocities $U_\infty = 40.0$ m/s at $X_{VG}/h = 20$ and 40, respectively. The axial velocity component has been normalized by the free stream velocity $U_\infty = 40.0$ m/s. Again, the boundary layer thickness of the uncontrolled flow at $X_{VG}/h = 40$ was determined from the measurements by a spanwise average of the mean velocity field and is indicated by a white horizontal line in figure 7.14.

The three-dimensionality of the boundary layer persists at this higher free stream velocity and it is therefore again remarked that the spanwise median velocity profile has been subtracted from the mean field in order to better reveal the structures of the longitudinal vortices generated by the devices. Further, the reflections seen in figure 7.5 appear also in these measurements in the same position, see figure 7.13. Further, the strong reflections from the airfoil surface remain, corrupting the signal in these regions and causing low signal-to-noise ratios.

The resolved complete vortical macro-motions in the average induced effects of the actuators in figures 7.13 and 7.14 are somewhat less obvious here, but can still be seen centered at, e.g., $y/h = 1$, $z/h = 1$ and 6 in the two figures. The structures have the same basic characteristics as for the lower Reynolds number, indicating that the complete vortical motions in the average sense, however not resolved, are present in the current case as well. This also further strengthens the hypothesis that the structures are Reynolds number independent for the current range.

A characteristic snapshot of the velocity vector field of the uncontrolled flow at $X_{VG}/h = 40$ is displayed in figure 7.15. This turbulent boundary layer is similar to the one obtained at the lower free stream velocity seen in figure 7.8.

Figures 7.16 and 7.17 show typical snapshots of instantaneous realizations of the controlled flow at positions $X_{VG}/h = 20$ and 40, respectively. The instantaneous complete vortical motions are not as evident as for the lower Reynolds number. This might not be solely caused by the difference in induced actuator effect at the higher Reynolds number, but can also be assigned to the spanwise flow disturbance and the large impact of reflections. The higher degree of order in the structures in the controlled flow as opposed to the uncontrolled one is again evident and the structures seem to be able to survive the conditions provided by the higher free stream velocity.

Considering the normalized velocity profiles for the present case seen in figures 7.18 and 7.19, corresponding to the ones found in the lower Reynolds number case in figures 7.11 and 7.12, the trend is in substance the same. This once again suggests that the actuators induce the same kind of flow process at this higher Reynolds number. Also at this Reynolds number, the induced effect of the actuators on average does not stretch beyond $y/h \approx 5$.

### 7.3.2 Flow at maximum lift; $\alpha = 18.0°$

When vortex generators are attached to the blade at 20% chord, polar measurements made by LM Glasfiber show that the lift coefficient $C_L$ is maximum for an angle of attack of $\alpha = 18.0°$. The measurements were limited to a free stream velocity of $U_\infty = 15.1$ m/s in order to reduce vibrations of the test section and hence also their impact on the flow, most probably caused mainly by the shedding at the 2D airfoil at this high angle of attack. Further, the measurements conducted for $\alpha = 18.0°$ are subject to much more three-dimensionality of the boundary layer than the measurements for $\alpha = 6.5°$. In the outer layer at this higher angle of attack, the largest deviations from zero in the spanwise velocity W can be as large as 5-10% of the free stream velocity, the largest deviations being present in the most downstream measurements.

Studying the most upstream position, figures 7.20 and 7.21 show snapshots peculiar to the controlled boundary layer flow at $X_{VG}/h = 20$. These two types of snapshots are about equally frequent and describe a turbulent boundary layer that is intermittently dominated by the organized structures generated by the actuating devices, reminiscent of the structures seen in the snapshots for $\alpha = 6.5°$. The turbulent boundary layer dominates the flow during the remainder. The spanwise averaged velocity profile obtained from the ensemble averaged flow in the same position is shown in figure 7.22. This figure shows a well attached profile, which can be explained either by the effect of the actuators or the fact that this position lies upstream of the separation point where the flow is still accelerating. Most probably the explanation is a combination of both.

Figures 7.24 and 7.25 show two typical snapshots of instantaneous realizations of the controlled flow at $X_{VG}/h = 48$ (corresponding to 45% chord). A representative snapshot of the corresponding uncontrolled flow is displayed in figure 7.23, revealing that the flow is subject to separation. While the snapshot in figure 7.24 portrays a separated and highly irregular turbulent boundary layer, figure 7.25 displays a flow behavior which again reminds of the organized structures previously observed in the snapshots of the controlled flow for both angles of attack. The distribution between the two kinds of snapshots displayed in figures 7.24 and 7.25 seems to be fairly equal, again strongly indicating that

the boundary layer flow separates intermittently. Comparing the instantaneous structures with and without actuators, one can conclude that the snapshot of the controlled flow in figure 7.24 has a similar structure as that of the uncontrolled one in figure 7.23, however, less separated. The coherent structures can still be seen in the flow at times, whereas at other times, their effect is not strong enough to counteract separation and thus drowns in the intermittent bursts of strong flow pulsations.

The effect of the actuators is still clearly visible in the flow though. Figure 7.26 displays the free stream normalized ensemble and spanwise averaged streamwise velocity profiles for the controlled and uncontrolled flow, respectively. Even though a fair amount of the realizations have similar appearance to that in figure 7.24, the separation obstructing effect on the mean flow leaves no further doubts to the efficiency of the actuating devices. A large contribution to this might be the large impact of the intermittent influence of the more structured and organized device induced structures seen in figure 7.25. It is also noted that the effect of the actuators reaches across the entire height of the boundary layer, even though their height corresponds to an order of magnitude less.

## 7.4 Conclusions

The results show that, by using Stereoscopic PIV, one can detect the large scale flow structures created by vortex generators on a DU 91-W2-250 profile at Reynolds numbers $\mathrm{Re} = 0.9 \cdot 10^6$ and $2.4 \cdot 10^6$, at an angle of attack of $\alpha = 6.5°$. The vortices and their redistribution of streamwise momentum in the boundary layer are clearly displayed in the velocity vector maps, both as snapshots and in the average sense, and the effect is qualitatively the same for the respective measurements for the two measuring positions and Reynolds numbers. This indicates that the flow structures are fairly independent of Reynolds number within the considered range. For the higher Reynolds number case, the flow structures seem to be slightly more compact and the secondary velocities are generally larger. The patterns of the controlled flow are very similar, also to the ones found at considerably lower Reynolds numbers, see Chapters 5 and 6. This indicates that the structures exist and are fairly similar independently of Reynolds number within the considered range.

Similar patterns appear intermittently at $\alpha = 18.0°$ at both $\mathrm{X}_{VG}/\mathrm{h} = 20$ and 48 (45% chord), where the flow structures sometimes are too weak to counteract, and are dominated by, separation. Despite this, nevertheless, the vortices can be clearly distinguished in snapshots at these positions and their impact in terms of separation control has proven to be significant in the most downstream position. Further, it is worth noting that the vortices still are intact and effective at distances exceeding $\mathrm{X}_{VG}/\mathrm{h} = 48$, which is large compared to what has mostly been reported in previous studies of submerged vortex generators, typically reaching to about $\mathrm{X}_{VG}/\mathrm{h} = 10$-$20$ [76].

In essence, it is observed that the momentum deficit and the secondary vortical macro motions of the vortices persists for a row of vortex generators producing counter-rotating vortices at higher Reynolds numbers that are more relevant in many applications such as, e.g., on wind turbine blades. Knowing the parameters of the vortices, this information can be used to construct models

of the flow to optimize the effect of the vortex generators. This can, e.g., be conducted in a similar fashion as performed by [77] by introducing body forces acting as a numerical vortex generator, but further improving the analysis by knowing the relationship between the axial and azimuthal velocity components. Another option is to construct a theoretical model for the infinite vortex row, also including the mirror vortices to account for the presence of the wall.

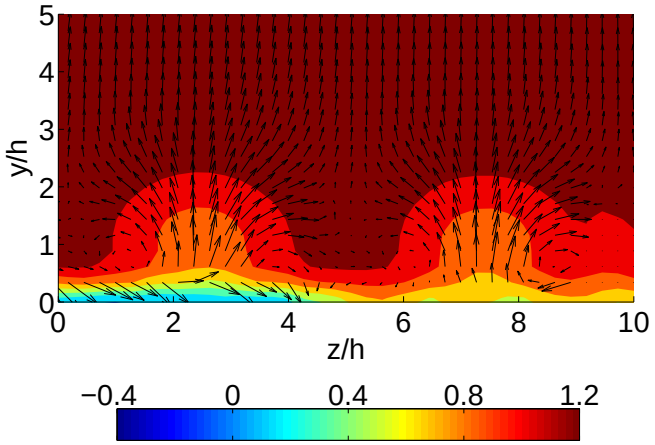


Figure 7.5: Average velocity vector map of the controlled flow for angle of attack $\alpha = 6.5°$ and free stream velocity $U_\infty = 15.4$ m/s at $X_{VG}/h = 20$. The plot is zoomed-in to an area corresponding to about a quarter of the field of view. The colors display the out-of-plane velocities normalized by the free stream velocity. Since the local flow on the blade is not parallel to the free stream, the origin of the z-axis has been chosen arbitrarily at one of the downwash regions. In the span $9 < z/h < 10$, the 3C velocity vector map is distorted by reflections from one of the vortex generators. Spurious vectors, located in the position of this reflection, protruding the view have been removed.

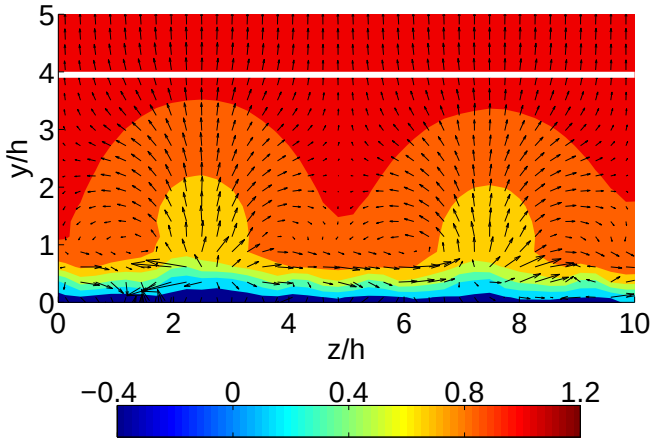


Figure 7.6: Average velocity vector map of the controlled flow for angle of attack $\alpha = 6.5°$ and free stream velocity $U_\infty = 15.4$ m/s at $X_{VG}/h = 40$. The white line indicates the boundary layer thickness obtained from the measured uncontrolled flow. The plot is zoomed-in to an area corresponding to about a quarter of the field of view. The colors display the out-of-plane velocities normalized by the free stream velocity. Since the local flow on the blade is not parallel to the free stream, the origin of the z-axis has been chosen arbitrarily at one of the downwash regions.

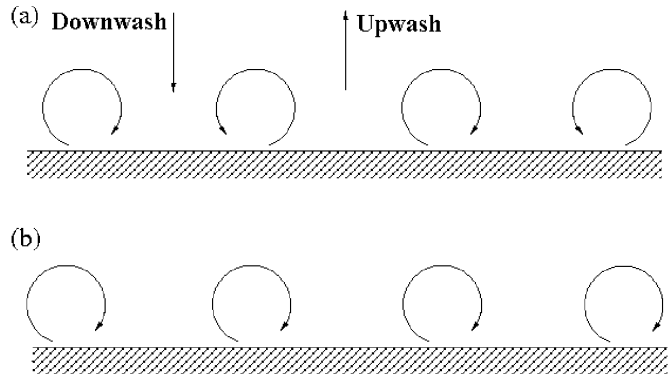


Figure 7.7: Schematic of the mixing structures downstream of vortex generators in a (a) counter-rotating and (b) co-rotating configuration. In the case of counter-rotating vortices (a), two dominant momentum redistribution processes can be identified; the downwash, where high momentum fluid is transported towards the wall and the upwash, where the retarded fluid is advected away from the wall. Arrows in the figure indicate the direction of the advection for both processes. In the case of co-rotating vortices (b) simultaneous upwash and downwash occurs in each spacing between vortices.

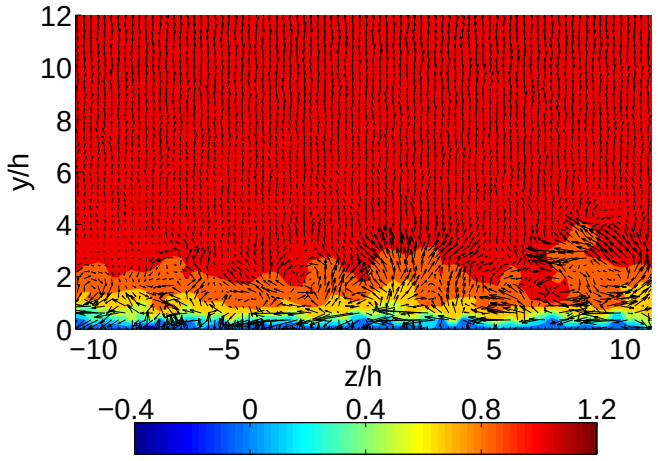


Figure 7.8: Instantaneous snapshot of the velocity vector field of the uncontrolled flow for an angle of attack $\alpha = 6.5°$ and free stream velocity $U_\infty = 15.4\,\mathrm{m/s}$ at $X_{VG}/h = 40$. The figure displays a representative realization for the uncontrolled flow. The colors display the out-of-plane velocities normalized by the free stream velocity. To improve the clarity of the figure, the velocity vectors have been scaled down by a factor of 2/3 in the snapshot compared to the average velocity fields.

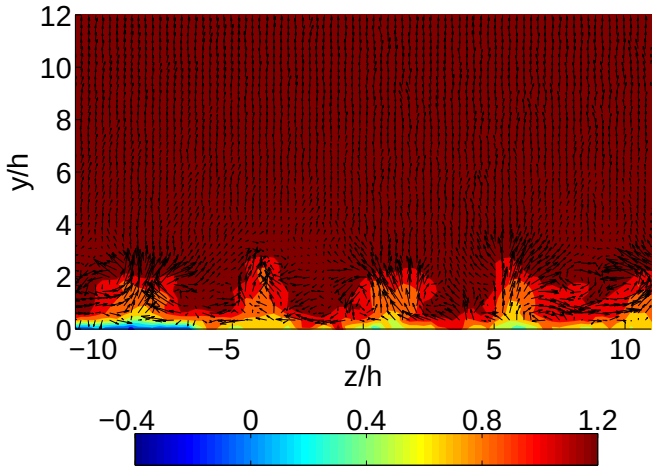


Figure 7.9: Instantaneous snapshot of the velocity vector field of the controlled flow for an angle of attack $\alpha = 6.5°$ and free stream velocity $U_\infty = 15.4$ m/s at $X_{VG}/h = 20$. The colors display the out-of-plane velocities normalized by the free stream velocity. To improve the clarity of the figure, the velocity vectors have been scaled down by a factor of 2/3 in the snapshots compared to the average velocity fields.

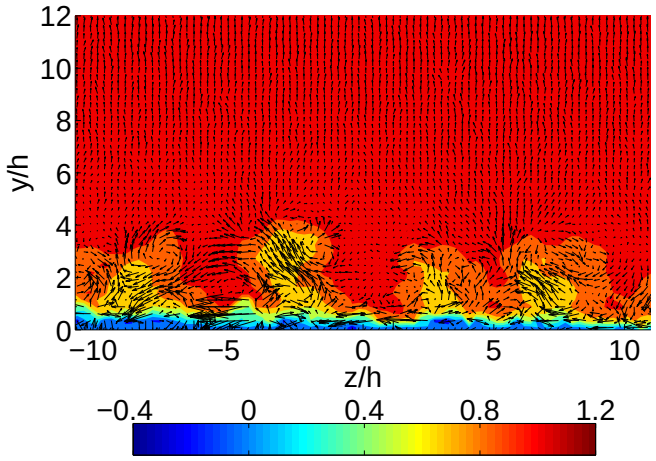


Figure 7.10: Instantaneous snapshot of the velocity vector field of the controlled flow for an angle of attack $\alpha = 6.5°$ and free stream velocity $U_\infty = 15.4$ m/s at $X_{VG}/h = 40$. The colors display the out-of-plane velocities normalized by the free stream velocity. To improve the clarity of the figure, the velocity vectors have been scaled down by a factor of 2/3 in the snapshots compared to the average velocity fields.

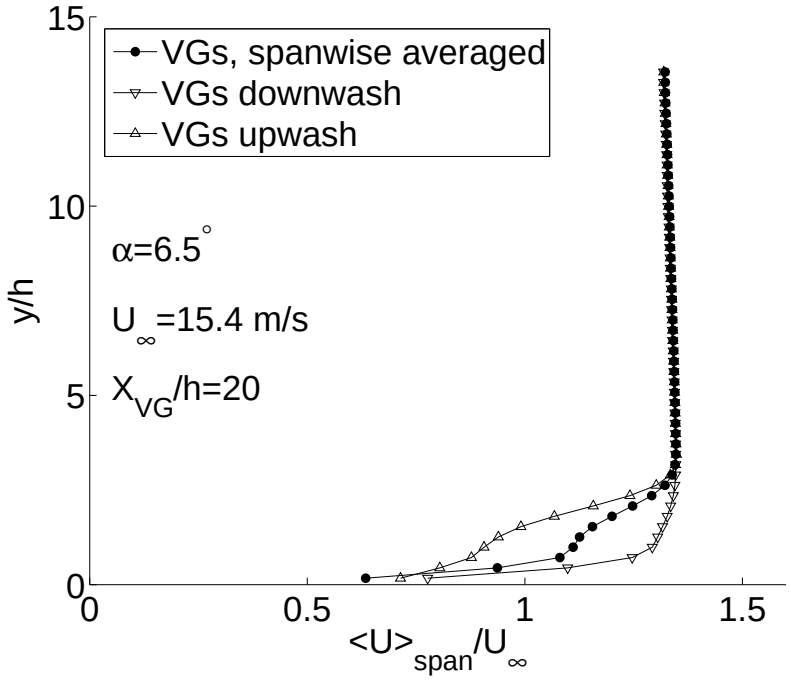


Figure 7.11: Velocity profiles for $\alpha = 6.5°$, $U_\infty = 15.4$ m/s and $X_{VG}/h = 20$. The figure displays spanwise averaged velocity profiles from the mean controlled velocity field as well as profiles from the mean velocity field extracted in the upwash and downwash regions.

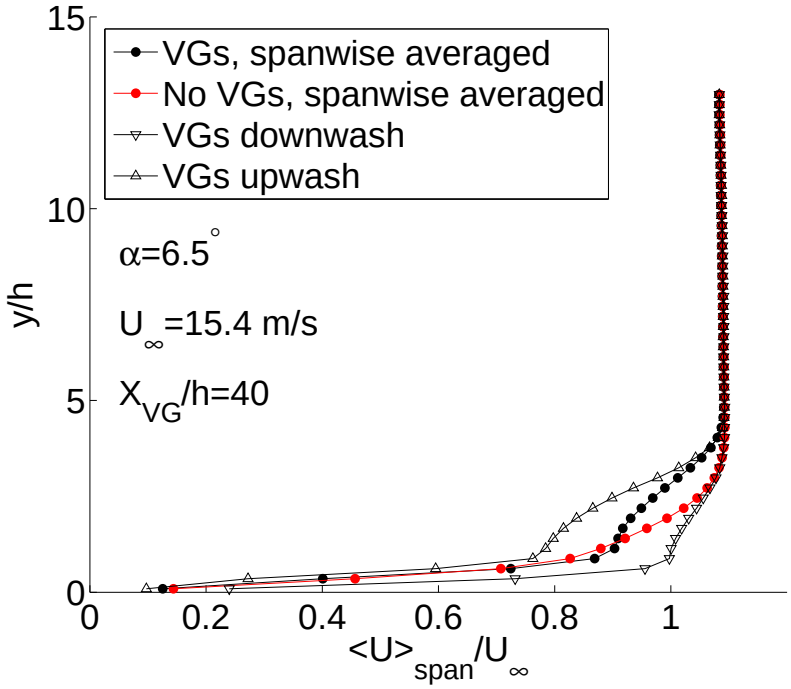


Figure 7.12: Velocity profiles for $\alpha = 6.5°$, $U_\infty = 15.4$ m/s and $X_{VG}/h = 40$. The figure displays spanwise averaged velocity profiles from the mean controlled and uncontrolled velocity field as well as profiles from the mean velocity field extracted in the upwash and downwash regions.

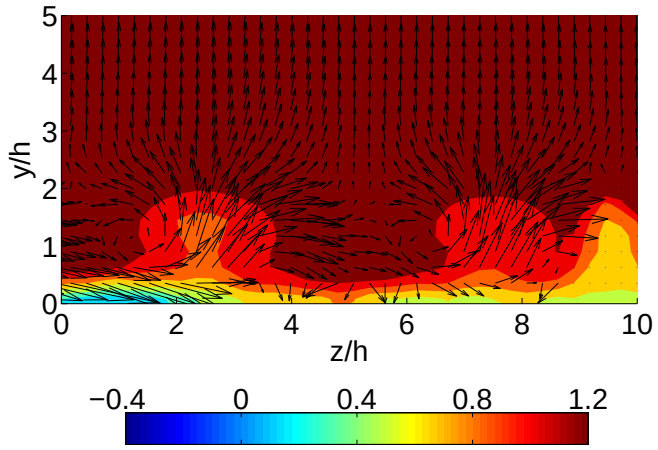


Figure 7.13: Average velocity vector map of the controlled flow for angle of attack $\alpha = 6.5°$ and free stream velocity $U_\infty = 40.0$ m/s at $X_{VG}/h = 20$. The plot is zoomed-in to an area corresponding to about a quarter of the field of view. The colors display the out-of-plane velocities normalized by the free stream velocity. Since the local flow on the blade is not parallel to the free stream, the origin of the z-axis has been arbitrarily chosen at one of the downwash regions. In the span $9 < z/h < 10$, the 3C velocity vector map is distorted by reflections from one of the vortex generators. Spurious vectors, located in the position of this reflection, protruding the view have been removed.

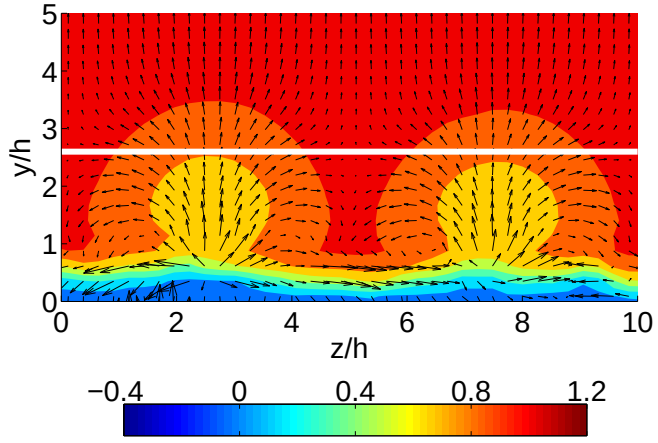


Figure 7.14: Average velocity vector map of the controlled flow for angle of attack $\alpha = 6.5°$ and free stream velocity $U_\infty = 40.0$ m/s at $X_{VG}/h = 40$. The white line indicates the boundary layer thickness obtained from the measured uncontrolled flow. The plot is zoomed-in to an area corresponding to about a quarter of the field of view. The colors display the out-of-plane velocities normalized by the free stream velocity. Since the local flow on the blade is not parallel to the free stream, the origin of the z-axis has been arbitrarily chosen at one of the downwash regions.

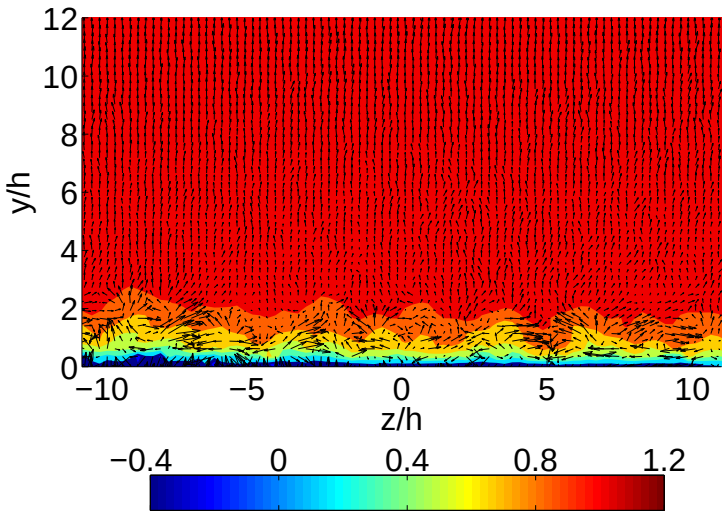


Figure 7.15: Instantaneous snapshot of the velocity vector field of the uncontrolled flow for an angle of attack $\alpha = 6.5^\circ$ and free stream velocity $U_\infty = 40.0$ m/s at $X_{VG}/h = 40$. The figure displays a typical realization for the uncontrolled flow. The colors display the out-of-plane velocities normalized by the free stream velocity. To improve the clarity of the figure, the velocity vectors have been scaled down by a factor of 2/3 in the snapshot compared to the average velocity fields.

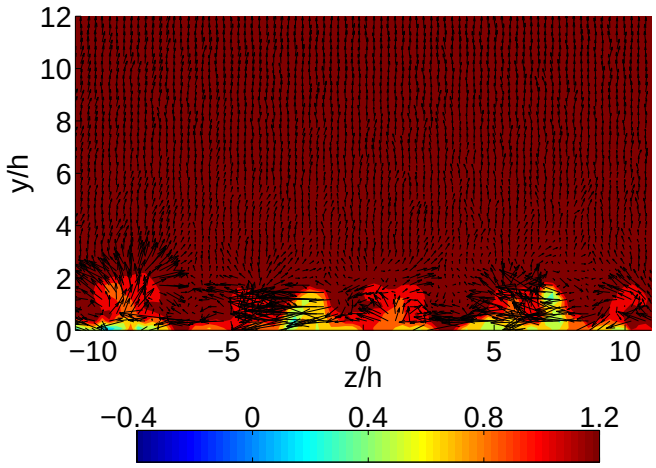


Figure 7.16: Instantaneous snapshot of the velocity vector field of the controlled flow for an angle of attack $\alpha = 6.5°$ and free stream velocity $U_\infty = 40.0$ m/s at $X_{VG}/h = 20$. The colors display the out-of-plane velocities normalized by the free stream velocity. To improve the clarity of the figure, the velocity vectors have been scaled down by a factor of 2/3 in the snapshots compared to the average velocity fields. Reflections are seen at positions z/h = -2 and 7.

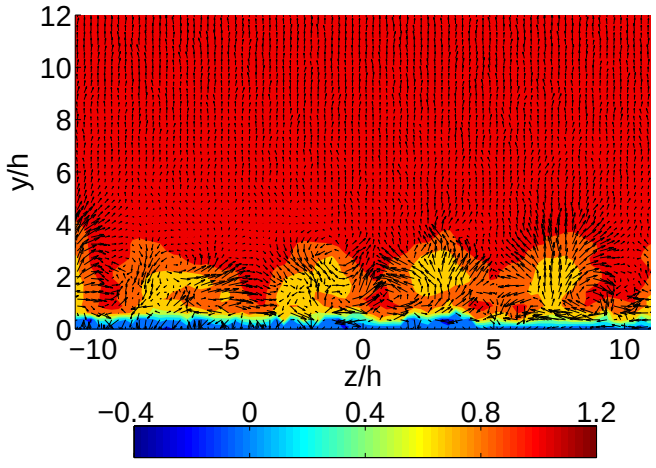


Figure 7.17: Instantaneous snapshot of the velocity vector field of the controlled flow for an angle of attack $\alpha = 6.5°$ and free stream velocity $U_\infty = 40.0$ m/s at $X_{VG}/h = 40$. The colors display the out-of-plane velocities normalized by the free stream velocity. To improve the clarity of the figure, the velocity vectors have been scaled down by a factor of 2/3 in the snapshots compared to the average velocity fields.

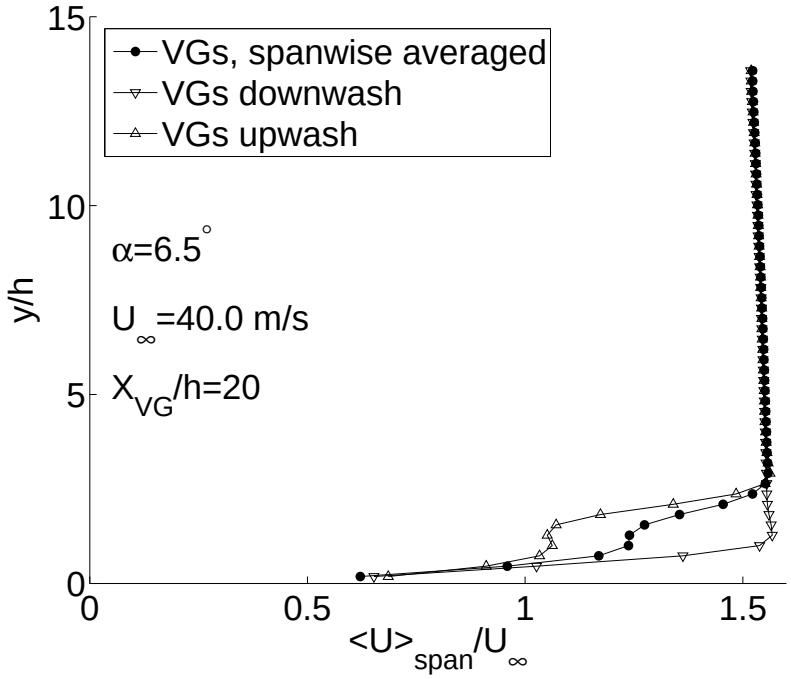


Figure 7.18: Velocity profiles for $\alpha = 6.5°$, $U_\infty = 40.0$ m/s and $X_{VG}/h = 20$. The figure displays spanwise averaged velocity profiles from the mean controlled velocity field as well as profiles from the mean velocity field extracted in the upwash and downwash regions.

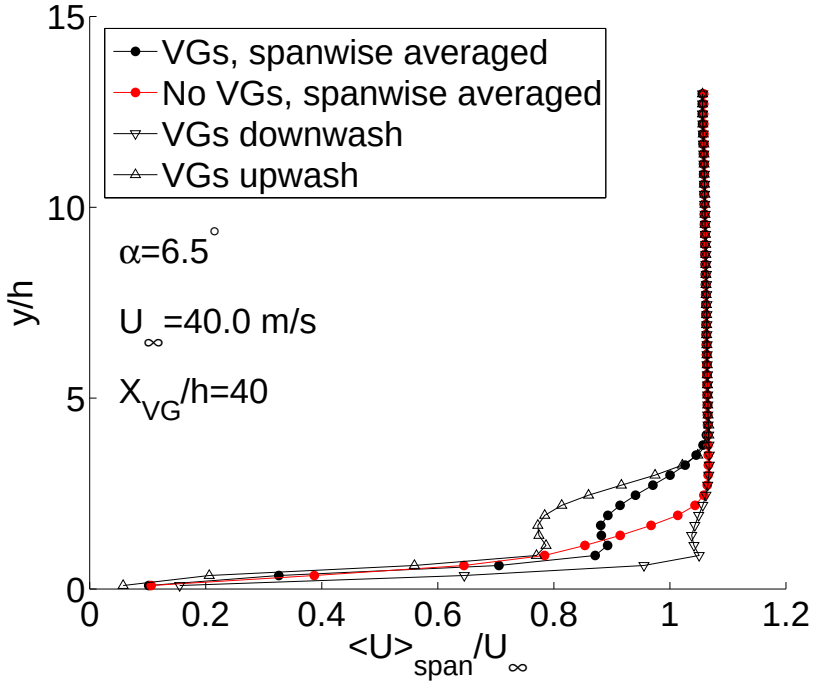


Figure 7.19: Velocity profiles for $\alpha = 6.5°$, $U_\infty = 40.0$ m/s and $X_{VG}/h = 40$. The figure displays spanwise averaged velocity profiles from the mean controlled and uncontrolled velocity field as well as profiles from the mean velocity field extracted in the upwash and downwash regions.

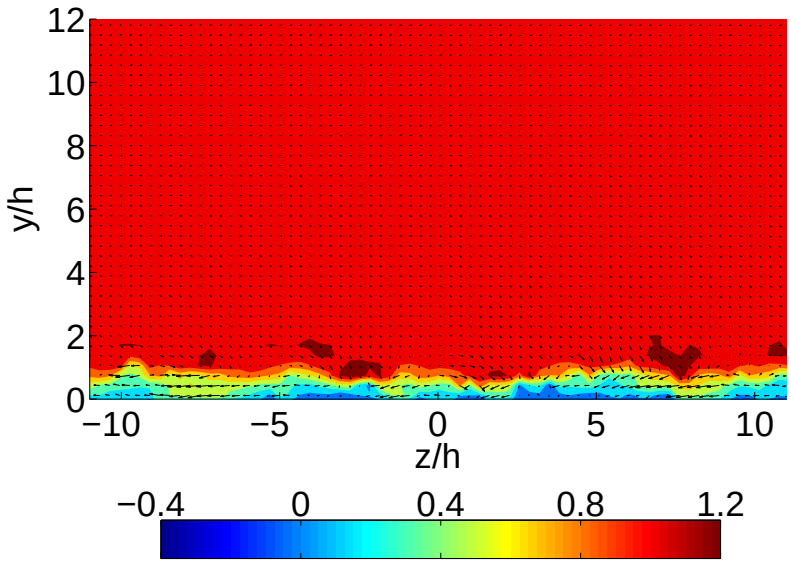


Figure 7.20: One rather representative snapshot of the controlled flow at $\alpha = 18.0°$ and $X_{VG}/h = 20$. The boundary layer has a very steep gradient as the wall is approached. To improve the clarity of the figure, the velocity vectors have been scaled down by a factor of 2/3 in the snapshot compared to the average velocity fields.

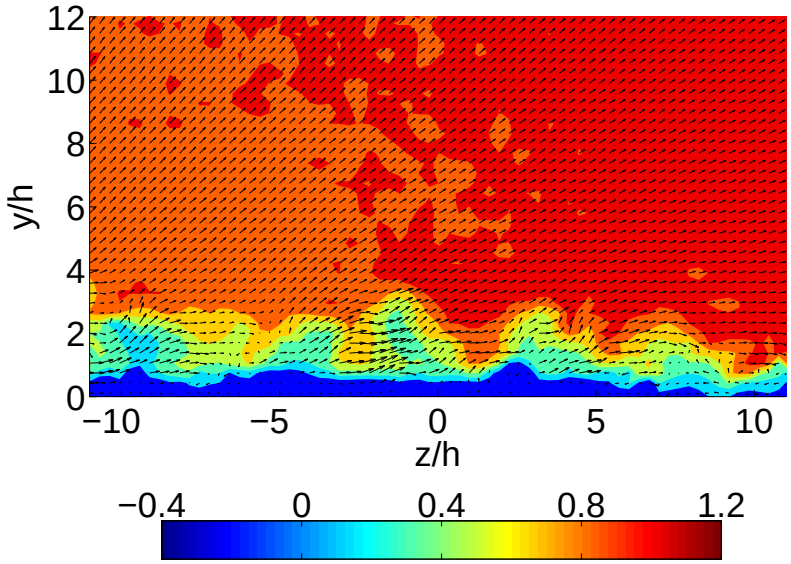


Figure 7.21: Another rather representative snapshot of the controlled flow at $\alpha = 18.0°$ and $X_{VG}/h = 20$, accentuating the periodicity of the organized actuator induced structures. To improve the clarity of the figure, the velocity vectors have been scaled down by a factor of 2/3 in the snapshot compared to the average velocity fields.

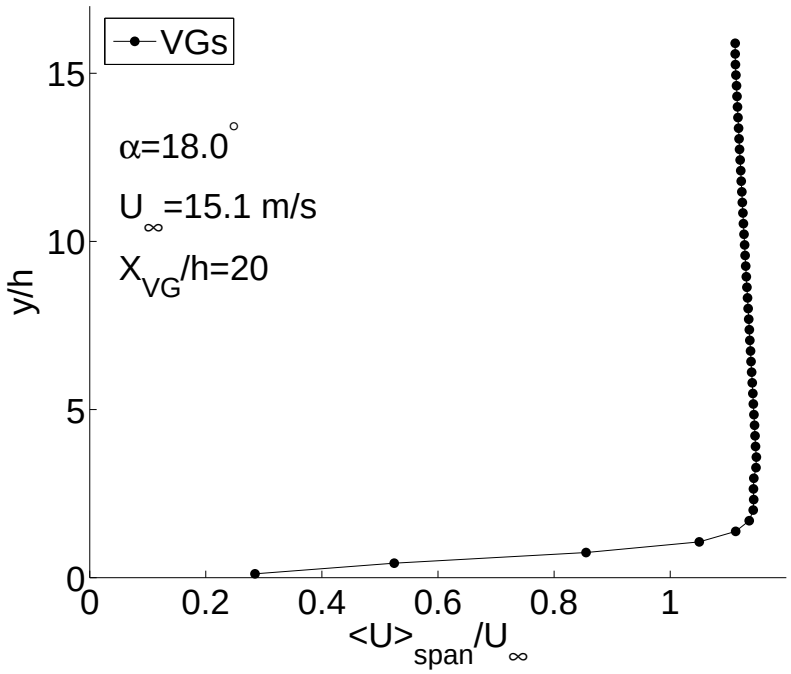


Figure 7.22: Spanwise averaged axial velocity for angle of attack $\alpha = 18.0°$ and free stream velocity $U_\infty = 15.1$ m/s at $X_{VG}/h = 20$.

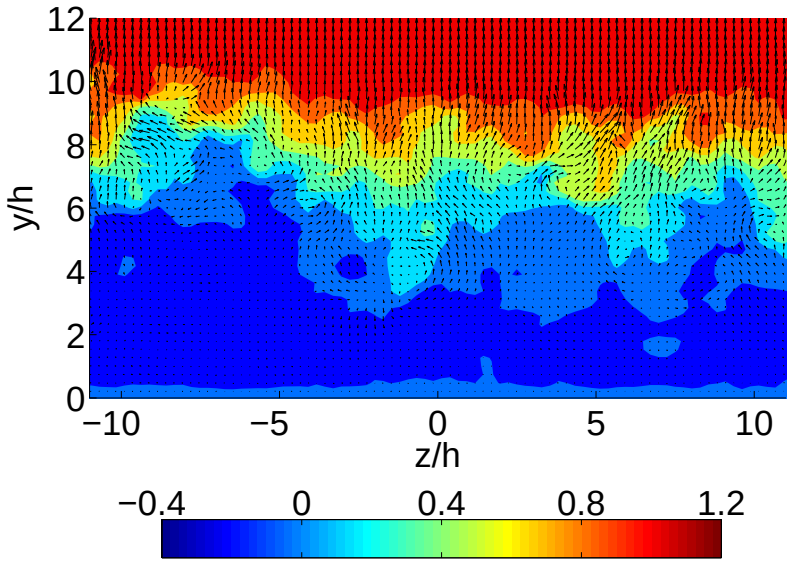


Figure 7.23: One rather representative snapshot of the uncontrolled flow at $\alpha = 18.0°$ and $X_{VG}/h = 48$, accentuating the impact of the high turbulence level of the flow. To improve the clarity of the figure, the velocity vectors have been scaled down by a factor of 2/3 in the snapshot compared to the average velocity fields.

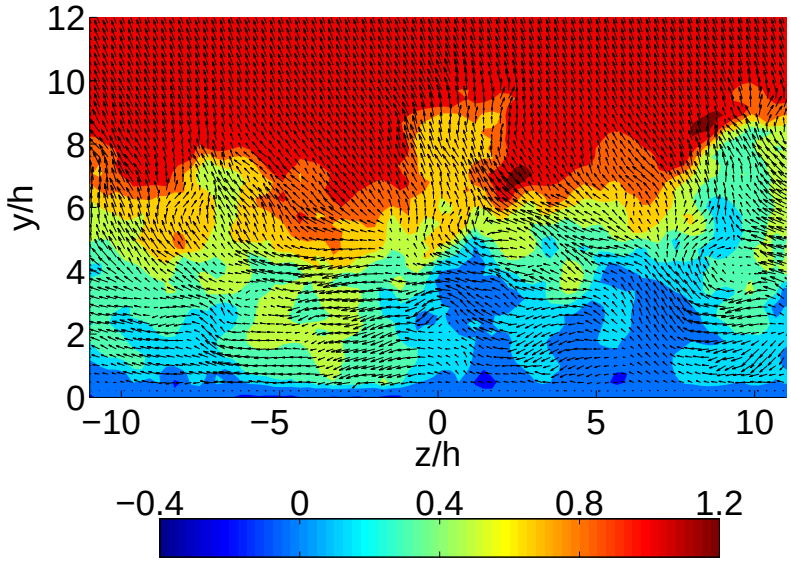


Figure 7.24: One rather representative snapshot of the controlled flow at $\alpha = 18.0°$ and $X_{VG}/h = 48$, accentuating the high turbulence level of the flow. To improve the clarity of the figure, the velocity vectors have been scaled down by a factor of $2/3$ in the snapshot compared to the average velocity fields.

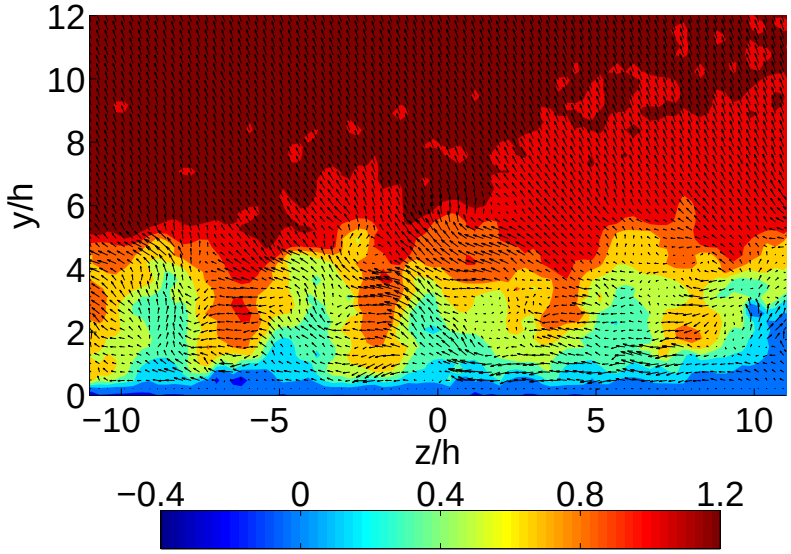


Figure 7.25: Another rather representative snapshot of the controlled flow at $\alpha = 18.0°$ and $X_{VG}/h = 48$, accentuating the periodicity of the organized actuator induced structures. To improve the clarity of the figure, the velocity vectors have been scaled down by a factor of $2/3$ in the snapshot compared to the average velocity fields.

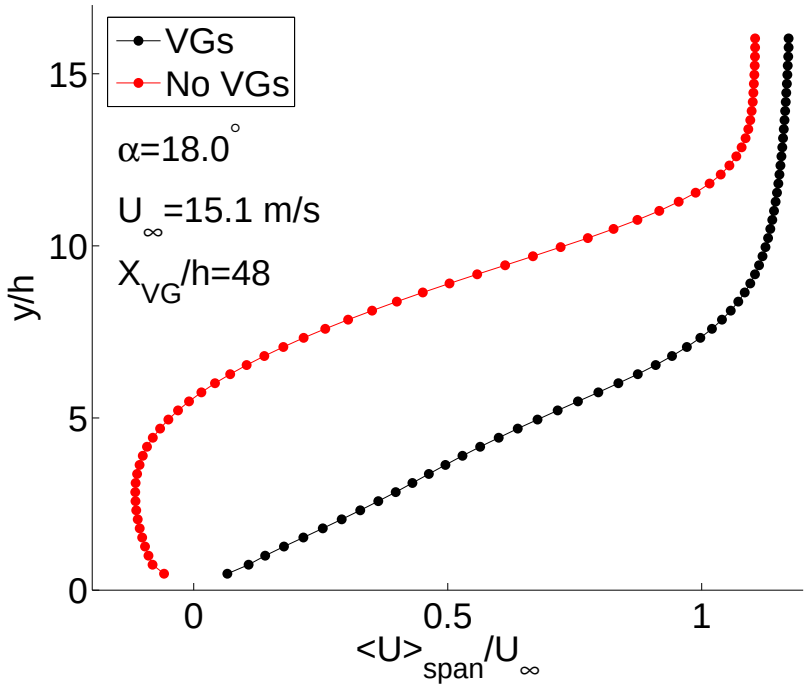


Figure 7.26: Spanwise averaged axial velocity for the controlled (VGs) and uncontrolled (No VGs) flow for an angle of attack of $\alpha = 18.0°$ and free stream velocity $U_\infty = 15.1$ m/s at $X_{VG}/h = 48$.

# Part IV

# Dynamics of Embedded Vortices and Implications

# Chapter 8

# Investigation of the Dynamics of the Embedded Vortices

In an attempt to study the dynamics of the vortex generator induced vortices, time-series obtained by Hot-Wire Anemometry (HWA) were used to construct power spectra. The idea was that, if present in the flow, a periodic large scale oscillation frequency will appear in the spectrum as a distinct spike, revealing the dynamic behavior of the device induced vortices. Comparison of spectra computed from measurements conducted in the same position just downstream of the devices, measuring both the actuated and incident flow, should reveal the induced dynamic behavior of the embedded vortices. HWA was employed both for these measurements behind the vortex generators as well as for characterizing the inlet. Some time series measurements of the inlet flow were also performed by LDA, when no HWA system was available. This data was processed as burst-mode LDA spectra, applying the direct Fourier transform due to the random sampling and residence time weighting due to the intermittent nature of the signal, see Chapter 11. Due to the substantial difference in requirements of computing power and time between the burst-mode LDA and FFT spectra, not to mention the higher noise floor caused by the intermittent LDA signal, essentially burying the spectrum, the HWA measurements were analyzed in this study.

## 8.1 Introduction

Power spectra are often used not only to study turbulence, but also to detect dominating frequencies from large scale structures such as vortex shedding in a cylinder wake and other periodic flow; see, e.g., Gjelstrup *et al.* [50]. In this work, they are employed with the intention to detect and separate dominant distinct frequencies from the remaining flow in the wakes of vortex generators. Further, the inlet of the test section, also corresponding to the inlet configuration of the studies described in Chapters 5 and 6, was characterized by traversing the probe across the height of the channel.

The average velocity profile measured closest to the inlet displays periodic variations, corresponding to jets emerging through the holes in the inlet grid. This trend is seen in both the streamwise and spanwise velocity components

as well as in the normal and shear stresses. This is also reflected in the power spectral measurements, where higher energy is assigned to the lower frequencies (larger scales) periodically across the channel height. The flow is, however, on average smoothed out and behaves well at a position beyond which all measurements have been carried out in the current and other studies (see Chapters 5 and 6). Further, none of the measurements conducted downstream of vortex generators displayed any peak from periodic oscillations of the induced vortices.

## 8.2 Experimental setup and arrangement

### 8.2.1 Wind tunnel

The measurements were carried out in a closed-circuit wind tunnel with an 8:1 contraction ratio and a test section of cross sectional area 300×600 mm and length 2 m. The measurements were conducted at a free stream velocity of $U_\infty = 1$ m/s, corresponding to a Reynolds number $Re_h$ =1 700 based on the vortex generator height. At this low velocity, the turbulent inflow is assured by a turbulence generating inlet grid with mesh length M = 39 mm, situated at the beginning of the test section. From the measurement data, the turbulence intensity at the inlet was estimated to 13%.

The HWA inlet characterization measurements were conducted at three positions downstream of the inlet grid; 10, 35 and 70 cm. These positions were chosen to study the development of the flow up to 70 cm, where the vortex generators later were applied. At each downstream location, the probe was traversed through 96 points with a distance of 2 mm between each point, ranging between 10 to 200 mm from the wall. The sampling frequency was chosen to $f_s = 5$ kHz with a total record length of T = 20 s at each point. Two velocity components were recorded; the streamwise and the spanwise (wall parallel). Further, LDA measurements were performed at mid-channel 300 mm downstream of the turbulence generating inlet grid, also with the same velocity components. LDA time series with a sample size of N = 70 000 were obtained with an average sampling rate of 350 Hz. The instantaneous velocities as well as the residence times were measured and collected for each measurement series. Due to the demanding requirements of computing power and time between the burst-mode LDA and FFT spectra, as well as due to the higher noise floor caused by the intermittent LDA signal, essentially burying the spectrum, the HWA measurements were analyzed in this study.

The vortex generators were rectangular with a height of 25 mm, corresponding to the local boundary layer thickness. The actuator length was twice its height, i.e., the aspect ratio was 2:1. Three configurations were chosen for the study of the vortex generator induced flow;

- Incident flow with no actuators present.
- One single actuator positioned at mid-channel at an angle of about 18° to the oncoming flow.
- An actuator cascade positioned in a fashion producing counter-rotating vortices. The configuration is the same as the one employed in Chapter 6, see figure 6.2, but with rectangular vanes and positioned directly on the test section wall.

Time series measurements were performed at three downstream positions behind the vortex generator trailing edge; 10, 20 and 50 mm at the height of the vortex generator. The sampling frequency was set to $f_s$ =10 kHz and the total record length of each measurement was chosen to T = 400 s.

### 8.2.2 HWA setup

Data was acquired using a Dantec Dynamics StreamLine system with a 55P61 gold-plated/miniature X-wire probe which was positioned at the spanwise center of the channel to measure the streamwise (U) and wall parallel (V) velocity components. The probe was positioned in the flow so that the predominant flow direction attacks the wires under an angle of 45°. The length and diameter of the sensing wires were 1.25 mm and 5 $\mu$m, respectively. A NI DAQ A/D converter and the StreamWare 4.10 software were used for acquisition.

Angular calibration was performed in a FlowUnit StreamLine calibration system between ±15 degrees with increments of 5 degrees at 1 m/s, corresponding to the wind tunnel velocity at which the measurement were to be conducted. The effective cooling velocities were expressed in terms of a fourth order polynomial function of anemometer output voltages and the unknown parameters were found using a nonlinear least-squares curve fit.

## 8.3 Results and discussion

### 8.3.1 Characterization of inlet flow

In order to interpret the power spectra of the actuator dynamics measurements, it is essential to understand the flow incident on the devices. Therefore, the flow at the inlet and even further downstream has been measured to characterize the inlet velocity profiles as well as the frequency content of the flow.

#### 8.3.1.1 Inlet profiles

The inlet profiles were, due to practical reasons, only measured in the lower half of the channel closest to the wall of the placement of the vortex generators, covering about 2/3 of the full channel width. Further, measurements were not conducted closer than 10 mm to the wall for similar practical reasons. A characterization of the full inlet in terms of profiles of moment before the re-design of the tunnel can be found in the PhD thesis of Schmidt [123].

Figure 8.1 shows the mean axial (U) velocity profiles measured by HWA at 10, 35 and 70 cm downstream of the inlet grid, respectively. From the profile at 10 cm, it is apparent that the inlet grid gives rise to jet-like structures which, on average, are smoothed out as one moves further downstream. The mean spanwise (V) velocity profiles measured simultaneously at the corresponding positions can be seen in figure 8.2. Even here, the jet-like behavior shows up in the profile at 10 cm due to the sideways movements of the structures caused by the varying pressure field across the channel. Since one can expect a similar flow behavior of the other stream-normal component, this profile indicates mixing in the two components perpendicular to the flow direction. Hence, due to the alternating high and low pressure regions that this situation is causing, the flow will become unsteady. This unsteadiness is mainly restricted to macro motions and should therefore primarily be located at low frequencies in power spectra.

Another indication of this is the profiles of the normal (<uu> and <vv>) and shear (<uv>) stresses, shown in figures 8.3, 8.4 and 8.5, respectively. These variations are present here as well, showing a strong correlation between the velocity components in the shear stresses <uv>, see figure 8.5. The structures seen at 10 cm have previously been observed by Ullum *et al.* [142] in PIV measurements in the same channel prior to the re-design of the wind tunnel.

At the intermediate position 35 cm, the flow is not settled. Most of the energy resides in the axial component and is distributed non-uniformly across the channel. This is reflected also in the stresses. At 70 cm, which is the position at which the actuators have been positioned in the following part of the current investigation, both the mean velocity and stress profiles have a much more regular trend and the shear stress is close to zero in the free stream.

#### 8.3.1.2 Time series from inlet

In order to study the variations of the frequency content across the inlet, time series have been acquired along a wall-normal traverse and power spectra have been computed for all of these points. The results are shown as color plots in figures 8.6 through 8.14, displaying the power spectral content as a function of distance to the wall. The magnitude of the spectra are displayed as colors on a logarithmic scale. The first three figures display $S_{11}(f)$ as a function of distance from the wall at downstream positions 10, 35 and 70 cm, respectively, while the next three show the same dependency for $S_{22}(f)$ and the last three for $S_{12}(f)$.

At the most upstream position 10 cm, figures 8.6, 8.9 and 8.12 clearly display high energetic (large scale) structures occurring periodically across the inlet, as was expected from the previous discussion of the average velocity profiles. Studying the trend as one moves downstream, the energy becomes increasingly more uniform across the height of the channel. Across the frequency range, the power spectra vary smoothly without any dominant peaks that indicate large scale periodic disturbances. Since no distinct peaks are present in the spectra, but it is established that the flow is unsteady, the large scale fluctuations must be non-periodic or, at the most, quasi-periodic. This should manifest itself as energy distributed across a wider range of frequencies in stead of at one distinct and narrow one.

### 8.3.2 Dynamics of actuator induced flow

The actuator induced flow was characterized by measuring time series in three configurations; a single vortex generator, behind one actuator in a cascade generating counter-rotating vortices and the incident flow with no vanes present. The vortex generators were rectangular of height 25 mm with an aspect ratio of 2:1. Three measuring positions were chosen; 10, 20 and 50 mm downstream of the actuator trailing edge at the height of the vortex generator. Figures 8.15 through 8.23 show the power spectra derived from the measurement data, the first three being the two autospectra and the crosspectrum at 10 mm downstream of the actuator(s) trailing edge position. The following three correspond 20 mm and the last three 50 mm downstream of the devices.

As can be seen in the figures, no distinct peaks appear in any of the spectra. Hence, one can only conclude that the actuators do not have any such significant effect on the dynamics under the present conditions (Reynolds number, device configuration, inlet turbulence etc.).

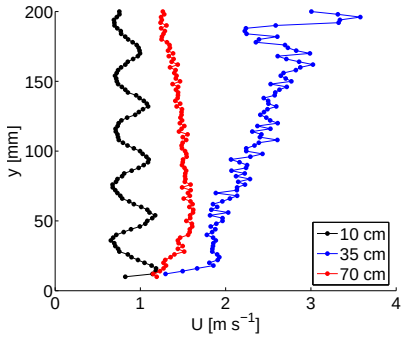


Figure 8.1: Mean axial velocity profiles at 10, 35 and 70 cm downstream of the inlet grid.

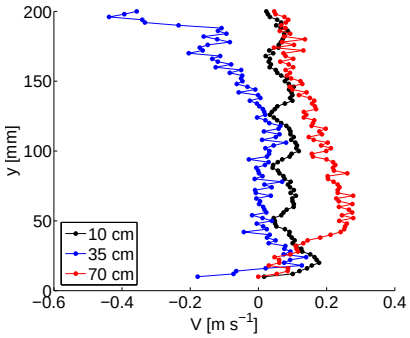


Figure 8.2: Mean spanwise velocity profiles at 10, 35 and 70 cm downstream of the inlet grid.

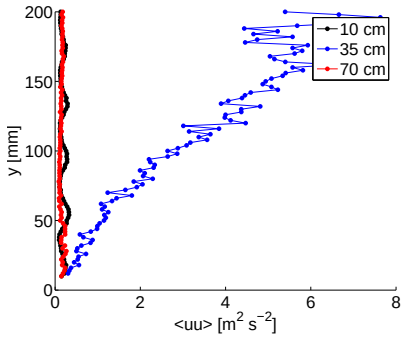


Figure 8.3: Mean profiles of normal stresses <uu> at 10, 35 and 70 cm downstream of the inlet grid.

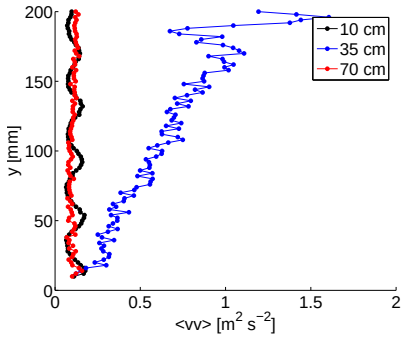


Figure 8.4: Mean profiles of normal stresses <vv> at 10, 35 and 70 cm downstream of the inlet grid.

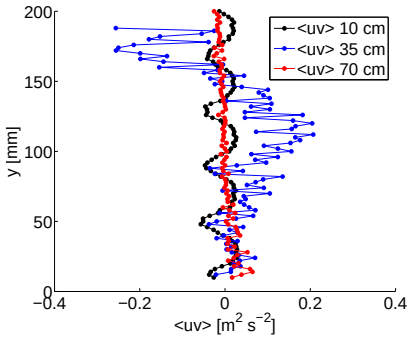


Figure 8.5: Mean profiles of shear stresses <uv> at 10, 35 and 70 cm downstream of the inlet grid.

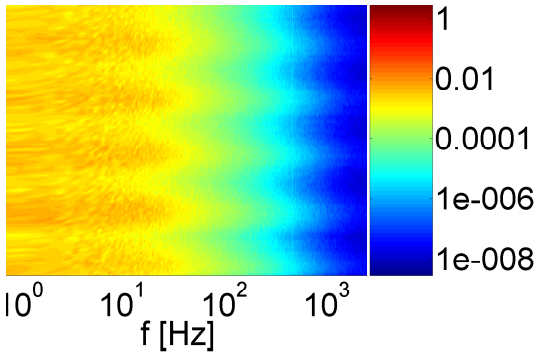


Figure 8.6: $S_{11}(f)$ at a distance of 10 cm downstream of the inlet as a function of distance to the wall. The magnitude of the spectrum is displayed as colors on a logarithmic scale.

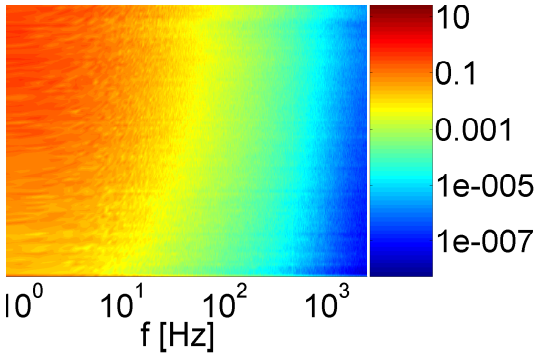


Figure 8.7: $S_{11}(f)$ at a distance of 35 cm downstream of the inlet as a function of distance to the wall. The magnitude of the spectrum is displayed as colors on a logarithmic scale.

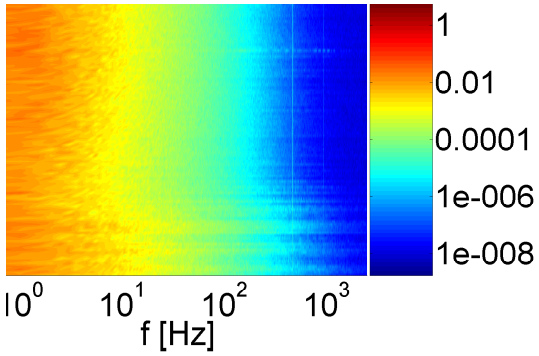


Figure 8.8: $S_{11}(f)$ at a distance of 70 cm downstream of the inlet as a function of distance to the wall. The magnitude of the spectrum is displayed as colors on a logarithmic scale.

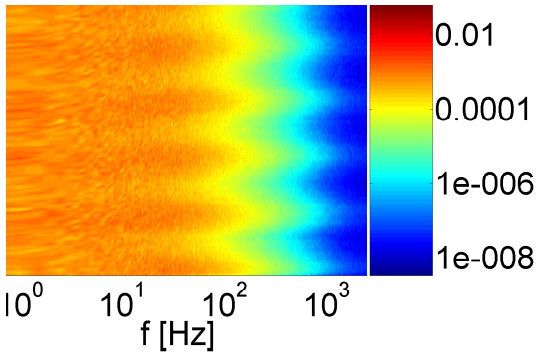


Figure 8.9: $S_{22}(f)$ at a distance of 10 cm downstream of the inlet as a function of distance to the wall. The magnitude of the spectrum is displayed as colors on a logarithmic scale.

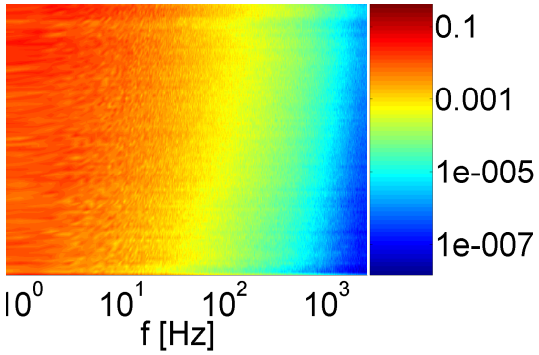


Figure 8.10: $S_{22}(f)$ at a distance of 35 cm downstream of the inlet as a function of distance to the wall. The magnitude of the spectrum is displayed as colors on a logarithmic scale.

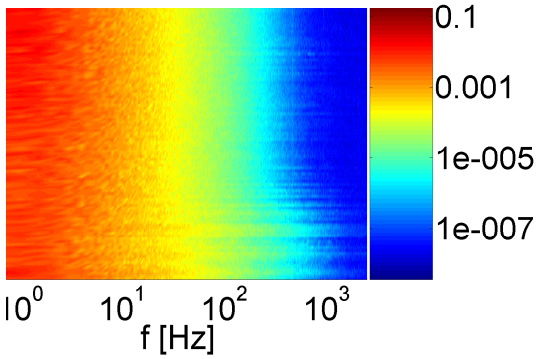


Figure 8.11: $S_{22}(f)$ at a distance of 70 cm downstream of the inlet as a function of distance to the wall. The magnitude of the spectrum is displayed as colors on a logarithmic scale.

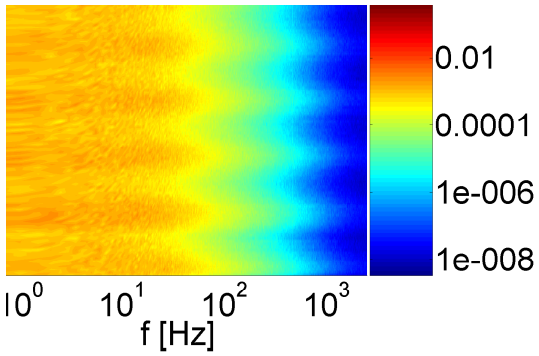


Figure 8.12: $S_{12}(f)$ at a distance of 10 cm downstream of the inlet as a function of distance to the wall. The magnitude of the spectrum is displayed as colors on a logarithmic scale.

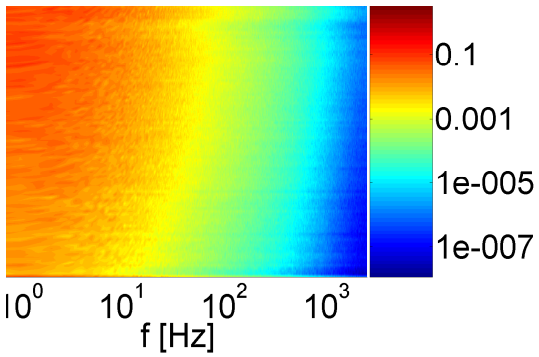


Figure 8.13: $S_{12}(f)$ at a distance of 35 cm downstream of the inlet as a function of distance to the wall. The magnitude of the spectrum is displayed as colors on a logarithmic scale.

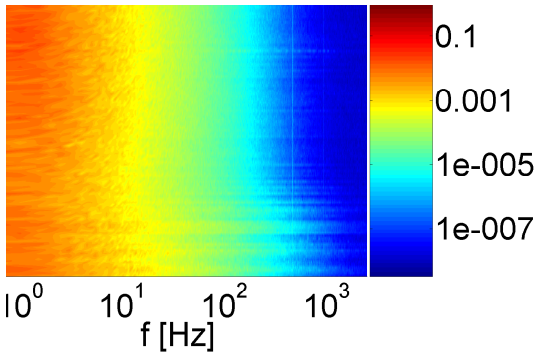


Figure 8.14: $S_{12}(f)$ at a distance of 70 cm downstream of the inlet as a function of distance to the wall. The magnitude of the spectrum is displayed as colors on a logarithmic scale.

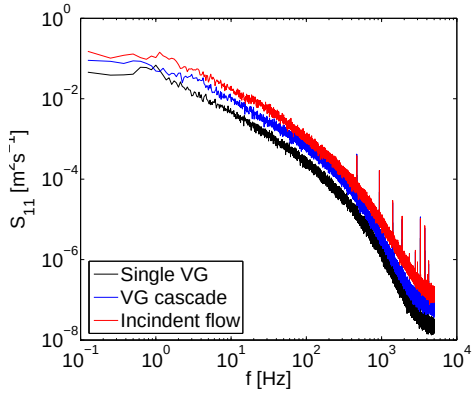


Figure 8.15: $S_{11}(f)$ from HWA data measured 10 mm downstream of the vortex generator positions. The spectra behind a single actuator, a cascade and the incident flow are represented.

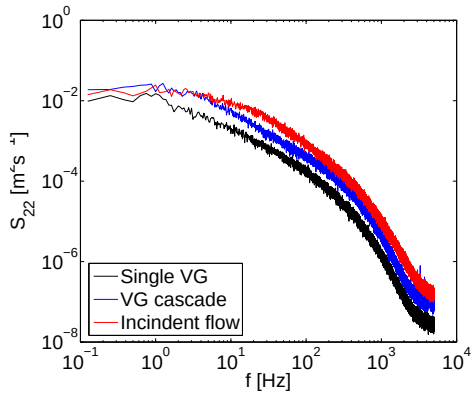


Figure 8.16: $S_{22}(f)$ from HWA data measured 10 mm downstream of the vortex generator positions. The spectra behind a single actuator, a cascade and the incident flow are represented.

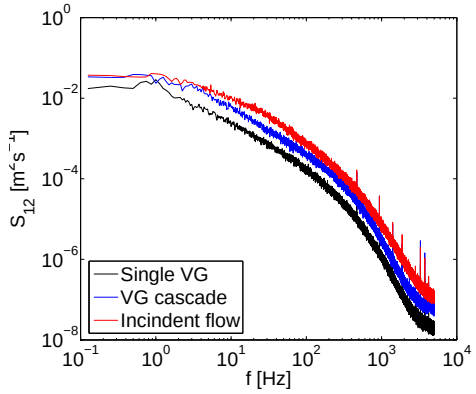


Figure 8.17: $S_{12}(f)$ from HWA data measured 10 mm downstream of the vortex generator positions. The spectra behind a single actuator, a cascade and the incident flow are represented.

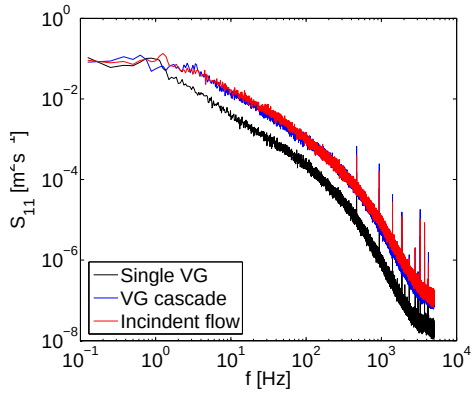


Figure 8.18: $S_{11}(f)$ from HWA data measured 20 mm downstream of the vortex generator positions. The spectra behind a single actuator, a cascade and the incident flow are represented.

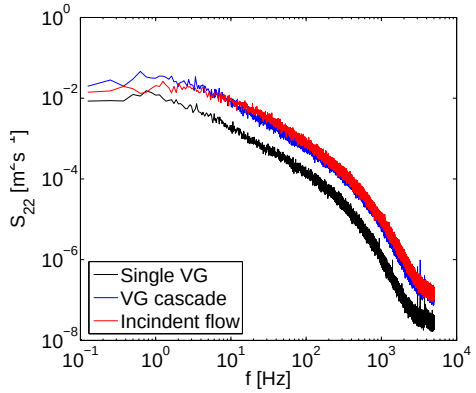


Figure 8.19: $S_{22}(f)$ from HWA data measured 20 mm downstream of the vortex generator positions. The spectra behind a single actuator, a cascade and the incident flow are represented.

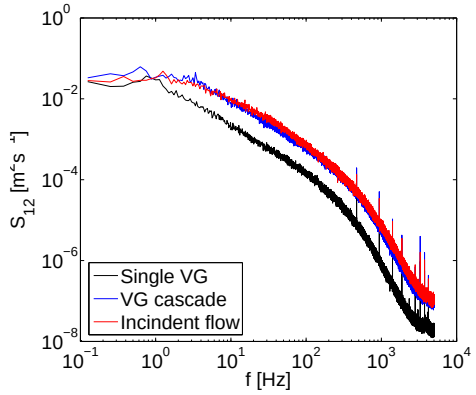


Figure 8.20: $S_{12}(f)$ from HWA data measured 20 mm downstream of the vortex generator positions. The spectra behind a single actuator, a cascade and the incident flow are represented.

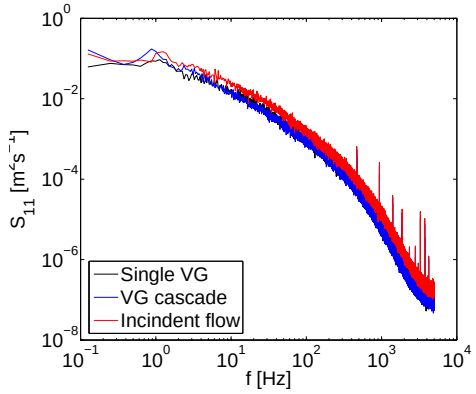


Figure 8.21: $S_{11}(f)$ from HWA data measured 50 mm downstream of the vortex generator positions. The spectra behind a single actuator, a cascade and the incident flow are represented.

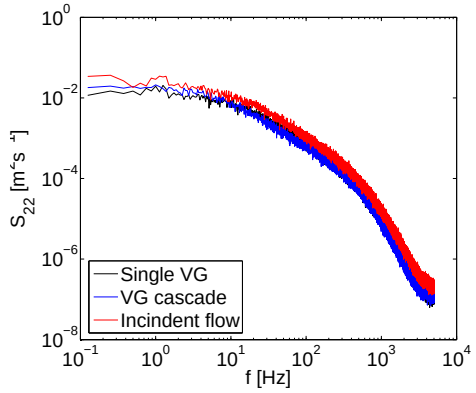


Figure 8.22: $S_{22}(f)$ from HWA data measured 50 mm downstream of the vortex generator positions. The spectra behind a single actuator, a cascade and the incident flow are represented.

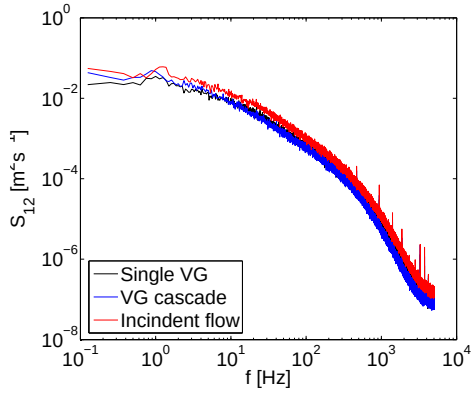


Figure 8.23: $S_{12}(f)$ from HWA data measured 50 mm downstream of the vortex generator positions. The spectra behind a single actuator, a cascade and the incident flow are represented.

## 8.4 Conclusions

The average inlet profiles display jet-like effects at the most upstream measuring position, which on average homogenize when moving downstream. These effects have previously been observed in the same wind tunnel under similar conditions with the same turbulence generating inlet grid present, see Ullum *et al.* [142]. Power spectra from across the entire measured profile also display this behavior in the most upstream position, but the energy across the channel becomes much more smoothly distributed in the more downstream positions investigated.

Power spectra derived from HWA measurements behind a single vortex generator, as well as behind one in a cascade, were produced to attempt to detect peaks corresponding to the frequency of the movement of the device induced vortices. The uncontrolled flow was measured in the same positions as a reference. The spectra do not show any distinct peaks, suggesting that the vortices have a quasi- or non-periodic behavior with a more complex pattern.

This can, however, not be considered a general result, since the spectra might look different if measured, e.g., at a different Reynolds number, oncoming turbulent/laminar flow, actuator configuration etc. Further, the background flow might contain strong turbulent pulsations or even large scale fluctuating motions that kill or dominate any vortex generator induced dynamics. It is therefore hard to draw any conclusions from the present results. The experiments should preferably be reconducted after removing the turbulence generating inlet grid in order to be able to draw more definite conclusions for the present configuration and Reynolds number.

# Chapter 9

# Correction for Effects of Random Noise in Spectra and Correlations

A new technique is described for the estimation and removal of the additive random noise component in spectra and correlations. The methodology is illustrated using power spectra and correlations from recent hot-wire experiments in axisymmetric wake turbulence behind a disc. In addition to retaining the correct total energy, the determination of other quantities attained from spectra such as the integral time scale are improved. The magnitude of the noise spectrum can be determined from the converged constant value of the spectrum in the high frequency end, where turbulence dissipates and white noise is the only remaining component. By characterizing the noise and verifying that it is additive to the spectrum, the white broad-band spectral noise can be subtracted from the signal, resulting in a spectral estimator converging to zero at high frequencies. The noise removal methodology presented here can be applied to both temporally and spatially separated data as well as to virtually all measurement techniques and numerical simulations where white noise appears.

## 9.1 Introduction

Random noise in data can often need special care, in particular when one wants to attain quantities derived from spectra; e.g., the integral time scale and turbulence kinetic energy in the case of turbulent flow. Consider a constant random noise contribution to the spectrum which offsets the spectrum by the magnitude of the flat spectral noise level. In order to obtain the energy, one needs to integrate the power spectrum across the band-width. This procedure does not discriminate between the noise and signal contributions to the energy estimate, leading to an over-prediction of the energy due to the inclusion of the noise contribution in the integral. Even though the noise level seems to be small, the whole-line integral of the noise spectrum might be non-negligibly large compared to the actual energy. The noise will also add to the integral scale, determined from the low-frequency asymptote, resulting in over-prediction of this quantity

as well.

The problem can be quite severe when measuring low turbulence intensity flows. For small enough turbulence intensities, the actual velocity fluctuations might be indistinguishable from the random noise contribution. At these low signal-to-noise ratios the noise will comprise a larger fraction of the measured signal, yielding large over-predictions of quantities attained from the power spectrum in general and the energy in particular. This can be particularly problematical for hot-wires, for example, which are restricted to flows of low or moderate turbulence intensities due to the unambiguity in flow direction and risk of probe fouling[1].

Noise suppression in power spectral estimates has previously been attempted by Benedict and Gould [9] and van Maanen and Tulleken [80] for LDA data using Kalman filters, assuming the noise to be white. In George [44], the frequency dependent noise resulting from random phase fluctuations or Doppler ambiguity was removed using a sequence of low-pass filters at frequencies beyond those of the turbulence. Nobach *et al.* [97] tried to suppress the noise in a power spectrum from LDA data using a FIR-filter, parameterized using the mean data rate. A sample-and-hold interpolation with uniform resampling was applied. In fact, one of the most commonly adapted methods to escape the noise problems is to use analog low-pass filters while measuring before digitization. This unretractable filtering removes anything above a certain cut-off frequency, however still leaving the frequencies below the cut-off frequency contaminated. Besides, it can also remove a part of the signal in addition to the noise. On the other hand, a less widely known effect of applying low-pass filtering is that it imposes its own integral time scale onto the signal, since the transfer function is convolved with the signal (multiplicated in frequency space) is time dependent. For these reasons, low-pass filtering is usually at best a less than ideal solution to the problem.

It has commonly been assumed that one can justify the removal of the flat white noise spectrum from spectral estimates. This is of course possible only if the signal and noise are uncorrelated. Therefore, identification and characterization of the random noise component in spectra and correlations is vital to the justification of its removal. If one understands how the noise appears in the data, it is possible to pinpoint the source in the spectral or correlation estimator and evaluate the noise contribution.

In this chapter, a method has been proposed for the removal of the random noise term in spectra and correlations. The theory is applied to temporal data, but is by no means limited to this and can also be applied to spatial data. Hot-wire anemometry (HWA) measurements in axisymmetric wake turbulence behind a circular disc have been utilized to provide examples of applications of the developed technique. The dominating noise term in a power spectral estimate for usual experimental realizations of equidistantly sampled data, such as hot-wire anemometry output, is identified to be random white step noise arising from the quantization errors of the A/D conversion process. This white noise can be traced to the noise variance term, i.e., the correlation of the noise at zero time lag, which is the only instant at which the random noise is correlated with

[1] The random noise contribution, in relation to the one of the signal, might be even further dominating if the hot-wire is operating at a low overheat ratio, if the wire material has a low temperature coefficient of resistance or if a thick wire with a high thermal capacity is used [33].

itself. This random noise contribution manifests itself as a spike at the origin in the autocorrelation. In the same manner, random noise in power spectra is confined to the self-products (the trace) in the discrete Fourier transform of the autocorrelation, where the trace contains both the total energy of the signal as well as all of the noise. Note that random noise does not affect cross-spectra for data obtained from separate channels, since the noise of different channels is uncorrelated even at zero time lag.

As will be seen later, it is argued for and assumed that the signal is uncorrelated with the random noise (note that this does NOT require statistical independence), resulting in the additivity of the signal and noise contributions to spectra. The random noise part of the spectrum should be frequency independent and therefore constant across frequency. Since the turbulent velocity fluctuations are not spectrally white, this difference in spectral characteristics can be used to distinguish the noise from the signal contribution in the spectral estimator. This discrepancy becomes apparent in the high frequency asymptote of a turbulence power spectrum, beyond the turbulence dissipation, where the only possible remaining signal is the noise. Clearly if the noise is additive to the spectrum, one can subtract off the constant random noise contribution from the remainder of the signal and recover the spectrum.

The work in this chapter can be applied to all measurements including; e.g., Particle Image Velocimetry (PIV) or pitot tube pressure measurements. In particular, if one accounts for the random sampling of the signal resulting from the sampling process, this technique can be applied to Lased Doppler Anemometry (LDA) measurements, which have a high white noise level due to the intermittency of the signal. PIV measurements are also subject to quantization errors on multiple levels due to the digitization of the particle images and the division of the measuring volume into finite sized interrogation areas. (Note that this is in addition to the filtering of the displacement vector across each interrogation area, also adversely affecting the turbulence statistics.) Even numerical errors such as discretization noise and roundoff errors in numerical flow simulations are often approximately spectrally white. To justify the application of this noise removal technique, one must only identify the sources of noise and evaluate whether it is reasonable to assume it to be uncorrelated with the signal. In addition, any spectra and correlations of order 2 or higher can be analyzed using the same methodology.

In the following section, a description of the experimental setup and measurements is provided. Then an introductory example of the noise removal in an autocorrelation function and the corresponding one-dimensional power spectrum from hot-wire measurements of an axisymmetric wake is given. These estimates are compared to two-point correlations with corresponding cross-spectra in order to shed light on the effects of noise in these estimates. The latter example has the important quality of consisting of data obtained from separate channels, yielding random noise from separate sources that are uncorrelated for all time lags. The noise removal technique is then demonstrated on the autospectrum and the noise free power spectrum is obtained. A discussion follows, highlighting the details of the signal processing and the distribution of the signal and noise parts of the signal. Finally the results are summarized and discussed.

## 9.2 Experimental setup and measurement

Wind tunnel measurements of axisymmetric wake turbulence behind a circular disc were analyzed in this study. The experiments were performed and documented by Tutkun, Johansson and George[2] (2008) [140]. Only a part of the complete data set collected during these measurements was used in this study. A summarized version of their experimental setup experiment is provided in Appendix A to provide continuity and completeness of the chapter.

## 9.3 Introductory example

The random noise removal technique is demonstrated by comparing the auto-correlation function and the corresponding one-dimensional power spectrum to estimates from a two-point correlation and its cross-spectrum from the same measurement campaign. In the first example, the random noise from one single source is correlated with itself, yielding zero correlation at all time lags except at the origin, where the diagonal terms are correlated with themselves yielding full correlation. In the second example, the noise generated at the separate channels is statistically independent for all time lags and therefore uncorrelated. Thus, the effects of the random noise that appear in the estimators in the first example are not observed in the two-point estimates.

Let's start the example by considering the power spectrum obtained from a set of HWA data using the decomposition of the instantaneous velocity, $\tilde{u}$, into mean and fluctuating velocities, $\tilde{u} = U + u$. For velocities sampled uniformly at discrete times, one can write

$$\tilde{u}_p = \tilde{u}(p\Delta t), \qquad p = 0, 1, 2, ..., N \tag{9.1}$$

$p$ being the sample number, $N$ the total number of samples in the 'block' of data, and $\Delta t = 1/f_s$ the sampling interval, whose reciprocal is the sampling frequency. One can express the block mean velocity as

$$U = \frac{1}{N} \sum_{p=0}^{N-1} \tilde{u}_p \tag{9.2}$$

and the block variance as

$$\overline{u^2} = \frac{1}{N} \sum_{p=0}^{N-1} u_p^2 = \mathrm{var}\{\tilde{u}\}. \tag{9.3}$$

Note that these estimators are really only useful for the true mean and variance if the samples are statistically independent, which for the closely spaced samples we consider here they generally are not. An estimate of the effective number of independent samples is closer to the record length divided by twice the integral scale of the process (cf., George 1978 [46]). From the expression for the discrete FFT of a finite time record with the usual selection of discrete

[2]Murat Tutkun at FFI, Norway, Peter B. V. Johansson at Volvo Aero Corporation and William K. George at CNRS UML in Lille, France are acknowledged for providing the data used in the current study.

frequency values for its computation (cf., George [49]),

$$\hat{u}_T(f_k) = \frac{T}{N}\sum_{p=0}^{N-1} e^{-i2\pi kp/N} u(t_p), \qquad f_k = \frac{k}{T} = \frac{k}{N\Delta t} \quad k = 0, 1, 2, \ldots, N-1 \tag{9.4}$$

where $T$ is the record length and $\Delta t$ is the time between two successive samples. The spectral estimator is given by

$$S_{11_T}(x, x; f_k) = \frac{\hat{u}_T(x; f_k)\hat{u}_T^*(x; f_k)}{T} = \frac{T}{N^2}\sum_{p=0}^{N-1}\sum_{q=0}^{N-1} e^{-i2\pi k(p-q)/N} u(x; t_p)u(x; t_q). \tag{9.5}$$

The subscript T indicates that the spectrum is computed over a finite record length. In general, $S_{1,1_T}$ in Eq. (9.5) will be a random quantity with 100% variability, and it will need to be averaged over independent blocks of data to produce a reasonable estimate of the true spectrum. The variability of this estimator will decrease as the inverse square root of the number of independent blocks of data used in computation (George [46]). A logarithmic and a linear plot of the autospectral estimators of a HWA data set is displayed in figures 9.1*a* and *b*, where 3600 independent blocks were used to produce the estimates. The spectra display convergence to a non-zero asymptote at high frequencies, representing the white noise level of the data.

Now, consider a cross-spectrum of the two-point correlation from the same set of measurements.

$$S_{11_T}(x, x'; f_k) = \frac{\hat{u}_T(x; f_k)\hat{u}_T^*(x'; f_k)}{T} = \frac{T}{N^2}\sum_{p=0}^{N-1}\sum_{q=0}^{N-1} e^{-i2\pi k(p-q)/N} u(x; t_p)u(x'; t_q). \tag{9.6}$$

where x and x′ denote two points in space separated by a finite distance. As above, this must be averaged over many blocks of statistically independent data to produce a convergent spectral estimator. In this example of the axisymmetric wake, the points are separated in the radial direction. The real and imaginary parts are displayed in a semi-logarithmic and a linear plot in figures 9.2*a* and *b*, where again 3600 independent blocks were used to produce the estimates. For these spectra the asymptote at high frequencies is zero.

To understand why the white noise disappears in the cross-spectrum, let's decompose the signal $u$ into signal $c$ and random noise $n$, $u(t) = c(t) + n(t)$. This decomposition can be implemented into the FFT based spectral estimator for the cross-spectrum.

$$\overline{S_{11_T}(x, x'; f_k)} = \frac{T}{N^2}\sum_{p=0}^{N-1}\sum_{q=0}^{N-1} e^{-i2\pi k(p-q)/N}\overline{[c(x; t_p) + n(x; t_p)][c(x'; t_q) + n(x'; t_q)]} \tag{9.7}$$

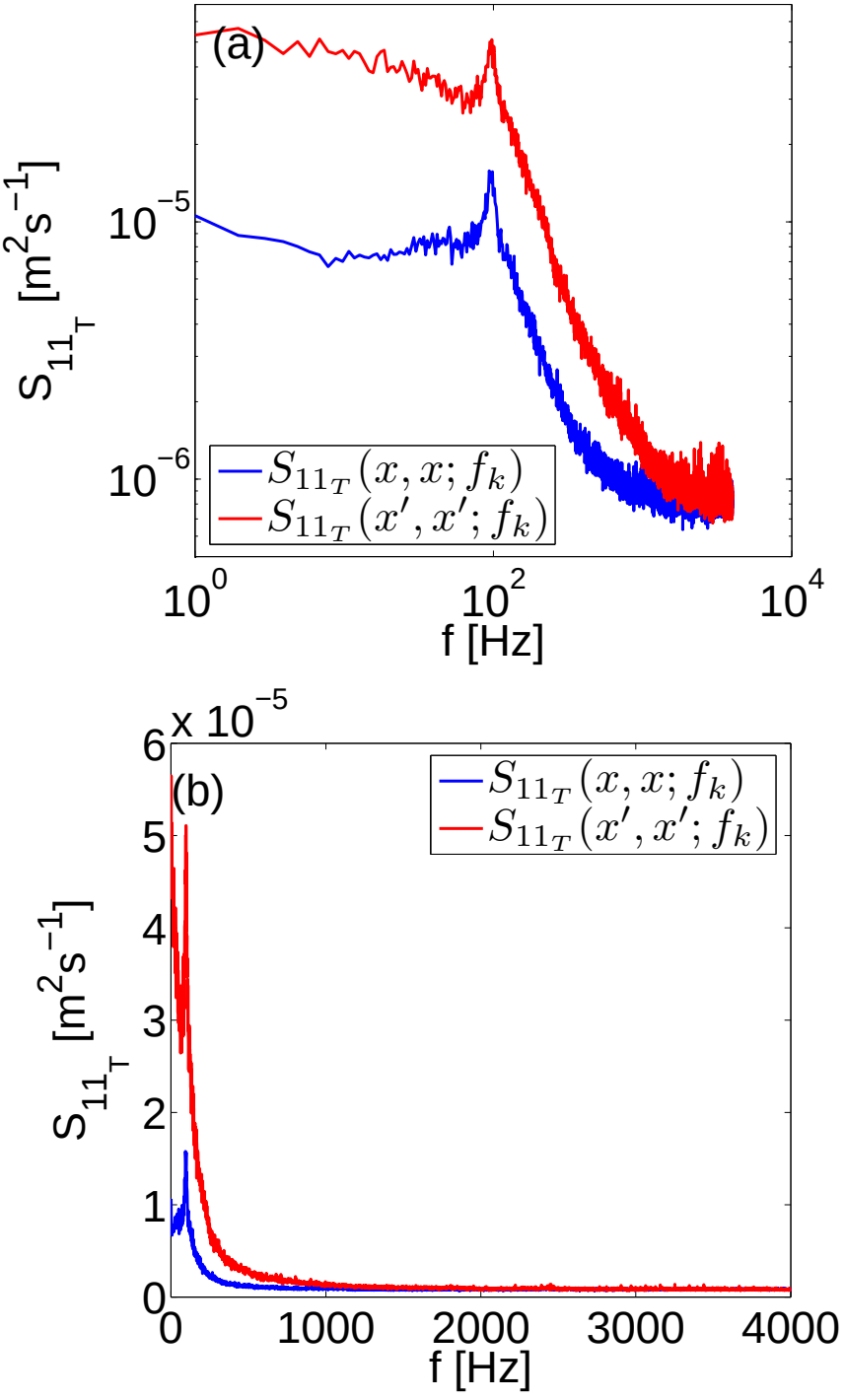


Figure 9.1: (a) Logarithmic and (b) linear plot of an autospectral estimator obtained from a HWA data set acquired in an axisymmetric wake behind a disc. As can be seen in the high frequency asymptote, the estimator converges to a finite value due to the presence of white noise.

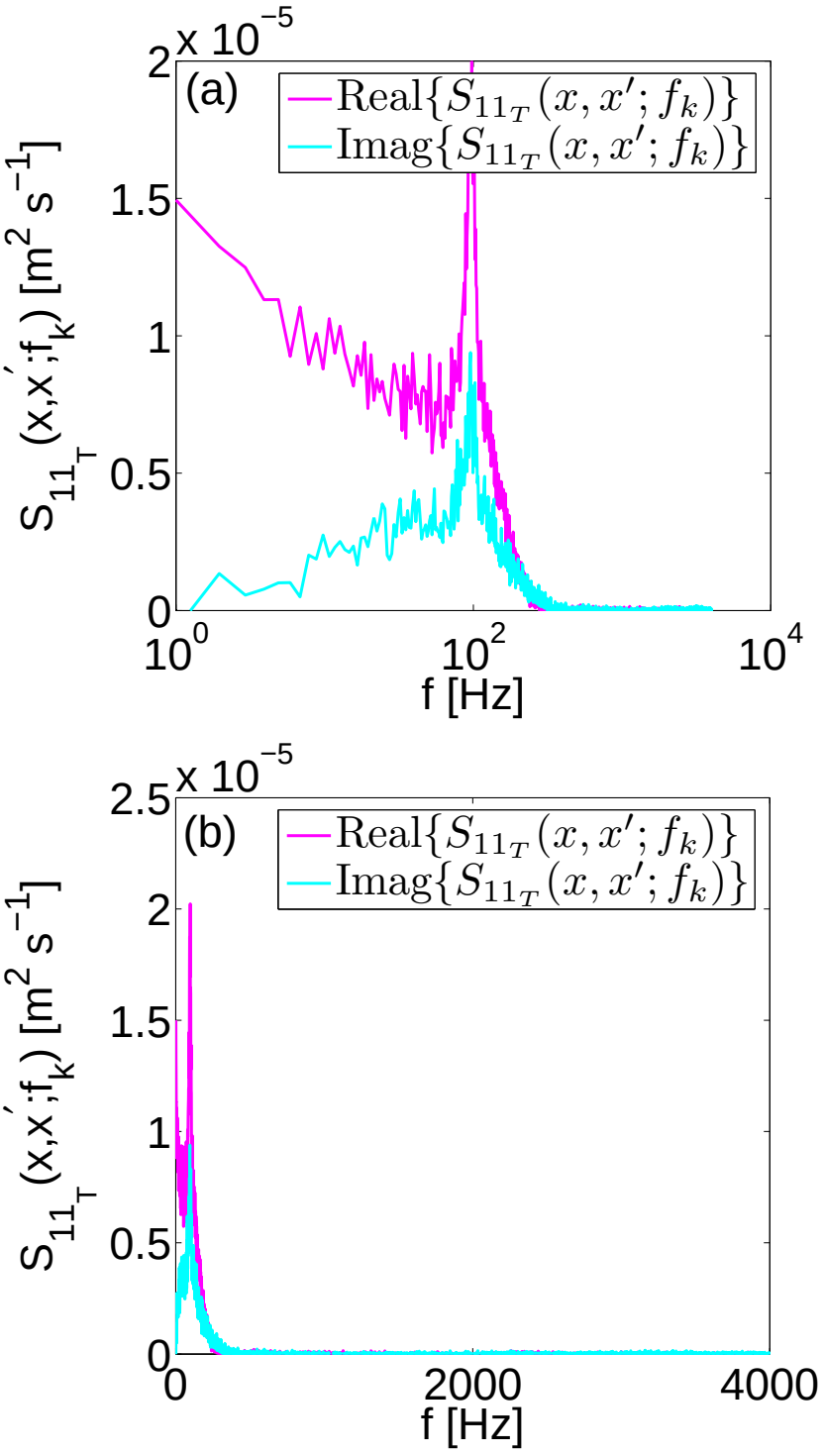


Figure 9.2: (a) Semi-logarithmic and (b) linear plot of a cross-spectral estimator of a HWA data set acquired in an axisymmetric wake behind a disc. At high frequencies, the estimators converge to zero.

Assuming that the noise is random and therefore always uncorrelated with the signal,

$$\overline{S_{11_T}(x,x';f_k)} = \frac{T}{N^2}\sum_{p=0}^{N-1}\sum_{q=0}^{N-1} e^{-i2\pi k(p-q)/N}\left[\overline{c(x;t_p)c(x';t_q)} + \underbrace{\overline{n(x;t_p)n(x';t_q)}}_{=0}\right], \tag{9.8}$$

where the first term is the signal cross-spectrum and the second term is the cross-spectrum of the noise. Since $n(x;t_p)$ and $n(x';t_q)$ are random and originate from separate channels, they are statistically independent and therefore uncorrelated. Thus, the noise term vanishes for converged estimators. For the previously considered $S_{11_T}$ autospectrum

$$\overline{S_{11_T}(x,x;f_k)} = \frac{T}{N^2}\sum_{p=0}^{N-1}\sum_{q=0}^{N-1} e^{-i2\pi k(p-q)/N}\left[\overline{c(x;t_p)c(x;t_q)} + \underbrace{\overline{n(x;t_p)n(x;t_q)}}_{\neq 0}\right], \tag{9.9}$$

where $n(x;t_p)$ and $n(x;t_q)$ originate from the same channel and the overbar indicates the true average (ensemble average based on an infinite number of statistically independent realizations). Since the noise is random, the last term vanishes for all but zero time lag, which must have perfect correlation since the diagonal terms are perfectly correlated with themselves. The noise can therefore be traced to the noise variance term, the so-called self-products for which $p = q$.

In the remainder of the chapter, the notation for the original autospectrum $S_{11_T}(x,x;f_k)$ is changed to $S_{\forall\, p,q}(f_k)$, since only the autospectrum will be considered, stressing the fact that all of the terms in the double sum are included in the estimator. One can divide the original spectrum into the spectrum of the self-products $S_{p=q}$ and the frequency content $S_{p\neq q}(f_k)$, all of which are displayed in a logarithmic and a linear plot in figures 9.3*a* and *b*.

$$\overline{S_{\forall\, p,q}(f_k)} = \underbrace{\frac{T}{N^2}\sum_{p=0}^{N-1}\overline{u^2(t_p)}}_{S_{p=q}} + \underbrace{\frac{T}{N^2}\sum_{\substack{p=0\\ p\neq q}}^{N-1}\sum_{q=0}^{N-1} e^{-i2\pi k(p-q)/N}\overline{u(t_p)u(t_q)}}_{S_{p\neq q}(f_k)} \tag{9.10}$$

where $p \neq q$ under the summation sign indicates that the diagonal terms for $p = q$ are omitted. The spectrum of the self-products $S_{p=q}$ can in turn be decomposed into the band-width limited spectrum of the signal $S_{\overline{c^2}}$ and noise $S_{\overline{n^2}}$ variances respectively. Since the exponential term cancels out for $p = q$, the contributions from these terms are the flat band-width limited spectra of the signal and noise variances, which are additive.

$$\overline{S_{p=q}} = \underbrace{\frac{T}{N^2}\sum_{p=0}^{N-1}\overline{c^2(t_p)}}_{S_{\overline{c^2}}} + \underbrace{\frac{T}{N^2}\sum_{p=0}^{N-1}\overline{n^2(t_p)}}_{S_{\overline{n^2}}} \tag{9.11}$$

Clearly from equation (9.11) the variances of both the signal and noise are

associated with the diagonal terms.

Both the signal and noise spectra in (9.11) are independent of frequency. It has previously been proposed to exclude the self-products to avoid the noise contribution $S_{\overline{n^2}}$ to the spectral estimator [46, 19], resulting in the following spectral estimator.

$$\overline{S_{p\neq q}(f_k)} = \frac{T}{N^2} \sum_{\substack{p=0 \\ p\neq q}}^{N-1} \sum_{q=0}^{N-1} e^{-i2\pi k(p-q)/N} \overline{u(t_p)u(t_q)} \tag{9.12}$$

However, a vital detail not observed in the process of subtracting the self-products $S_{p=q}$ was that the contribution to the spectrum from the signal variance $S_{\overline{c^2}}$ is also omitted. The effect of leaving out this contribution, corresponding to the total energy, is that the spectrum produced without the self-products is asymptotically negative and integrates to zero.

For data yielding a smooth converged spectrum without external disturbances, one can evaluate the constant spectral noise level $S_{\overline{n^2}}$ from the asymptote of the original spectrum. $S_{\overline{c^2}}$ can in turn be obtained from equation (9.11). Alternatively, $S_{\overline{c^2}}$ can analogously be found by adding an offset to the spectrum after subtracting the trace, so that the asymptote of the spectral estimator is zero at the high end. This offset corresponds to the constant band-width limited spectrum of the signal variance $S_{\overline{c^2}} = \overline{c^2}/f_s$. The noise corrected spectral estimator can thus be expressed as follows.

$$\overline{S_{p\neq q}(f_k)} + \overline{S_{\overline{c^2}}} = \frac{T}{N^2} \sum_{\substack{p=0 \\ p\neq q}}^{N-1} \sum_{q=0}^{N-1} e^{-i2\pi k(p-q)/N} \overline{u(t_p)u(t_q)} + \overline{S_{\overline{c^2}}} \tag{9.13}$$

This estimator approaches zero at the highest frequencies (see figures 9.3*a* and *b*), as one expects turbulence to behave. The remaining noise at high frequencies in the logarithmic plot is of the order of the machine accuracy, demonstrating the power of the technique.

Let's consider the impact of the random noise on the correlations: In the autocorrelation it becomes apparent that the random noise is confined to the trace (assuming it has not been low-pass filtered). The autocorrelation of the random noise must be zero everywhere except at zero time lag where the full correlation exists. Thus the noise appears as a spike at the origin. Figure 9.4 displays the autocovariance of the original and noise corrected spectra given by eqs (9.10) (9.13)respectively. The autocovariances are identical for all time lags except $\tau = 0$, where the discrepancy represents the noise variance which is also displayed in the plot. Fourier transforming this noise spike at the origin results in white band-width limited noise in the spectrum.

An alternative approach to quantifying the random noise impact is to perform a parabolic fitting to the autocorrelation around the origin to remove the noise spike and obtain the value corresponding to the signal variance at zero time lag. This is justified since the autocorrelation coefficient $\rho(\tau) = \rho(-\tau)$ is an even function, with Taylor series expansion around $\tau = 0$; $\rho(\tau) \cong 1 - \tau^2/\lambda$, where the Taylor microscale $\lambda^2 = -2/(d^2\rho/d\tau^2)_{\tau=0}$ [135]. Note that if the signal has been low-passed filtered at frequencies lower than the inverse of the Taylor

microscale, then it is this low-pass cutoff frequency that will set its value, not the process itself.

## 9.4 Supporting theoretical analysis

The methodology of this section follows closely that of George 1978 [46], 2009 [49]. Let us define a sampling function, $g(t)$, which selects values of the process being sampled at predetermined instants. For equidistant sampling, the sampling function can be written as

$$g(t) = \Delta t \sum_{p=1}^{N} \delta(t - p\Delta t) \tag{9.14}$$

where $g(t)$ is a generalized function. This sampling can be applied to the process one wants to measure, $u$, yielding the sampled signal $u_0$.

$$u_0(t) = u(t)g(t) \tag{9.15}$$

where $u_0$ only has meaning in the sense of generalized functions.

The signal $u_0$ also has imposed upon it an inherent error with a size that depends on the electronic noise, quantization of the signal due to resolution of the A/D converter and so on. Let us take a closer look at the autocovariance by dividing the fluctuating part of the signal into signal $c$ and random noise $n$, $u_0(t) = c(t) + n(t)$. Assume that the signal is a stationary random process, meaning that the ensemble average is independent of origin in time, so the statistical properties do not vary with time.

$$\overline{u_0(t)u_0(t+\tau)} = \overline{c(t)c(t+\tau)} + \overline{n(t)n(t+\tau)} + \overline{c(t)n(t+\tau)} + \overline{n(t)c(t+\tau)} \tag{9.16}$$

The first term on the right-hand-side is the noise free signal autocovariance. The second term depends only on the noise and is simply the autocovariance of the noise. The third and fourth terms are the signal to noise correlations. Assuming that the signal and noise are uncorrelated (which is almost always true), the last two terms on the right hand side can be discarded to obtain:

$$\overline{u_0(t)u_0(t+\tau)} = \overline{c(t)c(t+\tau)} + \overline{n(t)n(t+\tau)}. \tag{9.17}$$

Since the noise is random, it must be uncorrelated for non-zero time lags. However, at zero time lag the noise is fully correlated since it is correlated with itself. The noise can therefore be traced and isolated to the noise variance term.

$$\overline{n(t)n(t+\tau)} = \overline{n^2}\delta(\tau)/f_s \tag{9.18}$$

where $f_s$ is the band-width limiting frequency, usually the sampling frequency. Thus, the theoretical noise term imposes a spike at the origin of the autocovariance.

Using the Wiener-Khinchin theorem to obtain the power spectrum, Fourier transforming this spike results in corresponding white noise in the spectrum,

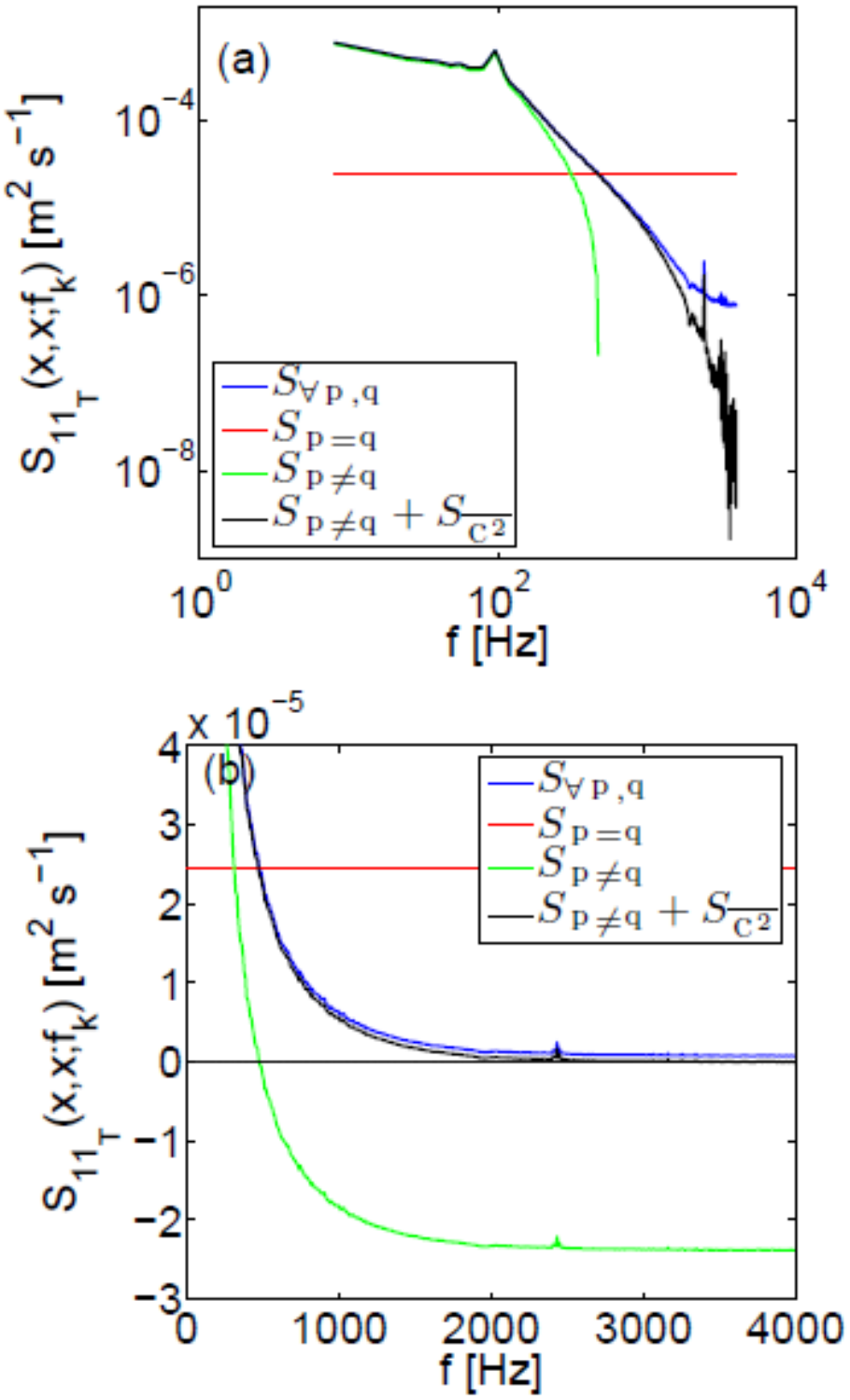


Figure 9.3: (a) Logarithmic and (b) linear and zoomed-in plot of spectral estimators of a HWA data set acquired in an axisymmetric wake behind a disc. $S_{\forall\, p,q}$ is the original spectral estimator, $S_{p=q}$ is the spectral estimator of the self-products, $S_{p\neq q}$ is the original spectral estimator with the spectral estimator of the self-products subtracted away and $S_{p\neq q} + S_{\overline{c^2}}$ is the corrected noise free spectral estimator.

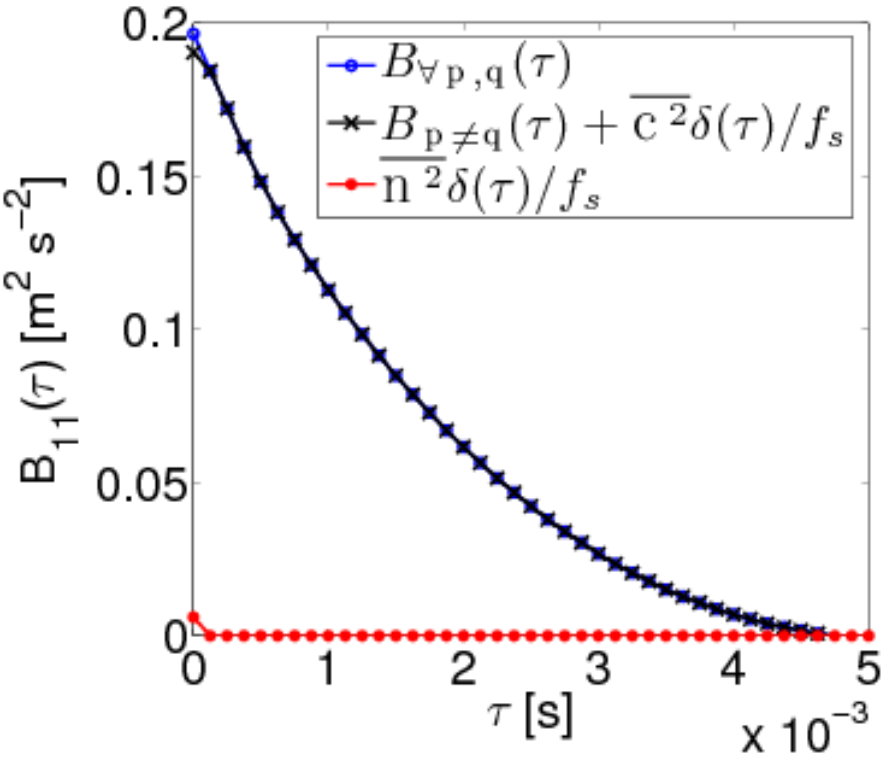


Figure 9.4: Autocovariance of the original (blue line) and noise corrected (black line) autospectra, obtained by the inverse Fourier transform. The autocovariances are identical for all time lags except at $\tau = 0$, where the discrepancy corresponds to the noise variance which is also displayed in the plot (red line).

with a flat spectral distribution.

$$B_0(\tau) = B(\tau) + \overline{n^2}\delta(\tau)/f_s \quad (9.19)$$

$$S_0(f) = S(f) + \overline{n^2}/f_s \quad (9.20)$$

Thus the noise variance is spread evenly over all possible frequencies. Alternatively it can be thought of as being spread evenly over an infinite band in such a way that its variance is $\overline{n^2}$, and then aliased at the sampling rate an infinite number of times to produce this value over the finite band $(-f_s/2, f_s/2)$.

Except for this spike and corresponding white noise, all of the information contained in the original signal is retained from the estimators of the autocovariance and the power spectrum of the sampled data. It is also recognized that the noise is additive to the spectrum. Figure 9.5 shows the autocovariance of the signal (purple) with the noise spike (grey) at the origin. Similarly figure 9.6 shows the power spectrum (purple) with the white noise (grey), originating from the spike in the autocovariance. If one could remove the noise terms in equations (9.19) and (9.20), namely $\overline{n^2}\delta(\tau)/f_s$ and $\overline{n^2}/f_s$, one could potentially recover the autocovariance and spectrum from the same estimates based on the sampled signal $u_0$.

The last term on the right-hand-side of equation (9.19), which is the autocovariance of the noise term in equation (9.18), can be shown in its discrete form as follows:

$$\overline{n(t_p)n(t_q)} = \overline{n^2}\delta_{pq}/f_s \quad (9.21)$$

For the sampled signal $u_0$, equations (9.11) and (9.12) write:

$$\overline{S_{p\neq q}(f_k)} = \frac{T}{N^2}\sum_{\substack{p=0\\p\neq q}}^{N-1}\sum_{q=0}^{N-1} e^{-i2\pi k(p-q)/N}\overline{u_0(t_p)u_0(t_q)} \quad (9.22)$$

where the trace

$$\overline{S_{p=q}} = \frac{T}{N^2}\sum_{p=0}^{N-1}\overline{u^2(t_p)} = \frac{T}{N^2}\sum_{p=0}^{N-1}\left[\overline{c^2(t_p)} + \overline{n^2(t_p)}\right] \quad (9.23)$$

has been subtracted from the original spectral estimator. The exponential term cancels out for $p = q$, leaving only the additive signal and noise variances multiplied by a constant $T/N$, corresponding to the inverse of the sampling frequency, $f_s$. Both the band-width limited spectrum of the signal variance and the white noise are independent of frequency, i.e., the spectra of the variance and the white noise have flat spectral distributions. This is consistent with the fact that one obtains the same value of the variance independently of the sampling frequency, as long as there are enough independent samples contributing to the statistics for the estimate to converge. Consequently, there is no concern of aliasing or underresolving when measuring this quantity [79]. Figure 9.7 shows a sketch of $S_{p=q}$, containing the band-width limited spectral estimators of the signal (purple) and noise (grey) variances respectively.

Figure 9.8 describes the spectral estimator where the self-products have been excluded (9.22) and the marked purple area corresponds to the spectral

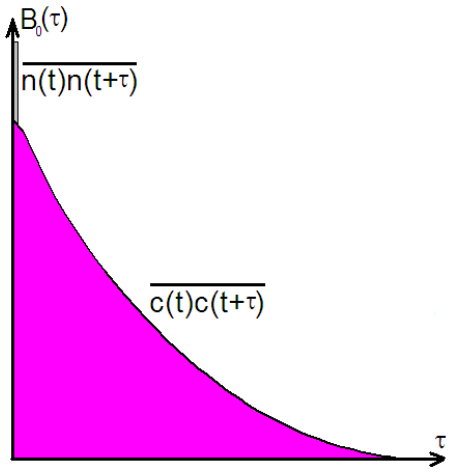


Figure 9.5: Sketch of the autocovariance $B_0(\tau)$ with the noise spike from $\overline{n(t)n(t+\tau)}$ at the origin and the signal autocovariance $\overline{c(t)c(t+\tau)}$ as a function of $\tau$.

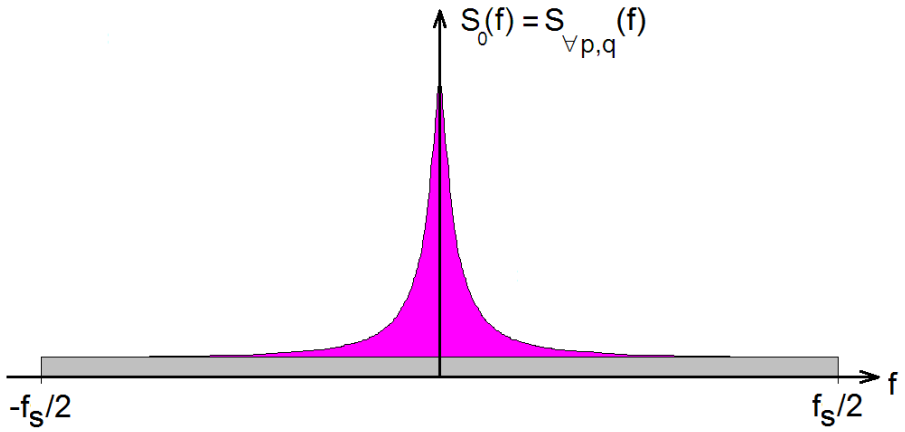


Figure 9.6: Sketch of the spectrum $S_0(f)$ with the frequency content of energy $\overline{c^2}$ obtained by integrating across the whole-line spectrum (purple) and white noise $\overline{n^2}$ (grey) originating from the spike in the autocovariance.

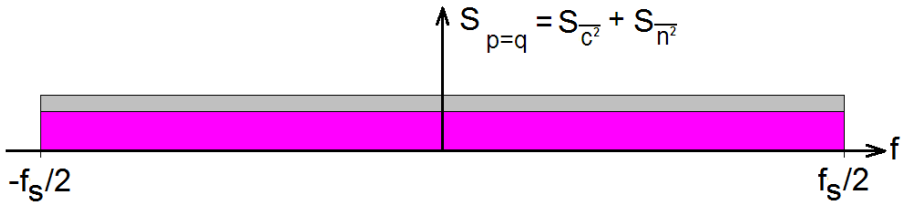


Figure 9.7: Sketch of the spectral estimator of the self-products $S_{p=q}$, containing both the signal and noise variance, both with flat distributions.

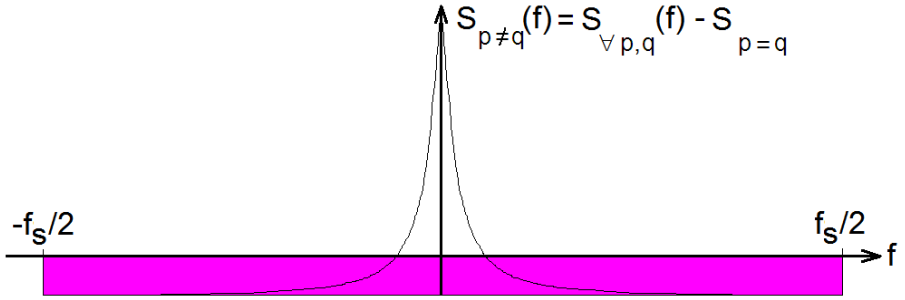


Figure 9.8: Sketch of the spectral estimator $S_{p\neq q}$, excluding the self-products.

estimator of the signal variance. Since the energy and noise have been subtracted from it, $S_{p\neq q}$ integrates to zero energy, which can be seen by integrating the exponential term over $k$:

$$\sum_{k=0}^{N-1} e^{-i2\pi k(p-q)/N} \tag{9.24}$$

Recognize that the sum is a geometric series

$$\sum_{k=0}^{N-1} r^k = \frac{1-r^N}{1-r} \tag{9.25}$$

and let $r = \mathrm{e}^{-i2\pi(p-q)/N}$, equation (9.25) becomes

$$\sum_{k=0}^{N-1} e^{-i2\pi k(p-q)/N} = \tag{9.26}$$

$$\frac{1-e^{-i2\pi(p-q)}}{1-e^{-i2\pi(p-q)/N}} = \frac{1-\cos 2\pi(p-q) - i\sin 2\pi(p-q)}{1-\cos 2\pi(p-q)/N - i\sin 2\pi(p-q)/N}.$$

Since it is noted that $p, q, k \epsilon \mathbf{N}$, for $p \neq q$ the arguments in the numerator always correspond to a positive or negative multiple of $2\pi$, resulting in a zero value of the numerator. The arguments in the denominator are never zero or $2\pi$, since $p \neq q$ and the largest value of $(p-q)$ is $|N-1|$. Therefore, it can be

concluded that

$$\sum_{k=0}^{N-1} e^{-i2\pi k(p-q)/N} = 0, \qquad p \neq q. \tag{9.27}$$

These terms constitute the frequency content or distribution of energy across frequency that we recognize as the spectrum. This can analogously be seen in the continuous case, where the whole-line integral of the spectrum

$$\int_{-\infty}^{\infty} S(f)\, df = \overline{u^2}. \tag{9.28}$$

Noting that $\overline{u(t)u(t+\tau)}_{|\tau=0} = \overline{u^2}$, it becomes obvious that

$$\int_{-\infty}^{\infty} \left[ S(f) - \frac{\overline{u^2}}{f_s} \right] df = 0. \tag{9.29}$$

Hence, when subtracting the self-products in order to remove the random noise variance, one inevitably also subtracts the signal variance.

Since the total energy is contained in the self-products, expression (9.22) needs to be compensated by the spectrum of the signal variance. The noise free spectrum should converge to zero at high frequencies due to dissipation. Offsetting the spectrum asymptote to zero, one recovers the noise free spectrum given in (9.13), as shown in figure 9.9. Integrating this spectral estimator consequently yields the total turbulence kinetic energy.

The computational cost for the first term on the right hand side of equation (9.13) is high, since it requires $N^2$ operations. However, if $N$ is an integer power of 2, 3 or 5 one can use the FFT algorithm (see; e.g., [23]), requiring only $N \log N$ (i.e., a reduction of $\log N/N$) operations. This tool, nowadays, is available in many commercial software packages. One can then manually compute and subtract the trace defined in equation (9.11) from equation (9.10) and compensate for the subtracted energy, leading to the same result. The FFT is more efficient than performing the double sum, since it assigns binary numbers to each sample and reverses the bits to obtain the Fourier coefficients according to the Danielson-Lanczos Lemma. See; e.g., [8, 23, 59] for more details on the FFT algorithm.

## 9.5 Summary

In the work presented here, a new technique is described for the removal of the additive random noise component in spectra and correlations. The methodology is illustrated using power spectra and correlations from recent hot-wire experiments in the axisymmetric wake behind a disc. For the autocovariance of white random noise, the self-products at zero time-lag are the only terms that are non-zero. Thus the white noise can therefore be isolated to the noise variance term. The random noise consequently manifests itself as a spike in the origin in the autocovariance, which transforms to band-limited white noise in the power spectrum. The reason why this kind of noise is not present in cross-spectra is that the noise components originating from two separate channels are random

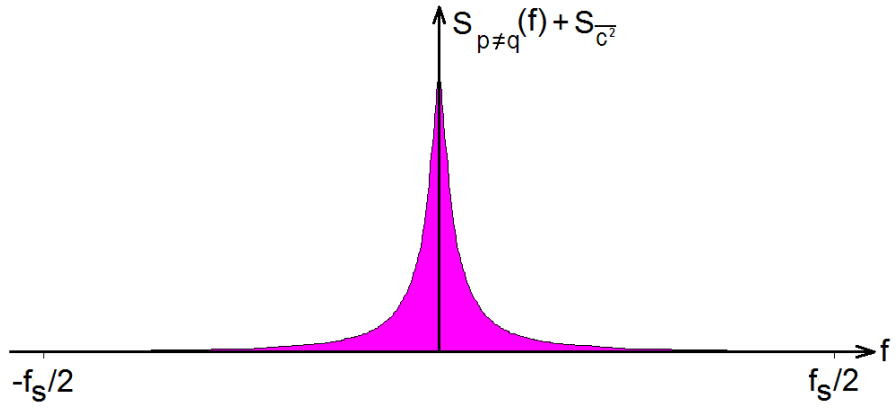


Figure 9.9: Sketch of the spectral estimator $S_{p\neq q}(f_k)+S_{\overline{c^2}}$. The noise is removed and the spectrum of the signal is recovered.

and uncorrelated for all time lags.

The magnitude of the resulting band-width limited noise spectrum is determined from the high frequency asymptote of the power spectrum, constituting only noise since all measurable turbulence has dissipated by the smallest scales or been filtered by the instrumentation. It has been verified that this white noise is additive to the spectrum and can be subtracted from the signal, resulting in a spectral estimator that converges to zero at high frequencies. The smoother the block averaged data of the spectral estimator is at high frequencies, the better the accuracy of the determination of the asymptote. The fluctuations that may still remain in $S_T(f)$ are due to the non-convergence of the block averaging, actual measured fluctuations due to various external disturbances disrupting the signal or rounding errors due to limitations in the machine precision. If one has a high quality signal with no external disturbances and sufficiently many blocks of record length, then the estimator will converge, leaving a smooth spectrum at the highest frequencies down to the machine accuracy.

By removing the noise, the determination of quantities attained from spectra and correlations are improved; e.g.,

- Even if the level of the spectral noise is small, its whole-line integral may be large. Noise removal makes it possible to obtain the correct total energy from power spectra.

- If one does not subtract the noise from the spectrum, then the time integral scale obtained from the value of the origin of the spectrum is overpredicted.

- In addition, if one were able to obtain sufficiently high resolution in the data, one could potentially use the noise removal technique to improve dissipation measurements.

The noise removal methodology presented here can be applied to data obtained with virtually any measurement techniques, including numerical simulations. Examples of white noise sources are electronic noise, discretization noise, roundoff errors, etc. In addition, because of the nature of the random noise from these self-products, this technique is not limited to temporal data analysis, but can also be implemented in spatial data analysis.

# Chapter 10

# Advanced Signal Processing

This chapter mainly serves as an introduction to Chapter 11 as a foundation for the signal processing applied to burst-mode LDA data. The chapter is primarily a brief summary on known results on regular and random sampling, which closely follows that of George *et al.* [46]. There are, however, some extensions and corrections. In the context of this thesis, the subject provides an important background for the subsequent chapter on LDA signal processing.

## 10.1 Equidistant discrete sampling

The Fourier transform and its inverse of a signal $u(t)$ can be defined in the following manner.

$$\hat{u}(f) = \int_{-\infty}^{\infty} e^{-i2\pi ft} u(t)\, dt \tag{10.1}$$

$$u(t) = \int_{-\infty}^{\infty} e^{+i2\pi ft} \hat{u}(f)\, df \tag{10.2}$$

$$\overline{\hat{u}(f)\hat{u}^*(f')} = S(f)\delta(f'-f) \tag{10.3}$$

These integrals can be assumed to almost always exist, at least in the sense of generalized functions.

In our case both $u(t)$ and $\hat{u}(t)$ are themselves stationary random processes. Hence they satisfy the following (cf., Lumley [78], George *et al.* [46, 48]):

$$B(\tau) = \int_{-\infty}^{\infty} e^{-i2\pi f\tau} S(f)\, df \tag{10.4}$$

$$S(f) = \int_{-\infty}^{\infty} e^{+i2\pi f\tau} B(\tau)\, d\tau \tag{10.5}$$

where $B(\tau)$ is the autocovariance and $S(f)$ is the spectrum. Both $B(\tau)$ and $S(f)$ are deterministic.

When acquiring data, however, the record length can never be infinite, and therefore one must define a finite estimator for the Fourier transform as:

$$\hat{u}_T(f) = \int_{-T/2}^{T/2} e^{-i2\pi ft} u(t)\, dt \tag{10.6}$$

The average value of the 1D spectral estimator defined by

$$S_T(f) = \frac{|\hat{u}_T(f)|^2}{T}, \tag{10.7}$$

can in turn be shown to provide an unbiased estimator of $S(f)$, at least in the limit as $T \to \infty$. This can easily be shown by substituting the 1D estimator of the Fourier transform of equation (10.6) into equation (10.7) to obtain:

$$S_T(f) = \frac{1}{T} \int_{-T/2}^{T/2} \int_{-T/2}^{T/2} \overline{u(t)u(t')} e^{i2\pi f(t-t')}\, dt\, dt' \tag{10.8}$$

Using the variable substitution $\tau = t - t'$ and $p = t' = t - \tau$, this can be transformed to yield:

$$\begin{aligned} S_T(f) = &\frac{1}{T} \int_0^T \left[ \int_{-T/2}^{T/2-\tau} dp \right] B(\tau) e^{i2\pi f\tau}\, d\tau \\ &+ \frac{1}{T} \int_{-T}^0 \left[ \int_{-T/2-\tau}^{T/2} dp \right] B(\tau) e^{i2\pi f\tau}\, d\tau \end{aligned} \tag{10.9}$$

It follows immediately that:

$$S_T(f) = \int_{-T}^{T} e^{i2\pi f\tau} B(\tau) \left[ 1 - \frac{|\tau|}{T} \right] d\tau. \tag{10.10}$$

Clearly:

$$\lim_{T\to\infty} \overline{S_T(f)} = S(f) \tag{10.11}$$

and therefore the estimator is unbiased, at least in the limit as $T \to \infty$. For finite values of $T$ the spectrum is always contaminated by the additional factor $1 - |\tau|/T$, and seriously unless $T$ is much greater than the integral scale of the process.

The variability

$$\varepsilon^2_{S_T} = \frac{\mathrm{var}\{S_T(f)\}}{\overline{[S(f)]^2}} \tag{10.12}$$

of the estimator can also be determined by assuming that fourth-order moments of $u(t)$ are jointly normal [46]. It is shown in Appendix B (see also Jenkins and Watts [59]) that $\mathrm{var}\{S_T(f)\} = \overline{[S(f)]^2}$ in the limit $T \to \infty$. Therefore the variability (or relative error) is unity in this limit, i.e.,

$$\varepsilon^2_{S_T} = \frac{\mathrm{var}\{S_T(f)\}}{\overline{[S(f)]^2}} = 1 \tag{10.13}$$

This can, however, be remedied by ensemble averaging over $M_b$ subdivi-

sions of a long record (see; e.g., Bendat and Piersol [8], pp. 423–425). (Note that these shorter records exacerbate the windowing problem noted above.) If the subdivided records have length $T_b$, a smoother estimate can be obtained from

$$\widehat{S}_T(f) = \frac{1}{M_b T_b} \sum_{j=1}^{M_b} |\hat{u}_{T,j}(f)|^2 \tag{10.14}$$

where $\widehat{S}_T(f)$ is the block-averaged spectral estimator. If these individual spectral estimates are statistically independent and the samples are identically distributed, then $\mathrm{var}\{X_M\} = \mathrm{var}[X]/M$, yielding

$$\mathrm{var}[\widehat{S}_T(f)] = \frac{\mathrm{var}[S_T(f)]}{M_b} = \frac{[S(f)]^2}{M_b}. \tag{10.15}$$

Hence, the normalized random rms-error for $\widehat{S}_T(f)$ is $\varepsilon_{\widehat{S}_T(f)} = 1/\sqrt{M_b}$.

Another method frequently employed is to average over different frequencies, so-called smoothing, since the Fourier components in non-overlapping frequency bands are uncorrelated. However, this approach reduces further the resolution in frequency space.

### 10.1.1 Discretization in time

In order to discretize the continuous one-dimensional spectrum, one can employ a sampling function $g(t)$. This sampling function (see, e.g., George *et al.* 1978 [46] and George 2009 [49]) can conveniently be represented by a series of Dirac delta functions distributed over the measured process in such a way as to select the values of the process being sampled. We can use this finite formulation since $\delta$ is used only as a distribution and the value of $\delta(0)$ does not matter for the analysis. For equidistantly sampled data, we can therefore define the sampling function in the following manner.

$$g(t) = \Delta t \sum_{n=-\infty}^{\infty} \delta(t - n\Delta t) \tag{10.16}$$

where $\Delta t$ is the uniform sampling interval, whose reciprocal is the sampling rate $f_s = 1/\Delta t$.

If one applies this sampling function onto the process $u(t)$, the sampled signal, $u_0(t)$, is given by:

$$u_0(t) = u(t)g(t) \tag{10.17}$$

It follows immediately that:

$$\overline{u_0(t)} = \overline{u(t)g(t)}. \tag{10.18}$$

Now consider the finite Fourier transform of the sampled signal, say $\hat{u}_{0_T}(f)$,

given by

$$\hat{u}_{0_T}(f) = \int_{-T/2}^{T/2} e^{-i2\pi ft} u(t) g(t)\, dt \tag{10.19}$$

By the shift theorem, the integration limits can be shifted from $(-T/2,T/2)$ to $(0,T)$, causing a phase-shift on the Fourier transform which is linear with frequency, shifting the time axis by $T/2$. This just corresponds to multiplying the Fourier coefficients by a factor $e^{i\pi fT}$. This phase shift has been omitted in the analysis, since there is no effect on the spectral analysis methodology developed in this study. (Note that this is, in general, not true for cross-spectral analysis.)

Discretizing this Fourier transform using basic definitions of integral calculus, one obtains a finite time estimate for the Fourier coefficients of $u(t)$.

$$\hat{u}_{0_T}(f) = \sum_{p=0}^{M-1} e^{-i2\pi fp\Delta t} u(t_p) \Delta t \tag{10.20}$$

where $M$ is the total number of samples, $T = M\Delta t$ is the total record length and $u(t_p) = u_p$ is the p'th sample at time $t_p$ which is the time of the p'th measurement.

Note that to this point we have not restricted the choices of frequency $f$. But since there are only $M$ data points, there are only $M$ independent equations (half this if complex). Therefore we can select $f$ for convenience. The time between samples $\Delta t$ is related to the sampling frequency by $\Delta t = 1/f_s = T/M$. The frequency resolution $\Delta f = 1/T$ provides the basis for the frequencies in the bandwidth and can for convenience be chosen in the following manner.

$$f_k = \frac{k}{T} = \frac{k}{M\Delta t} \qquad k = 0, 1, 2, ..., M-1 \tag{10.21}$$

Using $\Delta t = T/M$, we can express the Discrete Fourier Transform (DFT) pair.

$$\hat{u}_{0_T}(f_k) = \frac{T}{M} \sum_{p=0}^{M-1} e^{-i2\pi kp/M} u_{0_T}(t_p) \qquad k = 0, 1, 2, ..., M-1 \tag{10.22}$$

$$u_{0_T}(t_p) = \frac{1}{T} \sum_{k=0}^{M-1} e^{+i2\pi kp/M} \hat{u}_{0_T}(f_k) \qquad p = 0, 1, 2, ..., M-1 \tag{10.23}$$

Estimating the spectrum by inserting (10.20) into (10.7) results in the discretized spectral estimator

$$S_{0_T}(f_k) = \frac{T}{M^2} \sum_{p=0}^{M-1} \sum_{q=0}^{M-1} e^{-i2\pi k(p-q)/M} u(t_p) u(t_q). \tag{10.24}$$

This double sum can be implemented in two ways, both of which were used in this work. First the double sum can be computed directly, a computationally intensive procedure if the data set is large. Second, it can be performed by using

an FFT (Fast Fourier Transform) algorithm to compute equation (10.22). The latter is computationally faster by the ratio of $M \ln M/M^2$ (see; e.g., [8, 23, 59] for more details on the FFT algorithm).

### 10.1.2 Effect of windowing

The impact of having a finite record length can be evaluated by Fourier transforming the velocity

$$\hat{u}_T(f) = \int_{-T/2}^{T/2} e^{-i2\pi ft} u(t)\, dt = \int_{-\infty}^{\infty} e^{-i2\pi ft} u(t) W_T(t)\, dt \tag{10.25}$$

where the window $\mathrm{W}_T(\tau)$ is defined by:

$$W_T(\tau) = \begin{cases} 1, & |\tau| \leq T/2 \\ 0, & |\tau| > T/2 \end{cases} \tag{10.26}$$

From (10.25) and according to the convolution theorem;

$$\hat{u}_T(f) = \hat{u}(f) * \hat{W}_T(f) \tag{10.27}$$

The Fourier transform of the window can easily be found using Euler's identity.

$$\hat{W}_T(f) = \int_{-\infty}^{\infty} e^{-i2\pi f\tau} W_T(\tau)\, d\tau = \int_{-T/2}^{T/2} e^{-i2\pi f\tau}\, d\tau \tag{10.28}$$

$$= \left[ \frac{1}{-i2\pi f} e^{-i2\pi f\tau} \right]_{-T/2}^{T/2} = -\frac{1}{i2\pi f} \underbrace{\left[ e^{-i\pi fT} - e^{+i\pi fT} \right]}_{=-2i\sin(\pi fT)} = T\frac{\sin(\pi fT)}{\pi fT}$$

The essence of the convolution in (10.27) is that the Fourier transform of the window (10.28) will redistribute the energy of the signal across frequencies, contaminating the signal. Naturally, this is also evident when evaluating the spectrum and the only way to counteract this effect is by making the window larger. Note that in the limit as $T \to \infty$, $W_T(f) \to \delta(f)$, so convolution with it recovers the original spectrum.

### 10.1.3 Discretized random noise

Random noise is present in every sampled realization. Thus we can represent the signal as $u = c + n$, where $c$ is the signal and $n$ is the noise. If the noise is assumed to be completely random, its autocovariance is zero everywhere except at non-zero time lag. The noise is only present in the noise variance, resulting in a spike in the origin of the autocorrelation.

$$\overline{n(t)n(t+\tau)} = \begin{cases} \overline{n^2} & \tau = 0 \\ 0 & \tau \neq 0 \end{cases} \tag{10.29}$$

Alternatively this can be represented as:

$$\overline{n(t)n(t+\tau)} = N\delta(\tau) \tag{10.30}$$

where the integral of $N$ over the origin equals $\overline{n^2}$.

From this later formulation is it obvious that the corresponding noise spectrum is flat with level $N$ for all frequencies. Thus all frequencies above the sampling frequency will be aliased into the sampled ones many times, resulting in a flat noise spectrum of magnitude $\overline{n^2}/f_s$.

Therefore, it appears beneficial to remove all terms in the spectral estimator for which $p = q$; i.e., those at zero time lag. But since these terms do not only contain noise, this approach will also result in subtraction of the signal variance. One must therefore correct the spectral estimator for the subtraction of the energy as was shown in Chapter 9.

## 10.2 Random sampling

There exist situations where equidistantly spaced data cannot be obtained, e.g., in the case of instrumental drop-outs or when one cannot dictate the arrival time of the measurements. Examples come from astronomy, fluid and quantum mechanics. When studying turbulence, random sampling is inevitable for some measurement techniques like LDA where the object measured on (the scattering particle) also determines the sampling process. Two classes of random sampling are of interest: one where the sampling process is statistically independent of the sampled process and the other where they are statistically dependent. Burst-mode LDA falls into the second category. Nonetheless the first case is helpful in understanding the second, which is more difficult; so we consider it first. The field of random sampling has been developed by many independent investigators; e.g., Gaster and Roberts [41], Mayo [86, 87, 88] and Shapiro and Silverman [126] and is briefly reviewed here.

We begin by insisting that the random sampling process $g(t)$ be independent of the process being sampled $u(t)$. An immediate consequence is that $\overline{u_0(t)} = \overline{u(t)g(t)} = \overline{u(t)}\ \overline{g(t)}$. We further assume that both $u(t)$ and $g(t)$ are stationary random processes; i.e., their statistics are independent of origin in time. Let us choose a random sampling function which selects values of the velocity signal at random instants $t_i$ in time,

$$g(t) = \frac{\delta(t - t_i)}{\nu}, \qquad i = 1, 2, \ldots, \infty \tag{10.31}$$

where the sampling function has been normalized by $\nu$, which is the average sampling rate. Note that $\bar{g} = \nu/\nu = 1$. For long record lengths, the following approximation holds

$$\nu \simeq \frac{M}{T} \tag{10.32}$$

where $M$ is the number of samples and $T$ is the record length. One can show

that the following relations hold where $t' = t + \tau$, see Appendix C.

$$\overline{g(t)g(t')} = 1 + \frac{\delta(t'-t)}{\nu} \tag{10.33}$$

$$\overline{\left[g(t) - \overline{g(t)}\right]\left[g(t') - \overline{g(t')}\right]} = \frac{\delta(t'-t)}{\nu} \tag{10.34}$$

In the covariance function of the sampling function (10.33), the first term on the right hand side corresponds to the random overlap of the sampling function. When applied to the sampled velocity, this term represents the desired information. The second term is the overlap at $\tau = 0$ (i.e., the self-products), representing the noise term resulting from the intermittent nature of the sampled signal (i.e., the covariance of the random white noise in the signal). The autocovariance of the sampling function (10.34) is simply the self-noise term. Figure 10.1 provides a sketch of a randomly sampled signal in the form of Heaviside functions before taking the limit $\Delta t \to 0$ (labeled h before non-dimensionalization) illustrating the correlation of the sampling function for time lag $\tau \leq \Delta t$, for which the self-noise appears (second term on RHS of equation 10.33). $\tau > \Delta t$ accounts for the random overlap (first term on RHS of equation 10.33).

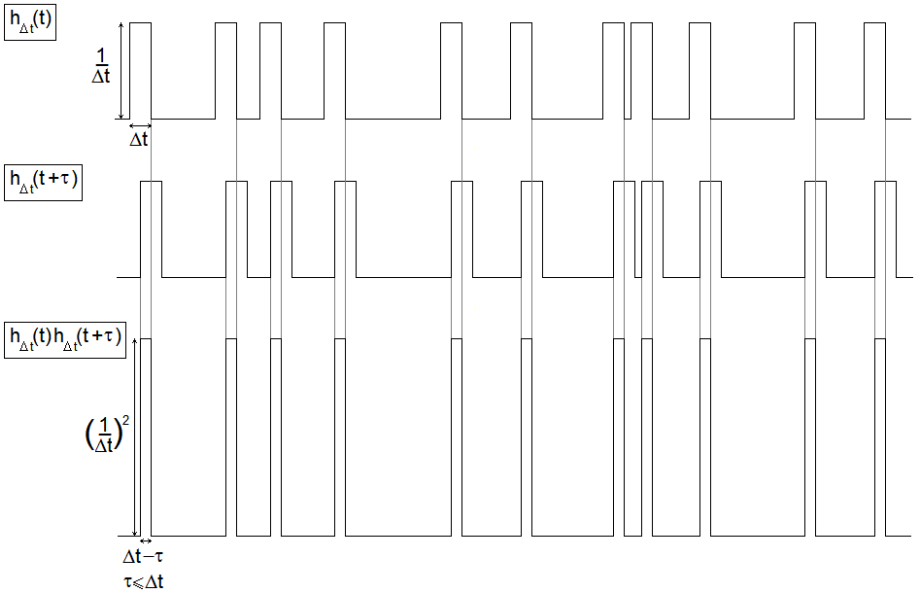


Figure 10.1: Sketch of the random sampling signals $h(t)$ and $h(t+\tau)$. The lowermost figure shows the correlation of the sampling function for time lag $\tau \leq \Delta t$.

Dividing the instantaneous velocity, $\tilde{u}$, into a mean, $U$, and a fluctuating, $u$, part according to the Reynolds decomposition, $\tilde{u} = U + u$, and utilizing relation (10.33) and that $\overline{g} = 1$, $\overline{u} = 0$ and $\overline{g(t)u(t)} = \overline{g(t)}\,\overline{u(t)}$, we can obtain

the autocovariance of the sampled signal as:

$$\begin{aligned}
\overline{u_0(t)u_0(t+\tau)} &= \overline{\Big[g(t)\tilde{u}(t) - \overline{g(t)}U\Big]\Big[g(t+\tau)\tilde{u}(t+\tau) - \overline{g(t+\tau)}U\Big]} \\
&= \overline{g(t)g(t+\tau)}\;\overline{\tilde{u}(t)\tilde{u}(t+\tau)} - U^2 \\
&= \left[1 + \frac{\delta(\tau)}{\nu}\right]\Big[U^2 + \overline{u(t)u(t+\tau)}\Big] - U^2 \\
&= \overline{u(t)u(t+\tau)} + \frac{\delta(\tau)}{\nu}\Big[U^2 + \overline{u(t)u(t+\tau)}\Big] \qquad (10.35)
\end{aligned}$$

or

$$B_{u_0}(\tau) = B_u(\tau) + \frac{\delta(\tau)}{\nu}\Big[U^2 + \overline{u^2}\Big], \qquad (10.36)$$

Fourier transforming yields immediately the spectral relation:

$$S_{u_0}(f) = S_u(f) + \frac{1}{\nu}\Big[U^2 + \overline{u^2}\Big]. \qquad (10.37)$$

The first term on the right hand side of (10.36), $B_u(\tau)$, is the autocovariance of the original signal, containing the contributions from both the signal, $B_c(\tau)$, and the random noise, $B_n(\tau) = N\delta(\tau)$, which manifests itself as a spike at the origin. Further, the second term on the right-hand-side also represents a spike at the origin in the autocovariance, so its contribution to the spectrum is white. This noise spike results from the intermittency of the sampled signal, $U^2\delta(\tau)/\nu$, and the superfluous signal variance and random noise $\overline{u^2} = \overline{c^2} + \overline{n^2}$, respectively:

$$B_{u_0}(\tau) = B_c(\tau) + B_n(\tau) + \frac{\delta(\tau)}{\nu}\Big[U^2 + \overline{c^2} + \overline{n^2}\Big], \qquad (10.38)$$

Analogously, the first term in (10.37) is the recovered spectrum, $S_c(f)$, including noise (detection noise etc.), $S_n$. The second term is also frequency independent noise, obtained by Fourier transforming the noise term of (10.36) containing the intermittent term as well as the white noise and redundant signal variance:

$$S_{u_0}(f) = S_c(f) + S_n + \frac{1}{\nu}\Big[U^2 + \overline{c^2} + \overline{n^2}\Big]. \qquad (10.39)$$

Since all of the noise terms are independent of frequency, their effect on the spectrum is simply the addition of a wide band, i.e., white noise.

In order to obtain the desired correct and noise free signal, the natural choice is to remove the effect of these terms, corresponding to a spike at the origin of the autocovariance. For the correlation function, the easiest way to do this is to utilize its symmetry about $\tau$ and extrapolate to $\tau = 0$ by fitting a parabola to the smallest values of $\tau$. One can also simply offset the spectrum by the high frequency asymptote, where the turbulence spectrum is negligible, so that it is zero.

### 10.2.1 Practical random sampling estimator

To derive a practical estimator, one requires expressions for the moments. For the mean value of the velocity, one can simply construct the estimator by integrating over the record length; i.e.,

$$U_{0_T}^R = \frac{1}{T}\int_0^T \tilde{u}(t)g(t)\,dt = \frac{1}{\nu T}\sum_{p=0}^{M-1}\tilde{u}(t_p), \tag{10.40}$$

where the $\tilde{u}(t_p)$ is the p'th instantaneous realization at time $t_p$ and $\nu T \cong M$ for large enough $T$. The superscript $R$ indicates that the estimator is valid for randomly sampled data. It is easy to show that this estimator is unbiased by taking its average; i.e.,

$$\overline{U_{0_T}^R} = \overline{\frac{1}{T}\int_0^T \tilde{u}_0(t)\,dt} = \frac{1}{T}\int_0^T \overline{\tilde{u}(t)}\;\overline{g(t)}\,dt = \overline{u(t)} \tag{10.41}$$

Estimating the variance in the same manner yields the following expression:

$$\sigma_{0_T}^{R\,2} = \frac{1}{M}\sum_{p=0}^{M-1}\left[\tilde{u}_p - U_{0_T}^R\right]^2 \tag{10.42}$$

To estimate the Fourier coefficients of the fluctuating velocity $u_{0_T}(t)$ for a finite record length $T$, the discrete Fourier transform can be approximated using basic definitions of integral calculus. Thus

$$\hat{u}_{0_T}(f) = \int_0^T e^{-i2\pi ft}u(t)g(t)\,dt \approx \frac{1}{\nu}\sum_{p=0}^{M-1} e^{-i2\pi f_k t_p}u(t_p) \tag{10.43}$$

Having an estimate of the Fourier coefficients, the one-dimensional power spectral estimator can be expressed as follows:

$$S_{0_T}^R(f_k) = \frac{|\hat{u}_{0_T}(f)|^2}{T} \approx \frac{1}{\nu^2 T}\sum_{p=0}^{M-1}\sum_{q=0}^{M-1} e^{-i2\pi f_k(t_p-t_q)}u(t_p)u(t_q) \tag{10.44}$$

The noise contained in the last terms in (10.36) and (10.37) is restricted to $\tau = 0$, the corresponding terms in the one-dimensional power spectral estimator being $p = q$. Thus this is the exact analog of the discussion of Chapter 9. By subtracting the self-products, one can avoid all of the random noise effects. However, this is done at the cost of subtracting away the energy contained in the variance of the recovered spectrum. If the self-products are removed when estimating the power spectrum, one must therefore compensate for the power spectrum of the signal variance by adding it back; i.e.,

$$S_{0_T}^R(f_k) = \frac{1}{\nu^2 T}\sum_{\substack{p=0\\ p\neq q}}^{M-1}\sum_{q=0}^{M-1} e^{-i2\pi f_k(t_p-t_q)}u(t_p)u(t_q) + \overline{c^2}\frac{1}{\nu} \tag{10.45}$$

The methodology for determining $\overline{c^2}$ independently was discussed in Chapter 9.

### 10.2.2 Variability of random sampling estimator

As a consequence of the random sampling, the spectral estimator is unaliased. This is a clear advantage over equidistant discrete sampling. However, the random sampling introduces an increased relative error of the spectral estimator $S^R_{0_T}(f)$. This can be analyzed by assuming that the fourth order moments of the sampled process, $u(t)$, are jointly Gaussian (see, e.g., Jenkins and Watts [59] and Lumley 1970 [78]); i.e.,

$$\overline{uu'u''u'''} = \overline{uu'} \cdot \overline{u''u'''} + \overline{uu''} \cdot \overline{u'u'''} + \overline{uu'''} \cdot \overline{u'u''} \tag{10.46}$$

Discounting the self-products in the autocovariances, $(u, u')$ and $(u'', u''')$ are non-overlapping pairs. Excluding these permutations and including in the probability of random overlap, one can see from figure 10.1 that (see also Gaster and Roberts [41]):

$$\overline{gg'g''g'''} = 1 + \frac{1}{\nu}[\delta(t''-t) + \delta(t'''-t) + \delta(t''-t') + \delta(t'''-t')]$$

$$+\frac{1}{\nu^2}[\delta(t''-t)\delta(t'''-t') + \delta(t'''-t)\delta(t''-t')] \tag{10.47}$$

It follows after considerable analysis (see Gaster and Roberts [41] or George *et al.* [46]) that

$$\epsilon^2_{S^R_{0_T}} = \frac{\mathrm{var}\{S^R_{0_T}(f)\}}{[S(f)]^2} = \left\{1 + \frac{S^R_{0_T}(0)}{S^R_{0_T}(f)}\left[\frac{1}{2\nu T_u}\right]\right\}^2 \tag{10.48}$$

Thus a smaller value of the spectrum leads to a higher statistical error. Since the spectrum is expected to fall off as the frequency increases, the error thus increases with frequency and is never smaller than unity. Some examples to remedy this are block averaging or using the time-slot approximation, see; e.g., George 1978 [46] and Buchhave 1979 [19].

The above analysis is valid under the assumptions that the fourth order moments of the velocities and sampling functions are jointly Gaussian and that the sampling process is independent of the process being sampled. Actually, the above expression for the sampling function (10.47) is faulty and should be derived according to Appendix D.

One can do the derivation without assuming the joint normality of the fourth order moments of the sampling function, yielding the following expression (see Appendix D for a derivation);

$$\epsilon^2_{S^R_{0_T}} = 1 + \frac{4}{\nu}\frac{B(0)}{S(f)} \tag{10.49}$$

This result indicates that the variability increases linearly with the origin of the autocorrelation (including both the signal and noise contributions). It also suggests that the variability is inversely proportional to the spectral value and the data rate $\nu$.

### 10.2.3 Effect of windowing

The impact of finite record length for randomly sampled signals can also be evaluated using the Wiener-Khinchin theorem and Fourier transforming the autocovariance of the sampled signal given by:

$$\overline{u_0(t)u_0(t')} = \overline{g(t)g(t')}\,\overline{u(t)u(t')} = \left[1 + \frac{1}{\nu}\delta(t'-t)\right] B_u(t'-t). \tag{10.50}$$

Letting $\tau = t' - t$, one can estimate the one-dimensional spectrum with the effects of random sampling and windowing as follows:

$$S_T(f) = \int_{-T}^{T} e^{-i2\pi f\tau} B(\tau)\left[1 + \frac{\delta(\tau)}{\nu}\right]\left[1 - \frac{|\tau|}{T}\right] d\tau \tag{10.51}$$

$$= \int_{-T}^{T} e^{-i2\pi f\tau} B(\tau)\left[1 - \frac{|\tau|}{T}\right] d\tau + \frac{1}{\nu}\int_{-T}^{T} e^{-i2\pi f\tau} B(\tau)\delta(\tau)\left[1 - \frac{|\tau|}{T}\right] d\tau$$

$$= S_T(f) + B(0)/\nu$$

From the above result, it is clear that no additional window effect is introduced by the random sampling. The last term is simply the big white noise term obtained for random sampling (see second term on the right-hand-side of equation 10.37).

### 10.2.4 Suppression of aliasing

When one has truly alias-free sampling, the average data rate is not critical, as it is for equidistantly sampled data, as long as the record length is long enough to obtain well converged statistics. One can, in principle, have as small average data rates as is desired if the point process has a high degree of randomness. Shapiro and Silverman [126] showed that the requirement of alias-free sampling is well met, e.g., if the point process is a Poisson process. Shapiro and Silverman suggested a random point process where the sampling instants $\{t_p\}_{p=0}^{M}$ are random and generated by a Poisson process so that $t_0 = 0$ and $t_p = t_{p-1} + \tau_p$, $p = 1, 2, \ldots$, where $\tau_p$ is the time between samples, which is itself a stochastic variable with a Poisson distribution. This process is commonly referred to as "additive random sampling". The drawback of sampling with low data rates is increased variability in the spectral estimator (10.48) as well as a higher white noise floor (10.37). One would also require a higher average data rate if the aim is to reconstruct the signal, which is not the case in the present work.

Some empirically obtained parameters for alias reduction in random sampling have been identified by Bilinsky and Mikelsons [13]. The degree of randomness of the sampling process is defined as the ratio $\sigma_{\tau_p}/\mu_{\tau_p}$, where $\sigma_{\tau_p}$ and $\mu_{\tau_p}$ are the standard deviation and the expected value of the time between samples $\tau_p$. If $\tau_p$ has a Poisson distribution, $\sigma_{\tau_p} = \mu_{\tau_p}$ and should hence be the optimal requirement for alias free sampling according to the theory of Shapiro and Silverman. Bilinsky and Mikelsons showed empirically that a higher degree of randomness yields less aliasing. Further, increasing the number of samples N also aided in suppressing aliasing.

# Chapter 11

# Burst-mode LDA Spectra

This chapter considers the problems of signal analysis which always arise when processing time series of burst-mode LDA data. The phrase "burst-mode LDA" refers to an LDA which operates with at most one particle present in the measuring volume at a time. For the signal to be interpreted correctly to avoid velocity bias, one must apply residence time-weighing to all statistical analysis. In addition, for time-series analysis, even though the randomly arriving particles eliminate aliasing (at least in principle), the self-noise from the random arrivals must be removed or it will dominate the spectra and correlations. A flaw in the earlier theory [19, 46], the goal of which was to provide an unbiased and unaliased spectral estimator from the random samples, is identified and corrected. The new methodology is illustrated using experiments in an axisymmetric turbulent far jet and a cylinder wake. The results are compared to corresponding hot-wire measurements. The smallest significant bit, decided by either word size of the measuring data or the design of the experiment, proved to be vital in estimating the spectrum, effectively deciding the highest frequency and therefore setting the threshold for the degree of aliasing. Hence, aliasing appears in the spectra despite the random arrivals of the scattering particles due to this limitation.

## 11.1 Introduction

The Laser Doppler Anemometer (LDA) can provide local time-resolved measurements of the velocity of small scattering particles dispersed into a fluid. Assuming that the particles follow the flow, one can measure fluid velocities non-intrusively. This is one advantage of LDA over Hot-Wire Anemometry (HWA). For some applications, such as combustion, liquid flows, gas flows or flows with particles or droplets, LDA is superior to HWA due to probe fouling problems associated with it. In addition, high turbulence intensity flows are usually not well suited for HWA measurements because of the ambiguity in measurement of direction of velocity. However, the determination of a power spectral estimator for data acquired using LDA has since its emergence provided signal processing related issues for fluid dynamicists due to its inherent random sampling and high velocity bias.

Consequently, a number of procedures have been proposed to perform spec-

tral analysis on LDA data. One is to reconstruct the autocorrelation function using the time-slot approximation and use the Fourier transform to obtain the autospectrum. But in the process of creating the time slots to approximate the autocorrelation, a convolution of this time slot, operating as a window, is imposed onto the autocorrelation. This results in filtering by the window function in frequency space, reducing the variance but at the expense of bias [46]. Another commonly used technique is the sample-and-hold procedure, which basically resamples the data at uniform intervals by the last acquired data point. This technique enables the direct application of the Fast Fourier Transform. However, the resampling distorts the signal, resulting in an unreliable spectral estimator both in the respect of its total energy content as well as its distribution across the frequencies of the band width. The estimator may be strongly biased with systematic errors [1, 93].

Further, electronic noise such as shot/quantum noise (caused by the quantum nature of the photon detection) and thermal/Johnson noise (caused by thermal fluctuations of electrons in the detector load resistor or the first amplifier stage) are usually the dominating white noise sources for a well designed LDA measurement. Random noise is only correlated at zero time lag, resulting in a spike at the origin in the autocorrelation, transforming to white noise in the spectrum in frequency space [46]. When comparing spectra obtained from different sources or using different signal processing techniques, the noise floor might vary considerably. It is therefore important to account for effects of random noise when comparing spectra, see Chapter 9. Noise suppression in spectra based on LDA data has previously been attempted by Benedict and Gould [9] and van Maanen and Tulleken [80] using Kalman filters, assuming the noise to be white. Nobach *et al.* [97] attempted to suppress the noise in a power spectrum from LDA data using an FIR-filter, parameterized using the mean particle rate. A sample-and-hold interpolation with equidistant resampling was applied. Tropea [137] has reviewed the various techniques used for spectrum estimation of LDA data. A comparison of the associated errors to many of these methods have been presented in Benedict *et al.* [10].

In the present work, the problems of signal analysis arising when processing "burst-mode LDA" data are discussed and tested. The term burst-mode LDA is here used in the sense of an LDA system where at most one scattering particle is present in the measuring volume at each instant and for most of the time, there are none. The sampled signal only treats one particle at a time and is highly intermittent, yielding increased random noise. An existing theory [19, 20, 45, 46] attempting to provide an unbiased and unaliased spectral estimator has been recapitulated, corrected and extended.

Using the principle of residence time-weighted averaging, the moments and spectra can, in principle, be completely recovered. The revised theory was applied to simultaneously acquired LDA and HWA data in an axisymmetric turbulent far jet [35] and LDA and HWA measurements in a cylinder wake [50] to successfully reconstruct the spectral estimator. The spectral estimator based on residence time-weighting for the LDA data has been compared to spectra based on corresponding HWA data computed in the regular fashion using the FFT, showing a high degree of concurrence for both data sets. Further, the noise suppression methodology for spectra and correlations developed in Chapter 9 was employed. The properties of the two data sets are also investigated in several ways, such as investigating the distributions of the interarrival times

of particles, residence times and velocity distributions; directly and residence time weighted. The shortcomings of the data sets and their implications on the results are discussed. The characteristic high white noise floor is observed in both cases under investigation. The appearance of aliasing spikes in the burst-mode LDA spectra, which were not expected due to the inherent random sampling of LDA, turned out to result from the smallest resolvable time in each data set. For the axisymmetric jet, the single precision word size set the limit while the double precision cylinder wake data was limited by the physical constraints of the experiment design.

## 11.2 Signal processing

### 11.2.1 Basic representation of the burst-mode LDA signal

A thorough description of the burst-mode LDA can be found in Buchhave *et al.* [20] and Buchhave [19]. The defining characteristic of the burst-mode LDA is that it operates with no scattering particles present in the measuring volume for a majority of the time and at most one scattering particle at a time. The particles arrive randomly in the measuring volume and sample the flow velocity randomly. Figure 11.1 displays a sketch of the velocity signal (curve) and the intermittent sampled signal (shaded areas). However, if one considers the particles to be randomly distributed at statistically independent locations in space (at least at one instant in time) and then lets the flow transport the particles through the measuring volume, it becomes apparent that the flow and the arrivals cannot be statistically independent. This means that the sampling process is not independent of the process being sampled.

The problem can, however, be addressed by considering the particle motions in Lagrangian space. Then one can use a sampling function that samples the velocity at the spatial location of the particle. Buchhave *et al.* 1979 [20] (see also Buchhave 1979 [19] and George 1975 [45]) suggested defining the sampled velocity by

$$\tilde{u}_0(t) = \int\int\int_{\text{all space}} \tilde{v}(\mathbf{a},t) g(\mathbf{a}) w(\mathbf{x}[\mathbf{a},t])\, d^3\mathbf{a} \tag{11.1}$$

where $\tilde{v}(\mathbf{a},t)$ is the velocity of the *particle* which had initial position, $\mathbf{a}$, of the particles. $g(\mathbf{a})$ is a sampling function that describes whether a particle is present or not at position $\mathbf{a}$ at the (arbitrarily chosen) initial instant. The positions of the particles are given by the displacement field, $\mathbf{x}(\mathbf{a},t)$. $w(\mathbf{x}[\mathbf{a},t])$ is a weighting function that accounts for the finite extent of the measuring volume, and effectively 'turns on' when the particle enters the volume and 'turns off' when it leaves. The weighting function $w(\mathbf{x}[\mathbf{a},t])$ is defined to be dimensionless and it is required that its integral over the volume must be the volume; i.e.,

$$V \equiv \int\int\int_{\text{all space}} w(\mathbf{x}[\mathbf{a},t])\, d\mathbf{x} \tag{11.2}$$

In an Eulerian frame the particles are not tracked, but rather captured while traveling through the scattering volume. One cannot usually capture any changes in the particle velocity as it moves through the volume due to the

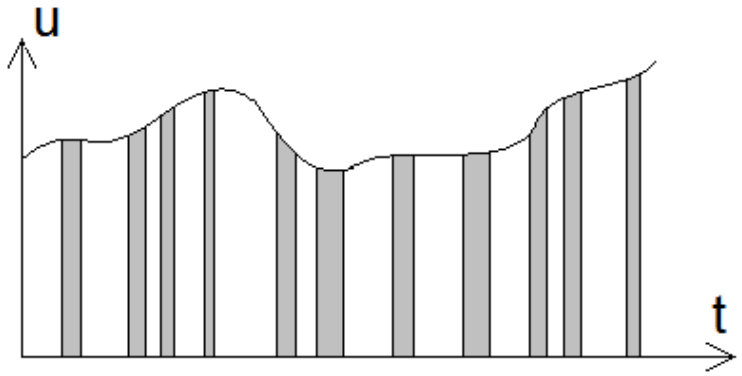


Figure 11.1: Sketch of velocity, $u$ (curve), along with the interrupted sampled signal, $u_0$ (shaded areas), resulting from random arrivals of particles carried by the flow.

limitations of the burst processor, so the obtained velocity is an approximation in the sense of a volume-averaged velocity;

$$\tilde{u}_{0i}^{vol}(t) = \int\int\int_{\text{all space}} \tilde{u}(\mathbf{x},t)g(\mathbf{x},t)w(\mathbf{x})d^3\mathbf{x}, \tag{11.3}$$

where $\tilde{u}(\mathbf{x},t)$ is the local Eulerian velocity at position $\mathbf{x}$. Another source adding to the uncertainty is that the particles may not follow the flow.

### 11.2.2 A new approach

In George and Lumley [43], it was shown that for stationary and homogeneous flow, the coordinate system for (11.1) could be switched from Lagrangian to Eulerian. A simple mapping would thereby yield the representation of the sampled signal in the Eulerian space (cf., George [45]). However, it was assumed that the particle distribution function $g(\mathbf{x})$ is independent from the velocity field, which turns out to be crucial; In recent years, studies have shown that particles tend to cluster if the densities of the particles and fluid differ (see, e.g., [22]).

One measure to avoid this assumption is by sticking with the Lagrangian representation. Then we only need to assume that the *particle* position is given by its displacement field, $\vec{x} = \vec{X}(\mathbf{a},t)$, which is in turn given by the integral time history of the *particle* velocity; i.e.,

$$x_i = X_i(\mathbf{a},t) = \int_0^t \tilde{v}_i(\mathbf{a},t')dt' \tag{11.4}$$

Note that we have not assumed that the particles exactly follow the flow, since we have not stated that $\tilde{v}_i(\mathbf{a},t)$ is the Lagrangian velocity of fluid particles.

### 11.2.3 Single point statistics

The previous interpretation is still essentially correct: when a (single) particle enters the scattering volume and is detected, then we determine its velocity,

$\tilde{u}_{0i}(t)$. From the definition it is clear from that it 'turns on' only when there is a particle in the scattering volume. If the process is a stationary random process, i.e., if the statistics of the process are independent of the origin in time, then the proper way to compute the statistics is the same way as before; namely to weight each realization by the residence time. So under the assumption of stationarity and randomness, the operational part is exactly the same. The big question is whether one can assume that $\tilde{u}_{0i}(t)$ is a stationary random process just because the underlying flow field is.

Let's begin with a simple average (over an infinite ensemble) of equation (11.1):

$$\langle \tilde{u}_{0i}(t) \rangle = \iiint_{\text{all space}} \langle \tilde{v}_i(\mathbf{a},t) w(\mathbf{x}[\mathbf{a},t]) g(\mathbf{a}) \rangle \, d^3\mathbf{a} \tag{11.5}$$

One cannot generally assume that the three quantities under the integral sign are statistically independent. The particle position depends on the velocity history, and both of these depend on the initial position of the particle. One solution is to uncouple the initial particle positions, $\mathbf{a}$, from these. If we assume that the particles are randomly scattered throughout the flow at $t = 0$, then $\mathbf{a}$ must be statistically independent from the other quantities, but only at $t = 0$.

Based on the new knowledge on particle clustering, there is no reason to believe that this uncoupling exists for $t > 0$. Thus, transforming equation (11.1) into Eulerian coordinates will yield problems, since we can't say that $g(\mathbf{x}[\mathbf{a},t])$ is statistically independent from the Eulerian velocity $\tilde{u}_i(\mathbf{x},t)$.

Instead, let's try to proceed in Lagrangian coordinates with equation (11.5). Since we have ensured that the initial locations are statistically independent, both of each other and of the velocity field, we can break the average into two parts; i.e.,

$$\langle \tilde{v}_i(\mathbf{a},t) w(\mathbf{x}[\mathbf{a},t]) g(\mathbf{a}) \rangle = \langle \tilde{v}_i(\mathbf{a},t) w(\mathbf{x}[\mathbf{a},t]) \rangle \; \langle g(\mathbf{a}) \rangle \tag{11.6}$$

Like before (see, e.g., Buchhave 1979 [19]), $\langle g(\mathbf{a}) \rangle = \mu$, where $\mu$ is the expected number of particles *per unit volume*. Thus:

$$\begin{aligned} \langle \tilde{u}_{0i}(t) \rangle &= \mu \iiint_{\text{all space}} \langle \tilde{v}_i(\mathbf{a},t) w(\mathbf{x}[\mathbf{a},t]) \rangle \, d^3\mathbf{a} \\ &= \mu V \left\langle \frac{1}{V} \iiint_{\text{all space}} \tilde{v}_i(\mathbf{a},t) w(\mathbf{x}[\mathbf{a},t]) \, d^3\mathbf{a} \right\rangle \end{aligned} \tag{11.7}$$

It remains to relate the integral over Lagrangian (or particle) space to the Eulerian volume-averaged velocity of equation (11.5) above. If we assume (for the moment at least) that the particles do follow the flow and the flow to be incompressible, then we can immediately transform the integral over initial condition coordinates into Eulerian (or spatial) ones yielding

$$\langle \tilde{u}_{0i}(t) \rangle = \mu V \int \int \int_{\text{all space}} \tilde{u}_i(\mathbf{x},t) w(\mathbf{x}) d^3\mathbf{x} \tag{11.8}$$

But the integral on the right-hand side is just the volume-averaged Eulerian

velocity. Thus:

$$\langle \tilde{u}_{0i}(t) \rangle = \mu V \langle \tilde{u}_i^{vol}(t) \rangle. \tag{11.9}$$

Thus the mean of the burst-mode signal is the mean of the volume-averaged velocity as before, but multiplied by the expected number of particles in the volume (which is always less than unity).

Again, note that this last deduction presumes the particles to follow the flow. If they do not, residence time weighting produces the correct average of the wrong quantity.

### 11.2.4 Two-point statistics

Now let's compute the two-time statistics of $\tilde{u}_{0i}$. Again assuming the particles to have been randomly distributed initially, evaluating equation (11.1) at two different times, multiplying the integrals and averaging yields:

$$\langle \tilde{u}_{0i}(t) \tilde{u}_{0i}(t') \rangle = \tag{11.10}$$

$$\int\int\int\int\int\int_{\text{all space}} \langle \tilde{v}_i(\mathbf{a},t) w(\mathbf{x}[\mathbf{a},t]) \tilde{v}_i(\mathbf{a}',t') w(\mathbf{x}[\mathbf{a}',t']) \rangle \, \langle g(\mathbf{a}) g(\mathbf{a}') \rangle \, d^3\mathbf{a} \, d^3\mathbf{a}'$$

From before we already know that (cf., George and Lumley [43]):

$$\langle g(\mathbf{a}) g(\mathbf{a}') \rangle = \mu^2 + \mu \delta(\mathbf{a}' - \mathbf{a}) \tag{11.11}$$

Therefore:

$$\langle \tilde{u}_{0i}(t) \tilde{u}_{0i}(t') \rangle = \tag{11.12}$$

$$\mu^2 \int\int\int\int\int\int_{\text{all space}} \langle \{\tilde{v}_i(\mathbf{a},t) w(\mathbf{x}[\mathbf{a},t])\} \{\tilde{v}_i(\mathbf{a}',t') w(\mathbf{x}[\mathbf{a}',t'])\} \rangle \; d^3\mathbf{a} \, d^3\mathbf{a}'$$

$$+\mu \int\int\int_{\text{all space}} \langle \{\tilde{v}_i(\mathbf{a},t) w(\mathbf{x}[\mathbf{a},t])\} \{\tilde{v}_i(\mathbf{a},t') w(\mathbf{x}[\mathbf{a},t'])\} \rangle \; d^3\mathbf{a}$$

The double integral on the RHS is just the correlations of the instantaneous volume-averaged velocities. This can be shown more clearly by rewriting the first integral of equation (11.12) as follows:

$$\mu^2 \int\int\int\int\int\int_{\text{all space}} \langle \{\tilde{v}_i(\mathbf{a},t) w(\mathbf{x}[\mathbf{a},t])\} \{\tilde{v}_i(\mathbf{a}',t') w(\mathbf{x}[\mathbf{a}',t'])\} \rangle \; d^3\mathbf{a} \, d^3\mathbf{a}'$$

$$= (\mu V)^2 \langle \tilde{u}_{0i}^{vol}(t) \tilde{u}_{0i}^{vol}(t') \rangle$$

where the last step follows from assuming the particles follow the flow, incompressibility and mapping back to an Eulerian frame as before. This is, of course, the sought for correlation.

The second integral in equation (11.12) is a consequence of the intermittency of the characteristic LDA off-on signal, see Chapter 9. The quantity under the integral sign is evaluated for only a single particle, since it requires the initial particle position to be the same ($\mathbf{a}' = \mathbf{a}$), if the particle spends only a very short time in the scattering volume, $t' \approx t$. So to the level of our measuring

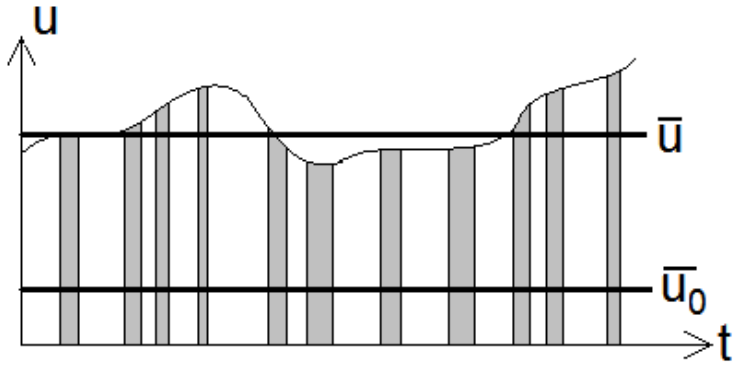


Figure 11.2: Sketch similar to figure 11.1 with the addition of indications of the mean velocity, $\overline{u}$ and the average of the intermittent signal, $\overline{u_0}$.

equipment, the entire expression can be approximated by:

$$\mu \int\limits_{\text{all space}}\int\int \langle\{\tilde{v}_i(\mathbf{a},t)w(\mathbf{x}[\mathbf{a},t])\}\{\tilde{v}_i(\mathbf{a},t')w(\mathbf{x}[\mathbf{a},t'])\}\rangle \; d^3\mathbf{a} \approx \mu V\langle[\tilde{u}_{0i}^{vol}(t)]^2\rangle \quad (11.13)$$

where we have assumed that $[w(\mathbf{x})]^2 \approx w(\mathbf{x})$, since it is usually just '1' or '0'. (This is why the integral produces a $V$, not a $V^2$). Note that the quantity $\langle[\tilde{u}_{0i}^{vol}(t)]^2\rangle$ still includes both the mean and fluctuating components, so it can be very large indeed. The reason why this term becomes so large is just an effect of subtracting off the wrong mean, since the mean value of the signal, $\overline{u}$, and the interrupted signal, $\overline{u_0}$, typically differ quite considerably, see figure 11.2.

## 11.3 Practical burst-mode algorithms

### 11.3.1 Single-point statistics

Thus a correct estimate for the burst-mode sampled mean value of the velocity of a stationary random field can be obtained by averaging the signal over the time that the signal is being measured (cf., Buchhave [19]); i.e.,

$$U_{0_T}^B = \frac{1}{T}\int_0^T \tilde{u}_0(t)\,dt$$

$$= \frac{1}{T}\Big\{\int_{t_1}^{t_1+\Delta t_1} \tilde{u}_0(t)dt + \int_{t_2}^{t_2+\Delta t_2} \tilde{u}_0(t)dt + \ldots + \int_{t_M}^{t_M+\Delta t_M} \tilde{u}_0(t)dt\Big\} \quad (11.14)$$

where $t_p$ and $\Delta t_p$ are respectively the arrival and residence times of the p'th particle and the superscript $B$ indicates that the estimator is valid for burst-mode LDA data. This corresponds to a weighted average of the velocity, weighting the measured velocities by the time that the particles are present in the measuring volume, thus eliminating the high-velocity bias.

The burst-mode LDA usually produces only a single realization for each particle. This is equivalent to assuming the velocity of the particle to be constant while passing through the measuring volume. To within this approximation, the

expression for the mean value of equation (11.14) can be written as:

$$U^B_{0_T} = \frac{\sum_{p=0}^{M-1} \tilde{u}(t_p)\Delta t_p}{\sum_{p=0}^{M-1} \Delta t_p} \tag{11.15}$$

The sum of the residence times is the "on-time" of the signal, which for large values of $M$ can be expressed as follows.

$$\mu VT = \sum_{p=0}^{M-1} \Delta t_p \tag{11.16}$$

Thus the normalization time should be the sum of the residence times, since this is the time over which the velocity is being measured and consequently the time over which one should integrate to obtain an unbiased estimate.

The estimator of the variance can be obtained in the same manner as the estimator of the mean value [19], yielding

$$\sigma^{B\,2}_{0_T} = \frac{\sum_{p=0}^{M-1} (\tilde{u}(t_p) - U^B_{0_T})^2 \Delta t_p}{\sum_{p=0}^{M-1} \Delta t_p}. \tag{11.17}$$

### 11.3.2 Burst-mode spectra

The Fourier coefficients for the finite Fourier transform can also be obtained from equation (10.20) by similarly approximating the interrupted integral and discretizing; i.e.,

$$\hat{u}_{0_T}(f) = \int_0^T e^{-i2\pi ft} u_0(t)\, dt \tag{11.18}$$

$$= \int_{t_1}^{t_1+\Delta t_1} e^{-i2\pi ft} u_0(t) dt + \int_{t_2}^{t_2+\Delta t_2} e^{-i2\pi ft} u_0(t) dt + \ldots + \int_{t_M}^{t_M+\Delta t_M} e^{-i2\pi ft} u_0(t) dt$$

$$= \sum_{p=0}^{M-1} e^{-i2\pi f_k t_p} u(t_p) \Delta t_p$$

where $\Delta t_p$ is the residence time. From this, a practical spectral estimator can now be obtained as (see, e.g., [20, 46]);

$$S(f) = \frac{1}{(\mu V)^2} S^B_{0_T}(f)$$

$$= \frac{T}{(\sum_{p=0}^{M-1} \Delta t_p)^2} \sum_{p=0}^{M-1} \sum_{q=0}^{M-1} e^{-i2\pi f(t_p - t_q)} u(t_p) u(t_q) \Delta t_p \Delta t_q \tag{11.19}$$

This is exactly the direct estimator assumed by Buchhave 1979 [19], but deduced here from first principles.

The self-products ($p = q$) contain the intermittency noise described in Chapter 9. Buchhave *et al.* [20] and George *et al.* [46] suggest eliminating it by omitting the self-products. Unfortunately, as noted in Chapter 9, this

also eliminates all of the energy and yields a spectrum with negative values (which integrates to zero). The 'fix' is the same as that proposed in Chapter 9. Since the part thrown away by neglecting the self-products is the same at all frequencies, simply add the energy back; i.e.,

$$\tilde{S}(f) = \frac{T}{(\sum_{p=0}^{M-1} \Delta t_p)^2} \sum_{\substack{p=0 \\ p \neq q}}^{M-1} \sum_{q=0}^{M-1} e^{-i2\pi f(t_p - t_q)} u(t_p) u(t_q) \Delta t_p \Delta t_q + \frac{\overline{c^2}}{\nu} \qquad (11.20)$$

This algorithm will be used extensively in the following sections. The relative error of this estimator is given by equation (10.48) [46].

## 11.4 Experimental setups

The experimental method for the measurements performed on the axisymmetric turbulent far jet can be found in Frohnapfel [35]. The data of Frohnapfel includes simultaneously acquired HWA and LDA data including the residence times from measurements performed in an axisymmetric turbulent far jet 30.3 diameters downstream of the jet exit. The sampling frequency for the HWA data is $f_s = 40\,000\,\mathrm{Hz}$. The average sampling rate for the LDA data was substantially lower, $\nu = 318\,\mathrm{Hz}$.

In addition, HWA data with LDA data including residence times was acquired under similar conditions in the wake of a circular cylinder in a wind tunnel at DTU[1]. The experimental setup should be roughly the same as described by Gjelstrup *et al.* [50]. However, some important details are corrected and highlighted in the following.

The circular cylinder had a diameter of 6 mm and was mounted in a square test section of width 300 mm in a closed loop wind tunnel. The material and mounting (firm or flexible) of the cylinder is unknown, however, it is known that it is some kind of metal and solid (as opposed to hollow). The HWA and LDA time series were acquired at the same position 26 mm downstream of the cylinder. The HWA measurements were acquired with a sampling frequency of $f_s = 100\,\mathrm{kHz}$ at a Reynolds number of 7 400 ($\mathrm{U} = 18.5\,\mathrm{m/s}$) based on the cylinder diameter. The average data rate for the LDA is $\nu = 94\,\mathrm{kHz}$ and the corresponding Reynolds number is 8 600 ($\mathrm{U} = 21.5\,\mathrm{m/s}$). Thus the ratio of the mean velocities of the HWA and LDA data sets is $U_{LDA}/U_{CTA} = 1.16$, which is important to bear in mind when making comparisons. The spectra computed from these two data sets are compared despite the fact that they are acquired under slightly different conditions.

## 11.5 Properties of acquired data sets

In this section, the statistical and dynamic properties of the acquired time series are investigated for comparison to each other as well as for meeting the requirements of the assumptions inherent in the theory.

[1] These were kindly provided by Holger Nobach at Max-Planck Institut für Dynamik und Selbstorganisation. The HWA data set was downloaded from *http://ldvproc.nambis.de/data/dtudata.html*, while the LDA data were obtained directly from Holger Nobach.

### 11.5.1 Axisymmetric turbulent far jet

A plot showing a part of the time history of the simultaneously acquired HWA and LDA measurements is displayed in figure 11.3. The peaks representing the sampled LDA signal have a width corresponding to the residence time of each particle. Because the residence times are very short compared to the average time between samples, the variable widths of the peaks are not visible in the plot. As can be seen in the figure, the agreement between these two data sets is good. As pointed out by Capp [21], the scatter plot of velocities to residence times should display an inversely proportional behavior, since higher velocities should generally yield shorter residence times and vice versa. The data at hand does indeed show this, see figure 11.4.

**Inter-arrival times**

Figure 11.5 displays the histogram of the interarrival times of the seeding particles $\tau_n$ along with the corresponding exponential probability density function

$$P_\tau(c) = \nu e^{-\nu c} \tag{11.21}$$

where we let $c$ denote the variable representing the interarrival times, $\tau_n$. It is clear from the figure that the time between samples does indeed have an approximately exponential distribution with the parameter, $\nu$, the average data rate. This implies that the sampling process is Poisson with rate $\nu$, see e.g. Milton and Arnold [92] pp. 111–112; i.e.,

$$P\{N(t) = k\} = \frac{(\nu t)^k}{k!} e^{-\nu t}, \quad k = 0,\, 1,\, 2,\, \ldots \tag{11.22}$$

where $N(t)$ is the number of events taking place during $]0, t]$.

Thus, the sampling can meet the requirements of being alias-free, as was discussed in section 10.2. Further, since the sampling process can be considered to be Poisson, it seems plausible to assume that the events occur independently of the time since the last event. Note that this does not imply that the arrival time statistics are statistically independent of the particle velocities which bring them, as commonly assumed.

**Transit/residence time statistics**

It was stated by Reist [116] that many aerosols have a lognormal particle size distribution. What characterizes this distribution is that the logarithm of the random variable is normally distributed. One can claim that the residence time is indirectly coupled to the size of the particle since a larger particle will be 'visible' for a longer time than a smaller one. This is because it scatters more light and therefore exceeds the detection threshold longer while traveling across the scattering volume. Assuming the particle size distribution to be lognormal, it is reasonable to postulate that the distribution of the transit times might be as well. Figures 11.6, 11.7 and 11.8 show the histogram of the residence times along with the corresponding lognormal probability distribution;

$$P_{\Delta t}(c) = \frac{1}{c\sigma_{_{LN}}\sqrt{2\pi}} e^{-(\ln(c)-\mu_{_{LN}})^2/2\sigma^2_{_{LN}}} \tag{11.23}$$

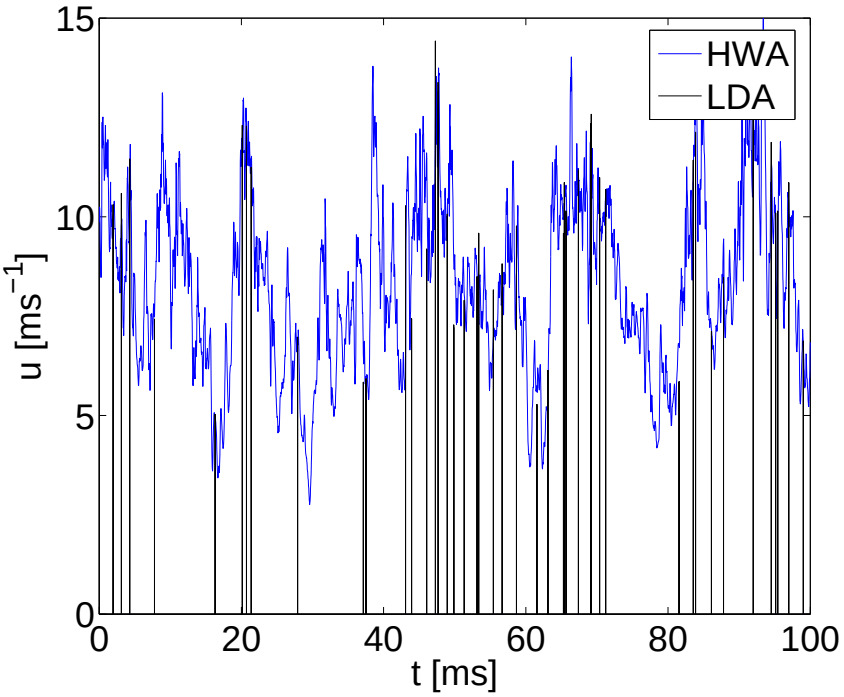


Figure 11.3: Axisymmetric turbulent jet data (from Frohnapfel [35]): Time history of the sampled HWA and LDA signal.

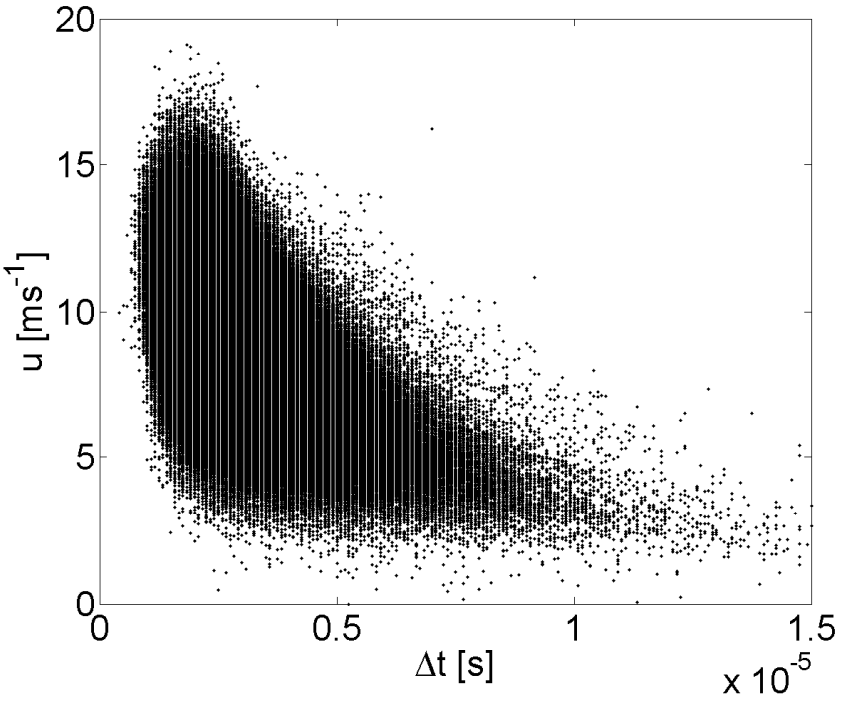


Figure 11.4: Axisymmetric turbulent jet data (from Frohnapfel [35]): Scatter plot of velocities to residence times.

where $\mu_{LN}$ and $\sigma_{LN}$ are the mean and standard deviation of the natural logarithm of the variable, since by definition, the logarithm of the variable is normally distributed. These values were obtained directly from the measurement data. It is seen that the lognormal distribution describes the distribution of the transit times quite well. All three plots display a quite good collapse. The same plot with a logarithmic x-axis seen in figure 11.7 displays a normal distribution as expected, however, the histogram is slightly skewed. Evidence of the skewness is further amplified in the same plot with a logarithmic y-axis seen in figure 11.8, even though this effect is relatively small.

**Velocity statistics**

As a check of the intermittency and symmetry of the flow, histograms of the velocity fluctuations are displayed in figures 11.9-11.14. First, the histogram and pdf of the velocity fluctuations from the LDA measurements are shown in a linear (figure 11.9) and a semilogarithmic (figure 11.10) plot. The corresponding figures are then shown for the HWA data displayed in figures 11.11 and 11.12 and for the residence time weighted LDA data in figures 11.13 and 11.14. Comparison of the histograms to the arithmetic LDA and HWA Gaussian pdfs,

$$P_u(c) = \frac{1}{\sqrt{2\pi}\sigma} e^{-\frac{(c-\mu)^2}{2\sigma^2}} \tag{11.24}$$

where $\mu$ and $\sigma$ are the arithmetic mean velocity and standard deviations, respectively, show that the velocities are quite well described by the normal distributions except in the extremes where the histograms end abruptly. This is a sign of clipping of the data, which is a consequence of the dynamic range of the data being smaller than that of the measured flow. Hence, the statistics are biased and the clipping will yield erroneous values for the moments. This probably could have been eliminated by changing the filter and frequency shift settings.

One can determine whether the turbulence is intermittent or not from how the velocities are distributed across the range of the occurrences. For a fully turbulent flow, the velocities are expected to display a Gaussian distribution. If the turbulent flow is intermittent, the fraction of the time the flow is turbulent to the fraction that the flow is not will redistribute the probability of the occurrences (see, e.g., Tennekes and Lumley [135]). The intermittent bursts will cause the distribution to deviate from the Gaussian by larger excursions from the mean, redistributing occurrences to the extremes yielding a flatter distribution. The fourth central moment, $\overline{u^4}$, can be used as a measure for the flatness of the distribution. The kurtosis is defined by non-dimensionalizing this quantity with the second moment; i.e.,

$$K = \frac{\overline{u^4}}{\overline{u^2}^2} \tag{11.25}$$

It is well known that for a Gaussian pdf, the kurtosis equals three. For the pdf of an intermittent flow, as described above, the kurtosis is expected to have a value larger than three. However, due to the clipping of the measurement data, one cannot determine whether the flow is intermittent in this manner.

The third central moment, $\overline{u^3}$, provides a measure of the lack of symmetry

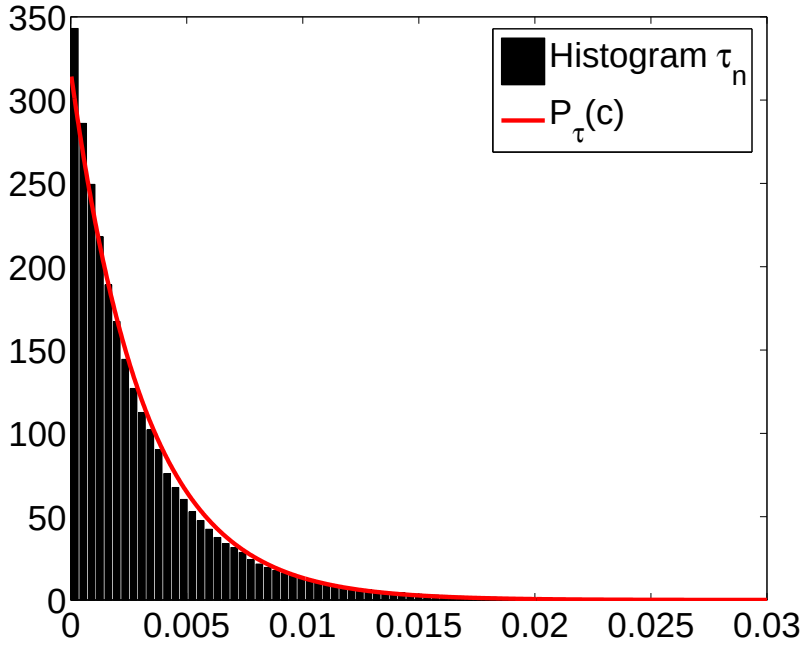


Figure 11.5: Axisymmetric turbulent jet data (from Frohnapfel [35]): Histogram of interarrival times of the seeding particles $\tau_n$ and the corresponding exponential probability density function $P_\tau(c)$.

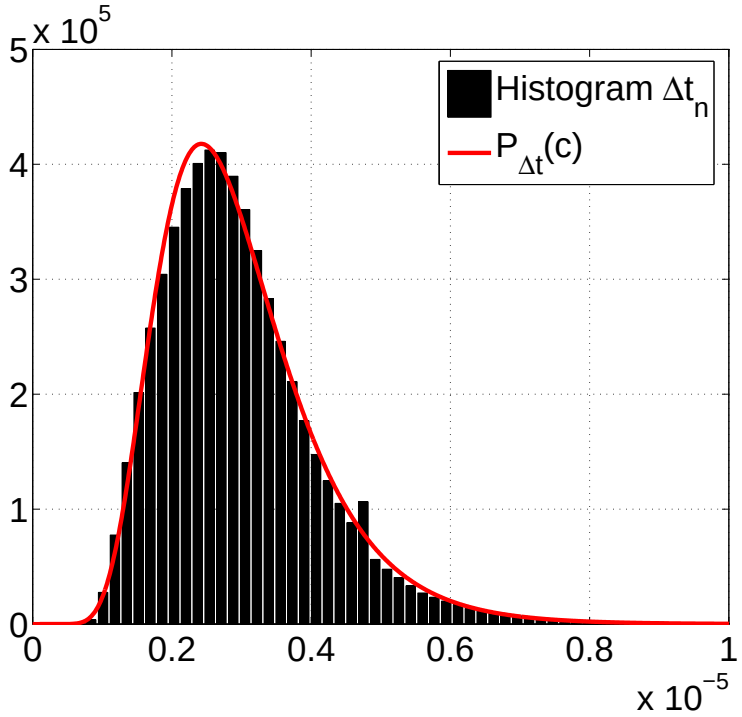


Figure 11.6: Axisymmetric turbulent jet data (from Frohnapfel [35]): Histogram of residence times $\Delta t_n$ and the corresponding lognormal probability density function $P_{\Delta t}(c)$.

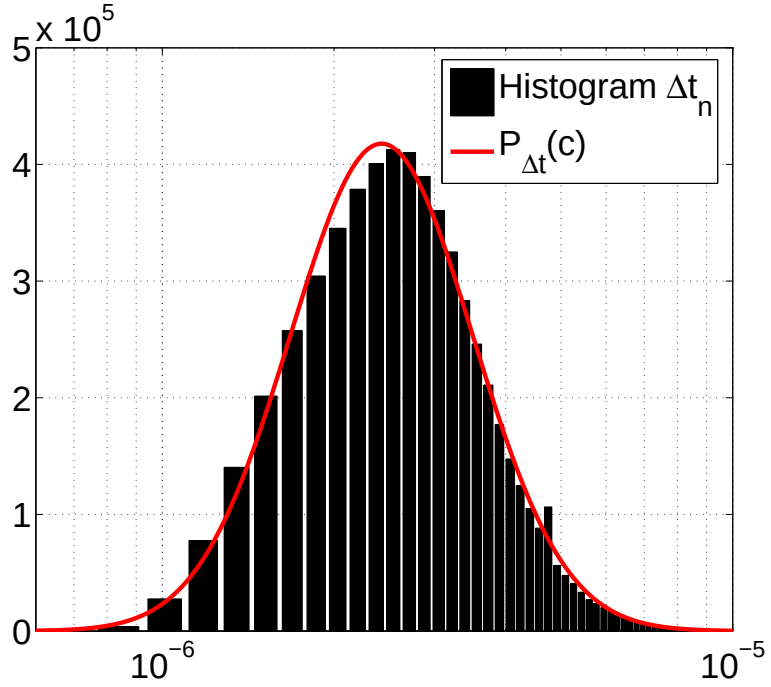


Figure 11.7: Axisymmetric turbulent jet data (from Frohnapfel [35]): Histogram of residence times $\Delta t_n$ and the corresponding lognormal probability density function $P_{\Delta t}(c)$ plotted with a logarithmic variable axis.

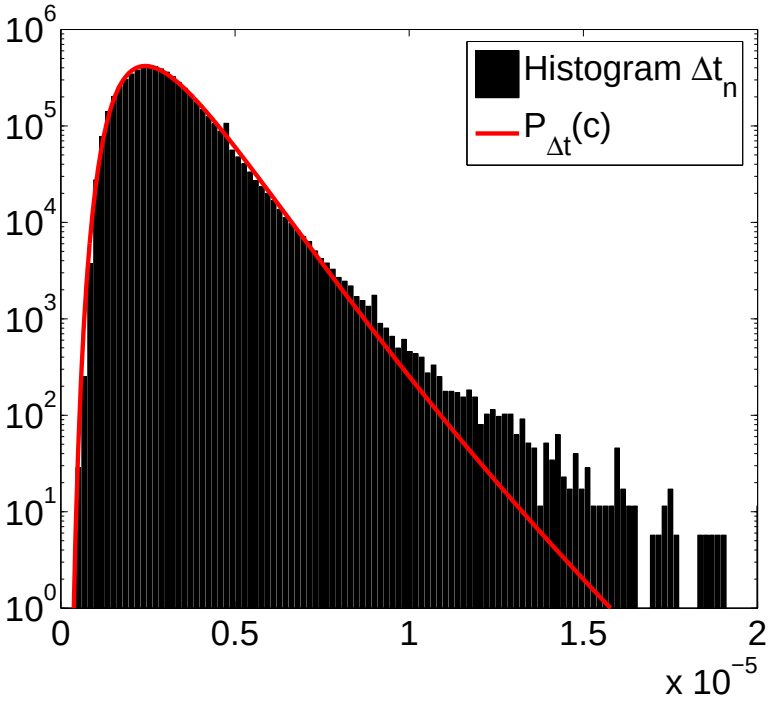


Figure 11.8: Axisymmetric turbulent jet data (from Frohnapfel [35]): Histogram of residence times $\Delta t_n$ and the corresponding lognormal probability density function $P_{\Delta t}(c)$ plotted with a logarithmic frequency axis.

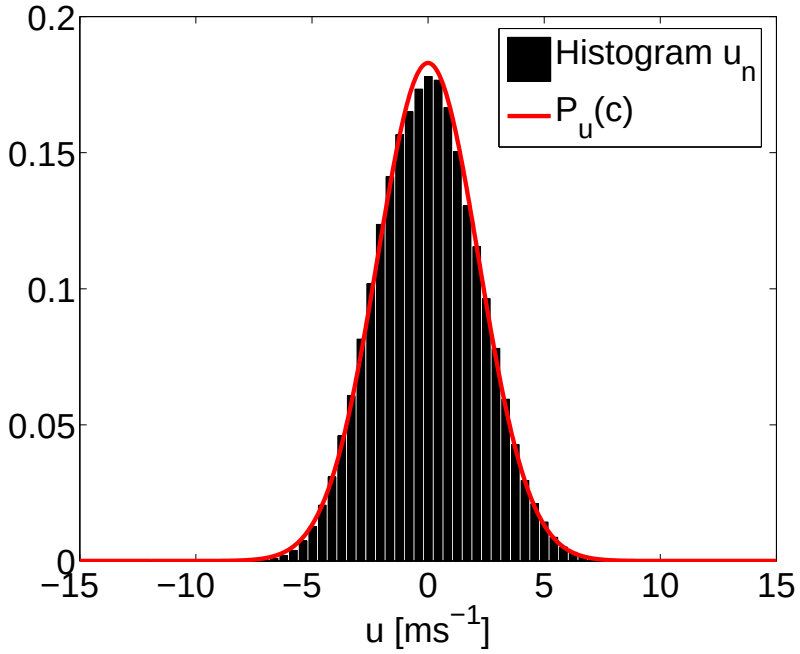


Figure 11.9: Axisymmetric turbulent jet data (from Frohnapfel [35]): Histogram of LDA velocity fluctuations $u_n$ and the corresponding Gaussian probability density function $P_u(c)$.

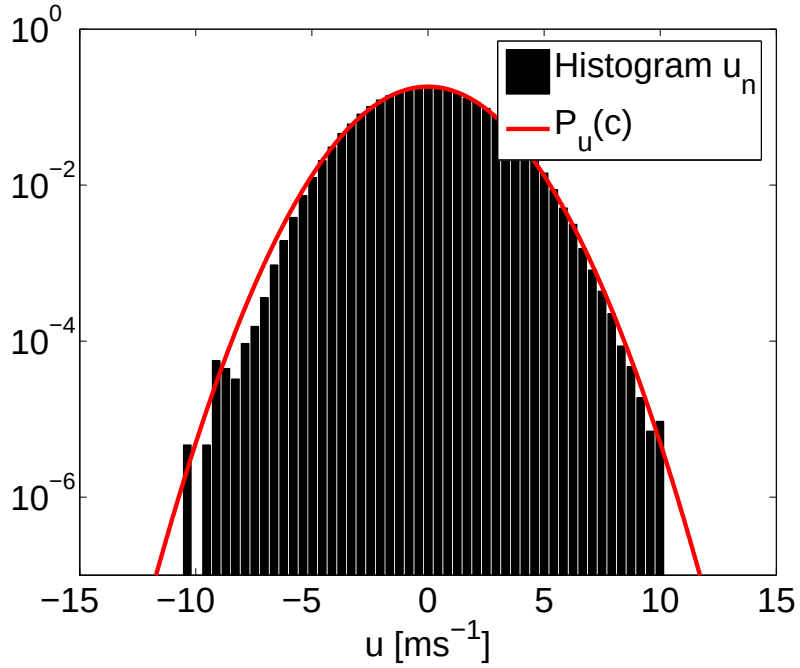


Figure 11.10: Axisymmetric turbulent jet data (from Frohnapfel [35]): Histogram of LDA velocity fluctuations $u_n$ and the corresponding Gaussian probability density function $P_u(c)$. The y-axis is logarithmic to accentuate the discrepancies between the histogram and the pdf.

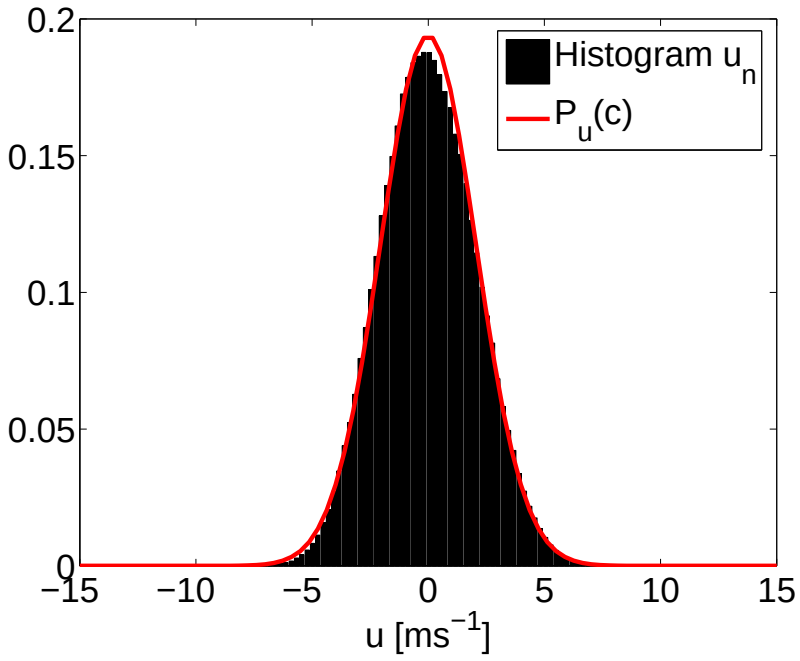


Figure 11.11: Axisymmetric turbulent jet data (from Frohnapfel [35]): Histogram of velocity fluctuations $u_n$ from HWA measurements and the corresponding Gaussian probability density function $P_u(c)$.

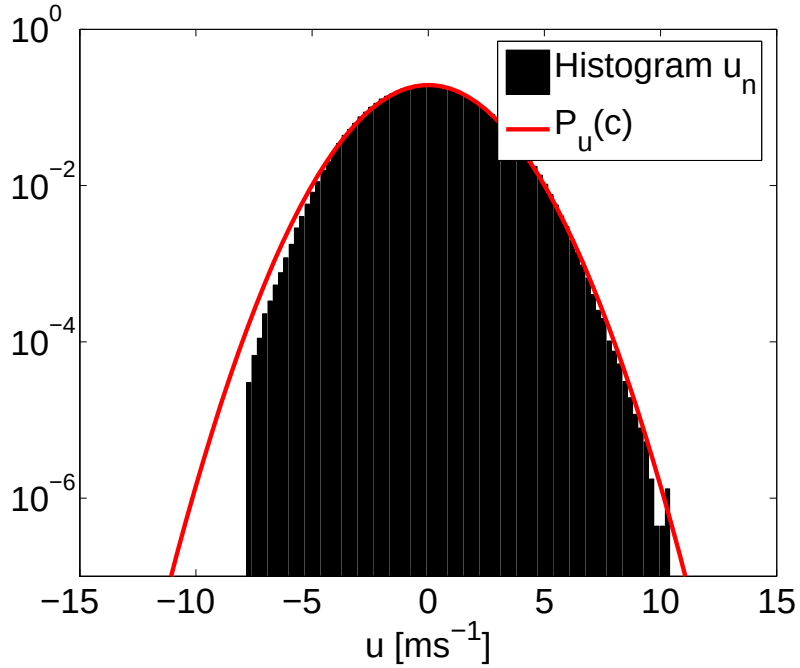


Figure 11.12: Axisymmetric turbulent jet data (from Frohnapfel [35]): Histogram of velocity fluctuations $u_n$ from HWA measurements and the corresponding Gaussian probability density function $P_u(c)$. The y-axis is logarithmic to accentuate the discrepancies between the histogram and the pdf.

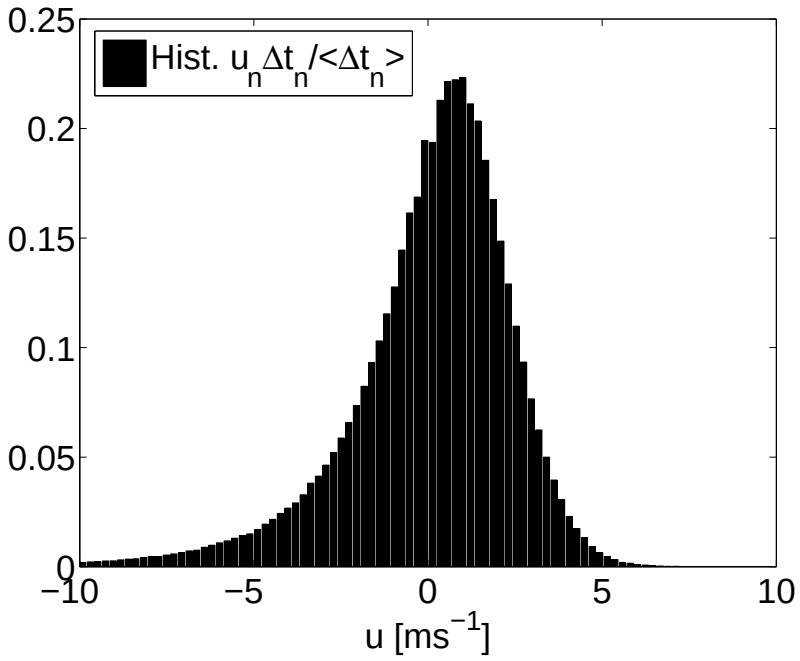


Figure 11.13: Axisymmetric turbulent jet data (from Frohnapfel [35]): Histogram of residence time weighted velocity fluctuations $u_{\mathrm{RTW}} = u_n \Delta t_n / < \Delta t_n >$, where $<>$ indicates ensemble averaging.

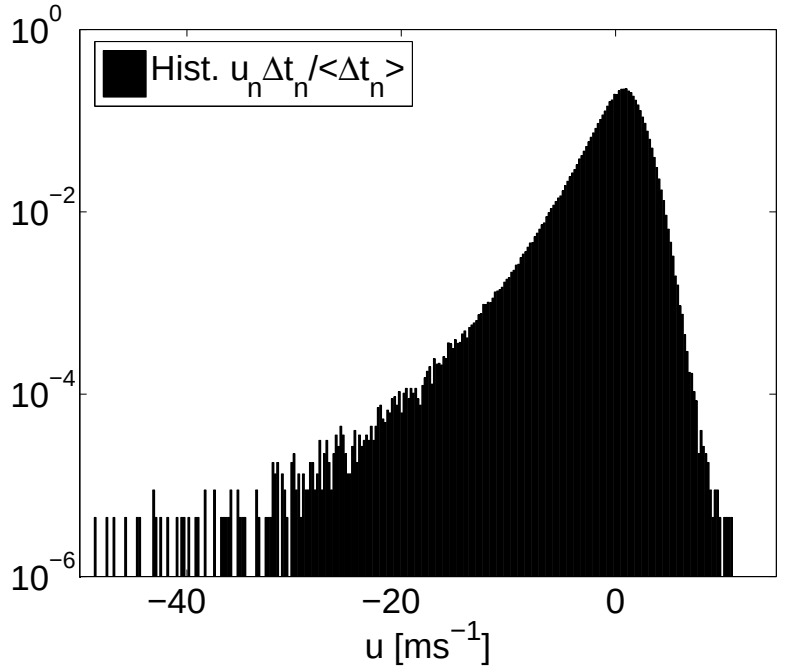


Figure 11.14: Axisymmetric turbulent jet data (from Frohnapfel [35]): Histogram of residence time weighted velocity fluctuations $u_{\mathrm{RTW}} = u_n \Delta t_n / < \Delta t_n >$, where $<>$ indicates ensemble averaging.

Table 11.1: Values of skewness and kurtosis obtained from the LDA and HWA measurement data and corresponding data in Hussein *et al.* [58].

| | S [-] | K [-] |
|---|---|---|
| $\text{LDA}_{\text{RTW}}$ | -0.058 | 3.25 |
| HWA | 0.088 | 2.83 |
| $\text{LDA}_{\text{RTW}}$ [58] | 0.101 | - |
| HWA [58] | 0.099 | - |

in the probability density. The skewness can be defined as the third central moment non-dimensionalized by three halves power of the second one, where a non-zero skewness/third moment indicates an asymmetric pdf.

$$S = \frac{\overline{u^3}}{\overline{u^2}^{3/2}} \tag{11.26}$$

The sign of the skewness cannot be determined directly from the velocities from the LDA or HWA measurements shown in linear and semilogarithmic plots in figures 11.9–11.12. The plots clearly show asymmetries, but the exact value of the skewness is unreliable because of the clipping. However, the sign of the third moment can be justified from a simple modified eddy viscosity model; i.e.,

$$\overline{u^2 \cdot u} = -\nu_t \frac{\partial \overline{u^2}}{\partial x} \tag{11.27}$$

where $\nu_t > 0$. For an axisymmetric jet, the centerline velocity is inversely proportional to the distance from the nozzle, x; i.e., $U_c \sim 1/x$. Assuming $u^2 \propto U_c^2 \sim 1/x^2$ and inserting this into the above relation yields

$$\nu_t \frac{\partial \overline{u^2}}{\partial x} \propto -2\frac{1}{x^3} \tag{11.28}$$

Clearly $\overline{u^3} \sim +2\nu_t/x^3$, hence the skewness should be positive.

In table 11.1, the values of the skewness and kurtosis found from the LDA and HWA measurement data along with values from Hussein *et al.* [58] are compared. Due to the clipping of the measurement data, the estimated moments will be erroneous and thus one cannot deduce much from these values. Further, the clipping does not occur at the same velocities in the HWA and LDA data sets, which will further add to the ambiguities since different clipping will yield different biases when estimating moments. The data sets from [58], which do not suffer clipping, show good agreement of the skewness determined from the LDA RTW and HWA data. Further, the skewness found from these data is positive, which is in line with the above discussion applying the eddy viscosity model.

The residence time weighted velocities $u_n \Delta t_n$ reveal a different picture where the occurrences of large deviations are more probable in the negative end. This is simply a consequence of weighting the velocities by the residence times, which have a highly non-symmetric distribution with exclusively positive values. Figures 11.13 and 11.14 display the histogram of the residence time weighted

velocities on linear and semilogarithmic plots, respectively. A higher velocity should correlate well with a shorter residence time and vice versa. Therefore, the high velocities are generally coupled to the residence times in the lower end of the $\Delta t$ distribution. Hence, the histogram of the residence time weighted velocities should drop rapidly in the high end as the residence times in the low end rapidly approach zero. For velocities below the average value, the corresponding residence times are generally found in the higher end. The histogram of the residence times will in this end approach zero slowly, as do the velocities in the lower end. The pdf for the residence time weighted velocities should thus be a composite (or convolution) of the Gaussian pdf for the velocities (figures 11.9 and 11.10) and the lognormal pdf for the residence times (figures 11.13 and 11.14) and thus plausibly correspond to the histogram of the residence time weighted velocities seen in figures 11.13 and 11.14.

**Block length and time dependent particle concentration**

When computing spectra from randomly sampled data using block averaging, it is important to keep the block lengths in physical time of constant length. The main reason is to avoid windowing effects, which might appear for some of the shorter blocks, even if the experiment is well designed.

To see how the variations in sampling rate affected the block length, the data was divided into 2000 blocks of 500 samples each. The record length $T_b$ of the blocks are shown in the order of their acquisition, see figure 11.15. It is apparent from the figure that the block lengths vary considerably with time, which is a consequence of the varying seeding density which determines the sampling rate. Thus, the sampling rate will decrease with block number in four "streaks", which appear due to the introduction of new seeding particles. This was apparently done at block number 0, 573, 934 and 1429. As a rough measure, the record length of the blocks $T_b$ should be inversely proportional to the particle concentration c (since the number of points per block was constant). Thus,

$$T_b \propto \frac{1}{c} \tag{11.29}$$

This is displayed in figure 11.16.

If we assume that the decay of particle concentration is proportional to the concentration itself, the resulting decay is exponential in time; i.e.,

$$c(t) = c_0 e^{-kt} \tag{11.30}$$

where c(t) is the time dependent concentration, $c_0$ is a constant corresponding to the concentration at t=0 and k is a disintegration constant. After some manipulation, one can rewrite the identity in the following manner,

$$\ln\left[\frac{c(t)}{c_0}\right] = -kt \tag{11.31}$$

enabling the determination of the constant k. The left hand side of this identity is determined from the data for each decay process and displayed against the cumulative sum of the record lengths in figure 11.17. A simple curve fitting (green line) provides the inclination corresponding to the constant k=$1.35/1000\,s^{-1}$.

The inverse time constant is thus

$$\frac{1}{k} = \frac{1000}{1.35} = 741\,s. \tag{11.32}$$

The reduction of particles can be assigned to many factors. It is reasonable to assume that a prominent one probably is the screens and walls inside the jet. As a check of how large this effect is, one can compare the time constant k to the jet volume mass flow. For this argument, it is assumed that the particles are distributed relatively homogeneously throughout the enclosure volume. The total volume of the enclosure is $2{\times}2{\times}10\ \mathrm{m}^3{=}40\ \mathrm{m}^3$. The exit velocity of the jet is 40 m/s and the diameter of the nozzle is 10 mm, hence the flow rate of the jet is $\dot{v} = 40\,\pi\,0.005^2\ \mathrm{m}^3\mathrm{s}^{-1}$. The time constant, i.e., the time it takes for all of the air in the room to pass through the jet, is

$$\tau = \frac{V}{\dot{v}} = \frac{40}{40\,\pi\,0.005^2} = 12\ 732\,s. \tag{11.33}$$

Hence only about 6% of the reduction of particles can be assigned to the screens and walls inside the jet.

Evaporation might be another significant cause of the strong particle decay. We start by assuming the droplets to be spherical, that the evaporation process is quasi-steady, the droplet temperature is uniform, the mass fraction of vapor at the droplet surface is determined by liquid-vapor equilibrium at the droplet temperature and that all thermophysical properties are constant. For a spherical droplet, its mass is given by

$$m = \frac{4}{3}\pi R^3 \rho_d \tag{11.34}$$

where R is the radius of the droplet and $\rho_d$ is the droplet liquid density. Fourier's law for heat flux applied to the droplet surface

$$\dot{q}_{r=R} = -\lambda \frac{\partial T}{\partial r}|_{r=R} \tag{11.35}$$

where $\lambda$ is the thermal conductivity yields a mass flux of

$$\dot{m} = 4\pi R^2 \left\{ -\lambda \frac{T - T_\infty}{R} \right\}. \tag{11.36}$$

T is the temperature of the drop and $\mathrm{T}_\infty$ is the temperature of the ambient ($r \to \infty$).

From (11.34) one obtains

$$\dot{m} = \frac{4}{3}\pi 3 R^2 \dot{R} \rho_d. \tag{11.37}$$

Setting (11.36) and (11.37) equal and integrating the expression with respect to time results in

$$R^2 - R_0^2 = -\frac{2\lambda}{\rho_d}[T - T_\infty](t - t_0). \tag{11.38}$$

Hence, for evaporation, the square of the radius decreases linearly with time. This expression is analogous to the well established $d^2$-law, often applied in combustion applications to obtain a time constant for the particle evaporation. Within combustion, the relation is most often applied for burning droplets, even though its derivation was originally performed for evaporating droplets. The $d^2$-law can straightforwardly be proven [138] with the same assumptions as for the derivation above. This law, which has been verified experimentally [66], also states that the square of the particle diameter varies linearly with time;

$$D^2(t) = D_0^2 - Kt \tag{11.39}$$

where D(t) and $D_0$ are the particle diameters at arbitrary time t and t=0, respectively, and K is the evaporation constant given by

$$K = \frac{8\rho_{\text{air}}\mathcal{D}_{12}}{\rho_{\text{l}}} \ln(1+B) \tag{11.40}$$

where $\rho_{\text{air}}$ and $\rho_{\text{l}}$ are the density of the surrounding air and the particle liquid, respectively, $\mathcal{D}_{12}$ is the mass diffusivity (a.k.a. the binary diffusion number) between medium 1 and 2 and B is the Spalding mass transfer number. $\ln(1+B)$ can be approximated at the particle surface radius r=$r_s$ using the gaseous velocity $v_s$ of the species leaving the surface [66].

$$\ln(1+B) \approx \frac{r_s v_s}{\mathcal{D}_{12}} \tag{11.41}$$

The droplet lifetime $t_d$ is thus simple to evaluate. For D(t)=0 in (11.39);

$$t_d = \frac{D_0^2}{K} \approx \frac{D_0^2\rho_{\text{l}}}{8\rho_{\text{air}}} \frac{1}{r_s v_s} \tag{11.42}$$

Let's estimate these parameters roughly by the following values; $D_0 = 10^{-6}$ m, $\rho_{\text{l}} = 10^3$ kg/m$^3$, $\rho_{\text{air}} = 1$ kg/m$^3$, $r_s = D_0/2 = 0.5 \cdot 10^{-6}$ m and $v_s = 10^{-6}$ m/s where $v_s$ was chosen based on the dimensions of the particles. Inserting these values yields a time scale $t_d$;

$$t_d \approx \frac{(10^{-6})^2 \cdot 10^3}{8 \cdot 1} \frac{1}{0.5 \cdot 10^{-6} \cdot 10^{-6}} \approx 250\ s. \tag{11.43}$$

Hence, using the estimated values above, the particles evaporate with a time constant roughly corresponding to that of the measurements.

As was pointed out earlier, due to the lognormality of the residence time distribution it is highly plausible that the size distribution of the seeding is also lognormal. Bias-free LDA measurements require statistically uniform spatial seeding. This problem was solved by filling the enclosure with smoke and letting the jet distribute the aerosol. Since the buffer capacity of the BSA had an upper limit corresponding to 600 Hz, the measurements were not initialized until 45 minutes = 2700 s after the introduction of the seeding, yielding an average data rate below this frequency. The measurements were continued for 15 minutes = 900 s, by which the data rate had dropped to about 150 Hz, corresponding to more than one sample every two integral time scales. Comparing this time span of 900 s to the initiation time for the particle concentration to

approach uniformity of 2700 s, it is plausible that all of the particles of diameter corresponding to the peak of the distribution have already evaporated to undetectability, which happens at about $d_p \approx 0.1\mu$m [4]. Hence, only the exponentially decaying part of the distribution remains, resulting in an exponential decay of the particle concentration as the particles evaporate. The $d^2$ dependence of the time will only add to the exponent as a multiplicative factor inside the exponent and thus will not cause the decay to deviate from the exponential trend. It is thus plausible that evaporation is the main factor in the diminution of the seeding particle concentration.

Another possible factor leading to particle decay might be the leakage from the enclosure, meaning that the particles are not confined to the tent. Since the tent was relatively tight, this was probably not a major factor. Further causes could be sticking of the particles to each other (agglomeration), sticking to the walls of the enclosure, the floor, traversing system etc. might also contribute to the decrease in particle concentration.

### 11.5.2 Cylinder wake

Figure 11.18 displays the histogram of the interarrival times of the seeding particles $\tau_n$ and the corresponding exponential probability density function $P_\tau(c)$ (11.21). For this data set, it is apparent that there is a deviation at the lowest values from the exponential distribution found in the previous data set.

As for the former data set, the residence times have a lognormal distribution, see figures 11.19-11.21. It is again assumed that this is related to the lognormal distribution of the particle size.

The histogram of the LDA velocity fluctuations, shown in figures 11.22 and 11.23, display a distribution which does not fit as well to the Gaussian pdf as the data of the axisymmetric jet. The pattern is very similar for the HWA velocities as seen in figures 11.24 and 11.25, indicating that the departure from the Gaussian is flow related. The effect seems to be a combination of skewness and large kurtosis. Both of these are consistent with the highly intermittent nature of the near wake. Again, clipping of the data reduces the data, hampering determination of the moments.

Figure 11.28 displays the inverse of the block lengths for blocks obtained by diving the data set into units of 500 samples each. The block lengths as well as their inverses do not vary considerably with time, with the exception of a few spurious data points. Since the 250 blocks have a record length of $T_b = 0.01$ s, the total record length is $T = 0.01 \cdot 250 = 2.5$ s. This makes sense, since the diminution in particle concentration can be assumed not to vary very fast (i.e., with a time scale $\gg T_b$), so these variations are probably very small on the relevant measured time scale. And even if it would, an equilibrium between the number of generated and evaporated/diffused/agglomerated particles might have been reached whose variations might be substantially slower than the record length. Yet another possibility, which seems likely regarding the high seeding density, is that the seeding was continuously generated and fed into the flow (in particular if the wind tunnel is an open type).

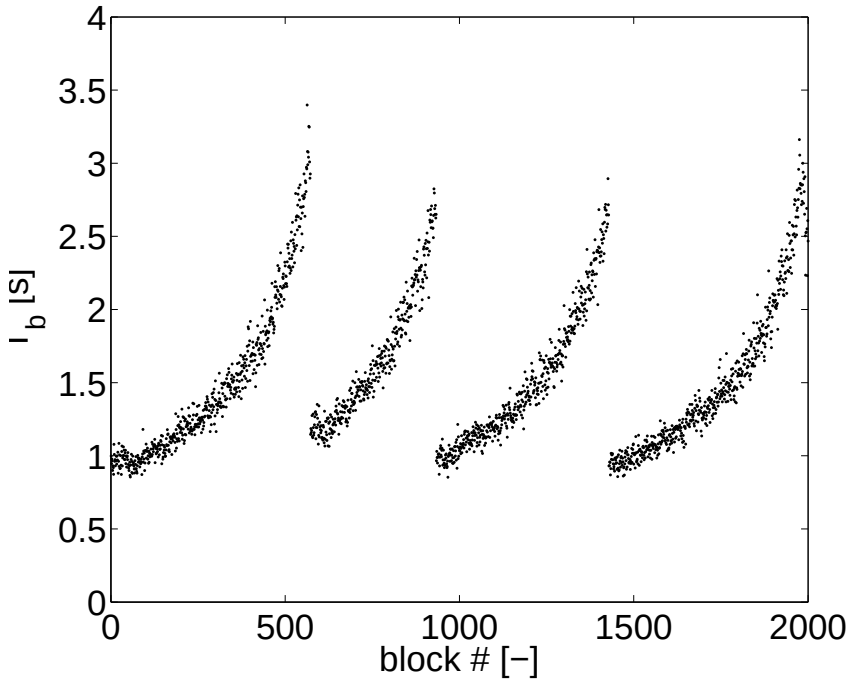


Figure 11.15: Axisymmetric turbulent jet data (from Frohnapfel [35]): Consecutive block lengths in seconds for constant number of samples ($N_s = 500$) per block.

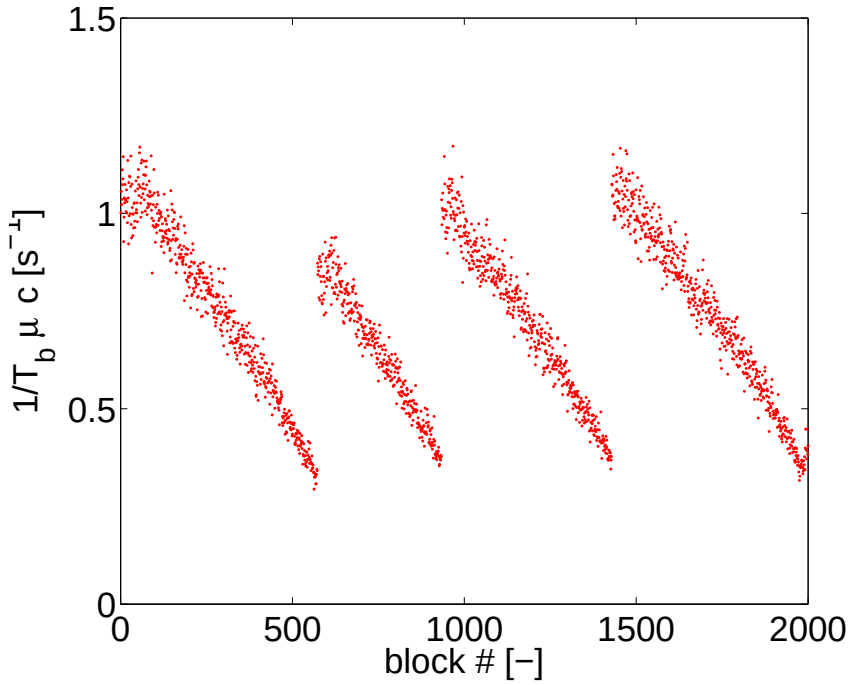


Figure 11.16: Axisymmetric turbulent jet data (from Frohnapfel [35]): Inverse of block lengths shown consecutively for each block. This quantity is proportional to the particle concentration.

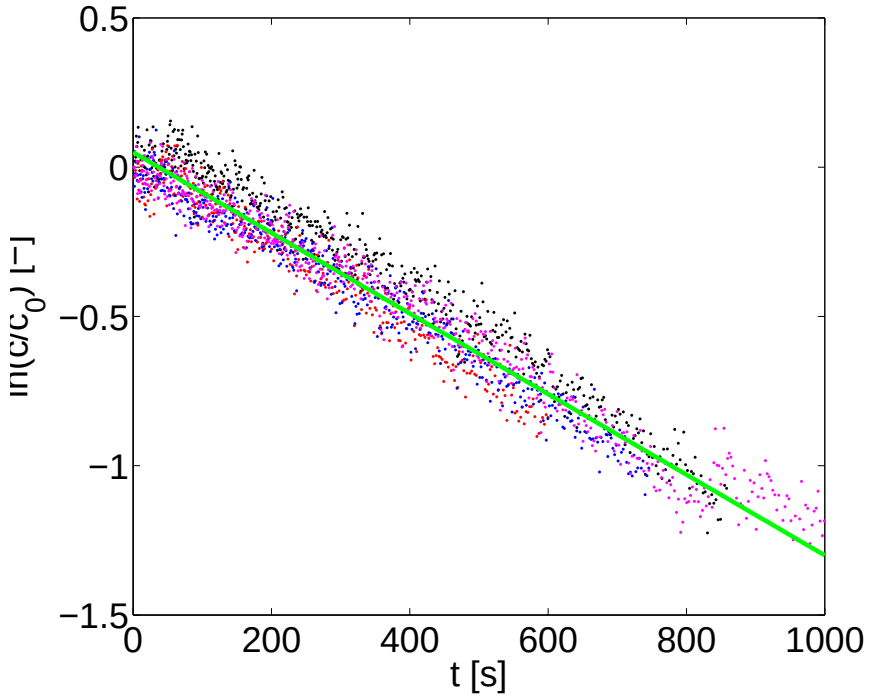


Figure 11.17: Axisymmetric turbulent jet data (from Frohnapfel [35]): Determination of the disintegration constant k, found from the inclination of the curves $\ln(c(t)/c_0)$.

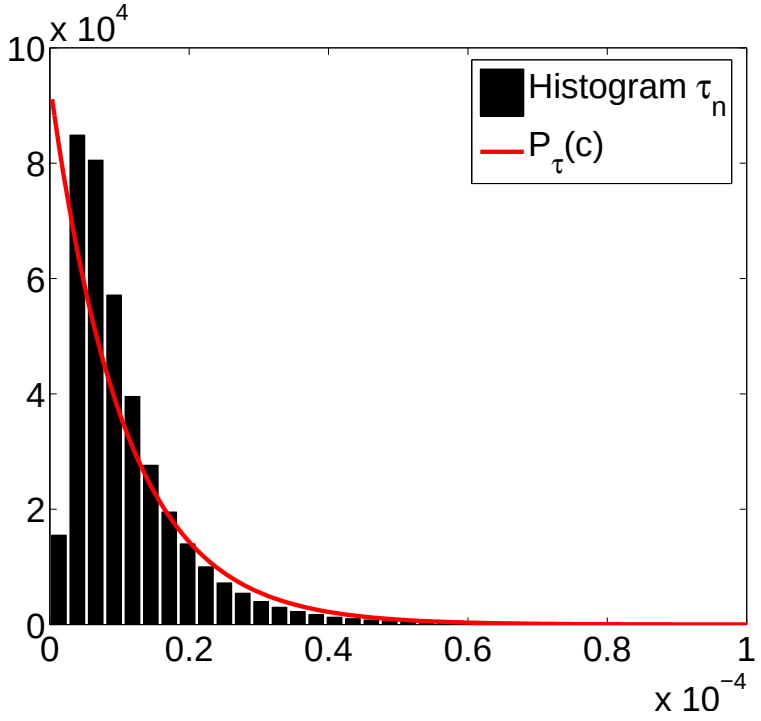


Figure 11.18: Cylinder wake data (from Nobach [96]): Histogram of inter-arrival times of the seeding particles $\tau_n$ and the corresponding exponential probability density function $P_\tau(c)$.

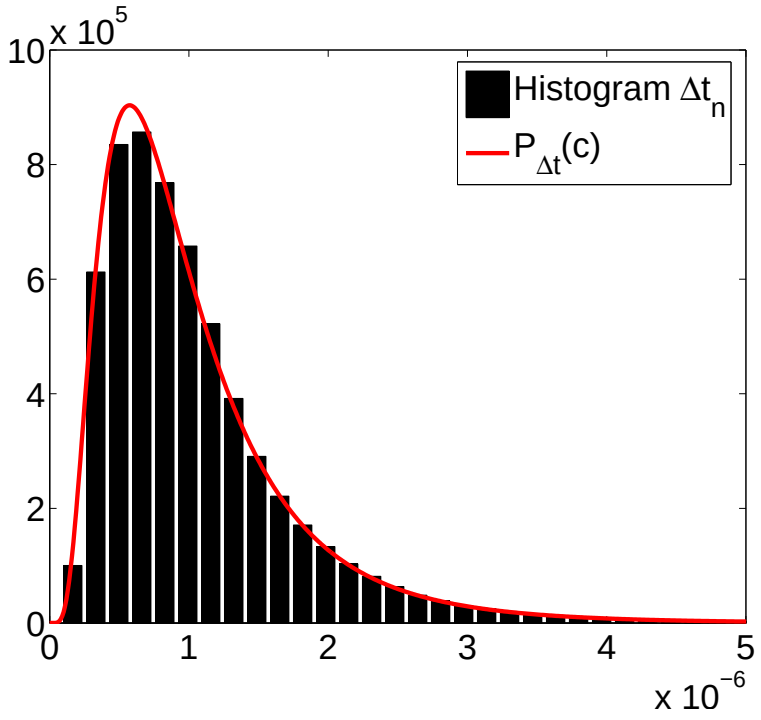


Figure 11.19: Cylinder wake data (from Nobach [96]): Histogram of residence times $\Delta t_n$ and the corresponding lognormal probability density function $P_{\Delta t}(c)$.

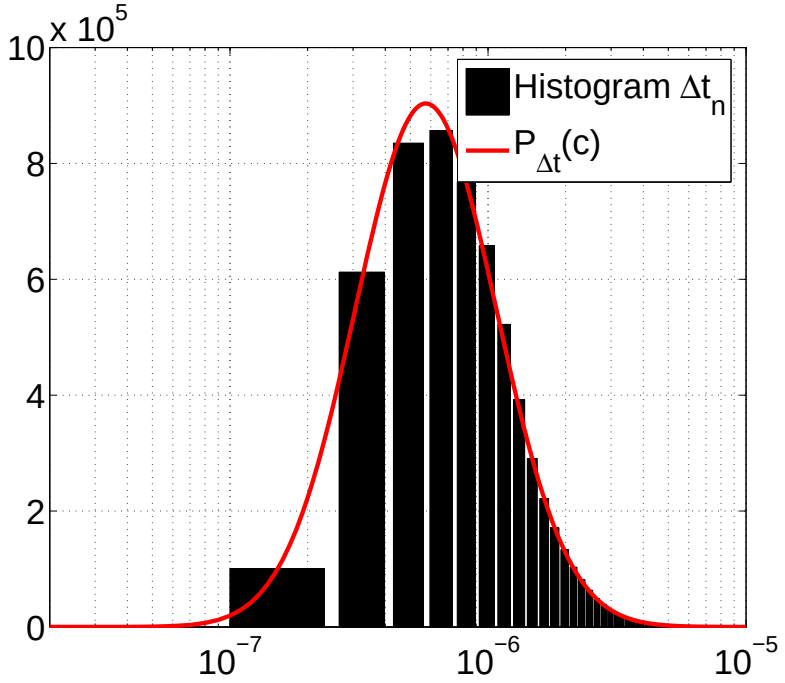


Figure 11.20: Cylinder wake data (from Nobach [96]): Histogram of residence times $\Delta t_n$ and the corresponding lognormal probability density function $P_{\Delta t}(c)$ plotted with a logarithmic variable axis.

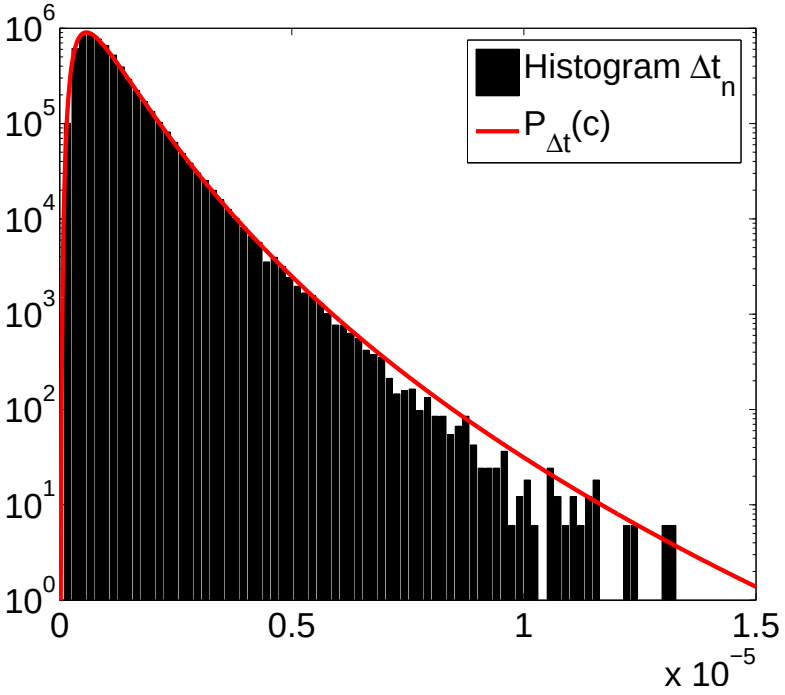


Figure 11.21: Cylinder wake data (from Nobach [96]): Histogram of residence times $\Delta t_n$ and the corresponding lognormal probability density function $P_{\Delta t}(c)$ plotted with a logarithmic frequency axis.

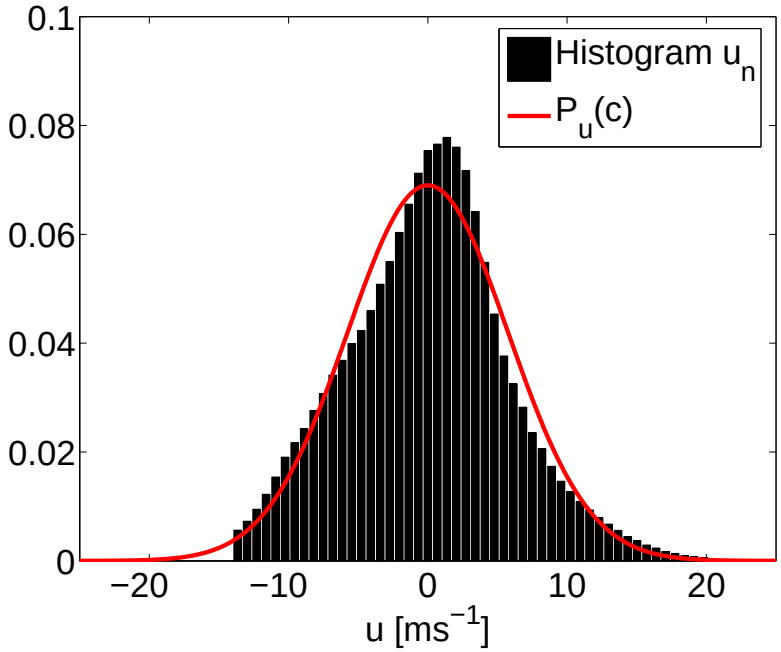


Figure 11.22: Cylinder wake data (from Nobach [96]): Histogram of LDA velocity fluctuations $u_n$ and the corresponding Gaussian probability density function $P_u(c)$.

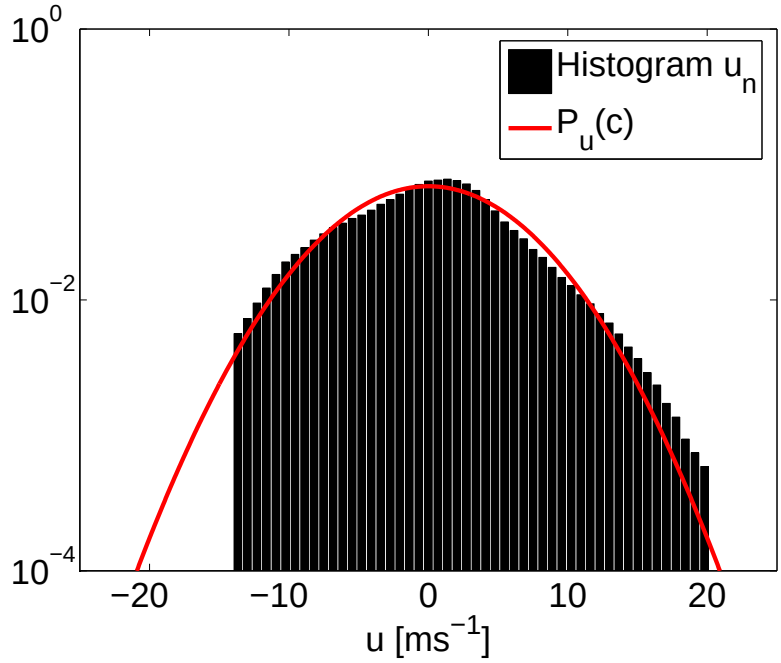


Figure 11.23: Cylinder wake data (from Nobach [96]): Histogram of LDA velocity fluctuations $u_n$ and the corresponding Gaussian probability density function $P_u(c)$. The y-axis is logarithmic to accentuate the discrepancies between the histogram and the pdf.

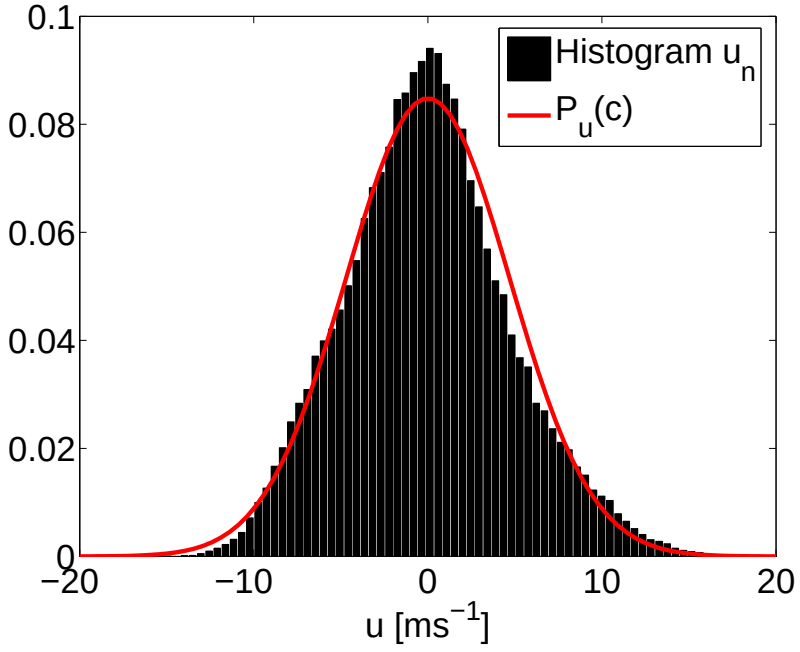


Figure 11.24: Cylinder wake data (from Nobach [96]): Histogram of velocity fluctuations $u_n$ from HWA measurements and the corresponding Gaussian probability density function $P_u(c)$.

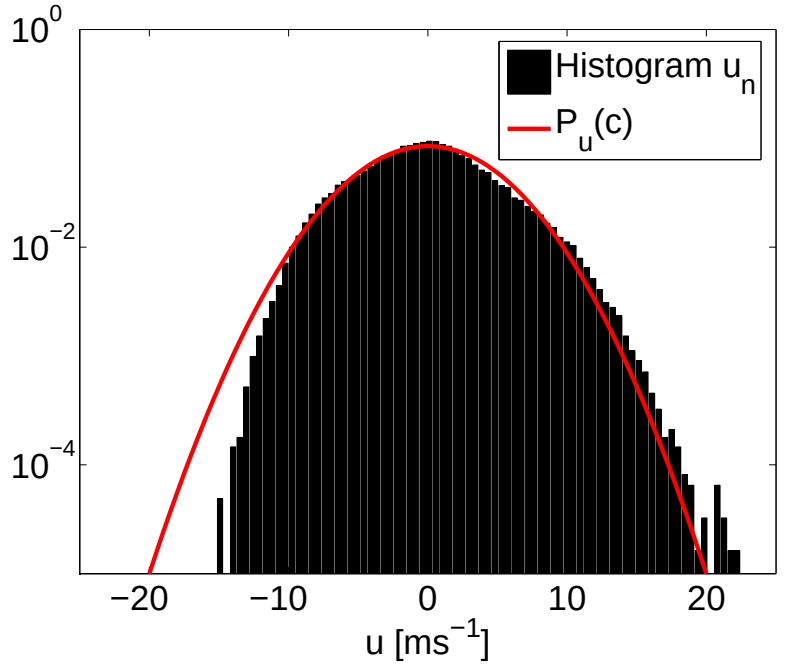


Figure 11.25: Cylinder wake data (from Nobach [96]): Histogram of velocity fluctuations $u_n$ from HWA measurements and the corresponding Gaussian probability density function $P_u(c)$. The y-axis is logarithmic to accentuate the discrepancies between the histogram and the pdf.

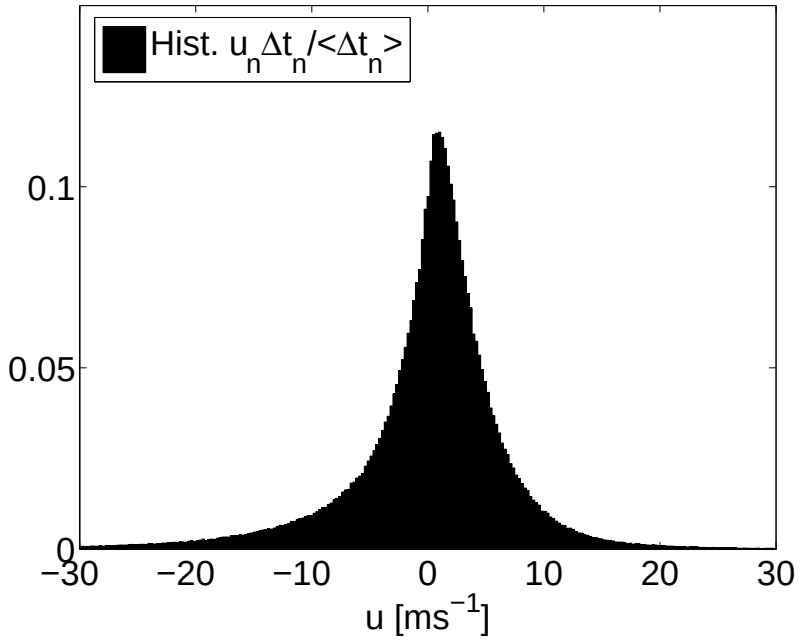


Figure 11.26: Cylinder wake data (from Nobach [96]): Histogram of residence time weighted velocity fluctuations $u_{RTW} = u_n \Delta t_n / < \Delta t_n >$ , where <> indicates ensemble averaging.

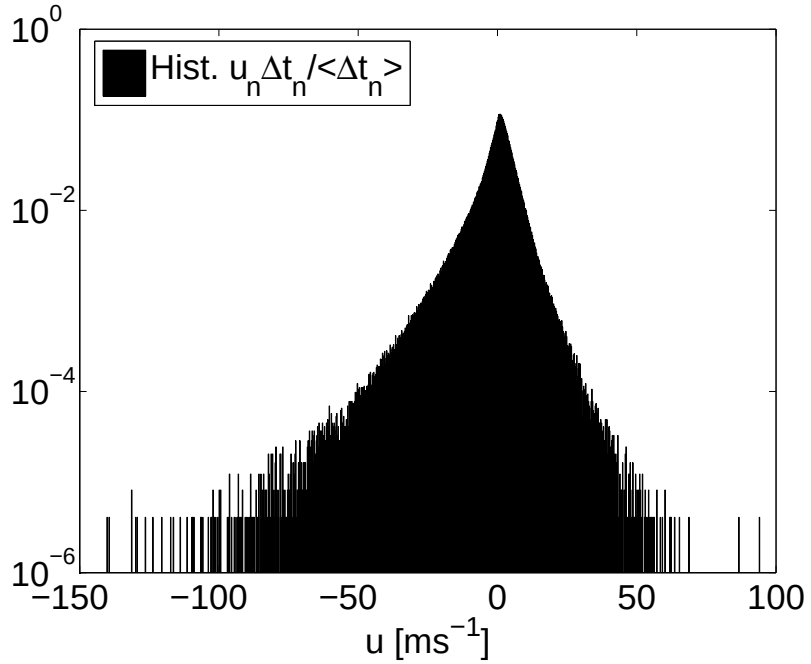


Figure 11.27: Cylinder wake data (from Nobach [96]): Histogram of residence time weighted velocity fluctuations $u_{RTW} = u_n \Delta t_n / < \Delta t_n >$ , where <> indicates ensemble averaging.

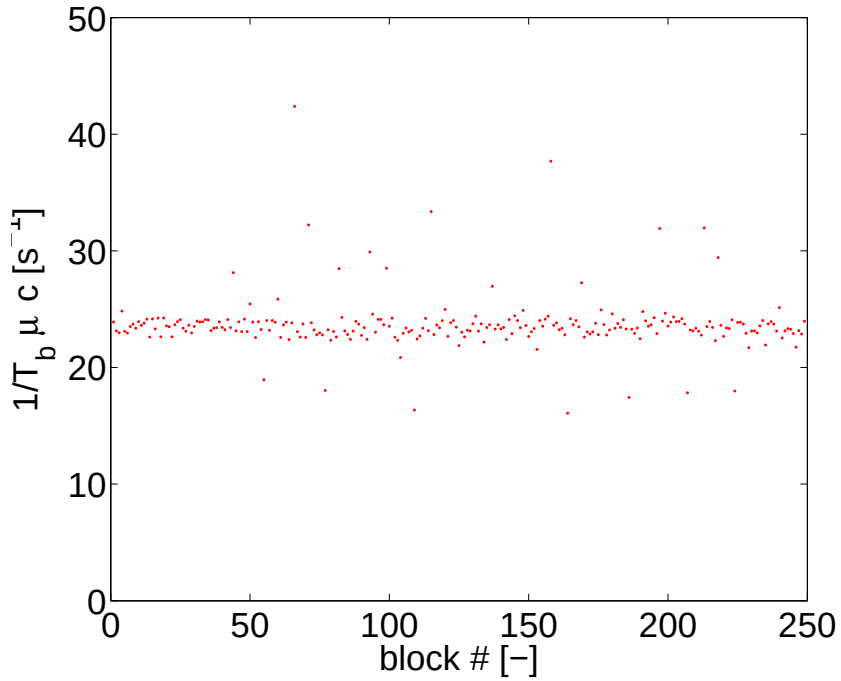


Figure 11.28: Cylinder wake data (from Nobach [96]): Inverse of block lengths shown consecutively for each block. This quantity is proportional to the particle concentration.

## 11.6 Results

For both data sets at hand, the power spectra based on the HWA data are computed using the FFT and the estimator based on residence time weighting (11.19) in order to check that the algorithm is producing the expected result. The burst-mode LDA spectra are then compared to the HWA FFT spectra. For the sake of completion, the error of applying the arithmetic expressions for the moments is also derived and comparisons are made between these estimates.

### 11.6.1 Axisymmetric turbulent far jet

The HWA FFT (Fast Fourier Transform) and HWA RTW (Residence Time Weighting) spectra (11.19) are displayed in a logarithmic plot in figure 11.29. Implementing the HWA data into the RTW algorithm and substituting the residence times by a constant yields a spectrum concurring well with the one obtained using the FFT on the same data set. This is a good check of the correctness of the RTW algorithm. Two versions of the HWA FFT spectrum are presented; one with a shorter record length (black) and one obtained using a substantially longer record length (magenta). Table 11.2 summarizes the parameters used for evaluating the spectra using the various methods. N is the total number of samples, $\mathrm{N}_s$ is the number of samples per block, $\mathrm{N}_b$ the number of blocks, $\mathrm{T}_b$ the record length and $\mathrm{f}_s$ the sampling frequency. $\nu$ is the average data rate for the LDA measurements.

The RTW spectrum is only computed using the shorter record length, since the computations are relatively slow compared to using the FFT. Even so, the spectra collapse nicely in the common frequency range. The leveling out of the shorter record length HWA $\mathrm{FFT}_{\mathrm{short}}$ spectrum at the highest frequencies is due to a windowing effect. The effect of the window is to redistribute energy from the lower frequencies to the higher ones by what is commonly referred to as spectral leakage. If longer block lengths are used, as has been done when computing the HWA $\mathrm{FFT}_{\mathrm{long}}$ spectrum ($T_b = 1.00\ s$), the spectrum rolls off faster than the HWA $\mathrm{FFT}_{\mathrm{short}}$ spectrum ($T_b = 0.10\ s$) at the higher frequencies.

The integral time scale was found from the one-dimensional HWA $\mathrm{FFT}_{\mathrm{long}}$ spectrum, by extrapolating the spectrum to zero frequency, to be about $\mathrm{T}_u = S_{11}(0)/2\overline{u^2} \approx 0.001\,\mathrm{s}$. In order to avoid window effects when performing the Fourier transform, the record length should be much longer than the integral time scale, i.e., $\mathrm{T}_b \gg \mathrm{T}_u$. Since the RTW algorithm is substantially computationally heavier than that of the FFT ($N^2$ versus $N \log_2 N$), it is not practically feasible to compute the HWA RTW spectrum for such long records with the current sampling frequency. The maximum record length of the LDA data time series was limited to about 1.5 s due to the conditions under which the data was acquired. The integral time scale was previously estimated to about 1 ms, which is well below the record length of the blocks.

The difference between the HWA $\mathrm{FFT}_{\mathrm{short}}$ and HWA RTW spectra needs further investigation. The ratio found from the values of the spectra in the high frequency end is $1.27{\cdot}10^{-7}/2.47{\cdot}10^{-8} \approx 5$. Two potentially prominent effects that could contribute to this difference in level of the noise floors were identified; the numerical error propagation due to the difference in number of operations and the difference in word size.

Table 11.2: Axisymmetric turbulent jet data: Parameters used for computing the spectra for the axisymmetric turbulent far jet displayed in figures 11.29 and 11.30.

| | N | $N_s$ | $N_b$ | $T_b$ [s] | $f_s$ / $\nu$ [$s^{-1}$] |
|---|---|---|---|---|---|
| HWA $FFT_{short}$ | 1 000 000 | 4 000 | 250 | 0.10 | 40 000 |
| HWA RTW | 1 000 000 | 4 000 | 250 | 0.10 | 40 000 |
| HWA $FFT_{long}$ | 10 000 000 | 40 000 | 250 | 1.00 | 40 000 |
| LDA $RTW_{\forall\, blocks}$ | 540 907 | 139–575 | 1 620 | 1.00 | 318 |
| LDA $RTW_{reduced}$ | 540 907 | 139–575 | 736 | 1.00 | 318 |

First consider the numerical error propagation due to the difference in number of operations. With 4 000 points per block, the FFT requires $4\,000 \log_2 4\,000 = 47\,900$ operations in contrast to the RTW algorithm, which requires $4\,000^2 = 16 \cdot 10^6$ operations. Assuming that the accumulated numerical (round-off) error propagates to be a random walk process, the expected mean square error after N steps is of the order of N (i.e., rms $\propto \sqrt{N}$). This mean square 'noise' should be spread evenly over the frequency band (i.e., white). The numerical errors of the FFT and RTW algorithm should thus relate as follows:

$$\frac{4\,000^2}{4\,000 \log_2 4\,000} \approx 330 \tag{11.44}$$

The corresponding ratio found from the values of the spectra in the high frequency end is significantly lower.

Second, the impact of different word sizes to the spectra. The HWA FFT spectrum was computed using Matlab, which employs double precision (64 bits), while the HWA RTW spectrum was computed in Fortran 90, which as default applies single precision (32 bits) unless otherwise specified. The second moment of the noise can be determined from the pdf of the minimum step size $\Delta$. For the pdf $p_\Delta(c)$ to integrate to unity in the interval $-\Delta/2 \le c \le \Delta/2$, it should be defined as

$$p_\Delta(c) = \begin{cases} 1/\Delta, & -\Delta/2 \le c \le \Delta/2 \\ 0, & |c| > \Delta/2 \end{cases} \tag{11.45}$$

where the second moment of the random noise is given by

$$\overline{n^2} = \int_{-\infty}^{\infty} c^2 p_\Delta(c)\, dc = \frac{1}{\Delta} \int_{-\Delta/2}^{\Delta/2} c^2\, dc = \frac{1}{\Delta} \left[ \frac{c^3}{3} \right]_{-\Delta/2}^{\Delta/2} = \frac{\Delta^2}{12}. \tag{11.46}$$

Thus the noise floor for a bandwidth limited (sampling rate $f_s$) spectrum is given by

$$\frac{\overline{n^2}}{f_s} = \frac{\Delta^2}{12 f_s}. \tag{11.47}$$

Since the spectra are computed from the same data set, $f_s$ does not change.

The ratio between the noise floors is thus;

$$\frac{\overline{n^2_{\mathrm{RTW}}}}{\overline{n^2_{\mathrm{FFT}}}} = \frac{\Delta^2_{RTW}}{\Delta^2_{FFT}} \approx 5. \tag{11.48}$$

Using this to relate the smallest significant number $\Delta$ for the respective algorithms

$$\Delta_{RTW} \approx 2.2\Delta_{FFT} \tag{11.49}$$

it becomes apparent that the difference is quite small. A closer look at the data going into and coming out of the respective algorithms reveals that the data read in from the binary files from which the measurement data is originally stored is single precision. From these binary files, the data is read in using Matlab, which decodes the data to double precision, meaning that the remaining part of the mantissa is supplemented with noise.

Single precision is represented by a mantissa (significand) of 24 bits (implicit) of which one is used to store the sign of the number. When one of the bits is used to store the sign, the number of decimal digits that can be represented by single precision is $\log_{10} 2^{23} \approx 6.9$. A possible explanation to the discrepancy of $\Delta_{RTW}$ and $\Delta_{FFT}$ is that the measurement data in the original files was stored using 24 bits, where no bit was occupied to store the sign since time always is assigned a positive value. Fortran 90 uses a precision of 24 bits, but since the sign is vital for programming purposes the decimal digits in the mantissa are only represented by 23 bits. Thus, $\Delta_{RTW} = 2^{-23}$ and $\Delta_{FFT} = 2^{-24}$; yielding $\Delta_{RTW}/\Delta_{FFT} = 2$ which is quite close to the constant obtained in (11.49). Since the bit range of the data/algorithms can explain almost all of the contribution to this ratio in noise levels, the contribution to the error associated with each operation must be much smaller, and can hence be considered more or less insignificant in this context.

The LDA RTW spectrum using this pre-defined block length of 1.0 s yielded the spectral estimator shown in figure 11.30. Apart from the substantially higher noise floor, the LDA RTW spectrum displays peaks that seem to be reoccurring, not unlike aliasing. This was not expected given that the data were effectively randomly sampled. Clearly there was something missing in our understanding.

The mean velocity for each block for a block length of 2.0 s is shown in figure 11.31. It is seen that the mean velocity variations between the blocks is quite high. The variability of the mean velocity

$$\varepsilon^2_U = \frac{1}{N}\frac{\mathrm{var}\{u\}}{U^2} = \frac{1}{2\cdot 10^5}\frac{34}{22^2} \approx 0.35\cdot 10^{-6} \tag{11.50}$$

yielding $\varepsilon_U \approx 0.6\cdot 10^{-3}$, which is substantially smaller than the variations seen in figure 11.30. This indicates that the fan might not produce a very stable flow. Even more interesting, however, is the sudden jump of the curve at about block number 1100. Similar jumps in the flow characteristics are seen in the very first blocks as well as around block number 450. This is likely caused by variations in the performance of the fan powering the jet. Hence, the mean value of the velocity which was obtained from the data has a bias error coupled to these sudden changes. These variations in the mean velocity across the

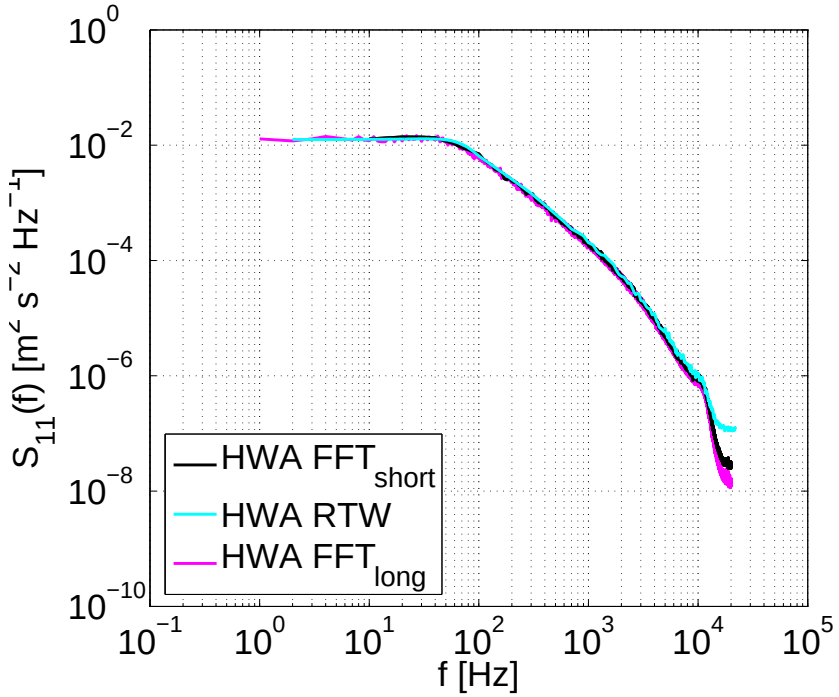


Figure 11.29: Axisymmetric turbulent jet: Frequency spectrum computed from the HWA data using the FFT with a shorter block length (black) and the estimator based on residence time weighting RTW (11.20) (light blue) as well as the HWA FFT spectrum obtained using a substantially longer record length (magenta).

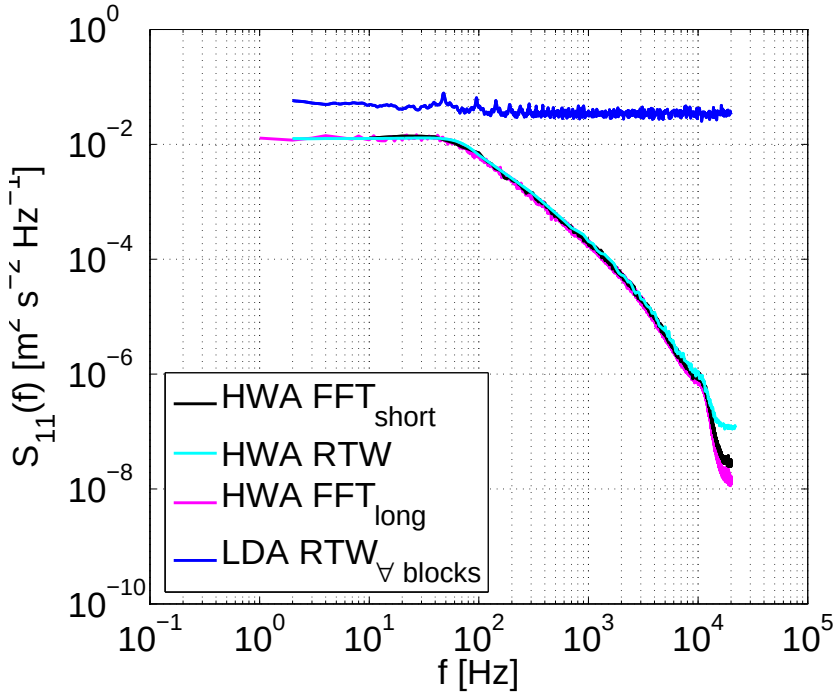


Figure 11.30: Axisymmetric turbulent jet: The same frequency spectra as in figure 11.29 as well as the burst-mode spectrum obtained from the LDA data using residence time weighting (blue).

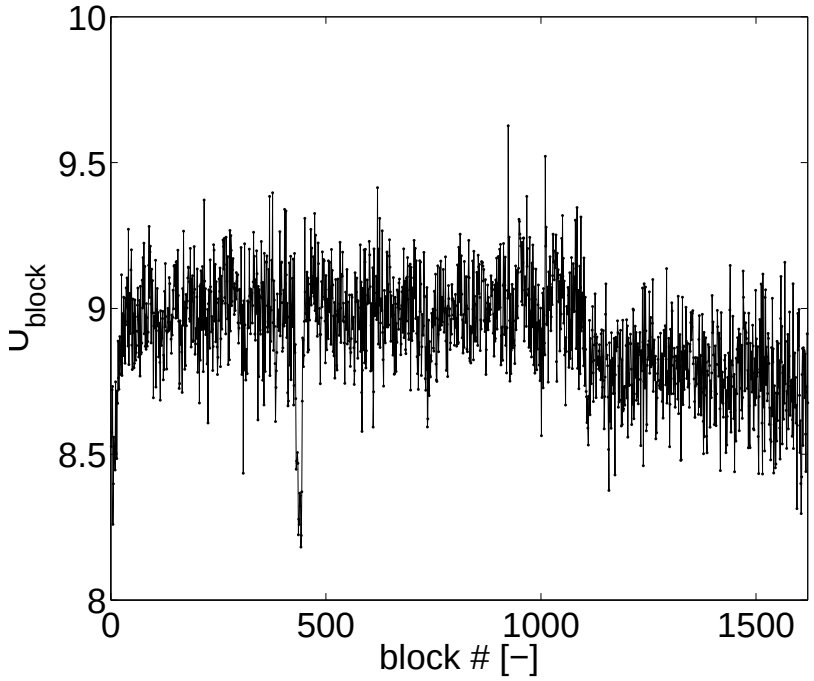


Figure 11.31: Axisymmetric turbulent jet: Variation in mean velocity as a function of block number. In the present case $T_b$ =2.0 s.

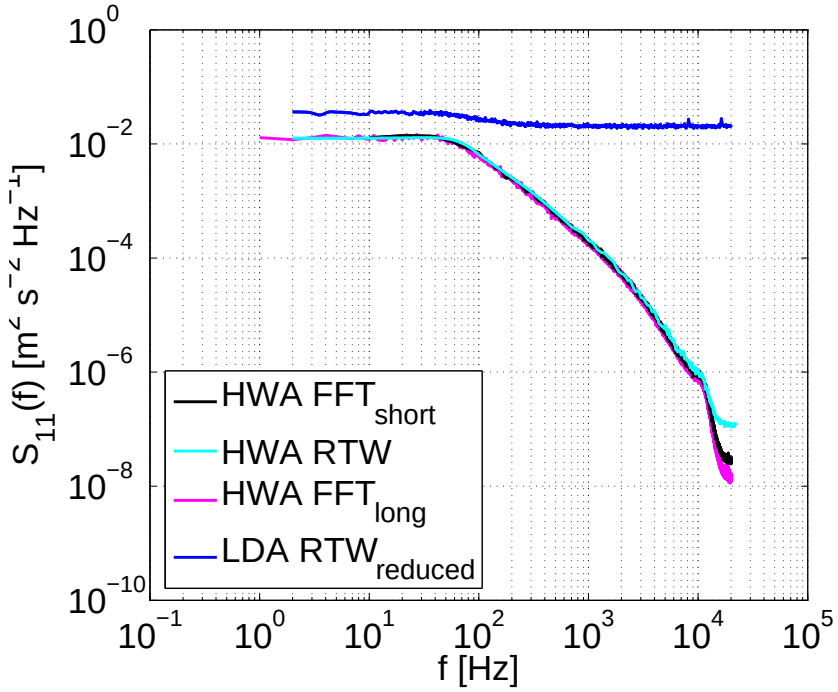


Figure 11.32: Axisymmetric turbulent jet: This figure displays the same spectra as in figure 11.30 with the exception that the burst-mode LDA RTW spectrum has been reduced to only include blocks whose mean velocity lie in the range of 20% of the mean value of the mean velocities obtained up to block number 1100 as seen in figure 11.31.

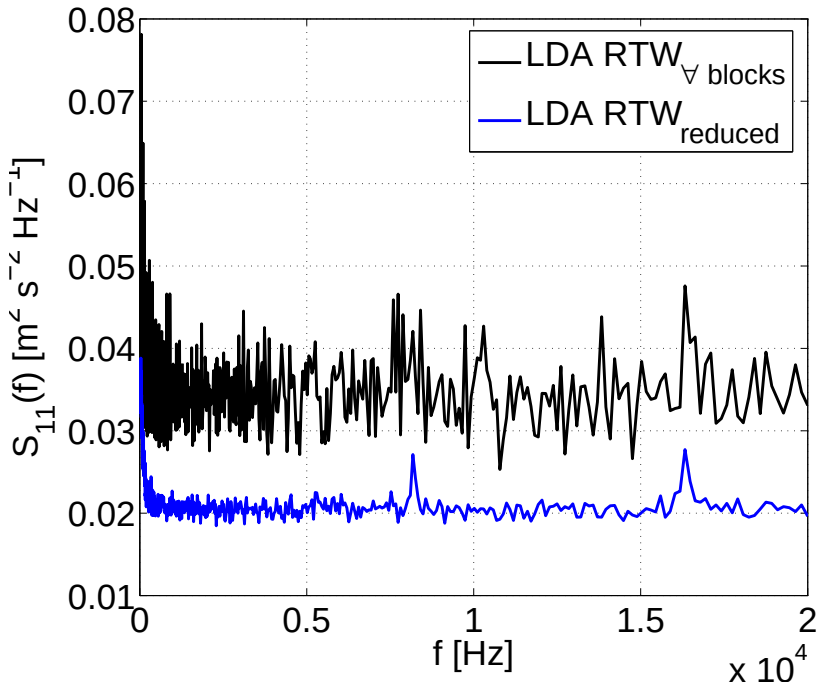


Figure 11.33: Axisymmetric turbulent jet: The burst-mode LDA spectra from figures 11.30 and 11.32 displayed on a linear plot to accentuate the impact of reducing the blocks with a significantly deviating mean value.

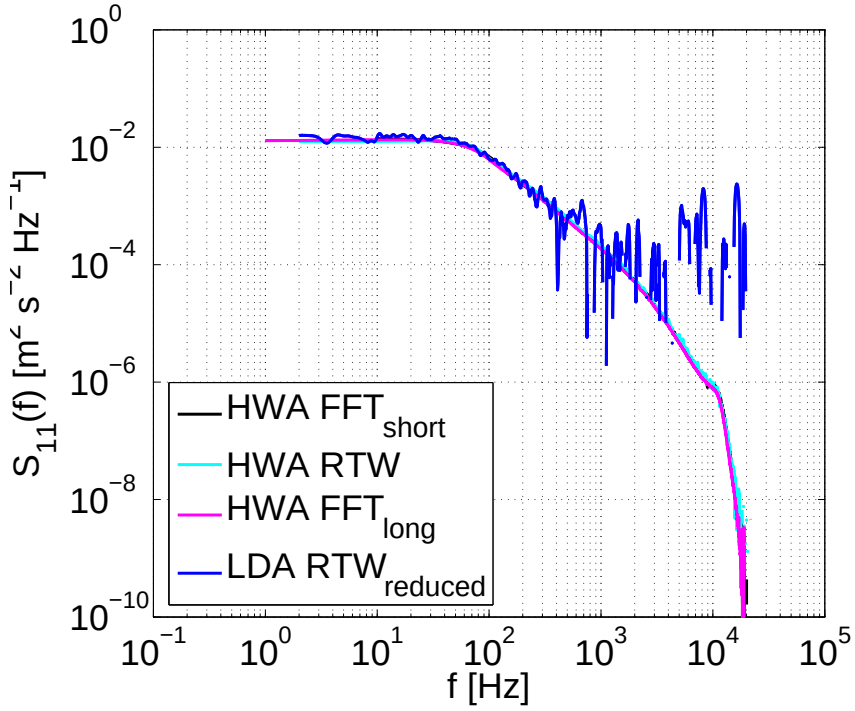


Figure 11.34: Axisymmetric turbulent jet: The spectra from figure 11.32 corrected for the intermittent noise.

block number will thus yield larger fluctuations over more or less the entire range, since the wrong mean is subtracted off. As can be understood simply by looking at the expression for the spectral estimator (11.20), this will yield both an overprediction of the spectrum as well as increased variability. Therefore, let us only include the blocks that have a mean value which does not deviate more than 20% from the mean value of the mean velocities obtained up to block number 1100. The result is shown in figure 11.32, which displays a spectrum which is more well behaved than the previous one in the sense that is has lower variability and noise floor, even though the amount of blocks used is significantly lower. This does, however, not take care of all of the reoccurring peaks. The cleaned up LDA RTW spectrum displays two peaks at frequencies of about 8 and 16 kHz. For a uniformly sampled signal, one would probably recognize this behavior as a result of aliasing. Both of these LDA RTW spectra are for comparison also plotted on a linear scale in figure 11.33. The effect of record length was investigated in a parametric study later on in section 11.6.3 (figure 11.43), confirming that this is not an effect of the finite window.

The main argument for applying random sampling in signal processing is to obtain an alias-free digital signal; see, e.g., [12, 82, 83, 84, 85]. What was not described in the earlier work on developing the theory for the spectral estimator [45, 46] and initially not considered in the present work, was that the application of random sampling does not exclude aliases completely for finite records, but merely reduces it [13]. For a further discussion on these matters, see section 11.6.3.

Figure 11.34 displays the same spectra as in figure 11.32 corrected for the random noise impact. Due to the aliasing, the spectrum is not resolved at frequencies beyond about 4 kHz and further, the collapse of the noise corrected LDA $\mathrm{RTW}_{\mathrm{reduced}}$ and HWA spectra is worsened by the high variability of the estimate.

### 11.6.2 Cylinder wake

In the same fashion as for the previous case, the HWA FFT and HWA RTW spectra are compared in figure 11.35. As expected, since they have the same block length and number of blocks, the HWA $\mathrm{FFT}_{\mathrm{short}}$ and HWA RTW spectra agree well, showing an almost perfect collapse even at the highest frequencies. In this case, the range of the data is small enough for the word size of the data not to impact the resulting spectrum. This supports the previous discussion that the RTW algorithm in itself does not introduce significantly more white noise due to the larger number of operations. Comparing the HWA $\mathrm{FFT}_{\mathrm{short}}$ and HWA RTW estimates with the HWA $\mathrm{FFT}_{\mathrm{long}}$ spectrum, which has a four times longer block length, the latter one rolls off faster. This can again be explained by the windowing effect, which is reduced by the longer blocks. The parameters used for evaluating the spectra are displayed in table 11.3. N is the total number of samples, $\mathrm{N}_s$ is the number of samples per block, $\mathrm{N}_b$ the number of blocks, $\mathrm{T}_b$ the record length and $\mathrm{f}_s$ the sampling frequency. $\nu$ is the average data rate for the LDA measurements. The sampling frequency of the HWA data, $\mathrm{f}_s = 100\,000\,\mathrm{Hz}$, and the average sampling rate of the LDA measurements, $\nu = 93\,944\,\mathrm{Hz}$, are of the same order of magnitude.

For this measurement campaign, the record lengths were relatively short. This is problematic in the sense that one is more limited to how well converged

Table 11.3: Parameters used for computing the spectra for the cylinder wake flow displayed in figures 11.35 and 11.36.

| | N | $N_s$ | $N_b$ | $T_b$ [s] | $f_s$ / $\nu$ [$s^{-1}$] |
|---|---|---|---|---|---|
| HWA $FFT_{short}$ | 131 072 | 1 024 | 128 | 0.01 | 100 000 |
| HWA RTW | 131 072 | 1 024 | 128 | 0.01 | 100 000 |
| HWA $FFT_{long}$ | 131 072 | 4 096 | 32 | 0.04 | 100 000 |
| LDA RTW | 995 775 | 1–2 738 | 1 060 | 0.01 | 93 944 |

spectra one can obtain which also capture the lowest frequencies, since the number of blocks and the block lengths are limited by the record length. The solution is hence to find a tradeoff between block length and number of blocks that gives a satisfactory result for the sought for information.

Figure 11.36 displays the same spectral estimates as the previous figure with the addition of the LDA RTW spectrum, which is shifted to higher values than the HWA spectra. This is expected, since the LDA and HWA data of this data set were acquired in flows of slightly different free stream velocities and therefore should integrate to different energies. Further, the noise floor resulting from the random noise is higher for the LDA measurements due to the intermittency of the measured signal. But the peak shows up at exactly the same frequency. This was not expected for a shedding peak whose frequency varies with the free stream velocity according to:

$$f_{\text{shedding}} = \frac{S_r U}{d} \tag{11.51}$$

where $f_{shedding}$ is the shedding frequency, $S_r$ the Strouhal number, U the free stream velocity and d the cylinder diameter. If the observed frequency is due to vortex shedding, the expected shedding frequency should be $f_{shedding} = 617\,Hz$ for the HWA measurements and $f_{shedding} = 717\,Hz$ for the LDA measurements. Thus the difference between the peaks for the HWA and LDA spectra should be clearly visible in the plot, which they are not. Both observed peaks are found at a frequency of 1 kHz.

In order to remove the effect of the different free stream velocities of the HWA and LDA data sets, the wavenumber spectra were compared, see figure 11.37. Assuming that Taylor's frozen field hypothesis is applicable to the flow, the temporal and spatial spectra are related as follows

$$F_{11}^1(k) = \frac{U}{2\pi} S_{11}\left(\frac{k_1 U}{2\pi}\right), \qquad k_1 = \frac{2\pi f}{U} \tag{11.52}$$

where $F_{11}^1(k)$ is the wavenumber spectrum, U is the free stream velocity and $k_1$ is the wavenumber. The wavenumber is independent of the free stream velocity; $k = 2\pi f/U = 2\pi/\lambda$, $f = U/\lambda$. Since the difference in free stream velocity between the HWA and LDA measurements is small, this action should yield comparable spectra. If the peak was truly the results of a convected disturbance, the peaks for the two measurements should line up in the wavenumber spectrum. This is clearly not the case. Hence, the disturbance must be temporal, as was already suspected from the discussion on the different Strouhal numbers.

However, the flow corresponding to the spectra have different energies and therefore obviously the spectra should not integrate to the same value. The expression for drag on a cylinder, yielding a measure of the loss in energy in the flow due to the presence of the cylinder, is commonly normalized by the energy to obtain the drag coefficient

$$C_D = \frac{F_D}{\frac{1}{2}\rho U^2 A} \tag{11.53}$$

which is only very weakly dependent on the Reynolds number for $\mathrm{Re} \sim 10\,000$ (see; e.g., Batchelor [7]). In order to obtain spectra that integrate to the same energy, the wavenumber spectra were normalized with respect to energy. In common practice, one would normalize by the turbulence intensity and the integral length scale. But since the turbulence intensity is at most weakly dependent of the Reynolds number and therefore can be considered to be nearly constant once the flow is fully turbulent ($\overline{u^2}/U^2 \approx$ constant) [40], the square of the free stream velocity can be used instead. Further, the HWA and LDA measurements were performed in the same position and the integral length scale is only weakly dependent on the Reynolds number [40]. Since the geometry is fixed and all other length scales are approximately proportional, one might just as well use the cylinder diameter d for normalization. Hence, the similarity scaling for low wavenumbers (energy variables) can be normalized by the factor $\mathrm{u^2L} \sim \mathrm{U^2d}$ [64]. These turbulent contributions to the spectrum should thus collapse by this normalization, removing the effect of different energies due to different free stream velocities at the large, convective scales. The wavenumber spectrum normalized by the square of the free stream velocity times the cylinder diameter is displayed in figure 11.38, showing good concurrence for the large, convective scales. Aside from the unexplained peak, the wavenumber spectra show a better collapse after the energy normalization since the similar flows have approximately the same energy distribution across frequency. This is even more prominent for the noise corrected normalized wavenumber spectra in figure 11.39. The mean velocity of each block shown in figure 11.40 displays much more stable variations over time than the axisymmetric jet data.

The measurements were executed at a distance of 26 mm downstream of a cylinder of diameter 6 mm, spanning the width of the test section of 300 mm. Since the position of the measurements was very close to the cylinder, it is highly probable that the measurement probes are situated inside the separated vortex shedding region of the cylinder wake, yielding a time dependent flow which is not a pure convected disturbance. If so, Taylor's frozen field hypothesis would not apply in this case. This could be one reason why the peaks in the normalized wavenumber spectra for the HWA and LDA data sets do not coincide. But this can be ruled out by the non-constancy of the Strouhal numbers, as noted above. Clearly, an explanation for the peak must be sought elsewhere.

If one instead normalizes the frequency spectra using the same arguments as for the wavenumber spectra in figure 11.38, a nice collapse of the curves is obtained. The frequency of the peak is the same for both free stream velocities, indicating that the source of the emergence of the peak is not flow driven. Let's investigate the alternative of the flow being affected by vibrations of the cylinder.

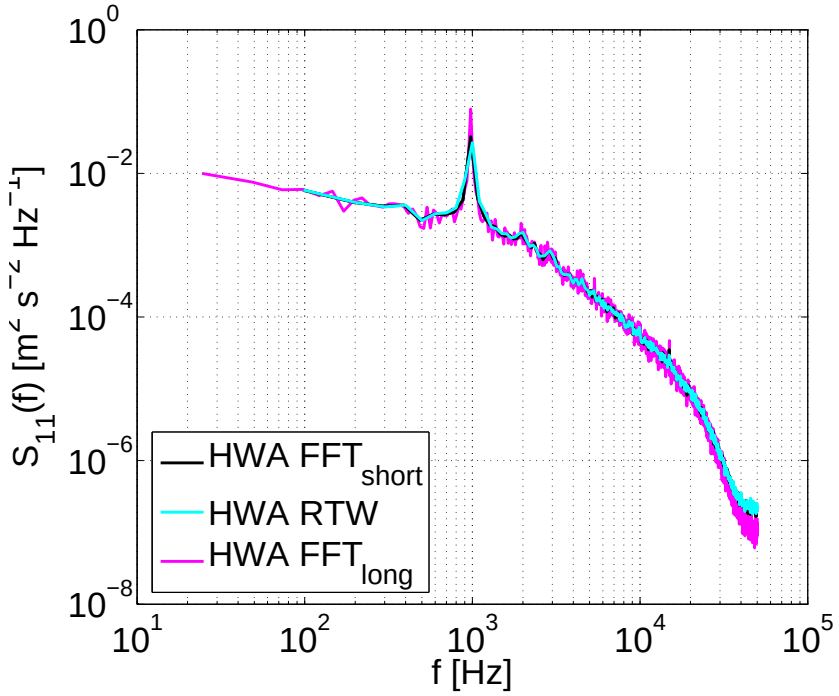


Figure 11.35: Cylinder wake: Frequency spectra computed from the HWA data using the FFT with a shorter block length (black) and the estimator based on residence time weighting RTW (11.20) (light blue) as well as the HWA FFT spectrum obtained using a substantially longer record length (magenta).

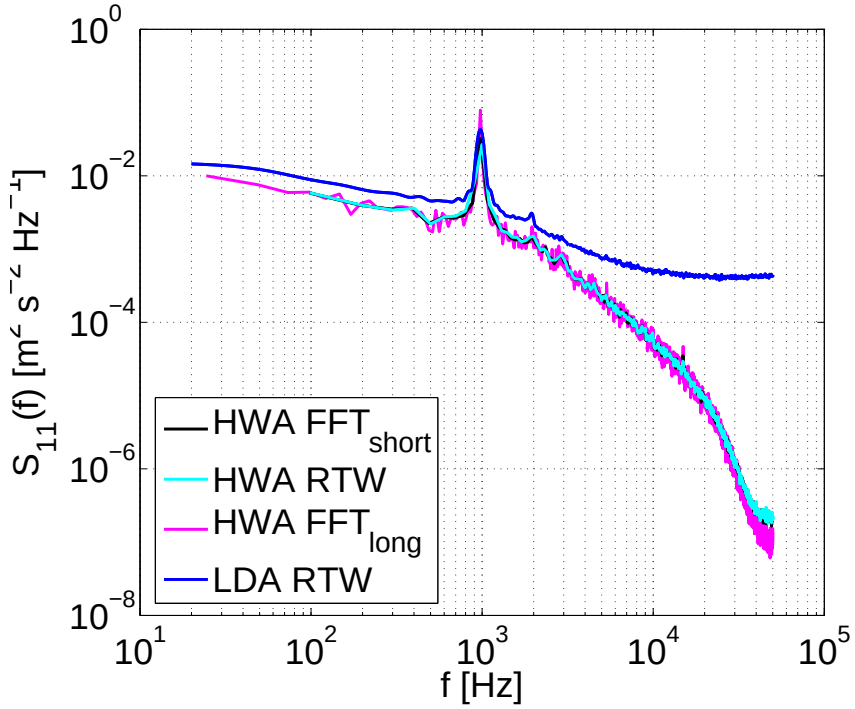


Figure 11.36: Cylinder wake: HWA power spectra shown in the previous figure compared to the RTW LDA spectrum (dark blue).

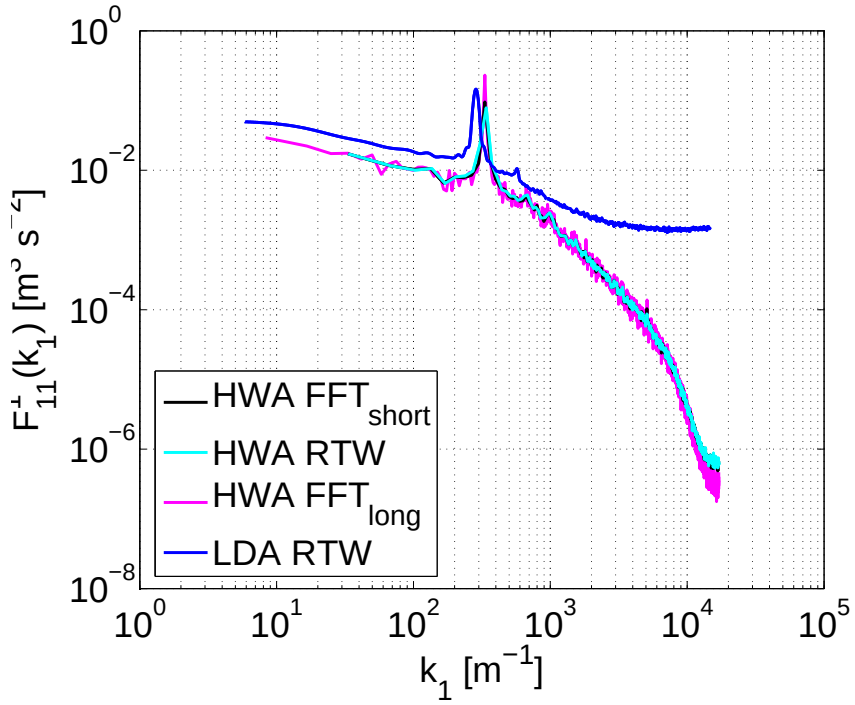


Figure 11.37: Cylinder wake: Normalized wavenumber spectra computed from the HWA data using the FFT with a shorter block length (black) and the estimator based on residence time weighting RTW (11.20) (light blue) as well as the HWA FFT spectrum obtained using a substantially longer record length (magenta).

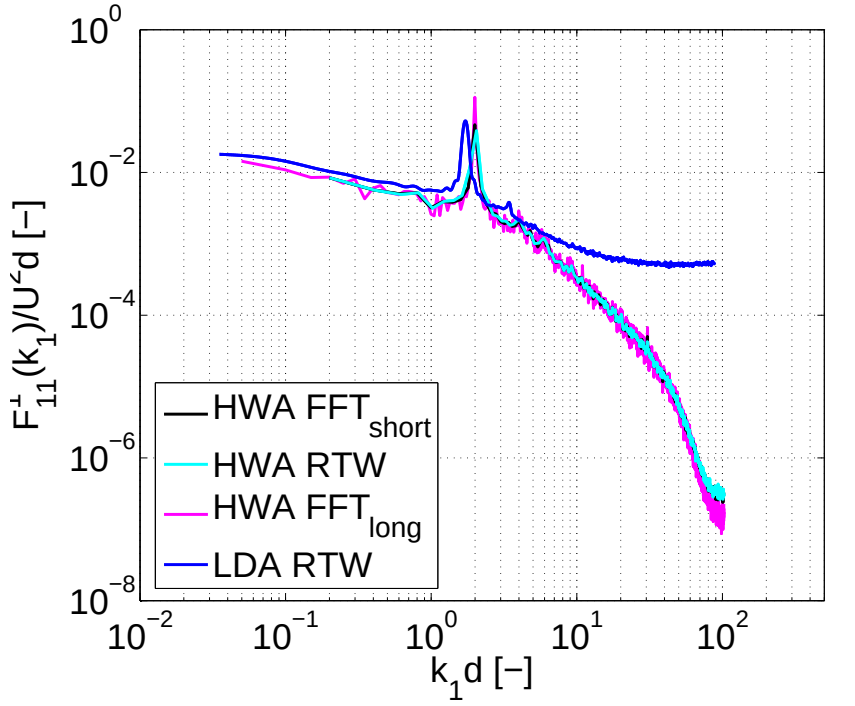


Figure 11.38: Cylinder wake: Normalized wavenumber spectra computed from the HWA data using the FFT with a shorter block length (black) and the estimator based on residence time weighting RTW (11.20) (light blue) as well as the HWA FFT spectrum obtained using a substantially longer record length (magenta).

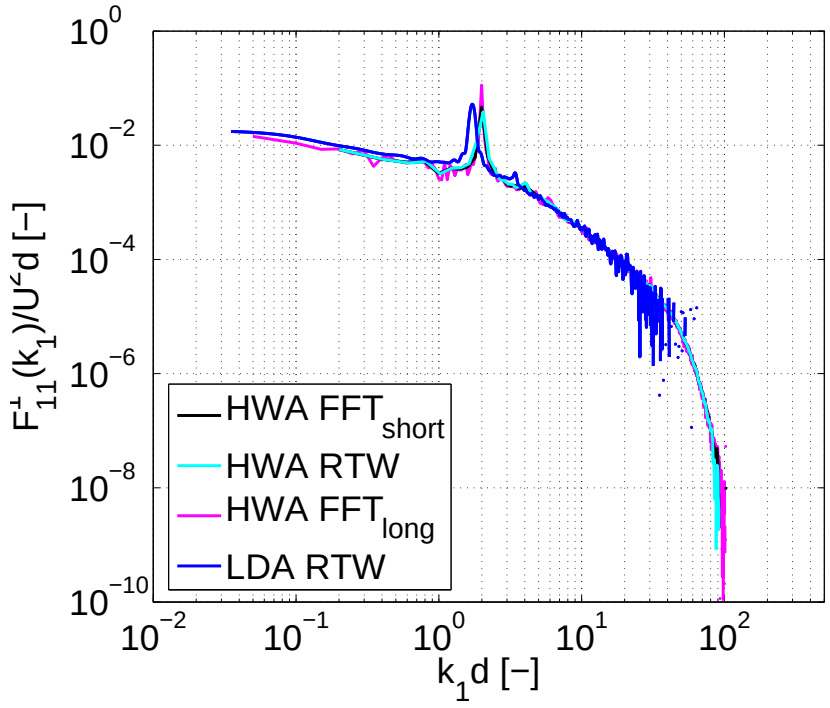


Figure 11.39: Cylinder wake: Normalized random noise corrected wavenumber spectra computed from the HWA data using the FFT with a shorter block length (black) and the estimator based on residence time weighting RTW (11.20) (light blue) as well as the HWA FFT spectrum obtained using a substantially longer record length (magenta).

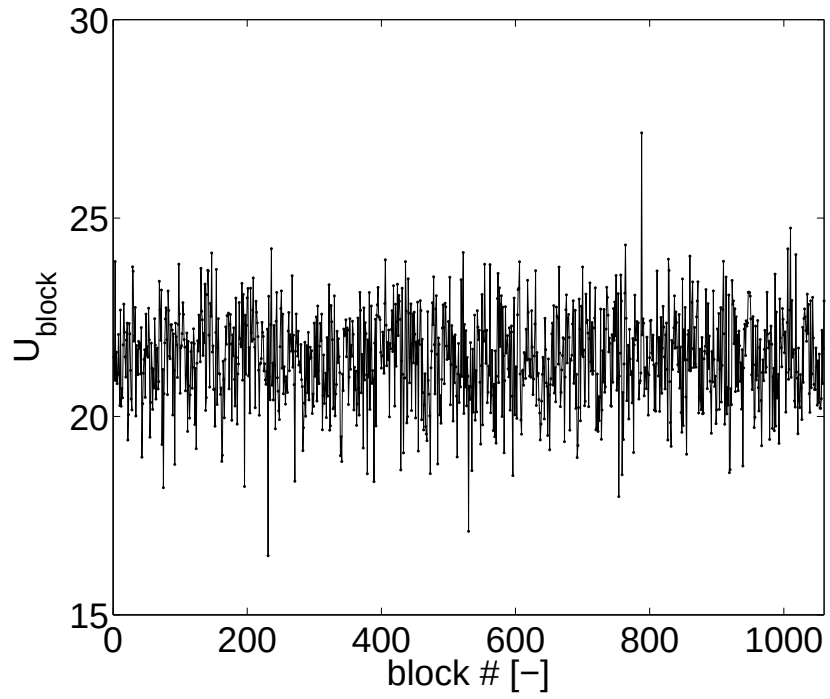


Figure 11.40: Cylinder wake: Variation in mean velocity as a function of block number.

The eigenfrequency $f_{eig.}$ for a rod is given by the following relation,

$$f_{\text{eig.}} = k\sqrt{\frac{EI}{mL^4}} \tag{11.54}$$

where E is the elasticity module, I is the moment of inertia, m is the mass of the rod and L is the rod length. k is a coefficient that depends on the support of the ends of the rod. It is known that the rod is solid and made out of some kind of common metal, most probably iron or aluminum. Hence, the elasticity module and mass can be guessed. The only remaining unknown is the support of the ends of the rod. If the ends of the rod are firmly fixed in their positions or alternatively free, there are no matching eigenfrequencies for aluminum or iron. However, for semi-fixed ends the eigenfrequency of the second mode for both iron and aluminum is very close to 1 kHz. This explains the appearance of the peak as an effect of the eigenfrequency of the rod. The reason why the first mode ($f_{eig.} \approx 250\,\text{Hz}$) is not seen in the spectra might be that the frequency of the second mode is closer to the shedding frequency of the cylinder wake ($f_{shedding} = 667\,\text{Hz}$), reinforcing and energizing the second mode.

As expected, the LDA spectra generally have a higher noise floor than HWA spectra, due to the intermittency of the sampled signal. Applying a Savitzky-Golay filter and implementing the noise reduction technique to the LDA RTW spectrum results in the LDA RTW spectrum shown in figure 11.42. The high relative error at the highest frequencies is due to the relatively few blocks. This was expected since the variability of the spectral estimator for randomly sampled data increases as the spectrum itself decreases. Nonetheless the results do suggest that the algorithms could have produced the correct spectral values had sufficient data been acquired.

Since the peaks are temporal disturbances and the spectrum (turbulence) is convective, the turbulence can only be compared between the two data sets of different free stream velocities in wavenumber space. In contrast, for temporal disturbances, like the peak in the present case, comparison can only be justified in frequency space. Therefore, it is not possible to make a transformation to compare both the turbulence and the peak in the same plot.

### 11.6.3 Appearance of spikes in the power spectra

As noted above, a somewhat surprising discovery is the emergence of periodically occurring peaks in the burst-mode LDA spectra. Figure 11.43 shows the spectra from the axisymmetric jet data computed for different record lengths; $T_b = 1.0\,\text{s}$, 1.5 s and 2.0 s. All spectra show distinct peaks at frequencies $f = 0.8{\cdot}10^4$ and $1.6{\cdot}10^4$. Further, figure 11.44 shows how the spectra from the axisymmetric jet data behave when varying the average data rate. This was done by excluding intermediate measurement points when computing the spectra. Since the variability of the spectra increases with the decreased number of blocks obtained from the reduced data sets, it is hard to distinguish any spikes from the noise.

In the spectra derived from the cylinder wake data, the periodically occurring peaks appear with a much larger spacing in frequency. The first peak occurs at a relatively high frequency where all turbulence has dissipated. The spectrum has been estimated for three record lengths; 10, 9 and 8 ms, see figure

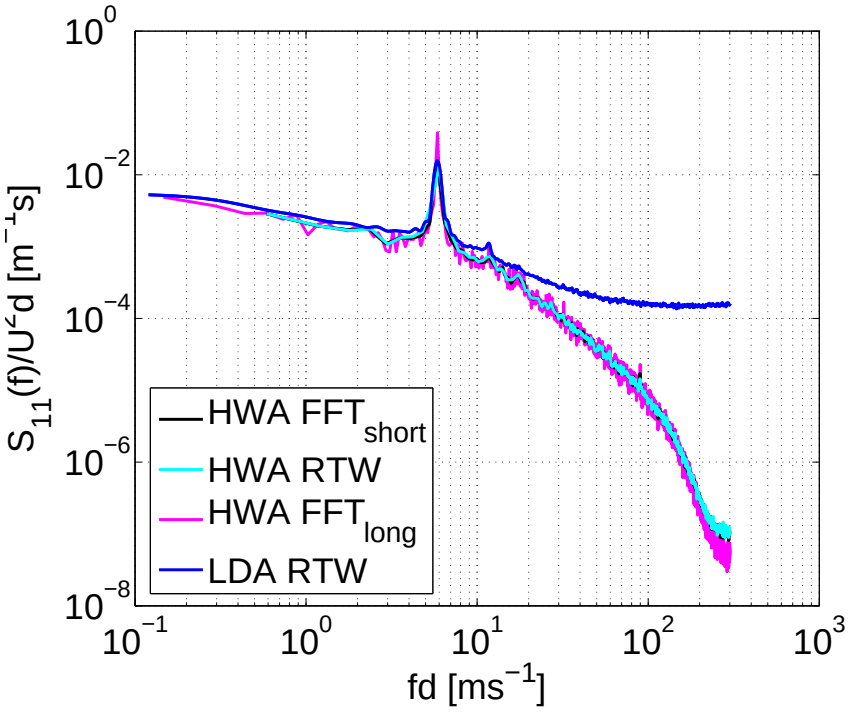


Figure 11.41: Cylinder wake: Logarithmic plot showing the normalized wavenumber spectra computed from the HWA data using the FFT with a shorter block length (black) and the estimator based on residence time weighting RTW (11.20) (light blue) as well as the HWA FFT spectrum obtained using a substantially longer record length (magenta).

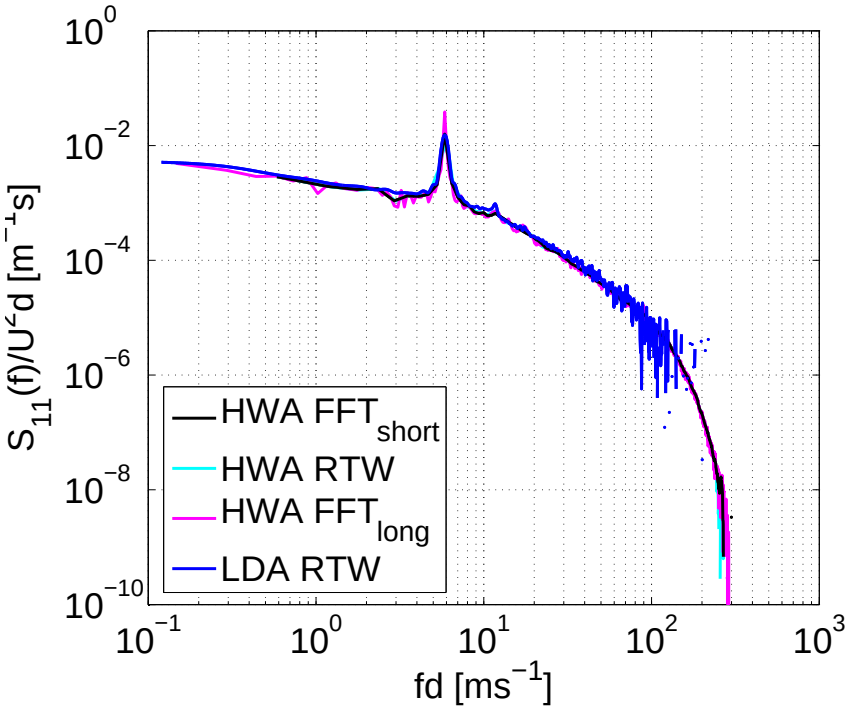


Figure 11.42: Cylinder wake: Logarithmic plot showing the random noise corrected normalized wavenumber spectra computed from the HWA data using the FFT with a shorter block length (black) and the estimator based on residence time weighting RTW (11.20) (light blue) as well as the HWA FFT spectrum obtained using a substantially longer record length (magenta).

11.48. Except for the peak appearing at f = 0.3 MHz in the 10 ms record length spectrum, the first harmonic appears at f = 0.75 MHz in all spectra. For the 10 and 9 ms spectra, the second and third harmonics are clearly visible at f = 1.50 and 2.25 MHz, but these are not seen in the 8 ms spectrum. In addition, peaks occur more or less symmetrically around these harmonics, probably stemming from the peak resolved only in the 10 ms spectrum at f = 0.3 MHz. By examining the peaks more carefully, it is clear that they are always spaced 0.3 MHz away from any main harmonic or one of its own harmonics. At this point, it is unclear why the additional peak(s) appear. For this data set, the data were quite limited in terms of record length even before reducing the data; therefore, no parametric study of varying the data rate could be conducted.

The periodicity of the peaks is reminiscent of harmonics or aliasing effects. This alternative was at first not considered, since the assumption of random sampling supposedly would kill all aliasing effects [46]. This assumption was, in turn, based on the assumption that the fluid is incompressible [43]. It had not been considered how the particles responded to changes in the flow in general and the compressibility of the particle distribution in particular. Even if the flow can be considered to be incompressible, it does not mean that the same assumption can be made about the particle distribution. Recent work in the field has revealed that particles in turbulent flows can redistribute as a consequence of the vortices present in the flow, see Collins and Keswani [22]. If the density of the particles is significantly different to that of the surrounding fluid, the pressure distribution resulting from the presence of the vortices will redistribute and inhomogenize an initially homogeneous particle distribution. If the particles are lighter than the surrounding fluid, they will gather up in the centers of the vortex cores, whereas if the particles are heavier they will most probably cluster up at the edges of the vortex cores in between vortices. The appearance of particle clustering can be compared to the patterns seen at the bottom of swimming pools, where the changes in refractive index of the water gives rise to dark and bright patterns when light hits the water surface. Particles are believed to cluster in similar "streaks", spanning widths much larger than their thickness. If particle clustering does occur at the outset so the initial particle distribution is not truly random, this violates the assumption of random sampling of LDA measurements since the sampling process is no longer independent of the process being sampled. But even if the particles were randomly distributed initially, clustering complicates the interpretation of the measurements as Eulerian velocities, since the particles would not be following the flow. In other words, the residence-time weighted measurements would correctly produce the volume-averaged particle velocity, but not the Eulerian velocity that is generally sought. If the process is not additive and random (i.e., all parts of any input signal are sampled with equal and constant probability) the spectra display signs of aliasing in the spectrum. Further, variations in the seeding density over time, which are typical for LDA measurements, contribute to the added uncertainty of the sampling process being random and additive since the statistical properties are changing with time.

An alternative explanation comes from the field of random sampling where it has been shown that the kind of peaks seen in the spectra of both data sets can appear as a result of aliasing, despite the irregular sampling; cf., [13, 14, 126]. It is stated that aliasing is suppressed in proportion to the degree of randomness $\sigma_{\tau_n}/\mu_{\tau_n}$ of the interarrival times of the particles [13, 14]. These

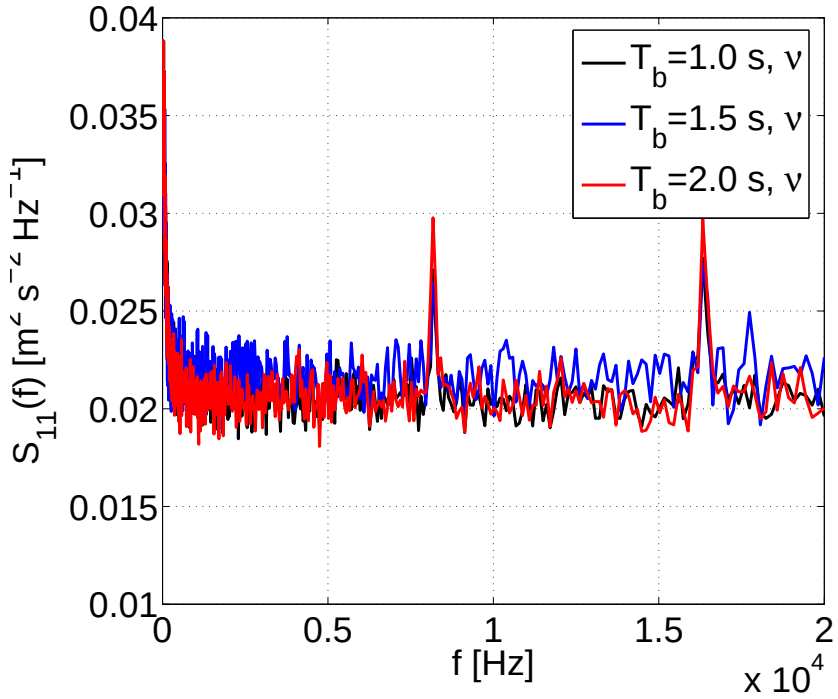


Figure 11.43: Axisymmetric turbulent jet: Burst-mode LDA spectra derived from the axisymmetric jet data for blocks of varying record length; 1.0, 1.5 and 2.0 s.

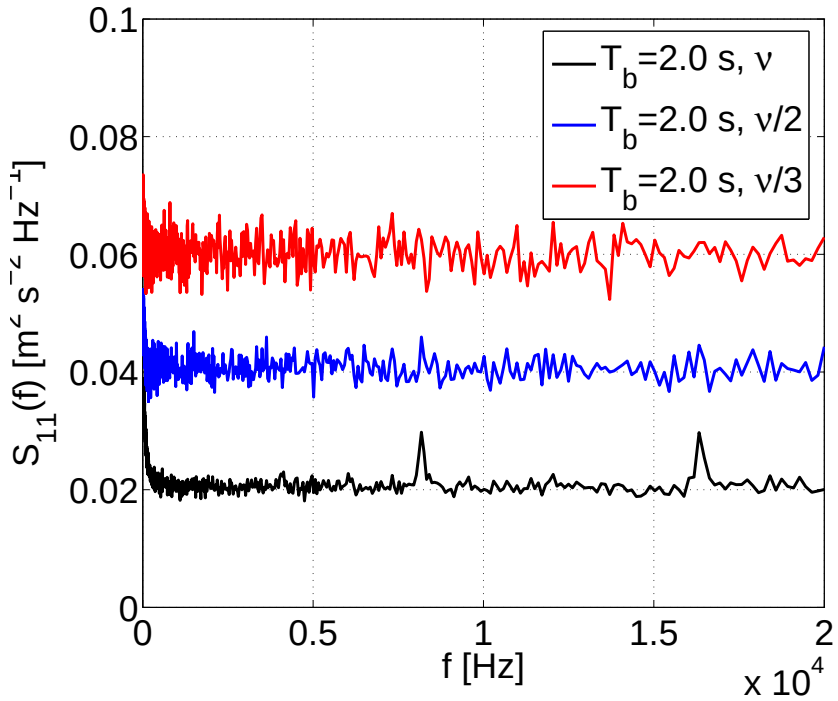


Figure 11.44: Axisymmetric turbulent jet: Burst-mode LDA spectra derived from the axisymmetric jet data computed for varying data rates; $\nu$, $\nu/2$, $\nu/3$ and $\nu/4$.

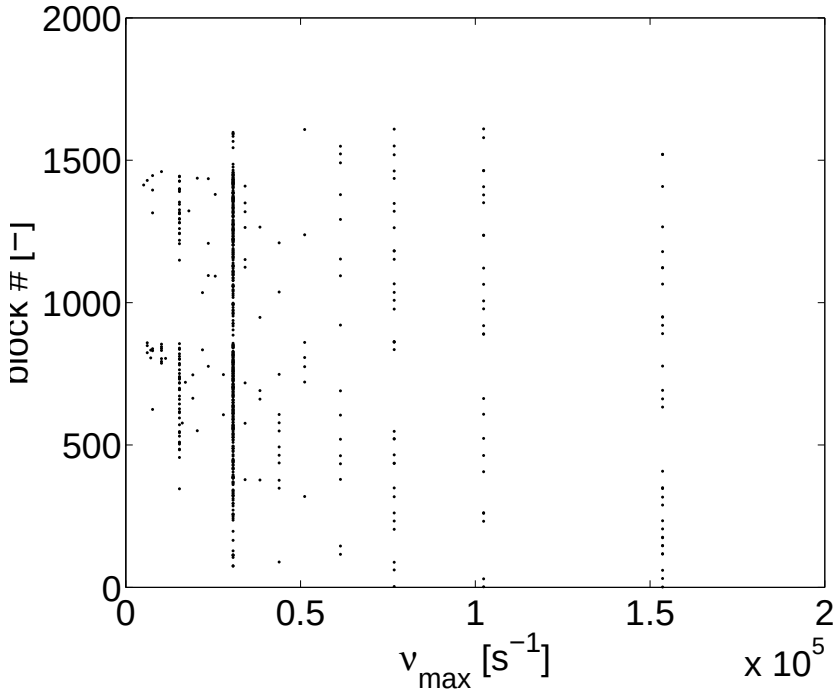


Figure 11.45: Axisymmetric turbulent jet: Maximum data rate $\nu_{max}$ for each block, large view.

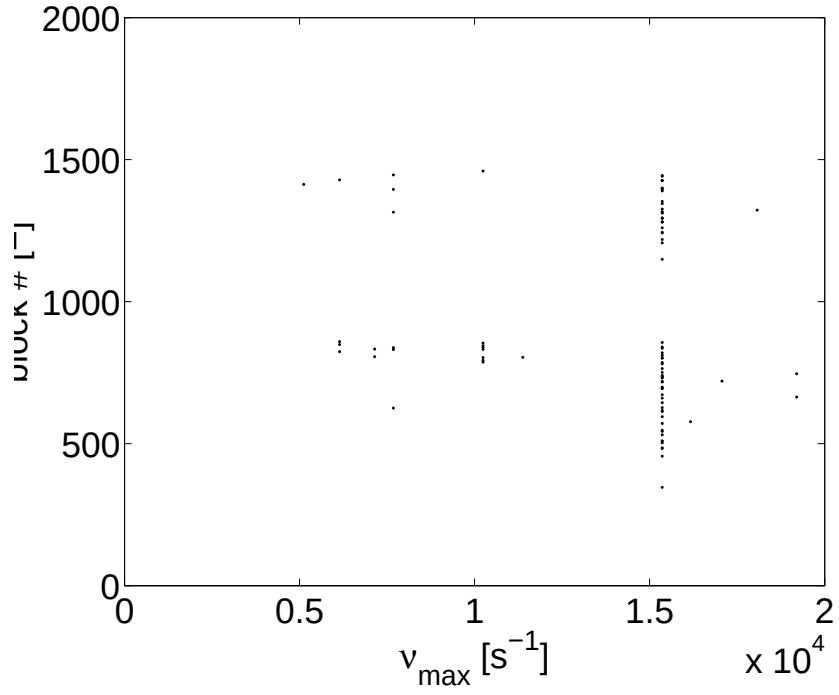


Figure 11.46: Axisymmetric turbulent jet: Maximum data rate $\nu_{max}$ for each block, small view.

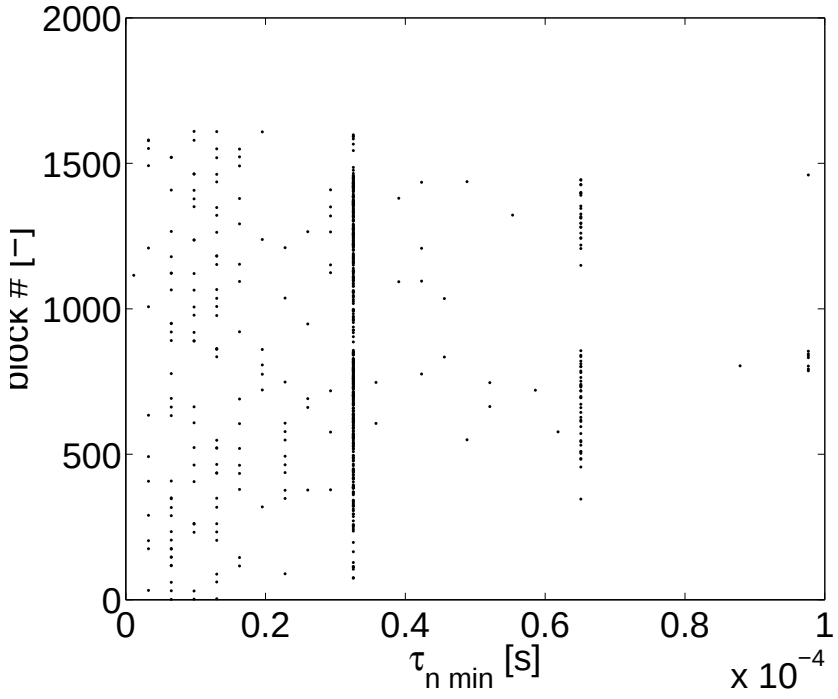


Figure 11.47: Axisymmetric turbulent jet: Minimum arrival time $\tau_n$ for each block.

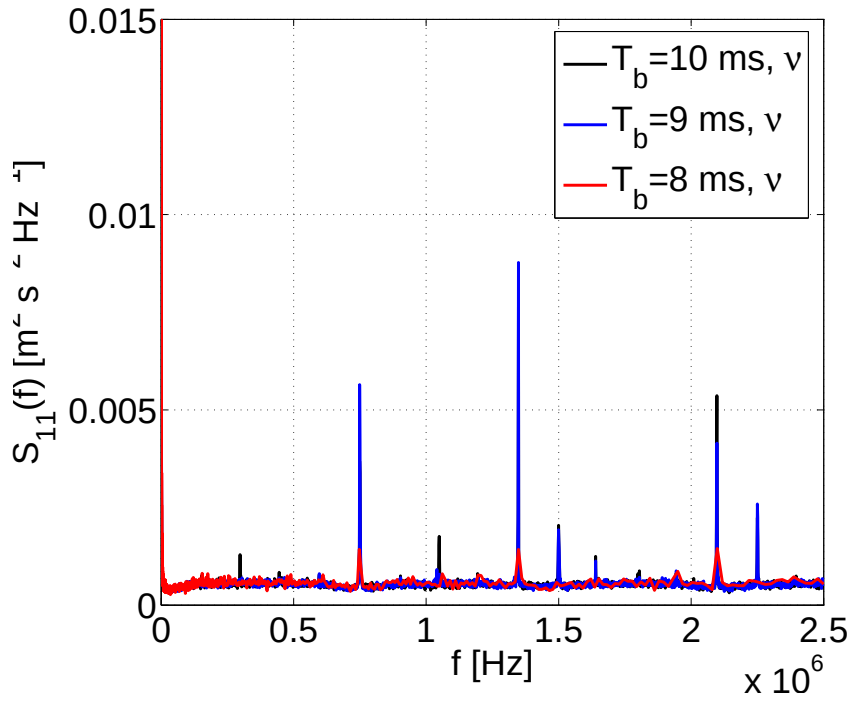


Figure 11.48: Cylinder wake: Burst-mode LDA spectra derived from the cylinder wake data for blocks of varying record length; 10, 9 and 8 ms.

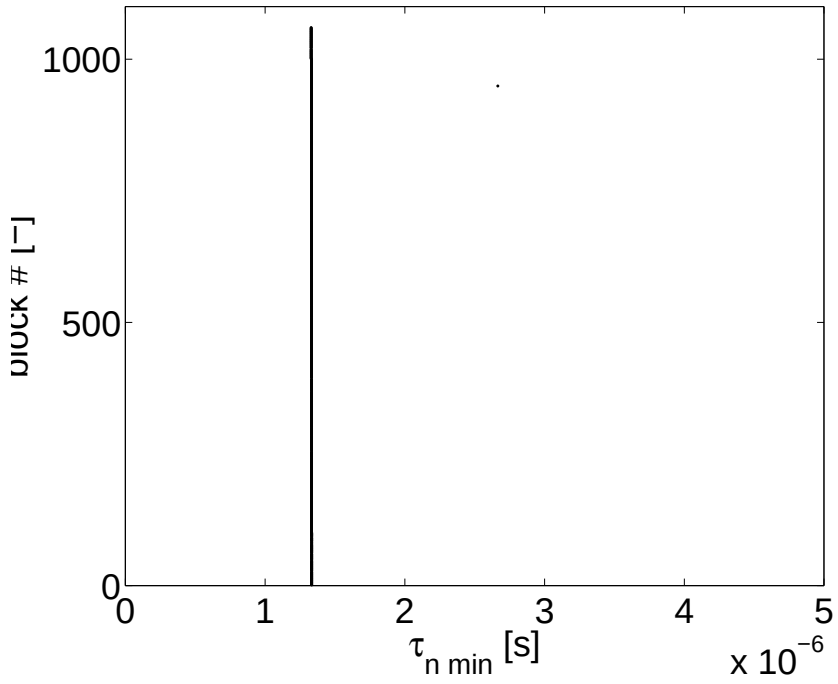


Figure 11.49: Cylinder wake: Minimum arrival time $\tau_n$ for each block.

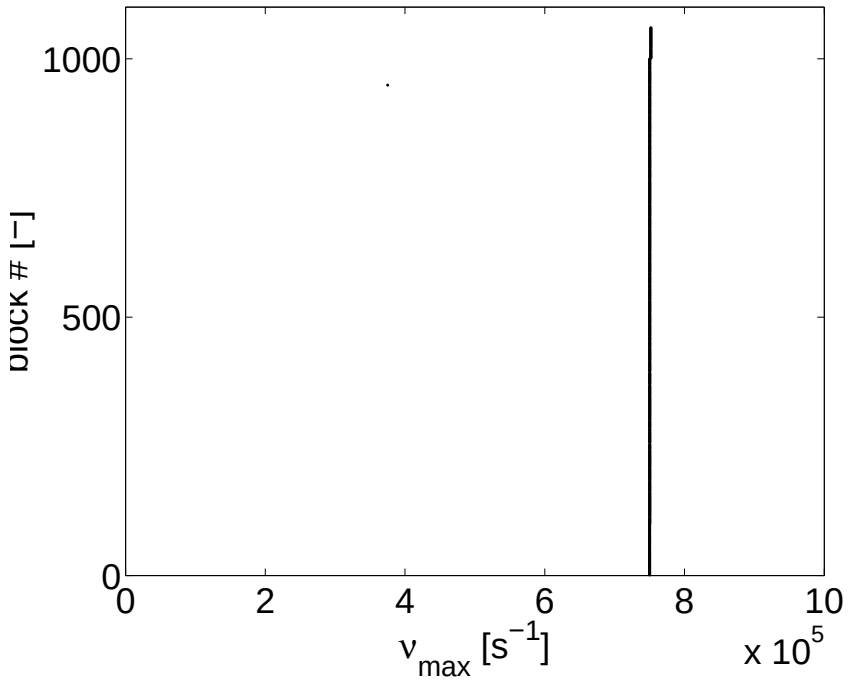


Figure 11.50: Cylinder wake: Maximum data rate $\nu_{max}$ for each block.

Table 11.4: Degree of randomness of the sampling obtained from the standard deviation $\sigma_{\tau_n}$ and mean value $\mu_{\tau_n}$ of the interarrival times of the particles for the axisymmetric jet and cylinder wake data.

| Data set | $\sigma_{\tau_n}/\mu_{\tau_n}$ | $\sigma^2_{\tau_n}$ | $\sigma_{\tau_n}$ | $\mu_{\tau_n}$ |
|---|---|---|---|---|
| Axisymmetric jet | 1.12 | $1.25{\cdot}10^{-5}$ | $3.5{\cdot}10^{-3}$ | $3.1{\cdot}10^{-3}$ |
| Cylinder wake | 3.81 | $1.64{\cdot}10^{-9}$ | $4.05{\cdot}10^{-5}$ | $1.06{\cdot}10^{-5}$ |

values are presented for the data sets at hand in table 11.4. According to this measure, the sampling associated with the data set of the axisymmetric jet is more deterministic than that of the cylinder wake. It has also been shown that if the point process of the sampling/interarrival times is, e.g., a Poisson process, the sampling is alias-free [126]. For a Poisson distributed variable, its mean and variance should be equal and hence $\sigma_{\tau_n}/\mu_{\tau_n} = 1$. The axisymmetric jet data is close to this approximation, as seen both in figure 11.5 and table 11.4. Therefore, it is plausible that the events occur independently of time since the last event, as they should for this type of process. But even so, the burst-mode power spectrum in figure 11.30 derived from this data displays alias-like peaks.

For the corresponding spectrum derived from the cylinder wake data, the peaks appear at much higher frequencies, see figure 11.48. Hence, it seems that the alleged aliasing is more suppressed under these conditions than the ones in the previous case. The interarrival times for this data set, displayed in figure 11.18, has a sampling distribution which deviates from Poisson, but this, however, is not an exclusive requirement for random sampling. In fact, the degree of randomness found directly from the data, see table 11.4, is higher than for the jet data, which speaks for a stronger suppression of aliases according to existing theory [14].

Figure 11.47 displays the smallest interarrival time of the particles for each block of data for the axisymmetric jet. It is clear from the plot that the interarrival times are highly quantized, revealing that they are not resolved properly due to a limitation in word size. Disregarding spurious values and the small amount of blocks having $\tau_{n\,min}$ close to $0.98{\cdot}10^{-4}$ s or higher, which probably will have a most modest impact on the spectrum, the largest block minimum interarrival times appear at about $\max\{\tau_{n\,min}\} = 0.65{\cdot}10^{-4}$ s. The Nyquist-Shannon theorem states that one cannot resolve frequencies higher than half of the sampling frequency. This means that this reduced data can resolve time scales down to $\Delta t = 2 \cdot \tau_{n\,min} = 1.30{\cdot}10^{-4}$ s, corresponding to a data rate of $\nu = 1/1.30{\cdot}10^{-4}$ s $\approx 7.69$ kHz which is the same frequency as that of the first aliasing peak seen in figures 11.43 and 11.44. Similarly, figures 11.45 and 11.46 show a small and a large view of the reciprocal of the minimum interarrival times for each block, here referred to as the maximum data rate $\nu_{max}$. These are, naturally, also quantized accordingly. The minimum value of these block maximum data rates is $\nu_{max} = 1.54{\cdot}10^4$ s$^{-1}$, corresponding to the reciprocal of $\max\{\tau_{n\,min}\}$.

Hence, the occurrence of these reoccurring peaks can possibly be explained as aliasing resulting from the breakdown in random sampling resulting from smallest resolvable interarrival time. The word size of the stored measurement data determines the minimum time step and thereby also the maximum operat-

ing frequency. Even if the particles arrive randomly providing random sampling, the *acquired* sampling is not fully able to capture this due to the limitation in resolution/word size. The shortest interarrival times are heavily impacted by the limitation in data storage precision; therefore the dynamic range of the randomness is bounded by the minimum resolvable arrival time. So even if the flow in principle samples randomly, this cannot be fully captured by the instrument, which sets a threshold for the highest resolvable frequency in the flow.

For the cylinder wake data, which is stored in double precision, almost all block minimum interarrival times appear at $\max\{\tau_{n\,min}\} = 1.333{\cdot}10^{-6}$ s, see figure 11.49. In the frequency domain, this corresponds to a block maximum data rate of $\nu_{max} = 0.750{\cdot}10^{6}$ s$^{-1}$, see figure 11.50, which is also represented in the peak in figure 11.48. For a free stream velocity of U = 21.5 m/s, this corresponds to a displacement of $\mathrm{x} = \mathrm{U}{\cdot}\tau_{n\,min} = 21.5{\cdot}1.333{\cdot}10^{-6} \approx 30\mu$m, which is a typical measuring volume size for LDA measurements.

Thus, in the case of the axisymmetric jet, the word size constitutes the bottleneck in the data processing. By contrast, for the cylinder wake data the size of the measuring volume ultimately determines the frequency resolution of the spectrum.

### 11.6.4 Statistics of the spectral estimator

Figures 11.51 and 11.52 display the histograms of the realizations of the one-dimensional burst-mode power spectrum across the computed frequency span from the axisymmetric jet data and the cylinder wake data, respectively.

The distributions obtained from the measurement data are compared to the exponential probability density function given by

$$P(S_{11}(f)) = \frac{\nu}{\overline{u^2}} e^{-\nu S_{11}(f)/\overline{u^2}}. \tag{11.55}$$

The reason for the deviations in figures 11.51 and 11.52 is that the signal part of the spectrum varies with frequency, and hence the value of $\nu/\overline{u^2}$ depends on frequency. Therefore, let's only consider a range of frequencies where the variations in the spectrum are smaller than or equal to the variability of the spectral estimator. Such a range can be found where turbulence has dissipated and only the noise floor remains. Assuming that aliasing is sufficiently suppressed to resolve the noise floor, these histograms have been produced for both data sets, see figures 11.53 and 11.54 for the axisymmetric jet and cylinder wake data, respectively. In these plots, the histograms coincide well with the exponential distributions for both data sets.

### 11.6.5 Deviations in moments

As a measure of the effect of not applying residence time weighting to the moments, residence time weighted moments are compared to the ones obtained using regular arithmetic. To evaluate this error, let's perform a Taylor expansion of the residence time weighted mean velocity algorithm about the state of zero turbulence intensity. It will be necessary to assume that all particles pass through the center and traverse undisturbed. We will also consider only a one-dimensional flow, say $\tilde{u} = U + u$, where $U$ is the mean and $u_n$ the departure of

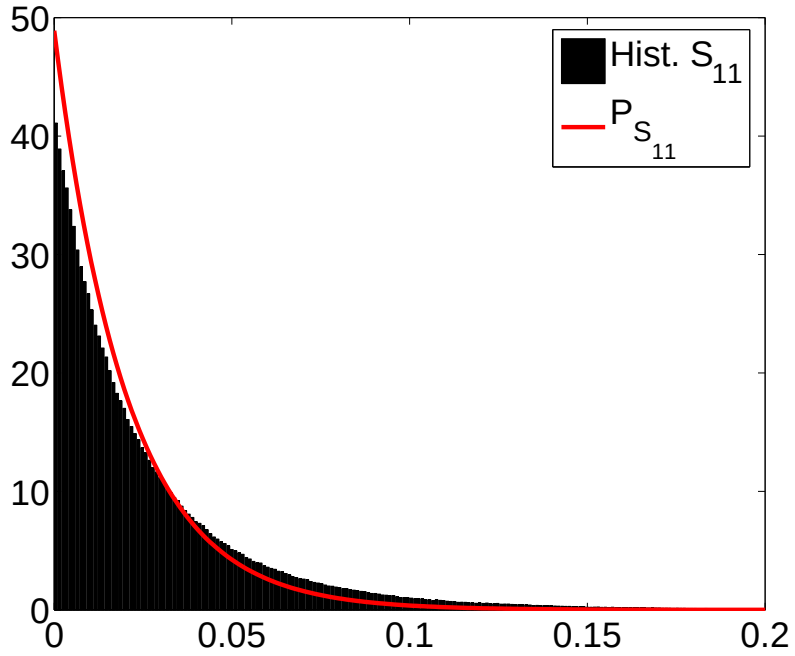


Figure 11.51: Axisymmetric jet: Distribution of realizations of the axisymmetric jet power spectrum for all blocks in the full frequency range.

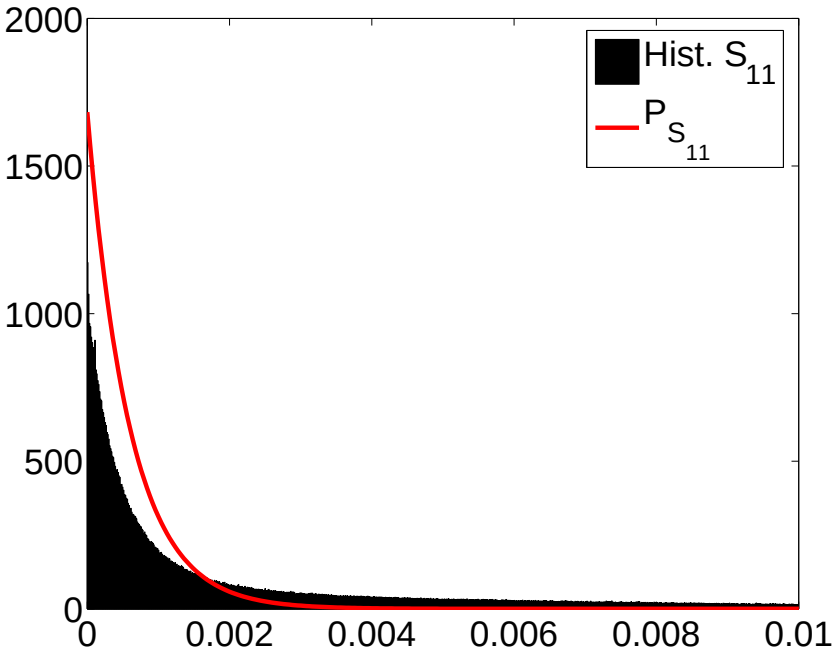


Figure 11.52: Cylinder wake: Distribution of realizations of the cylinder wake power spectrum for all blocks in the full frequency range.

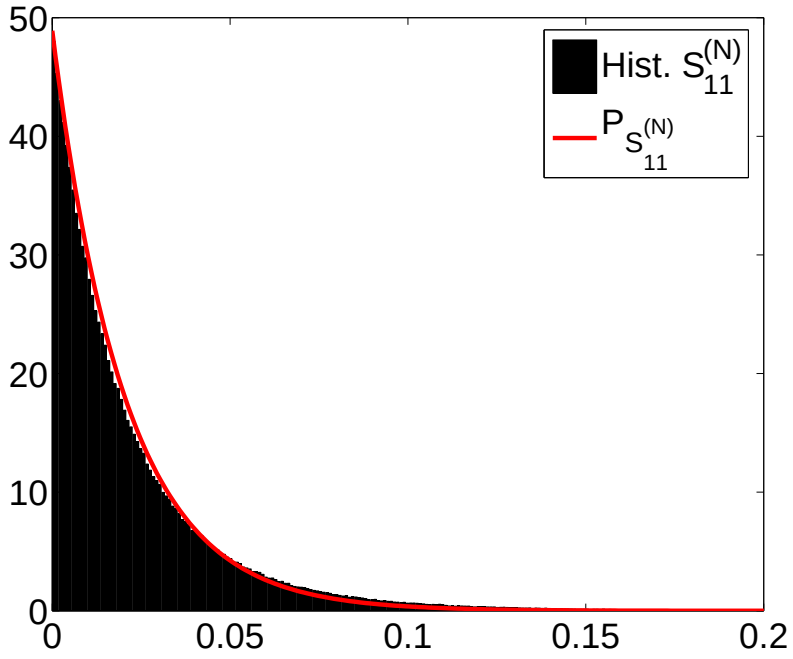


Figure 11.53: Axisymmetric jet: Distribution of realizations of the axisymmetric jet power spectrum for all blocks in the frequency range beyond dissipation, corresponding to the noise floor.

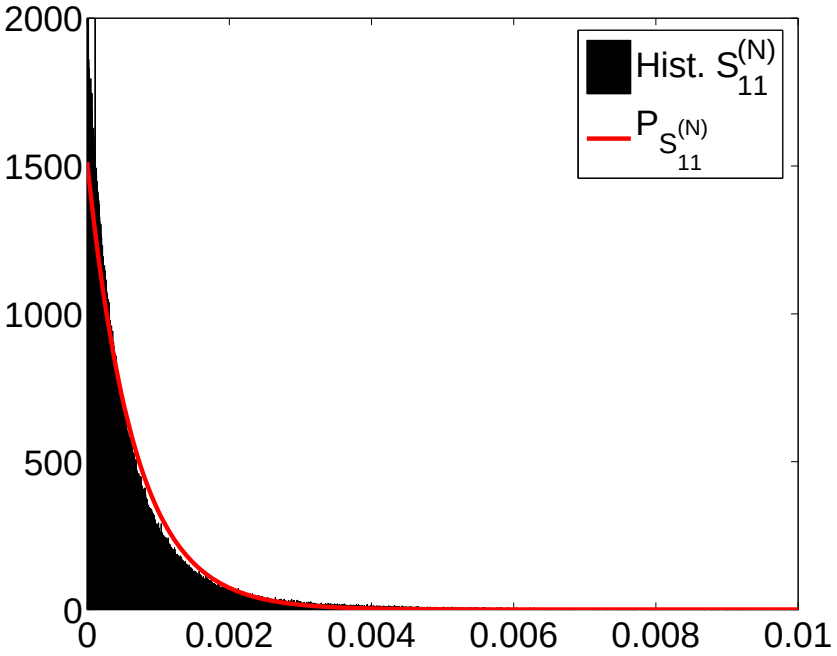


Figure 11.54: Cylinder wake: Distribution of realizations of the cylinder wake power spectrum for all blocks in the frequency range beyond dissipation, corresponding to the noise floor.

the $n^{th}$ realization from it. First consider the algorithm for the residence time weighted mean velocity:

$$U_{0T}^{B} = \frac{\sum_{n=0}^{N-1} \tilde{u}_n \Delta t_n}{\sum_{n=0}^{N-1} \Delta t_n} \tag{11.56}$$

The assumptions above imply the following approximate form for the sum of the residence times:

$$\sum_{n=0}^{N-1} \Delta t_n \approx \sum_{n=0}^{N-1} \frac{d}{U+u_n} = \frac{d}{U} \sum_{n=0}^{N-1} \frac{1}{1+\frac{u_n}{U}}$$

Expanding the denominator yields

$$\sum_{n=0}^{N-1} \Delta t_n \approx \frac{d}{U} \sum_{n=0}^{N-1} \left\{ 1 - \frac{u_n}{U} + \frac{u_n^2}{U^2} - \frac{u_n^3}{U^3} + \dots \right\}$$

$$\approx N\frac{d}{U} - 0 + \frac{d}{U} \sum_{n=0}^{N-1} \frac{u_n^2}{U^2} - \frac{d}{U} \sum_{n=0}^{N-1} \frac{u_n^3}{U^3} \approx N\frac{d}{U} \left\{ 1 + \frac{\overline{u^2}}{U^2} - \frac{\overline{u^3}}{U^3} \right\} \tag{11.57}$$

Similarly, the Taylor expansion of the residence time weighted mean velocity can be expanded to obtain:

$$U_{0T}^{B} \approx \frac{\sum_{n=0}^{N-1} \tilde{u}_n \Delta t_n}{\sum_{n=0}^{N-1} \Delta t_n}$$

$$\approx \frac{\sum_{n=0}^{N-1} (u_n + U) \frac{d}{U} \left\{ 1 - \frac{u_n}{U} + \frac{u_n^2}{U^2} - \frac{u_n^3}{U^3} + \dots \right\}}{N\frac{d}{U} \left\{ 1 + \frac{\overline{u^2}}{U^2} \right\}}$$

$$\approx \frac{\sum_{n=0}^{N-1} \frac{d}{U} \left\{ \left[ u_n - \frac{u_n^2}{U} + \frac{u_n^3}{U^2} - \frac{u_n^4}{U^3} + \dots \right] + \left[ U - u_n + \frac{u_n^2}{U} - \frac{u_n^3}{U^2} + \dots \right] \right\}}{N\frac{d}{U} \left\{ 1 + \frac{\overline{u^2}}{U^2} \right\}}$$

Thus to second order in $\overline{u^2}/U^2$,

$$U_{0T}^{B} \approx \frac{Nd}{N\frac{d}{U} \left\{ 1 + \frac{\overline{u^2}}{U^2} \right\}} \approx U \left\{ 1 - \frac{\overline{u^2}}{U^2} + \dots \right\} \tag{11.58}$$

Thus, the deviation of the arithmetic mean to the residence time weighted one is proportional to the variance and inversely proportional to the mean velocity.

$$\frac{\Delta U_{0T}^{B}}{U} = \frac{U_{0T}^{B} - U}{U} \approx -\frac{\overline{u^2}}{U^2} \tag{11.59}$$

The values from the axisymmetric jet and cylinder wake data are found in table 11.5 and show reasonable agreement between $\Delta U_{0T}^{B}/U$ and $-\overline{u^2}/U^2$ despite the clipping of the data discussed earlier.

We can apply the same analysis to the residence time estimator for the

Table 11.5: Deviations in the first moment obtained using arithmetic and residence time weighting.

| | $U_{Jet}$ | $U_{Cyl.\ wake}$ |
|---|---|---|
| $U_{RTW} = \sum_{n=0}^{N-1} \tilde{u}_n \Delta t_n / \sum_{n=0}^{N-1} \Delta t_n$ | 8.40 | 21.49 |
| $U_{ar.} = \frac{1}{N} \sum_{n=0}^{N-1} \tilde{u}_n$ | 8.91 | 22.55 |
| $\frac{\Delta U_{0T}^B}{U} = \frac{U_{0T}^B - U_{ar.}}{U_{ar.}}$ | -0.06 | -0.05 |
| $-\frac{\overline{u^2}_{ar.}}{U_{ar.}^2}$ | -0.06 | -0.07 |

variance:

$$\sigma_{0T}^{2\,B} = \frac{\sum_{n=0}^{N-1} u_n^2 \Delta t_n}{\sum_{n=0}^{N-1} \Delta t_n}$$

$$\approx \frac{\sum_{n=0}^{N-1} u_n^2 \frac{d}{U}\left\{1 - \frac{u_n}{U} + \frac{u_n^2}{U^2} - \frac{u_n^3}{U^3} + \frac{u_n^4}{U^4} - \dots\right\}}{N \frac{d}{U}\left\{1 - \frac{u_n}{U} + \frac{\overline{u^2}}{U^2} - \frac{\overline{u^3}}{U^3} + \frac{\overline{u^4}}{U^4} - \dots\right\}}$$

$$\approx \frac{N \frac{d}{U}\left\{\overline{u^2} - \frac{\overline{u^3}}{U} + \frac{\overline{u^4}}{U^2} - \dots\right\}}{N \frac{d}{U}\left\{1 - \frac{\overline{u}}{U} + \frac{\overline{u^2}}{U^2} - \frac{\overline{u^3}}{U^3} + \frac{\overline{u^4}}{U^4} - \dots\right\}}$$

$$\approx U^2 \frac{\frac{\overline{u^2}}{U^2} - \frac{\overline{u^3}}{U^3} + \frac{\overline{u^4}}{U^4} - \dots}{1 + \frac{\overline{u^2}}{U^2} - \frac{\overline{u^3}}{U^3} + \frac{\overline{u^4}}{U^4} - \dots} \tag{11.60}$$

Letting $x = \overline{u^2}/U^2 - \overline{u^3}/U^3 + \overline{u^4}/U^4 \dots$, one can expand the above expression for small x to obtain

$$\frac{x}{1+x} \approx x - x^2 + x^3 - \dots \tag{11.61}$$

Inserting this into the expression for the residence time weighted variance and recognizing that $\overline{u}/U = 0$,

$$\frac{\sigma_{0T}^{2\,B}}{U^2} \approx \left\{x - x^2 + x^3 - \dots\right\} \tag{11.62}$$

with a deviation proportional to:

$$\frac{\Delta\sigma^2}{U^2} = \frac{\sigma_{0T}^{2\,B} - \sigma^2}{U^2}$$

$$\approx -\frac{\overline{u^3}}{U^3} + \frac{\overline{u^4}}{U^4} - \frac{\overline{u^5}}{U^5} - \left[\frac{\overline{u^2}}{U^2} - \frac{\overline{u^3}}{U^3} + \frac{\overline{u^4}}{U^4} - \frac{\overline{u^5}}{U^5} + \dots\right]^2$$

Table 11.6: Deviations in the second moment obtained using arithmetic and residence time weighting.

| | $\overline{u^2}_{\text{Jet}}$ | $\overline{u^2}_{\text{Cyl. wake}}$ |
|---|---|---|
| $\overline{u^2}_{\text{RTW}} = \sum_{n=0}^{N-1} u_n^2 \Delta t_n / \sum_{n=0}^{N-1} \Delta t_n$ | 5.24 | 34.26 |
| $\overline{u^2}_{\text{ar.}} = \frac{1}{N} \sum_{n=0}^{N-1} u_n^2$ | 4.75 | 33.43 |
| $\frac{\overline{u^2}_{\text{RTW}} - \overline{u^2}_{\text{ar.}}}{U^2_{\text{ar.}}}$ | 0.06 | 0.04 |
| $\frac{\Delta\sigma^2_{\text{trunc.}}}{U^2_{\text{ar.}}}$ | 0.05 | 0.24 |

$$+\left[\frac{\overline{u^2}}{U^2} - \frac{\overline{u^3}}{U^3} + \frac{\overline{u^4}}{U^4} - \frac{\overline{u^5}}{U^5} + \dots\right]^3 - \dots \tag{11.63}$$

Actually, neither of the data sets provide very good tests, since we are working with very small differences ($\overline{u^2}/U^2 \ll 1$). For the axisymmetric jet data, a truncated version of this expression ($\Delta\sigma^2_{\text{trunc.}}/U^2$) was evaluated using up to the fourth moment of the velocity. These values found from the data sets are found in table 11.6 and show a reasonable agreement with the values of $\Delta\sigma^2/U^2 = (\sigma_0^2{}_T^B - \sigma^2_{\text{arithm.}})/U^2$ despite the clipping of the measurement data. The cylinder wake data does not display good concurrency, which is plausibly a consequence of the fluctuations being large compared to the mean value of the velocity, yielding a diverging estimate for higher order polynomials in x.

## 11.7 Summary and conclusions

Two different data sets consisting of LDA and corresponding HWA time series measurements are employed in the present study. The first data set was acquired at the centerline of an axisymmetric turbulent jet, while the other one was collected from a cylinder wake.

For the axisymmetric jet data, the interarrival times turned out to have an exponential distribution. The residence times have a lognormal distribution, most probably caused by a lognormal size distribution of the particles. The unweighted distribution of the measured LDA velocities is Gaussian, as for the HWA data. In the process, clipping of the data was discovered for both the LDA and the HWA data sets, which makes it impossible to determine the moments correctly. Further, the data rate of the axisymmetric jet measurements decayed exponentially, most probably due to evaporation of the particles and the particle size distribution. Clearly histograms would make a useful on-line diagnostic in future measurements. The above mentioned properties showed similar behavior for the cylinder wake data, with the exception that the interarrival times deviated from the exponential distribution and that the particle concentration was kept fairly constant during the course of the measurements.

The burst-mode RTW algorithm was initially verified by applying the HWA data sets to it, setting the residence times to some constant value and

comparing the estimator with the HWA FFT spectrum. For the jet data, the HWA FFT and HWA RTW spectra collapse for all frequencies but the very highest, due to the limitation in word size by default handled by Fortran 90. This effect was not significant for the burst-mode LDA spectrum derived from the cylinder wake data due to the smaller range of the spectral values.

The burst-mode LDA spectrum of the axisymmetric jet data showed high concurrence with the corresponding spectrum obtained from the HWA data using the FFT at low frequencies. At higher frequencies, the LDA RTW spectrum levels out at a relatively high value. Despite the assumed inherent random sampling of the LDA, aliasing peaks appeared due to the limitation in resolution of the measurement data. This limitation effectively sets the threshold for the highest resolvable frequency in the flow, inevitably leading to aliasing. Hence, even though the flow might provide random sampling at least to a high enough degree to suppress aliasing beyond the frequency span of interest, the precision of the data stored will eventually limit this randomness to a dynamic range bounded by the resolvable arrival time.

For the cylinder wake flow, the burst-mode LDA spectrum collapses well with the corresponding HWA FFT wavenumber spectrum across all frequencies. For this case, the HWA and LDA data sets are not qualitatively comparable, since they were acquired at different Reynolds numbers. However, since the Reynolds numbers are not very different, one can compare the wavenumber spectra (at least the convective disturbances, such as turbulence) after performing a normalization corresponding to the respective energies. The peak in the spectrum turned out to be a temporal disturbance, probably caused by vibrations of the cylinder, rather than a convective disturbance caused by shedding on the cylinder. Due to the intermittency of the LDA signal, the white noise level is substantially higher in the burst-mode LDA spectrum. This can, however, be somewhat compensated for by performing the noise correction described in Chapter 9, the limitation of the application of the method in the current case being in the high variability of the spectrum. The aliases appeared at very high frequencies in these burst-mode LDA spectra, seemingly ultimately caused by the limited resolution of the measuring volume.

# Chapter 12

# Resampling techniques for evaluating spectra from LDA data

Interpolation and resampling of Laser Doppler Anemometry (LDA) time series to a regular grid for the application of the Fast Fourier Transform is implemented and discussed. Two alternative techniques are tested: sample-and-hold, which holds the value of the last sample until the next particle arrival, and direct linear interpolation between the measuring points. The resulting power spectral estimates from two burst-mode LDA measurement campaigns with different sampling conditions are compared: measurements in an axisymmetric turbulent jet with a relatively low average data rate, and cylinder wake flow where the data rate is substantially higher. Power spectra computed from corresponding Hot-Wire Anemometry (HWA) measurements are shown as a reference for the LDA spectra. The results show that the spectra derived from the jet data, which has a quite low data density ($\nu\lambda_\tau = 0.7$) due to the low data rate, cannot predict the spectrum *at any frequency*. The sample-and-hold spectrum drops at a rate of $f^{-2}$, as was expected from theory, while the spectrum derived from linear interpolation performs even worse, dropping at an even higher rate. For the cylinder wake data, which has a substantially higher data density ($\nu\lambda_\tau = 94$), the data for both HWA and LDA is sampled well over the cut-off frequencies introduced by the finite probe lengths. The cut-off frequencies are both higher than the corresponding frequency for a rough estimate of the Taylor microscale. Both interpolated spectra perform well at the large convective scales, but fail in their prediction at the highest frequencies.

## 12.1 Introduction

Laser Doppler Anemometry (LDA) is a method for measuring the velocity of small scattering particles in a fluid. Assuming that the particles follow the flow, one can therefore measure fluid velocities. Other techniques commonly employed to acquire point measurements of flow velocities are Hot-Wire Anemometry (HWA) and Pitot tubes. Aside from the non-intrusiveness of the LDA,

it has some disadvantages to other techniques such as the intermittency of the signal, the random sampling and high velocity bias inherent in the measurements. These issues can, however, be dealt with by random noise cancelation in correlations and spectra (see Chapter 9), the application of the discrete Fourier transform instead of the FFT (see Chapter 11) and residence time weighting (see; e.g., [46, 20, 19]), respectively. Nonetheless, the continuous signal from the HWA considerably simplifies spectral analysis, since there are many standard methodologies (hardware and software) that can be implemented. A number of procedures have been proposed to perform spectral analysis on LDA data.

A common strategy is to interpolate the LDA time history and then resample it to enable the application of the Fast Fourier Transform (FFT). The goal is to create a continuous signal so it can be treated like a HWA. One of the most commonly employed techniques, the sample-and-hold procedure [4], basically resamples the data at uniform intervals by the last acquired data point. Other interpolation schemes are sometimes used, such as linear interpolation or spline fitting, as was recommended by Adrian and Yao [1], to reduce the magnitude of the step noise. However, the resampling distorts the signal, resulting in an unreliable spectral estimator both in the respect of its total energy content as well as its distribution across the frequencies of the band width. The estimator may be strongly biased with systematic errors [93].

In the present chapter, simultaneously acquired LDA and HWA measurements from an axisymmetric turbulent jet and LDA and HWA measurements acquired under similar conditions in a cylinder wake (see previous chapter) are used to exemplify the implementation of the sample-and-hold and linear interpolation and resampling schemes to obtain a spectral estimator. The data density of the LDA data of the axisymmetric jet is quite low, $\nu\lambda_\tau = 0.7$ (where $\lambda_\tau$ is the Taylor microscale), meaning, on average, less than one sample in one Taylor microscale. Thus, the flow is not very well represented by the data. This is also fairly obvious as can be seen in figure 12.1 where the frequency of the resampled data corresponds to the estimated frequency based on the convected Kolmogorov microscale. For the cylinder wake measurements, the average data density of the LDA ($\nu\lambda_\tau = 94$) was quite high and corresponds well to the estimated frequency based on the Kolmogorov microscale. This is well illustrated in the time history of the LDA signal, see figure 12.2, where the data rate is much closer to the frequency of the resampled data which also in this case corresponds to the estimated frequency based on the convected Kolmogorov microscale. However, since the amount of data from these measurements is quite scarce, this can not be benefited very well since the variability of the spectral estimator becomes large in the high frequency range where the spectrum drops; cf., Gaster and Roberts [41]. This can only be remedied by well converged statistics. Since the signal processing is the main concern in the present work, only a very brief summary of the experimental setups is presented. The interested reader is referred to [35] for the axisymmetric turbulent jet experiment and [50] for the cylinder wake experiment.

Power spectra are estimated from these LDA data sets using the sample-and-hold (S/H) and linear interpolation (LIN) schemes (see figures 12.3, 12.4, 12.5 and 12.6). The interpolated signal is resampled at the same rate as the HWA data. Further, power spectra computed in the regular fashion using the FFT from the HWA data are shown as a reference to enable comparison of the estimates based on the LDA data. The HWA measurements resolve the flow

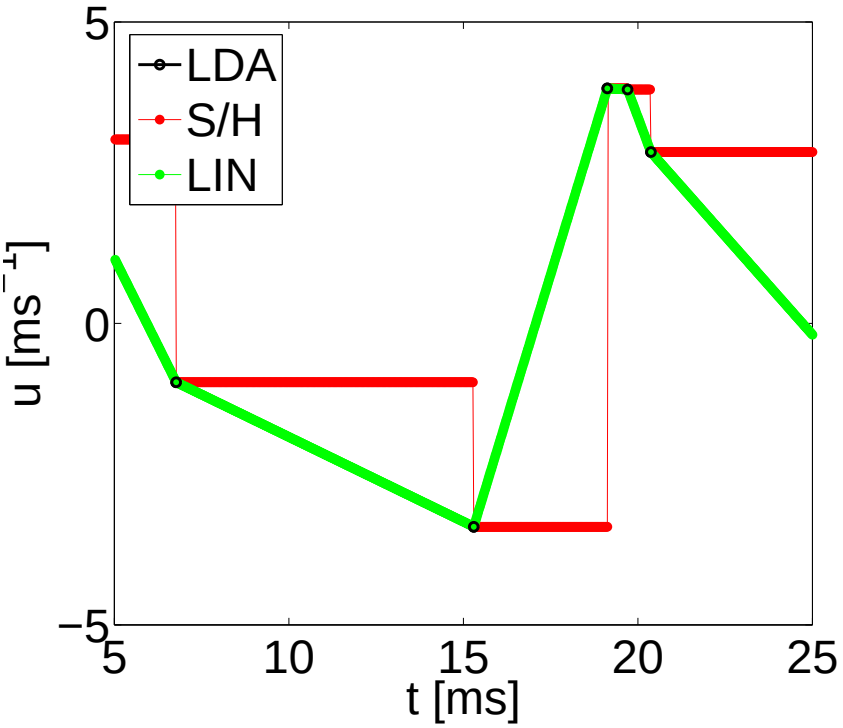


Figure 12.1: Time history of a part of the LDA signal of the axisymmetric turbulent far jet data with the interpolated and resampled signals S/H and LIN superimposed.

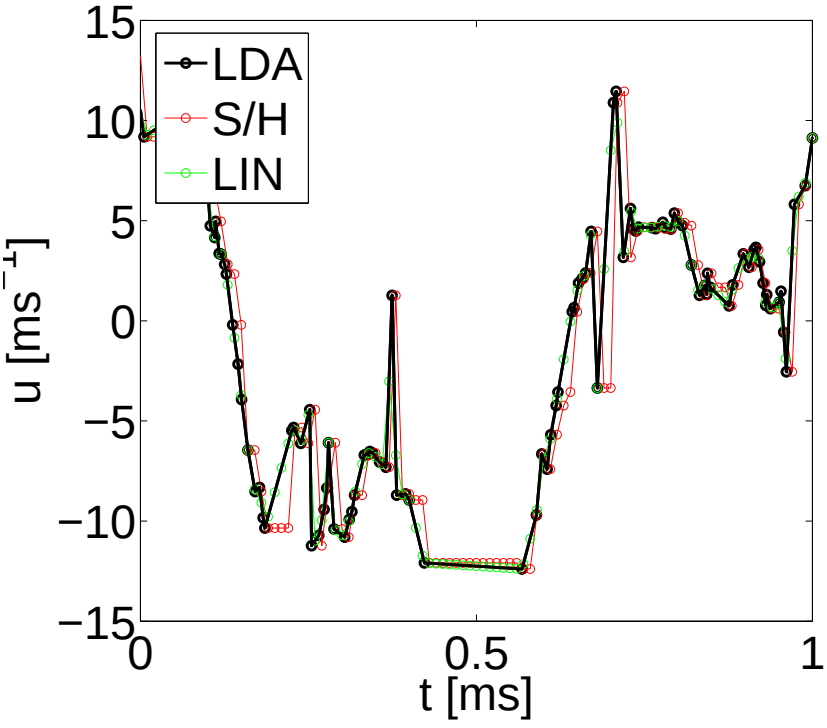


Figure 12.2: Time history of a part of the LDA signal of the cylinder wake data with the interpolated and resampled signals S/H and LIN superimposed.

up to slightly beyond the estimated Taylor microscales in both flows, where the finite wire length sets a threshold for the resolution and acts as a low-pass filter for higher frequency fluctuations. It is seen that the resampling schemes do indeed perform differently depending on the average LDA data density; For higher data densities, the resampling schemes perform considerably better than at low ones, for which the spectra are completely dominated by frequency dependent noise which falls off as $f^{-2}$ for the S/H scheme and even faster for the LIN scheme. However, even at considerable data densities, the S/H and LIN algorithms do not seem to capture the energy at the highest frequencies and the added step noise again kicks in.

## 12.2 Signal processing

In the following, theory is presented describing the noise generated by the S/H scheme. Because of the strongly deviating results for the LIN spectra, it was not considered necessary to develop a theory for power spectra obtained using that interpolation scheme.

### 12.2.1 Sample-and-hold

Interpolation and resampling methods such as sample-and-hold behave in a manner very similar to tracker 'drop-out', where the drop-outs have been replaced by the last acquired value. The main difference is that for tracker drop-out, it is assumed that the signal is mostly in; i.e., that the drop-outs are relatively scarce. When applying sample-and-hold to randomly arriving data, the signal is always 'dropped-out'.

The effects of tracker drop-out on the autocorrelation and spectra were investigated by Buchhave [19, 20], where it was shown that the mean and all higher moments of the velocity distribution are preserved when one holds the signal at its last measured value during drop-out. It was assumed that the occurrence of drop-outs was statistically independent of the velocity itself, and solely due to external factors (e.g., electronics, phase fluctuations etc.). It was possible to show that if the time between samples of the measured LDA signal were short compared to the flow integral scale, the spectrum could be correctly reproduced with the exception of an additive frequency dependent noise term given by:

$$S_N(f) \propto \frac{1}{1 + (2\pi f/\nu)^2} \tag{12.1}$$

Adrian and Yao [1] obtained a similar result with the same frequency dependent noise term when investigating the resulting spectrum from sampled and held burst-mode LDA data. This term acts as a low pass filter both on the spectrum and the frequency independent white noise term, and arises from the frequency content information lost during interpolation. This results in an $f^{-2}$ trend of the spectrum, increasing in strength with frequency in the range where the data rate $\nu$ is not large enough to suppress these effects throughout the bandwidth. Thus, for low data rates, Adrian and Yao predicted a spectrum that falls off as $f^{-2}$, whilst at higher data rates the spectrum is expected to be fairly well predicted up to a frequency of about $\nu/2\pi$.

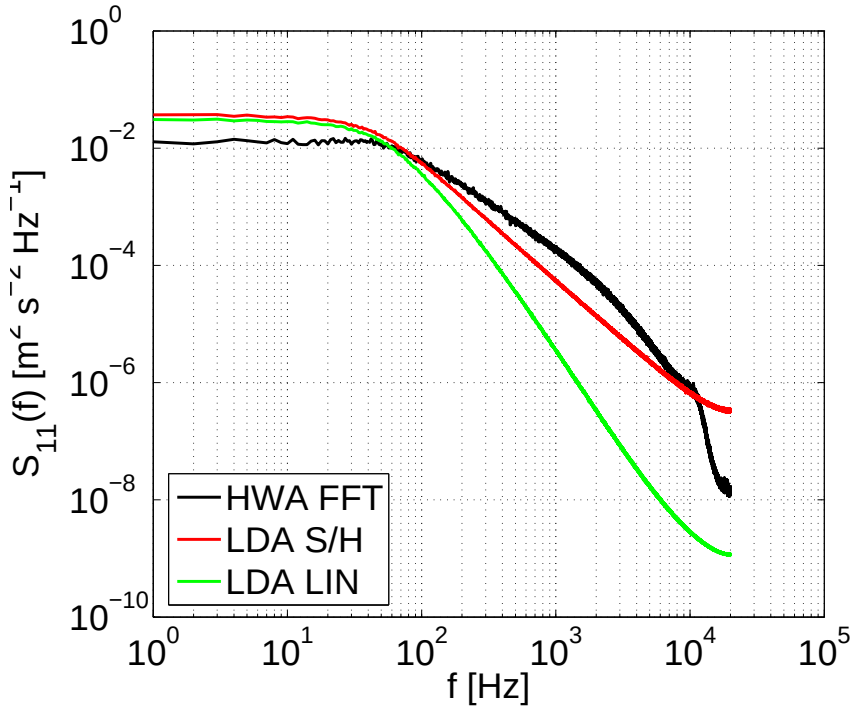


Figure 12.3: Axisymmetric turbulent jet power spectrum computed from the HWA data using the FFT (black) and estimates obtained from the LDA data using sample-and-hold S/H (red) and linear interpolation and resampling LIN (green).

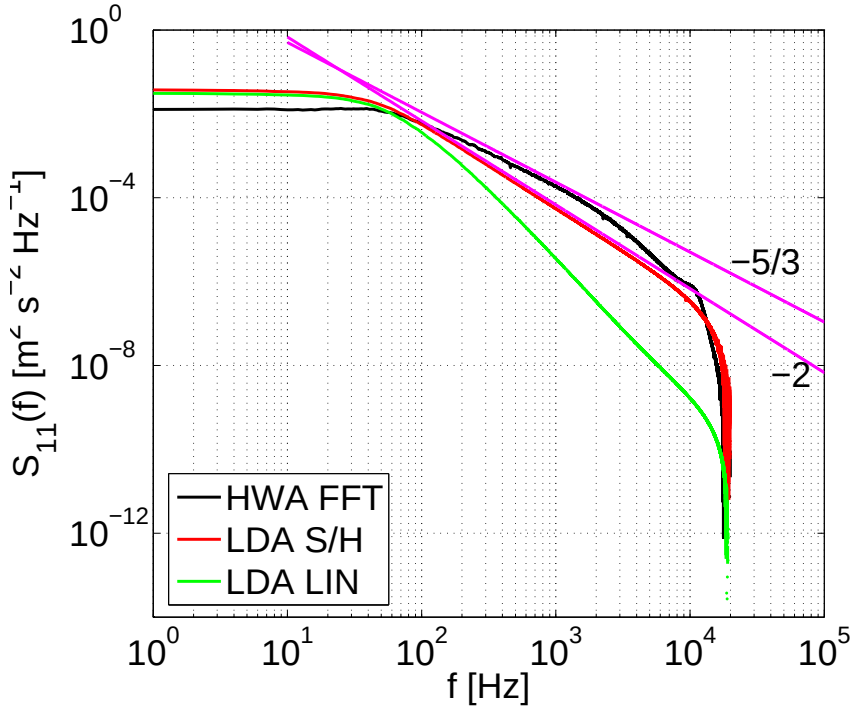


Figure 12.4: Axisymmetric turbulent jet random noise corrected power spectrum computed from the HWA data using the FFT (black) and corresponding estimates obtained from the LDA data using sample-and-hold S/H (red) and linear interpolation and resampling LIN (green). The figure also displays lines dropping off as $f^{-5/3}$ and $f^{-2}$ as a reference.

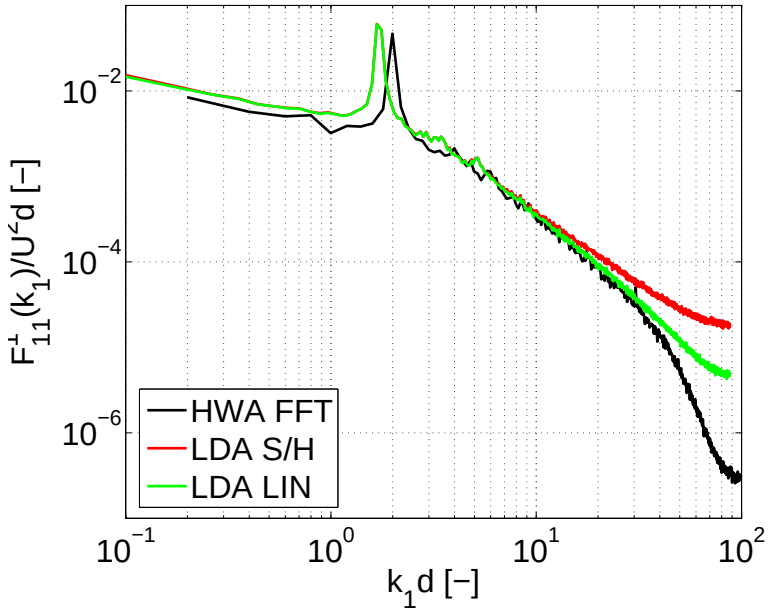


Figure 12.5: Cylinder wake power spectrum computed from the HWA data using the FFT (black) and the estimates obtained from the LDA data using sample-and-hold S/H (red) and linear interpolation and resampling LIN (green).

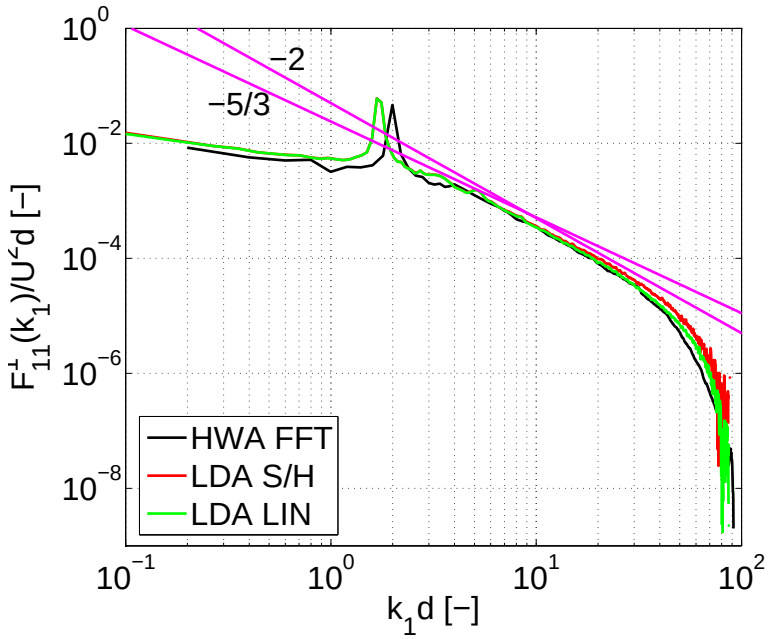


Figure 12.6: Cylinder wake noise corrected power spectrum computed from the HWA data using the FFT (black) as well as corresponding estimates obtained from the LDA data using sample-and-hold S/H (red) and linear interpolation and resampling LIN (green). The figure also displays lines dropping off as $f^{-5/3}$ and $f^{-2}$ as a reference.

## 12.3 Experimental setups

The experimental method for the measurements performed on the axisymmetric turbulent far jet can be found in Frohnapfel [35]. The data comprises simultaneously acquired HWA and LDA data including the residence times from measurements performed in an axisymmetric turbulent far jet 30.3 diameters downstream of the jet exit. The sampling rate of the HWA data is high enough to resolve the Kolmogorov microscale. However, the limiting cut-off frequency due to the finite wire length will cause low-pass filtering, meaning that the instrument cannot resolve scales slightly smaller than the Taylor microscale. Further, the average data density for the LDA data is quite low, $\nu = 318\,\mathrm{Hz}$, which yields a data density of $\nu\lambda_\tau = 0.7$. This means that, on average, a sample is taken every 0.7 Taylor microscale, hence the flow is not well represented by the sampled data.

In addition, HWA data with similarly acquired LDA data including residence times were obtained in the wake of a circular cylinder in a wind tunnel at DTU. These were kindly provided by Holger Nobach at Max-Planck Institut für Dynamik und Selbstorganisation[1]. The circular cylinder had a diameter of 6 mm and was mounted across the full span in a square test section of width 300 mm in a closed loop wind tunnel. The HWA and LDA time series were collected in the same position 26 mm downstream of the cylinder. The HWA measurements were acquired with a sampling frequency of $f_s = 100$ kHz at a Reynolds number of 7 400 (U = 18.5 m/s) based on the cylinder diameter. This is substantially higher than the wire cut-off frequency, $f_c^{(HWA)} = 13.4$ kHz, and therefore unnecessarily high. However, the cut-off frequency is high enough to resolve the Taylor microscale as approximated using the wavenumber spectrum. The average data rate for the LDA is $\nu = 94$ kHz and the corresponding Reynolds number is 8 600 (U = 21.5 m/s). The data density for the LDA measurements in this flow is considerably better for this set of measurements, $\nu\lambda_\tau = 94$. The cut-off frequency due to the finite dimensions of the scattering volume seems to be high enough for the measurements to resolve a significant part of the range of scales. Further, since the LDA and HWA data were acquired at slightly different free stream velocities, it is necessary to compare the wavenumber spectra and normalize by the energy (or a factor proportional to the energy) to enable comparison, see Chapter 11.

## 12.4 Flow length scales

**Integral scale**

The integral time scale is a rough measure of the interval over which the velocity signal is correlated with itself, and can be obtained by extrapolating the power spectrum to zero frequency: i.e.,

$$S_{11}(0) = \int_{-\infty}^{\infty} B_{11}(\tau)\, d\tau = 2\overline{u^2} T_u \tag{12.2}$$

where $T_u$ is the integral time scale (see, e.g., Tennekes and Lumley [135]). To

[1] The HWA data set was downloaded from *http : //ldvproc.nambis.de/data/dtudata.html*, while the LDA data were obtained directly from Holger Nobach.

avoid effects of windowing, the record length should preferably be much larger than this measure. Taylor's frozen field hypothesis can be used to approximate the corresponding integral scale:

$$L_u = UT_u = \frac{US_{11}(0)}{2\overline{u^2}} \tag{12.3}$$

These measures, as obtained from the HWA spectra, are displayed for both data sets in table 12.1.

**Kolmogorov microscale**

At the opposite end of the range of scales, the Kolmogorov microscale, $\eta_K$, gives a measure of the smallest dissipative length scales in the flow and is defined as:

$$\eta_K = \left[\frac{\nu^3}{\varepsilon}\right]^{1/4} \tag{12.4}$$

where $\varepsilon$ is the rate of dissipation of turbulence energy per unit mass and $\nu$ is the kinematic viscosity of the fluid. About 99% of the dissipation occurs at length scales larger than $2\pi\eta_K$, whereas the scales in the turbulence exist all the way down to the continuum limit, see George and Tutkun [48].

For convected disturbances, the highest frequency of interest in a flow is usually determined to correspond to the convection of the wavelength $\lambda_K = 2\pi\eta_K$ past the probe; i.e.,

$$f_K = \frac{U}{2\pi\eta_K} \tag{12.5}$$

where U is the convection velocity. If the disturbance is not convected, the highest frequency is characterized by the turbulence intensity instead of the convection velocity;

$$f_K \approx \frac{u'}{2\pi\eta_K}. \tag{12.6}$$

It is not obvious whether the cylinder wake flow measurements are dominated by temporal or convected disturbances. In Chapter 11 the main periodic disturbance has already been characterized as being temporal; i.e., not flow driven. However, the turbulence might still be dominated by convective disturbances, depending on how close to the cylinder the data is acquired.

As a rough method, one can estimate the dissipation rate from the one-dimensional wavenumber spectrum, assuming that the Kolmogorov inertial subrange theory applies; i.e., that there exists a $f^{-5/3}$ range (see, e.g., Gamard and George [40]). Further, one needs to assume that the spectral energy flux, $\varepsilon_K$, is constant and equal the dissipation $\varepsilon$. This also requires the existence of a spectral gap, which is really only present in the infinite Reynolds number limit. If these conditions are fulfilled, the whole-line one-dimensional spectrum can be expressed as (see; e.g., Tennekes and Lumley [135], pp. 273);

$$F_{11}(k_1) = \frac{9}{55}\alpha_K \varepsilon^{2/3} k_1^{-5/3} \tag{12.7}$$

where the Kolmogorov parameter $\alpha_K$ is assumed to be universal, or at least close to constant ($\alpha_K \approx 1.5 - 1.7$, typically). An estimate for the dissipation can now be obtained simply by solving for $\varepsilon$, which is where the plateau regions are appearing just before dissipation in the pre-multiplied one-dimensional wavenumber spectrum $F_{11}(k_1)k_1^{+5/3}$, see figures 12.7 and 12.8. These figures display the one-dimensional wavenumber spectra pre-multiplied by $k_1^{+5/3}$ of both the HWA data (computed using the FFT) as well as the LDA data (computed using residence time weighting as in equation 11.20). Since the inertial subrange does not really exist at the relatively low Reynolds numbers in any of the cases, the plateau regions (corresponding to the $k_1^{-5/3}$ range) are actually not very flat (see; e.g., George and Tutkun [48]).

Having an estimate for $\varepsilon$, one can also obtain an estimate for the Kolmogorov microscale from (12.4). The corresponding frequencies for the axisymmetric jet and cylinder wake flows are obtained from (12.5) and (12.6), respectively. For the cylinder wake flow, both the temporal and convected Kolmogorov microscale frequencies are estimated. These values, as obtained from the measurement data, are given in table 12.3. Though this is a crude assumption in the present cases, the method is nevertheless used to obtain a ballpark estimate. The Kolmogorov and Taylor microscales are already strict and conservative estimates for resolution requirements for spectral measurements, unless one wants to resolve the dissipation range which anyway usually requires a spatial resolution considerably smaller than the typical probe sizes.

Alternatively, for the jet, $\varepsilon$ is given by (see, e.g., Panchapakesan and Lumley [104] and Hussein *et al.* [58]);

$$\varepsilon = 0.42\frac{U_c^3}{x} \tag{12.8}$$

which gives a value of $\varepsilon$ which is more than twice as large as the previous estimate. This might seem significant, but comparing the resulting Kolmogorov microscales, the deviation is only 20%.

### Taylor microscale

In isotropic turbulence, the rate of dissipation is equal to (cf., Hinze [57]);

$$\varepsilon = 15\nu\overline{\left(\frac{\partial u}{\partial x}\right)^2} \tag{12.9}$$

The Taylor microscale, $\lambda_\tau$, is a length scale associated with the velocity gradients of the turbulent small scale structures. The longitudinal Taylor microscale is defined from (see; e.g., Tennekes and Lumley [135], pp. 66 or George "Lectures in Turbulence for the 21st Century" [49], pp. 164);

$$\overline{\left(\frac{\partial u}{\partial x}\right)^2} \equiv 2\frac{\overline{u^2}}{\lambda_\tau^2} \tag{12.10}$$

At large Reynolds numbers the small scale structures of the turbulence are

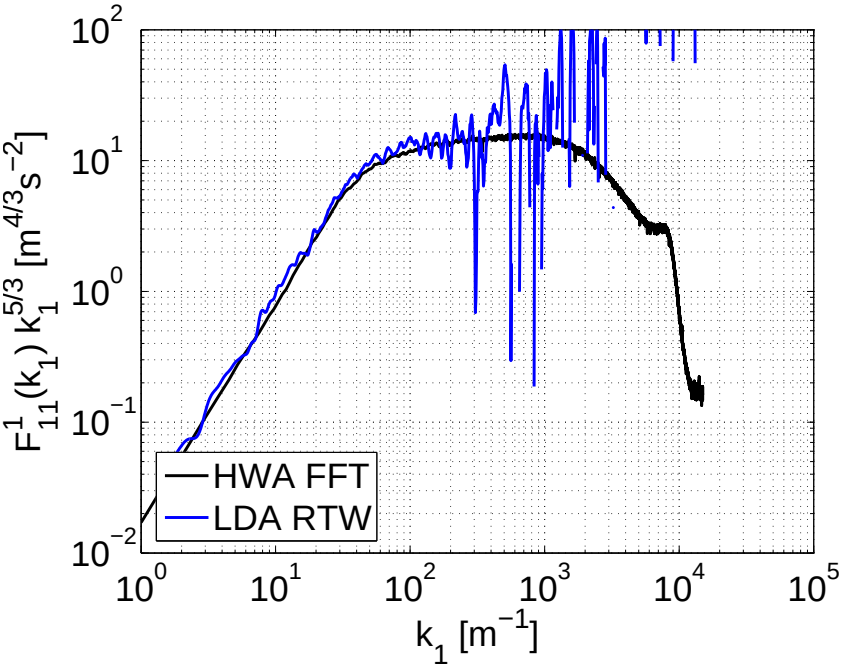


Figure 12.7: One-dimensional wavenumber spectrum from the axisymmetric jet HWA data of Frohnapfel [35] pre-multiplied by $k_1^{5/3}$ for estimation of dissipation.

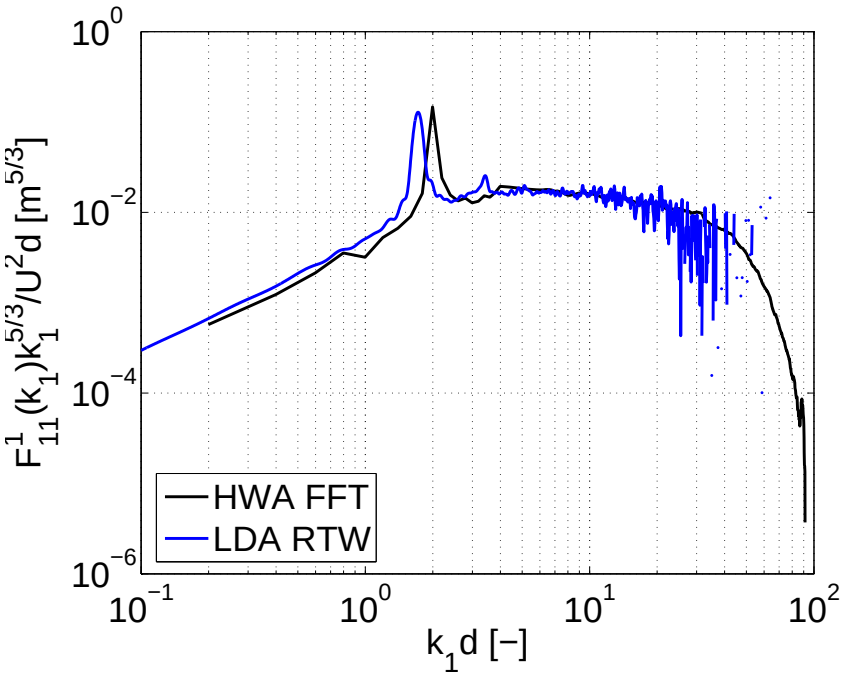


Figure 12.8: One-dimensional wavenumber spectrum from the cylinder wake HWA data of Nobach [96] normalized by energy variables and pre-multiplied by $k_1^{5/3}$ for estimation of dissipation.

approximately isotropic (see Tennekes and Lumley [135], pp. 262–267);

$$\varepsilon = 30\nu\frac{\overline{u^2}}{\lambda_\tau^2} \tag{12.11}$$

One could write the 'cut-off frequency' corresponding to the Taylor microscale as;

$$f_{\lambda_\tau} = \frac{U}{2\lambda_\tau} \tag{12.12}$$

These quantities have also been evaluated from the HWA measurement data and are presented in table 12.3 along with the Kolmogorov microscale estimates.

**Probe cut-off frequency**

By the Nyquist theorem, the cut-off frequency of a finite sized HWA probe with length $l$, is suggested by Wyngaard [156];

$$f_c = \frac{U}{2l} \tag{12.13}$$

The finite wire length will act as a low-pass filter, effectively setting the resolution of the measurements independently of the flow. Hence, there is no point in sampling much faster than twice this frequency, since it requires more data storage for the same record length and no further statistical convergence can be acquired by doing so.

For the LDA measurements, $l$ should correspond to the size of the scattering volume and is in the same way subject to spatial filtering; see, e.g., George and Lumley [43]. For LDA run in continuous mode, $l$ should correspond to the largest dimension of the measuring volume. For the burst-mode LDA, there is no averaging over the scattering volume if only a single particle is present in the volume. Hence, one could argue that $l$ should correspond to the smallest dimension of the scattering volume instead. The wire lengths, scattering volume dimensions and corresponding cut-off frequencies for both experiments (cf., Frohnapfel [35] and Gjelstrup [50]) can be found in table 12.2. For the LDA scattering volume, both dimensions are presented in the table.

**Comparison of estimated frequencies**

For an ideally designed experiment, the above mentioned frequencies should, if possible, relate as $f_{\lambda_\tau} < f_K \leq f_c^{(HWA)} = f_s$, where $f_s$ is the sampling frequency.

For the axisymmetric jet, the HWA sampling frequency was $f_s = 40$ kHz. The estimated frequencies relate as follows; $f_{\lambda_\tau} < f_c^{(HWA)} < f_K < f_s$. Thus, based on these crude estimates the measurements can resolve the Taylor microscale, but due to spatial filtering by the finite length wire, the Kolmogorov microscale cannot be resolved. Further, the sampling frequency, which seems to be chosen based on the Kolmogorov microscale, samples at a higher rate than can be resolved by the wire. The LDA was operating at an average data rate of $\nu = 318$ Hz and the estimated frequencies relate as; $\nu < f_{\lambda_\tau} < f_{c_{low}}^{(LDA)} < f_K < f_{c_{high}}^{(LDA)}$. Thus, from these estimates, the data rate itself is not sufficiently high to resolve the Taylor microscale, though the smallest dimension of the probe is

Table 12.1: Basic quantities of the acquired axisymmetric jet and cylinder wake data sets.

| Data set | U [m s$^{-1}$] | $\overline{u^2}$ [m$^2$ s$^{-2}$] | $S_{11}(0)$ [m$^2$ s$^{-1}$] | $L_u$ [m] |
|---|---|---|---|---|
| Jet | 8.40 | 4.75 | 0.0127 | 0.0112 |
| Wake | 21.50 | 33.43 | 0.0102 | 0.0033 |

Table 12.2: Probe dimensions and cut-off frequencies of the HWA and LDA measurements of the jet and cylinder wake flows.

| Data set | $l^{(HWA)}$ [m] | $f_c^{(HWA)}$ [s$^{-1}$] | $l^{(LDA)}$ [m] | $f_c^{(LDA)}$ [s$^{-1}$] |
|---|---|---|---|---|
| Jet | $1.25{\cdot}10^{-3}$ | $3.36{\cdot}10^{3}$ | $30/300\cdot10^{-6}$ | $140/14\cdot10^{3}$ |
| Wake | $0.80{\cdot}10^{-3}$ | $13.4{\cdot}10^{3}$ | $150/2500\cdot10^{-6}$ | $72/4.3\cdot10^{3}$ |

small enough to resolve the Kolmogorov microscale.

For the cylinder wake HWA measurements, with sampling frequency $f_s = 100\,\text{kHz}$, $f_{\lambda_\tau} < f_c^{(HWA)} < f_K^{temp.} < f_s < f_K^{conv.}$, about the same situation applies as for the HWA jet measurements: scales much larger than the Taylor microscale cannot be resolved due to the wire cut-off. But for the LDA measurements, with $\nu = 93\,944$ Hz, $f_{c_{low}}^{(LDA)} < f_{\lambda_\tau} < f_K < f_{c_{high}}^{(LDA)} < \nu$. Thus, if the higher cut-off frequency (smallest scattering volume dimension) dictates the spatial filtering, the flow is resolved down to the crude estimate of the Kolmogorov scale.

Now, the question is whether the estimated Taylor microscale is the actual one of the flow, or just the low-pass filtered one that the probe 'sees' due to its finite length. This can for example be seen in the autocorrelation, which will have a superimposed correlation of the instrument at small time separations over the one of the actual flow, yielding a different estimate from the parabolic fitting at the origin; see, e.g., [43]. Further, the HWA probe sizes are of the same order and only slightly smaller than the estimated Taylor microscales in both measurements. However, the probe size is smaller for the LDA and, as can be seen in figures 12.7 and 12.8, the burst-mode LDA spectra fit well to the HWA FFT ones within the frequency ranges corresponding to the wavenumbers of the plateaus to the extent that the relative error of the LDA burst-mode spectra doesn't kill the signal. Thus, the dissipation is estimated to roughly the same value from the LDA as from the HWA spectra. This indicates that the estimates of the Taylor microscales are actually not severely distorted due to the HWA probe sizes in both cases.

Table 12.3: Estimated small scale turbulence properties of the axisymmetric jet and cylinder wake flows.

| Data set | $\varepsilon$ [m$^2$s$^{-3}$] | $\eta_K$ [m] | $f_K^{temp.}$ [s$^{-1}$] | $f_K^{conv.}$ [s$^{-1}$] | $\lambda_\tau$ [m] | $f_{\lambda_\tau}$ [s$^{-1}$] |
|---|---|---|---|---|---|---|
| Jet | 434 | $53{\cdot}10^{-6}$ | - | $25{\cdot}10^{3}$ | $2.2{\cdot}10^{-3}$ | $1.9{\cdot}10^{3}$ |
| Wake | $13.7{\cdot}10^{3}$ | $22{\cdot}10^{-6}$ | $41{\cdot}10^{3}$ | $156{\cdot}10^{3}$ | $1.0{\cdot}10^{-3}$ | $10{\cdot}10^{3}$ |

**Data density**
Adrian and Yao [1] suggested a measure of the data density, which they defined as the mean number of samples in one Taylor microscale; $\nu\lambda_\tau$. For $\nu\lambda_\tau \gg 1$, the data can represent the signal fairly well. Using the estimates from table 12.3, the data densities are $\nu\lambda_\tau \approx 0.7$ for the axisymmetric jet and $\nu\lambda_\tau \approx 94$ for the cylinder wake measurements.

## 12.5 Results

The two data sets described above are used as examples for comparison of the performance of power spectra computed using the sample-and-hold (S/H) (see; e.g., [4]) and linear interpolation (LIN) schemes with uniform resampling to power spectra based on corresponding HWA data. The spectra computed from the LDA data have been resampled at the same rate as the HWA data in each corresponding case.

### 12.5.1 Axisymmetric turbulent far jet

Table 11.2 displays the parameters used for evaluating the spectra using the various methods. N is the total number of samples, $N_s$ is the number of samples per block, $N_b$ the number of blocks, $T_b$ the record length, $f_s$ the sampling frequency and $f_{\text{resampl.}}$ the resampling frequency. $\nu$ is the average data rate for the LDA measurements. The record length of the LDA data blocks was limited to less than or equal to 2 s due to the way the data was acquired. The record length of the blocks was chosen to 1 s. This is well above the integral time scale, which was estimated to $T_u = S_{11}(0)/2\overline{u^2} \approx 1$ ms. For the sake of comparison, the HWA data blocks were chosen to have the same block length as the resampled LDA data blocks.

Figure 12.1 displays a part of a record of the time history of the LDA signal along with the interpolated and resampled signals S/H and LIN. The resampling rate is about 126 times higher than the average data rate of the LDA measurements. The HWA and LDA spectral estimates are displayed in a logarithmic plot in figure 12.3. The HWA FFT spectrum is shown in black. The LDA S/H and LDA LIN spectra are displayed in red and green, respectively. To recover the spectral estimates at higher frequencies, the noise removal method described in Chapter 9 was applied to these spectra after implementing a first order Savitzky-Golay filter, see figure 12.4.

The S/H and LIN spectra are roughly of the same magnitude at low frequencies, however differing significantly from that of the HWA spectrum. Further, they have a distribution of energy across the band-width that differs from that of the reference HWA FFT spectrum. The problem with these methods is mainly that by interpolating and resampling, the new signal introduces energy at frequencies that is not present in the actual flow. The Fourier coefficients obtained when Fourier transforming the new signal will contain additional coefficients to that of the original signal, since one is forcing the signal toward values that are not actually in the flow. This leads to large discrepancies if the average data rate of the LDA is much smaller than the highest frequencies of the flow; i.e., if $\nu\lambda_\tau < 1$. Typically, this results in the intermediate range of the S/H spectrum having a constant slope of -2 and the spectrum starts rolling

Table 12.4: Parameters used for computing the spectra for the axisymmetric turbulent far jet displayed in figures 12.3 and 12.4.

| | N | $N_s$ | $N_b$ | $T_b$ [s] | $f_s$ / $\nu$ [Hz] | $f_{resampl.}$ |
|---|---|---|---|---|---|---|
| HWA FFT | 10 000 000 | 40 000 | 250 | 1.00 | 40 000 | - |
| LDA S/H | 10 000 000 | 40 000 | 250 | 1.00 | 318 | 40 000 |
| LDA LIN | 10 000 000 | 40 000 | 250 | 1.00 | 318 | 40 000 |

Table 12.5: Whole line integral of the axisymmetric jet spectra before and after random noise correction.

| $\int S(f)\,df$ | Uncorrected | Corrected |
|---|---|---|
| HWA FFT | 4.209 | 4.208 |
| LDA S/H | 4.822 | 4.811 |
| LDA LIN | 3.408 | 3.410 |

off at a frequency of about $\nu/2\pi = 318/2\pi \approx 50$ Hz, as expected from (12.1). When comparing the S/H spectrum to the HWA FFT one, it becomes increasingly apparent that its $f^{-2}$ slope is entirely due to the frequency dependent noise. Hence, the S/H spectrum is essentially buried in noise, or perhaps more correctly, has been transformed into noise. The same thing happens to the LIN spectrum, except that the effect is even worse. The roll-off of the spectrum is significantly steeper than even the S/H spectrum.

The whole-line integrals of the original and noise corrected spectra are listed in table 12.5. In this particular case, the S/H spectrum overpredicts the energy by about 15%, while the LIN spectrum underpredicts the energy by about 24%. This further confirms the lack of correctness of the algorithms applied to this case.

### 12.5.2 Cylinder wake

As was mentioned in Chapter 11, the LDA and HWA data of this data set were acquired in flows of slightly different free stream velocities. Since the free stream velocities only differ by about 16%, the spectra are considered to be sufficiently similar in distribution for comparison of the techniques if the spectra are compared in wavenumber space and normalized by the energy. Since the peak is a temporal disturbance, the peak will not line up between the spatial HWA and LDA spectra, whereas the convected turbulence should concur fairly

Table 12.6: Parameters used for computing the spectra for the cylinder wake flow displayed in figures 12.5 and 12.6.

| | N | $N_s$ | $N_b$ | $T_b$ [s] | $f_s$ / $\nu$ [Hz] | $f_{resampl.}$ |
|---|---|---|---|---|---|---|
| HWA FFT | 131 072 | 1 024 | 128 | 0.01 | 100 000 | - |
| LIN | 997 000 | 997 | 1000 | 0.01 | 93 944 | 100 000 |
| S/H | 997 000 | 997 | 1000 | 0.01 | 93 944 | 100 000 |

Table 12.7: Whole line integral of the cylinder wake spectra before and after random noise correction.

| $\int S(f)\,df$ | Uncorrected | Corrected |
|---|---|---|
| HWA FFT | 0.0649 | 0.0648 |
| S/H | 0.0821 | 0.0788 |
| LIN | 0.0780 | 0.0771 |

well since the difference in free stream velocity is small between the data sets. It was argued in Chapter 11 that since the turbulence intensity is only most weakly Reynolds number dependent for fully developed turbulent flow and the integral length scale is only weakly dependent on the Reynolds number, one can instead normalize by the free stream velocity squared times the cylinder diameter to compensate for the difference in energy.

The parameters used for evaluating the spectra are displayed in table 12.6. The sampling frequency of the HWA data, $f_s = 100\,000$ Hz, and the average data rate of the LDA measurements, $\nu = 93\,944$ Hz, are fairly similar. A short record of the time history of the LDA signal with the interpolated and resampled signals is displayed in figure 12.2.

As can be seen in figure 12.5, when the average sampling rate of the LDA data is large enough to resolve a larger portion of the turbulence scales of the flow ($\nu\lambda_\tau \gg 1$), the deviations between the true and interpolated signal are not as devastating to the resulting power spectrum. However, some discrepancies still exist in the higher frequency end, especially in the levels of the noise floors which are higher for the resampling methods and, again, highest for S/H. To check whether these discrepancies are solely the effect of different noise floors, let's again perform the noise correction from Chapter 9, see figure 12.6. As is seen in the figure, both S/H and LIN still overpredict the spectrum at the higher frequencies, which is most probably an effect of addition of higher frequencies to the spectrum stemming from the small discrepancies between the original and the interpolated and resampled signals; i.e., step noise. This indicates that the LDA data cannot necessarily represent the flow at the smallest scales, which is probably a consequence of the fact that the smallest dimension of the scattering volume ($l^{(LDA)} = 150\ \mu$m) is somewhat larger than the estimated Kolmogorov microscale ($\eta_K = 22\ \mu$m). Further, one has to take into account the uncertainty of estimating the smaller flow scales which might be overpredicted. The large convective scales are, however, well predicted. This should be expected, since the large frequencies of the flow are easier to capture using this type of methods.

The whole-line integrals of the noise uncorrected and corrected spectra are given in table 12.7. Even though the conditions for interpolation and resampling should be considerably improved for this high LDA data rate, the S/H and LIN algorithms overpredict the energy by 22% and 19%, respectively, after noise correction.

## 12.6 Summary and conclusions

In the axisymmetric jet flow, the average LDA data density $\nu\lambda_\tau = 0.7$ was low. Hence, the data rate was low compared to the time scales of the smallest

scales such as the Taylor microscale, leading to a domination of the frequency dependent $f^{-2}$ noise across the bandwidth. Comparing the S/H and HWA FFT spectra in figure 12.3, it is apparent that the turbulence is not visible in *any* part of the S/H spectrum. Under these conditions, S/H clearly cannot reproduce the spectrum. Further, the linear interpolation and resampling method showed the same behavior as sample-and-hold at the large convective scales in the low data rate jet spectrum. As the frequency increases, the spectrum rolls off at an even higher rate than S/H.

The average data rate of the LDA measurements displays a large effect on the frequency dependent noise arising due to signal drop-out reminiscent effect of the S/H method. For the cylinder wake flow, where the average LDA data density was quite large ($\nu\lambda_\tau = 94$), resolving a large portion of the scales in the frequency range of the flow, the effect was relatively small at the large convective scales. At the highest frequencies, however, both algorithms failed to predict the spectrum correctly. The explanation lies in the resolution of the highest frequencies of the LDA data; Even with a high enough particle arrival rate, the scattering volume size is about seven times larger than the estimated Kolmogorov microscale and hence the flow cannot be resolved below twice the size of this limiting spatial scale (according to Nyquist).

Despite the efforts and the numerous publications applying S/H to LDA data to construct spectral estimators, this method does not seem to apply well, except under very strict conditions which are rarely satisfied for LDA measurements. The only correct way, it seems, is to compute burst-mode LDA spectra using the residence time weighted methodology described in Chapter 11. However, if the data rate of the LDA measurements is high enough to resolve the convected Kolmogorov microscale, one can indeed resample the LDA signal equidistantly. The problem with LDA is that a high data rate will violate having only one particle at a time in the scattering volume, which will make it behave like a tracker with ambiguity noise (see [20]). Unless these conditions are fulfilled, which they rarely are for LDA measurements, building spectra using the S/H resampling and interpolation scheme yields a spectrum swamped in filtering effects and noise, essentially burying the spectrum beyond recognition. The typical data rate of LDA measurements is usually orders of magnitude lower than what is required to resolve the Kolmogorov scale or less, which is why S/H rarely should be used. Further, spatial filtering by the probe should always be considered; the probe size cannot be larger than the smallest eddies that one wants to resolve.

# Part V

# Summary and Future Work

# Chapter 13

# Summary and recommendations for future work

## Summary

The induced effect of passive actuator vortex generators has been investigated and characterized using Stereoscopic Particle Image Velocimetry (SPIV) in a low Reynolds number experiment. The vortices displayed helical symmetry across the vortex core, with helical parameters varying linearly with device angle. Further, the variations with downstream position of the helical parameters was investigated in the flow over a circular sector, also displaying linear dependence except at the abrupt change in geometry at the trailing edge of the bump. The performance of the devices in terms of separation control showed high efficiency in terms of reduction of recirculating flow. Further, the behavior and performance of vortex generators in a higher Reynolds number setting was investigated using Stereoscopic PIV in the newly built LM Glasfiber wind tunnel over a DU 91-W2-250 profile. The measurements displayed patterns similar to those found at lower Reynolds numbers in the above mentioned generic experiments. In addition, the differences between the measurements found at the lower and higher Reynolds numbers investigated in the LM Glasfiber wind tunnel can be considered small. This suggests that the same kind of flow process is active at the high and low Reynolds numbers within the considered range, indicating that it is plausible that the helical symmetry persists at these higher Reynolds numbers. For this experiment, the vortex generator geometry was optimized empirically from measured polars, showing a significant improvement in the measured controlled velocity profiles as compared to the uncontrolled one close to stall.

In the process of characterizing the inlet flow and dynamics of the vortex generator induced flow, burst-mode LDA spectra were computed from a theory developed by Buchhave and George (cf., [19, 46]). The theory builds on the residence time weighting of all statistical analysis of burst-mode LDA data, yielding correction for the high-velocity-bias. The burst-mode spectral estimator

is computed using the Direct Fourier Transform (DFT) due to the random sampling and residence time weighting. The obtained burst-mode LDA spectra show good concurrency with corresponding spectra obtained from Hot-Wire Anemometry (HWA) measurements. The properties of the data sets borrowed for these investigations and their spectra were investigated and aliasing peaks found in the burst-mode LDA spectra were explained by the finite resolution of the LDA data.

In conjunction with the application of the theory for burst-mode LDA spectra, a theory for the removal of the random noise in spectra and correlations was developed. The random noise impact, manifesting itself as white noise in the spectrum, or alternatively, as a spike at the origin of the autocorrelation, was localized to the self-products in the Direct Fourier Transform. Simply removing the spike will cause the resulting spectrum to integrate to zero energy. The reason for this is that in the process of removing the spike at the origin, the variance is also thrown away. One must therefore compensate for this whenever excluding the self-products from the DFT.

Further, the performance of commonly employed interpolation and resampling methods for estimating power spectra from LDA data was investigated. The results show that the applied methods cannot predict the spectra when the data rate of the LDA data is low compared to the time scales of the flow. The obtained sample-and-hold spectrum at the low data rate is buried in frequency dependent noise across most of the bandwidth, rolling off as $f^{-2}$ as predicted from theory. Linear interpolation and resampling yielded even worse results with a spectrum rolling off even faster.

In the investigation of the dynamics of the device induced vortices, no periodic oscillations were observed. The longitudinal vortices most probably have a random or, at best, quasi-periodic behavior.

## Recommendations for future work

Some of the ideas that emerged during the conduction of the work could not be pursued for practical reasons such as limitations of time and facilities. In the following, some suggestions are presented for the further development of the current work on characterization of the vortex generator induced vortices.

For future investigations, it would be highly interesting to further investigate the downstream development of the device induced vortices. This can constitute a basis for the development of a more advanced model for the vortices. A general analytical model for the vortices and their impact could potentially save large amounts of computational time and experimental effort, that commonly is invested for parametric studies for each single geometry of application. It is also interesting to further study and characterize the effect of submerged vortex generators, which are more impacted by the velocity gradients in the boundary layer.

The generic experiments had several limitations, such as the low Reynolds number yielding a non-realistic boundary layer without a log-layer. Also, the turbulence had to be tripped by an inlet grid, feeding turbulence to the boundary layer from the free stream. In order to obtain a realistic boundary layer and large enough structures to be resolvable, measurements should preferably be conducted in a larger wind tunnel with a more powerful fan to obtain large

and easily resolvable structures at higher, more realistic Reynolds numbers. This can ensure the existence of the log-layer and in general more realistic flow conditions for most applications. Also, the inlet conditions are important where a minimum of upstream disturbances (or at least known characteristics of them) is vital to control the inflow to the vortex generators, as was seen in Chapter 8.

CFD computations should preferably not be conducted for these flows for reasons expressed mainly in the introduction and Chapter 6. However, if this alternative is still considered, one should preferably take some more precautions. One example is to properly measure the inlet conditions using both SPIV and time resolved measurements preferably using HWA. These measurements can be applied to Proper Orthogonal Decomposition and Linear Stochastic Estimation to characterize the inlet, capturing both the temporal and spatial coherence of the flow, see Druault *et al.* [30].

It would also be interesting to conduct more extensive investigations of the experimental setup at the LM Glasfiber wind tunnel. For example, it would be interesting to investigate the effect of the vortex generators at more upstream positions, which was not possible due to the larger impact of reflections at these positions. If the application of Rhodamine 6G to the reflecting surfaces would have been accepted, those measurements would most probably have been possible. An alternative is to look further into if other types of Rhodamine that are non-toxic are available. Further, some of the obtained results can not be fully explained, only hypothesized, and might be interesting to pursue further in future experiments.

# Bibliography


[1] **ADRIAN, R. J. & YAO, C. S.** 1987 Power spectra of fluid velocities measured by laser doppler velocimetry. *Experiments in Fluids* **5**, 17–28.

[2] **ADRIAN, R. J.** 2007 Hairpin vortex organization in wall turbulence. *Physics of Fluids* **19**, 041301.

[3] **AGULLO, O. & VERGA, A. D.** 1997 Exact two vortices solutions of Navier-Stokes equations. *Physical Review Letters* **78**, 2361–2364.

[4] **ALBRECHT, H.-E., BORYS, M., DAMASCHKE, N. & TROPEA, C.** 2003 Laser Doppler and Phase Doppler Measurement Techniques. Springer-Verlag, Berlin, Heidelberg.

[5] **ALEKSEENKO, S. V., KUIBIN, P. A., OKULOV, V. L. & SHTORK, S. I.** 1999 Helical vortices in swirl flow. *Journal of Fluid Mechanics* **382**, 195–243.

[6] **BATCHELOR, G. K.** 1964 Axial flow in trailing line vortices. *Journal of Fluid Mechanics* **20**, 645–658.

[7] **BATCHELOR, G. K.** 1967 An Introduction to Fluid Dynamics, Cambridge University Press; ISBN: 0521663962.

[8] **BENDAT, J. S. & PIERSOL, A. G.** 2000 Random data: Analysis and Measurement Procedured, ($3^{rd}$ ed.) John Wiley & Sons, New York.

[9] **BENEDICT, L. H. & GOULD, R. D.** 1995 Experience using Kalman reconstruction for enhanced power spectrum estimates. *6th International Conference on Laser Anemometry* eds. Huang, T. T., Turner, J., Kawahashi, M., Otugen, M. V., pp. 1–7, ASME FED–Vol. 228.

[10] **BENEDICT, L. H., NOBACH, H. & TROPEA, C.** 2000 Estimation of turbulent velocity spectra from laser Doppler data. *Measurement Science and Technology* **11**, 1089–1104.

[11] **BETTERTON, J. G., HACKETT, K. C., ASHILL, P. R., WILSON, M.J., WOODCOCK, I.J., TILMAN, C.P. & LANGAN, K.J.** 2000 Laser Doppler anemometry investigation on subboundary layer vortex generators for flow control, *10th International Symposium on Applications of Laser Techniques to Fluid Mechanics*, Lisbon, July 10–13.

[12] **BEUTLER, F. J.** 1970 Alias-free randomly timed sampling of stochastic processes. *IEEE Transactions on Information Theory*, IT-16 **2**, 147–152.

[13] **BILINSKIS, I. & MIKELSONS, A.** 1990 Application of randomized or irregular sampling as an anti-aliasing technique. *Signal Processing V: Theories and Application*, Elsevier Science Publishers, Amsterdam, 505–508.

[14] **BILINSKIS, I. & MIKELSONS, A.** 1992 Randomized signal processing. Prentice Hall International, UK.

[15] **BJÖRCK, A.** 1993 2-D airfoil wind tunnel test at stall. *Proceedings IEA 7th symposium on aerodynamics of wind turbines.*

[16] **BRAGG, M. B. & GREGOREK, G. M.** 1987 Experimental study of airfoil performance with vortex generators. *Journal of Aircraft* **24**, 305–309.

[17] **BROEREN, A. P. & BRAGG, M. B.** 2001 Spanwise variation in the unsteady stalling flowfields of two-dimensional airfoil models, *AIAA Journal* **39**, 1641-1651.

[18] **BROWN, A. C., NAWROCKI, H. F. & PALEY, P. N.** 1968 Subsonic diffusers designed integrally with vortex generators. *Journal of Aircraft* **5**, 221–229.

[19] **BUCHHAVE, P.** 1979 Errors and Correction Methods in Turbulence Measurements with the LDA, Ph.D. Dissertation. Department of Mechanical Engineering, State University of New York at Buffalo.

[20] **BUCHHAVE, P., GEORGE, W. K. & LUMLEY, J. L.** 1979 The Measurement of Turbulence with the Laser-Doppler Anemometer. *Annual Review of Fluid Mechanics*, **11**, 443–504.

[21] **CAPP, S. P.** 1983 Experimental investigation of the turbulent axisymmetric jet, Ph.D. Dissertation. Department of Mechanical Engineering, State University of New York at Buffalo.

[22] **COLLINS, L. R. & KESWANI, A.** 2004 Reynolds number scaling of particle clustering in turbulent aerosols. *New Journal of Physics* **6**, 119.

[23] **COOLEY, J. W. & TUKEY, O. W.** 1965 An Algorithm for the Machine Calculation of Complex Fourier Series. *Mathematics of Computation* **19**, 297–301.

[24] **COUDERT, S. J. M. & SCHON, J-P.** 2001 Back-projection algorithm with misalignment corrections for 2D3C stereoscopic PIV. *Measurement Science and Technology* **12**, 1371–1381.

[25] **CROW, S. C.** 1970 Stability theory for a pair of trailing vortices. *AIAA Journal* **8**, 2172–2179.

[26] **CUTLER, A. & BRADSHAW, P.** 1986 The interaction between a strong longitudinal vortex and a turbulent boundary layer. *AIAA Paper*, 86-1071, New York.

[27] **CUTLER, A. & BRADSHAW, P.** 1989 Vortex/Boundary-layer interactions. *AIAA Paper*, 89-0083, New York.

[28] **DRITSCHEL, G.** 1985 The stability and energetics of corotating uniform vortices. *Journal of Fluid Mechanics* **157**, 95–134.

[29] **DRITSCHEL, G.** 1995 A general theory for two-dimensional vortex interactions. *Journal of Fluid Mechanics* **293**, 269–303.

[30] **DRUAULT, P., LARDEAU, S., BONNET, J. P., COIFFET, F., DELVILLE, J., LAMBALLAIS, E., LARGEAU, J. F. & PERRET, L.** 2005 A Methodology for the Generation of Realistic 3D Turbulent Unsteady Inlet Conditions for LES. *AIAA Journal* **42**, 447–456.

[31] **ESCUDIER, M. P.** 1988 Vortex breakdown: observations and explanations. *Progress in Aerospace Sciences* **25**, 189–229.

[32] **FEIR, J. B.** 1965 The effect of an arrangement of vortex generators installed to eliminate wind tunnel diffuser separation. *UTIAS Technical Note 87*, Institute for Aerospace Studies, University of Toronto, Toronto, Canada.

[33] **FINGERSON, L. M. & FREYMUTH, P.** 1983 Thermal anemometers, Fluid Mechanics Measurements (ed. Goldstein RJ), pp. 99–154, Hemisphere, Washington.

[34] **FOUCAUT, J., MILIAT, B., PERENNE, N. & STANISLAS, M.** 2004 Characterization of Different PIV Algorithms using the EUROPIV Synthetic Image Generator and Real Images from a Turbulent Boundary Layer. In: *Stanislas M et al (eds) Particle Image Velocimetry: Recent Improvement. Proc. of the EUROPIV 2 Workshop on Particle Image Velocimetry*, Zaragoza, Spain, March 31 - April 1, 2003. Springer, Berlin, Heidelberg New York.

[35] **FROHNAPFEL, B.** 2003 Multi-point similarity of the axisymmetric turbulent far jet and its implications for the POD, M.Sc. thesis. Department of Thermo and Fluid Dynamics, Chalmers University of Technology, Gothenburg. Lehrstuhl für Strömungsmechanik, Friedrich-Alexander-Universität, Erlangen-Nürnberg.

[36] **FUGLSANG, P. & BOVE, S.** 2008 Wind tunnel testing of airfoils involves more than just wall corrections. *European Wind Energy Conference*, Brussels, March 31 – April 3.

[37] **GAD-EL-HAK, M. & BANDYOPADHYAY, P. R.** 1994 Reynolds number effects in wall-bounded turbulent flows. *Applied Mechanics Reviews* **47**, 307–365.

[38] **GAD-EL-HAK, M.** 2000 Flow Control. Cambridge Uni. Press, Cambridge, pp. 174.

[39] **GADETSKII, V. M., SEREBRIISKII, I. A. M. & FOMIN, V. M.** 1972 Investigation of the influence of vortex generators on turbulent boundary layer separation. *Uchenye Zapiski TSAGI* **3**, 22–28.

[40] **GAMARD, S. & GEORGE, W. K.** 1999 Reynolds number dependence of energy spectra in the overlap region of isotropic turbulence. *Flow, Turbulence and Combustion* **63**, 443–477.

[41] **GASTER, M. & ROBERTS, J.B.** 1975 Spectral analysis of randomly sampled signals. *Journal of the Institute of Mathematics and Its Applications* **15**, 195–216.

[42] **GEISLER, R., SCHRÖDER, A., WILLERT, C. & ELSINGA, G. E.** 2008 Investigation of vortex-generators within a turbulent boundary layer flow using time-resolved tomographic PIV, *14th International Symposium on Applications of Laser Techniques to Fluid Mechanics*, Lisbon, Portugal, July 07–10.

[43] **GEORGE, W. K. & LUMLEY, J. L.** 1973 The laser-Doppler velocimeter and its application to the measurement of turbulence, *Journal of Fluid Mechanics* **60**, 321–362.

[44] **GEORGE, W. K.** 1974 The measurement of turbulence intensities using real-time laser-Doppler velocimetry, *Journal of Fluid Mechanics* **66**, 11–16.

[45] **GEORGE, W. K.** 1975 Limitations to Measurement Accuracy Inherent in the Laser Doppler Signal. *Proceedings of the LDA-Symposium*, Copenhagen, 20–63.

[46] **GEORGE. W. K., BEUTHER, P. D. & LUMLEY, J. L.** 1978 Processing of Random Signals. *Proceedings of the Dynamic Flow Conference*, Skovlunde, Denmark, (PO Box 121, DK-2740 Skovlunde), 757–800.

[47] **GEORGE, W. K. & DAVIDSON, L.** 2003 Role of Initial Conditions in Establishing Asymptotic Flow Behavior. *AIAA Journal* **42**, 438–446.

[48] **GEORGE, W. K. & TUTKUN, M.** 2009 Mind the Gap: A Guideline for LES. *Transactions of the Royal Society.*

[49] *www.turbulence-online.com*

[50] **GJELSTRUP, P., NOBACH, H., JØRGENSEN, F. E. & MEYER, K. E.** 2000 Experimental verification of novel spectral analysis algorithms for Laser Doppler Anemometry data. *Proc. of the 10th International Symposium on Applications of Laser Techniques to Fluid Mechanics*, July 10–13, Lisbon, Portugal.

[51] **GLAUSER, M. N. & GEORGE, W. K.** 1992 Application of multipoint measurements for flow characterization. *Experimental Thermal and Fluid Science* **5**, 617–632.

[52] **GODARD, G. & STANISLAS, M.** 2006 Control of a decelerating boundary layer. Part 1: Optimization of passive vortex generators. *Aerospace Science and Technology* **10**, 181–191.

[53] **GÖRTLER, H.** 1955 Dreidimensionales zur Stabilitätstheorie Laminarer Grenzschichten. *ZAMM* **35**, 326.

[54] **HEATON, C. J. & PEAKE, N.** 2007 Transient growth in vortices with axial flow. *Journal of Fluid Mechanics* **587**, 271–301.

[55] **HELMHOLTZ, H.** 1858 Über die Integration der Hüdrodünamischen Gleichungen welche den Wirbelbewegungen entsprechen. *Crelles J.* **55**, 25.

[56] **HENRY, J. R., WOOD, C. C. & WILBUR, S. W.** 1956 Summary of Subsonic Diffuser Data. *NACA RML-56F05*, Washington, D. C.

[57] **HINZE, J. O.** 1959 Turbulence. McGraw-Hill, New York.

[58] **HUSSEIN, H. J., CAPP, S. P. & GEORGE, W. K.** 1994 Velocity measurements in a high-Reynolds-number, momentum-conserving, axisymmetric, turbulent jet. *Journal of Fluid Mechanics* **258**, 31–75.

[59] **JENKINS, G. M. & WATTS, D. G.** 1968 Spectral analysis and its applications, Holden-Day, San Francisco.

[60] **JENKINS, L., GORTON, S.A. & ANDERS, S.** 2002 Flow control device evaluation for an internal flow with an adverse pressure gradient. *AIAA Paper 2002-0266*, 40th AIAA Aerospace Sciences Meeting and Exhibit, Reno.

[61] **JIMÉNEZ, J., MOFFATT, H. K. & VASCO, C.** 1996 The structure of the vortices in freely decaying two-dimensional turbulence. *Journal of Fluid Mechanics* **313**, 209–222.

[62] **JIMÉNEZ, J. & PINELLI, A.** 1999 The autonomous cycle of near wall turbulence. *Journal of Fluid Mechanics* **389**, 335–359.

[63] **JOHANSSON, P. B. V., & GEORGE, W. K.** 2006 Far Downstream Evolution of the High Reynolds Number Axisymmetric Wake Behind a Disk, Part 1: Single Point Statistics. *Journal of Fluid Mechanics* **555**, 363–385.

[64] **von KARMAN, T. & HOWARTH, L.** 1938 On the statistical theory of isotropic turbulence. *Proceedings of the Royal Society*, London, Series A **164**, 192.

[65] **KEANE, R. D. & ADRIAN, R. J.** 1990 Optimization of particle image velocimeters. Part I: Double pulsed systems *Measurement Science and Technology* **1**, 1202–1215.

[66] **KUO, K. K.** 2005 Principles of combustion. Second ed., John Wiley & Sons Inc, New York, pp. 376.

[67] **LAMB, H.** 1932 Hydrodynamics. Sixth ed., Cambridge Univ. Press, Cambridge.

[68] **LEIBOVICH, S.** 1978 The structure of vortex breakdown. *Annual Review of Fluid Mechanics* **10**, 221–246.

[69] **LEON-GARCIA, A. & WIDJAJA, I** 2004 Communication networks: fundamental concepts and key architectures. Second ed., McGraw-Hill, New York, pp. 845–849.

[70] **LEWEKE, T. & WILLIAMSON, C. H. K.** 1998 Cooperative elliptic instability of a vortex pair. *Journal of Fluid Mechanics* **360**, 85–119.

[71] **LIANDRAT, J., AUPOIX, B. & COUSTEIX, T.** 1986 Calculation of longitudinal vortices embedded in a turbulent boundary layer. *Fifth Symposium of Turbulent Shear Flows*, eds. F. Durst, B. E. Launder, F. W. Schmidt and J. H. Whitelaw, 7.17–7.22, Springer Verlag, New York.

[72] **LIN, J.C. & HOWARD, F.G.** 1989 Turbulent flow separation control through passive techniques. *AIAA 2nd Shear Flow Conference*, March 13-16 1989, Tempe AZ, AIAA Paper 89-0976.

[73] **LIN, J.C., HOWARD, F.G. & BUSHNELL, D.M.** 1990 Investigation of several passive and active methods for turbulent flow separation control. *AIAA 21st Fluid Dynamics, Plasma Dynamics and Laser Conference*, June 18-20 1990, Seattle, WA, AIAA Paper 90-1598.

[74] **LIN, J.C., SELBY, G.V. & HOWARD, F.G.** 1991 Exploratory study of vortex-generating devices for turbulent flow separation control. *29th Aerospace Sciences Meeting*, January 7-10, Reno, Nevada, AIAA Paper 91-0042.

[75] **LIN, J.C.** 1999 Control of turbulent boundary layer separation using microvortex generators. *AIAA Paper*, 99-3404.

[76] **LIN, J. C.** 2002 Review of research on low-profile vortex generators to control boundary-layer separation. *Progress in Aerospace Sciences* **38**, 389–420.

[77] **LIU, J., PIOMELLI, U. & SPALART, P. R.** 1996 Interaction between a spatially growing turbulent boundary layer and embedded streamwise vortices. *Journal of Fluid Mechanics* **326**, 151–179.

[78] **LUMLEY, J. L.** 1970 Stochastic Tools In Turbulence. Dover Publications.

[79] **LUMLEY, J. L.** 1965 Interpretation of Time Spectra Measured in High-Intensity Shear Flows. *Physics of Fluids* **8**, 1056–1062.

[80] **MAANEN, H. van & TULLEKEN, H.** 1994 Application of Kalman reconstruction to laser-Doppler anemometry data for estimation of turbulent velocity fluctuations. *Seventh International Symposium on Applications of Laser Technology to Fluid Mechanics* Lisbon, Portugal, paper 23.1.

[81] **MARTEMIANOV, S. & OKULOV, V. L.** 2004 On heat transfer enhancement in swirl pipe flows. *International Journal of Heat and Mass Transfer* **47**, 2379-2393.

[82] **MASRY, E.** 1971 Random sampling and reconstruction of spectra. *Information Control* **19**, 275–288.

[83] **MASRY, E.** 1978 Alias-free sampling: an alternative conceptualization and its applications. *IEEE Transactions on Information Theory*, IT-24 **3**, 317–324.

[84] **MASRY, E.** 1978 Spectral estimation of continuous-time processes: performance comparison between periodic and Poisson sampling schemes. *IEEE Transactions on Automatic Control*, AC-23 **4**, 679–685.

[85] **MASRY, E.** 1978 Poisson sampling and spectral estimation of continuous-time processes. *IEEE Transactions on Information Theory*, IT-24 **2**, 173–183.

[86] **MAYO, W T., SHAY, M. T. & RITER, S.** 1974 The development of new digital data processing techniques for turbulence measurements with a laser velocimeter. *Final Report (AEDC-TR-74-53), USAF Contract Co. F40600-73-C-003.*

[87] **MAYO, W. T.** 1975 Modeling of laser velocimeter signals as triply stochastic Poisson processes. In *Proc. Minn. Syrup. on Laser Doppler*, Univ. Minn., Bloomington.

[88] **MAYO, W. T.** 1978 Spectrum measurements with laser velocimeters. *Proceedings of the Dynamic Flow Conference*, Skovlunde, Denmark, (PO Box 121, DK-2740 Skovlunde), 851–868.

[89] **MEHTA, R. D. & BRADSHAW, P.** 1988 Longitudinal vortices imbedded in turbulent boundary layers Part 2. Vortex pair with 'common flow' upwards. *Journal of Fluid Mechanics* **188**, 529–546.

[90] **MELANDER, V., ZABUSKY, N. J. & McWILLIAMS, J. C.** 1988 Symmetric vortex merger in two dimensions: causes and conditions. *Journal of Fluid Mechanics* **195**, 303–340.

[91] **MEUNIER, P., EHRENSTEIN, U., LEWEKE, T. & ROSSI, M.** 2002 A merging criterion for two-dimensional co-rotating vortices. *Physics of Fluids* **14**, 2757–2766.

[92] **MILTON, J. S. & ARNOLD, J. C.** 1995 Introduction to probability and statistics. McGraw-Hill.

[93] **MÜLLER, E., NOBACH, H. & TROPEA, C.** 1994 LDA signal Reconstruction: Application to moment and spectral estimation. *Seventh International Symposium on Applications of Laser Technologies to Fluid Mechanics* Lisbon, Portugal, paper 23.2.

[94] **MYDLARSKI, L. & WARHAFT, Z.** 1996 On the onset of high-Reynolds-number grid-generated wind tunnel turbulence. *Journal of Fluid Mechanics* **320**, 331–368.

[95] **NICKERSON, J. D.** 1986 A study of vortex generators at low Reynolds numbers. *AIAA Paper*, 86-0155.

[96] *http://ldvproc.nambis.de/data/dtudata.html*

[97] **NOBACH, H., MÜLLER, E. & TROPEA, C.** 1998 Efficient estimation of power spectral density from laser Doppler anemometer data. *Experiments in Fluids* **24**, 499–509.

[98] **OKULOV, V. L.** 1996 The transition from the right helical symmetry to the left symmetry during vortex breakdown. *Technical Physics Letters* **22**, 798–800.

[99] **OKULOV, V. L.** 2004 On the stability of multiple helical vortices. *Journal of Fluid Mechanics* **521**, 319–342.

[100] **OKULOV, V. L., SØRENSEN, J. N. & VOIGT, L. K.** 2005 Vortex scenario and bubble generation in a cylindrical cavity with rotating top and bottom. *European Journal of Mechanics B/Fluids* **24**, 137-148.

[101] **ORLANDI, J. & JIMÉNEZ, J.** 1994 On the generation of turbulent wall friction. *Physics of Fluids* **6**, 634–641.

[102] **OVERMAN, A.** 1986 Steady-state solutions of the Euler equations in two dimensions II. Local analysis of limiting V-states. *SIAM Journal of Applied Mathematics* **46**, 765–800.

[103] **ØYE, S.** 1995 The Effect of Vortex Generators on the Performance of the ELKRAFT 1000 kW Turbine. *9th IEA Symposium on Aerodynamics of Wind Turbines*, Stockholm, Sweden, ISSN 0590–8809.

[104] **PANCHAPAKESAN, N. R. & LUMLEY, J. L.** 1993 Turbulence measurements in axisymmetric jets of air and helium. Part 1. Air jet. *Journal of Fluid Mechanics* **246**, 197–223.

[105] **PAPENFUß, H. D.** 2006 Aerodynamic Commissioning of the New Wind Tunnel at LM Glasfiber A/S (Lunderskov). LM Glasfiber Technical report, Lunderskov, Denmark.

[106] **PAULEY, W. R. & EATON, J. K.** 1988 Experimental study of the development of longitudinal vortex pairs embedded in a turbulent boundary layer. *AIAA Journal* **26**, 816–823.

[107] **PEARCEY, H. H.** 1961 Shock induced separation and its prevention by design and boundary layer control. In *Boundary Layer and Flow Control* (ed. G. V. Lachmann) **2**, pp. 1166–1344. Pergamon Press.

[108] **PEPPLER, I. L.** 1996 From The Ground Up. Aviation Publishers Co. Limited, Ottawa Ontario, Twenty Seventh Revised Edition, ISBN 09690054-9-0, pp. 23.

[109] **PIERREHUMBERT, R. T.** 1980 A family of steady, translating vortex pairs with distributed vorticity. *Journal of Fluid Mechanics* **99**, 129–144.

[110] **PRANDTL, L.** 1942 Führer durch die Strömungslehre. 3rd ed., Friedrich Vieweg & Sohn, Braunschweig, pp. 129–144.

[111] **RAFFEL, M., WILLERT, C. E., WERELEY, S. T. & KOMPENHANS, J.** 2007 Particle Image Velocimetry - A Practical Guide. Springer Verlag.

[112] **RAJA GOPAL, E. S.** 1963 Motion and stability of vortices in a finite channel: application to liquid Helium II. *Annals of Physics* **25**, 196–220.

[113] **RAJA GOPAL, E. S.** 1964 Oscillations of quantized vortices in rotating liquid Helium II. *Annals of Physics* **29**, 350–365.

[114] **RAO, D.M. & KARIYA, T.T.** 1988 Boundary-layer submerged vortex generators for separation control - an exploratory study. *Space Programs and Technologies*, 839–846.

[115] **RECK, M.** 2005 Computational fluid dynamics, with detached eddy simulation and the immersed boundary technique, applied to oscillating airfoils and vortex generators. PhD thesis, Tehcnical University of Denmark, Kgs. Lyngby, Denmark.

[116] **REIST, P. C.** 1993 Aerosol science and technology. $2^{nd}$ ed., McGraw-Hill.

[117] **ROBINSON, S. K.** 1991 Coherent motions in the turbulent boundary layer. *Annual Review of Fluid Mechanics* **23**, 601–639.

[118] **van ROOIJ, R. P. J. O. M. & TIMMER, W. A.** 2003 Roughness Sensitivity Considerations for Thick Rotor Blade Airfoils. *AIAA-paper* 2003-0350.

[119] **ROSENHEAD, L.** 1930 The spread of vorticity in the wake behind a cylinder. *Proceedings of the Royal Society A* **127**, 590–612.

[120] **SAFFMAN, G. & SZETO, R.** 1980 Equilibrium shapes of a pair of equal uniform vortices. *Physics of Fluids* **23**, 2339–2342.

[121] **SAFFMAN, P. G.** 1992 Vortex Dynamics. Cambridge Uni. Press, New York.

[122] **SCHLAYER, K.** 1928 Über die Stabilität der Karmanschen Wirbelstrasse gegenüber beliebigen Störungen in drei Dimensionen. *ZAMM* **8**, 352–372.

[123] **SCHMIDT, J. J.** 1997 Experimental and numerical investigation of separated flows. PhD thesis, Tehcnical University of Denmark, Kgs. Lyngby, Denmark.

[124] **SCHUBAUER, G. B. & SPANGENBERG, W. G.** 1960 Forced mixing in boundary layers. *Journal of Fluid Mechanics* **8**, 10–32.

[125] **SHABAKA, I. M. M. A., MEHTA, R. D. & BRADSHAW, P.** 1985 Longitudinal vortices imbedded in turbulent boundary layers. Part 1. Single vortex. *Journal of Fluid Mechanics* **155**, 37–57.

[126] **SHAPIRO, H. S. & SILVERMAN, R. A.** 1960 Alias-free sampling of random noise. *Journal of the Society for Industrial and Applied Mathematics* **8**, 225–248.

[127] **SMITH, F. T.** 1994 Theoretical prediction and design for vortex generators in turbulent boundary layers. *Journal of Fluid Mechanics* **270**, 91–131.

[128] **SOLOFF, S. M., ADRIAN, R. J. & LIU, Z. C.** 1997 Distortion compensation for generalized stereoscopic particle image velocimetry. *Measurement Science and Technology* **8**, 1441–1454.

[129] **STANIFORTH, R.** 1958 Some tests on cascades of compressor blades fitted with vortex generators. *NGTE Memorandum*, M.314, National Gas Turbine Establishment, Farnborough, Great Britain.

[130] **STANISLAS, M., OKAMOTO, K. & KÄHLER, C.** 2003 Main Results of the First Int. PIV Challenge. *Measurement Science and Technology* **14**, 63–89.

[131] **TAYLOR, H. D.** 1947 The elimination of diffuser separation by vortex generators. *Research Department Report No. R-4012-3.* United Aircraft Corporation, East Hartford, Connecticut.

[132] **TAYLOR, H. D.** 1948 Application of vortex generator mixing principles to diffusers. *Research Department Concluding Report No. R-15064-5.* United Aircraft Corporation, East Hartford, Connecticut.

[133] **TAYLOR, H. D.** 1948 Design criteria for and applications of the vortex generator mixing principle. *Research Department Report No. M-15038-1.* United Aircraft Corporation, East Hartford, Connecticut.

[134] **TAYLOR, H. D.** 1950 Summary report on vortex generators. *Research Department Report No. R-05280-9.* United Aircraft Corporation, East Hartford, Connecticut.

[135] **TENNEKES, H. & LUMLEY, J. L.** 1972 A First Course in Turbulence. MIT Press, Cambridge, Massachusetts.

[136] **TIMMER, W. A. & van ROOIJ, R. P. J. O. M.** 2003 Summary of the Delft University Wind Turbine Dedicated Airfoils. *AIAA-paper* 2003-0352.

[137] **TROPEA, C.** 1995 Laser Doppler anemometry: recent developments and future challenges. *Measurement Science and Technology* **6**, 605–619.

[138] **TURNS, S. R.** 2000 An Introduction to Combustion. Second ed., McGraw-Hill, Singapore, pp. 98–103.

[139] **TUTKUN, M.** 2006 Wind Tunnel Studies of Turbulent Wakes. Thesis for Licentiate of Engineering, Chalmers University of Technology, Göteborg, Sweden, ISSN 1652-8565.

[140] **TUTKUN, M., JOHANSSON, P. B. V., GEORGE, W. K.** 2008 Three-Component Vectorial Proper Orthogonal Decomposition of Axisymmetric Wake Behind a Disk. *AIAA Journal*, **46**, No 5, 1118–1134.

[141] **TUTKUN, M.** 2009 Structure of zero pressure gradient high Reynolds number turbulent boundary layers. PhD thesis, Chalmers University of Technology, Gothenburg, Sweden.

[142] **ULLUM, U., SCHMIDT, J. J., LARSEN, P. S. & McCLUSKEY, D. R.** 1998 Statistical analysis and accuracy of PIV data. *Journal of Visualization* **1**, 205–216.

[143] **VELTE, C. M., HANSEN, M. O. L. & JØNCK, K.** 2007 Experimental and Numerical Investigations of the Performance of Vortex Generators on Separation Control. *Journal of Physics: Conference Series* **75** (11pp)

[144] **VELTE, C. M., HANSEN, M. O. L. & CAVAR, D.** 2008 Flow analysis of vortex generators on wing sections by stereoscopic particle image velocimetry measurements. *Environmental Research Letters* **3**, 015006.

[145] **VELTE, C. M., HANSEN, M. O. L., MEYER, K. E. & FUGLSANG, P.** 2008 Evaluation of the performance of vortex generators on the DU 91–W2–250 profile using stereoscopic PIV. *Proceedings of the $4^{th}$ International Symposium on Energy, Informatics and Cybernetics: EIC 2008*, Orlando, Florida, USA.

[146] **VELTE, C. M., HANSEN, M. O. L. & OKULOV, V. L.** 2009 Helical Structure of Longitudinal Vortices Embedded in Turbulent Wall-Bounded Flow. *Journal of Fluid Mechanics* **619**, 167–177.

[147] **WALLIN, F.** 2008 Flow control and shape optimization of intermediate turbine ducts for turbofan engines. PhD thesis, Chalmers University of Technology, Gothenburg, Sweden.

[148] **WÄNSTRÖM, M., GEORGE, W. K., MEYER, K. E. & WESTERGAARD, C.** 2007 Identifying sources of stereoscopic PIV measurements errors on turbulent round jets. *Proceedings of FEDS* $5^{th}$ Joint ASME/JSME Fluids Engineering Conference.

[149] **WAUGH, W.** 1992 The efficiency of symmetric vortex merger. *Physics of Fluids* **4**, 1745–1758.

[150] **WENDT, B. J.** 2004 Parametric study of vortices shed from airfoil vortex generators. *AIAA Journal* **42**, 2185–2195.

[151] **WESTERWEEL, J.** 1993 Digital Particle Image Velocimetry - Theory and Application. University Press (Delft), PhD-thesis.

[152] **WESTERWEEL, J.** 2000 Theoretical Analysis of the Measurement Precision in Particle Image Velocimetry. *Experiments in Fluids* **29**, 3–12.

[153] **WHITE, F. M.** 2005 Fluid Mechanics 6 ed. Boston, McGraw-Hill.

[154] **WIENEKE, B.** 2005 Stereo-PIV using self-calibration on particle images. *Experiments in Fluids* **39**, 267–280.

[155] **WILLERT, C.** 1997 Stereoscopic digital particle image velocimetry for application in wind tunnel flows. *Measurement Science and Technology* **8**, 1465–1479.

[156] **WYNGAARD, J. C.** 1968 Measurement of small-scale turbulence structure with hot wires. *Journal of Scientific Instruments* **1**, 1105–1108.

[157] **YOU, D., WANG, M., MITTAL, R. & MOIN, P.** 2006 Large-eddy simulations of longitudinal vortices embedded in a turbulent boundary layer. *AIAA Journal* **44**, 3032–3039.

# Part VI

# Appendices

# Appendix A

# Experimental method for HWA measurements in Chapter 9

The measurements were made in a closed circuit, low turbulence intensity (less than 0.03%) wind tunnel of Chalmers University of Technology, Göteborg, Sweden. The wind tunnel test section has a cross-section area of $1.80 \times 1.25$ m$^2$ and a length of 3 m. The maximum achievable tunnel speed is 60 m s$^{-1}$. The tunnel has a temperature control unit which provides a constant flow temperature at an accuracy of $\pm 0.1°$. The measurements were conducted 1 m downstream of a circular disc of diameter $D = 20$ mm. This corresponded to a measurement location 50 disc diameters behind the disc. The disc was placed in the entrance of the test section immediately after the contraction and suspended with 3-pairs of wire. The disc had a thickness of 2 mm with sharp edges and was made of aluminum. The blockage introduced by the the disc was less than 0.014%, hence it was negligible.

The tunnel free stream velocity ($U_\infty$) was kept constant at 15.3 m s$^{-1}$ during the measurements. This free stream velocity corresponded to a Reynolds number based on disc diameter ($Re = U_\infty D/\nu$) of 20 400. 12 cross hot-wire probes were used to measure the axisymmetric wake simultaneously. The probes were located on two wings covering the cross-section of the axisymmetric wake at this downstream location. Each wing carried 6 probes and the probes were placed symmetrically about the centerline of the axisymmetric wake in the cylindrical coordinate system. One of the wings was movable to be able to measure different azimuthal separations simultaneously. The length and the diameter of the sensing wires on each probe were 2.8 mm and 5 $\mu$m respectively. The spacing between the sensors of the cross-wire probes was 0.7 mm.

24 single channel Dantec Miniature-CTA 54T30 hot-wire anemometers together with an IO Tech Wavebook 516 16 bit 1 MHz sample and hold analog/digital (A/D) converter with two expansion modules were used for the measurements. The sampling frequency throughout the measurements was 8 kHz. The finite sensing wire length at 15.3 m s$^{-1}$ free stream velocity resulted in the sensing wires acting like spatial low pass filters. The cutoff frequency of the filter because of the finite size of the sensing wire was 2730 Hz. In addition,

low pass filters built into the anemometers used in the experiments were set to 3 kHz to avoid aliasing due to high frequency electronic noise.

The sampled data was stored in blocks of 1.024 seconds, resulting in 8192 samples for each anemometer channel. The record length for each block corresponded to approximately 2000 integral time scales which minimized the effect of finite size of the record length. In total, 200 blocks of data were recorded to have small variability of the estimator of the spectra. The blocks were separated by 2000 integral time scales, so that any successive blocks of data were statistically uncorrelated, hence contributing to the statistical accuracy.

Angular calibration of the 12 cross hot-wire probes were performed simultaneously in the free stream of the wind tunnel. A grid between $\pm 12$ degrees in 4 degrees increment was used to be able to calibrate the wires. 12 different wind tunnel speeds from 11 to 18 m $s^{-1}$ were used at each grid point. The calibration grid and selection of tunnel velocities were designed using the reference data from the previous results documented by [63]. It essentially covered almost all possible ($\sim$99.9%) combinations of velocity direction and magnitude [140]. The method implemented in the calibration was to express the effective cooling velocities in terms of fourth order polynomial function of anemometer output voltages and to find the unknown parameters (calibration coefficients, yaw coefficients for each wires and the angle between the wires) using a nonlinear least-squares curve fit. Obtained relations between the effective cooling velocities and the anemometer output voltages were used to find the instantaneous turbulent velocity decomposed in two different directions. Further information about the experimental setup, the measurement procedure and the calibration methodology is documented by [139, 140].

# Appendix B

# Variability of spectral estimator for equidistant sampling

The relative error of the spectral estimator can be expressed in the following manner

$$\varepsilon_{S_T}^2 = \frac{\mathrm{var}\{S_T(f)\}}{\overline{[S_T(f)]^2}} \tag{B1}$$

where the nominator is simply the variance of the estimator. This can be expressed as

$$\mathrm{var}\{S_T(f)\} = \frac{\overline{|\hat{u}_T(f)|^2|\hat{u}_T(f)|^2}}{T^2} - \underbrace{\left|\frac{\overline{|\hat{u}_T(f)|^2}}{T}\right|^2}_{=\overline{[S_T(f)]^2}} \tag{B2}$$

It is trivial to see that the second term equals $\overline{[S_T(f)]^2}$. Let's evaluate the first term using the assumption that the fourth order moments are jointly Gaussian, i.e.,

$$\overline{uu'u''u'''} = \overline{uu'}\;\overline{u''u'''} + \overline{uu''}\;\overline{u'u'''} + \overline{uu'''}\;\overline{u'u''}. \tag{B3}$$

This yields;

$$\frac{\overline{|\hat{u}_T(f)|^2|\hat{u}_T(f)|^2}}{T^2} = \frac{1}{T^2}\left\langle \int_{-T/2}^{T/2}\int_{-T/2}^{T/2} e^{-i2\pi f(t'-t)}u(t)u(t')\,dtdt' \times \right.$$

$$\left. \int_{-T/2}^{T/2}\int_{-T/2}^{T/2} e^{-i2\pi f(t'''-t'')}u(t'')u(t''')\,dt''dt''' \right\rangle$$

$$= \frac{1}{T^2}\int_{-T/2}^{T/2}\int_{-T/2}^{T/2}\int_{-T/2}^{T/2}\int_{-T/2}^{T/2} e^{-i2\pi f(t'-t)-i2\pi f(t'''-t'')}\overline{uu'u''u'''}\,dtdt'dt''dt'''$$

$$= \frac{1}{T^2}\int_{-T/2}^{T/2}\int_{-T/2}^{T/2}\int_{-T/2}^{T/2}\int_{-T/2}^{T/2} e^{-i2\pi f(t'-t)-i2\pi f(t'''-t'')}\times$$

$$\Big[\underbrace{\overline{uu'}\;\overline{u''u'''}}_{1}+\underbrace{\overline{uu''}\;\overline{u'u'''}}_{2}+\underbrace{\overline{uu'''}\;\overline{u'u''}}_{3}\Big]\,dtdt'dt''dt''' \tag{B4}$$

Let's begin by evaluating the first term of (B4), which can be done by rearranging the quadruple integral into two double integrals and identifying them each to be the spectral estimator.

$$\underbrace{\frac{1}{T}\int_{-T/2}^{T/2}\int_{-T/2}^{T/2} e^{-i2\pi f(t'-t)}\overline{u(t)u(t')}\,dtdt'}_{=S_T(f)}\times$$

$$\underbrace{\frac{1}{T}\int_{-T/2}^{T/2}\int_{-T/2}^{T/2} e^{-i2\pi f(t'''-t'')}\overline{u(t'')u(t''')}\,dt''dt'''}_{=S_T(f)} = \overline{[S_T(f)]^2} \tag{B5}$$

The third term of (B4) can be evaluated simply by rearranging the terms in the exponential ($[(t'-t)+(t'''-t'')] = [(t'''-t)+(t'-t'')]$) and identifying the double integral as was done for the first term.

$$\frac{1}{T^2}\int_{-T/2}^{T/2}\int_{-T/2}^{T/2}\int_{-T/2}^{T/2}\int_{-T/2}^{T/2} e^{-i2\pi f(t'-t)-i2\pi f(t'''-t'')}\overline{u(t)u(t''')}\;\overline{u(t')u(t'')}$$

$$= \underbrace{\frac{1}{T}\int_{-T/2}^{T/2}\int_{-T/2}^{T/2} e^{-i2\pi f(t'''-t)}\overline{u(t)u(t''')}\,dtdt'''}_{=S_T(f)}\times$$

$$\underbrace{\frac{1}{T}\int_{-T/2}^{T/2}\int_{-T/2}^{T/2} e^{-i2\pi f(t'-t'')}\overline{u(t')u(t'')}\,dt'dt''}_{=S_T(f)} = \overline{[S_T(f)]^2} \tag{B6}$$

The second term of (B4) requires some additional attention. Use the variable transformation (see figure B.1)

$$\begin{cases} \tau &= t''-t \\ \tau' &= t'''-t' \end{cases}$$

so that

$$(t'-t)+(t'''-t'') = (t'-t)+[(t'+\tau')-(t+\tau)] = 2t'-2t+\tau'-\tau$$

and

$$\frac{1}{T^2}\int_{-T/2}^{T/2}\int_{-T/2}^{T/2}\int_{-T/2}^{T/2}\int_{-T/2}^{T/2} e^{-i2\pi f(t'-t)-i2\pi f(t'''-t'')}\overline{u(t)u(t'')}\;\overline{u(t')u(t''')}dtdt'dt''dt'''$$

$$= \frac{1}{T^2}\int_{-T/2}^{T/2} dt\int_{-T/2}^{T/2} dt'\int_{-T/2-t}^{T/2-t} d\tau\int_{-T/2-t'}^{T/2-t'} d\tau' e^{-i2\pi f[2t'-2t+\tau'-\tau]}B(\tau)\;B(\tau')$$

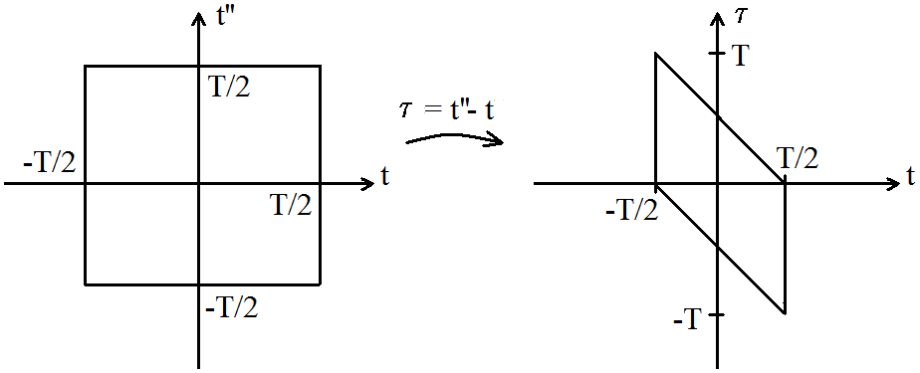


Figure B.1: Mapping corresponding to the applied variable transformation.

$$= \frac{1}{T^2}\left|\int_{-T/2}^{T/2} dt\, e^{-i4\pi ft}\int_{-T/2-t}^{T/2-t} d\tau\, e^{-i2\pi f\tau}B(\tau)\right|^2$$

The integration limits in the second integral both contain the variable t, but since t is subtracted from both limits, i.e., the integration limits are merely shifted by -t over an infinite domain, this dependency simply corresponds to a phase shift. The application of a variable transformation would hence terminate the t dependence in the limits and the spectrum is reproduced correctly. Let's use the variable transformation

$$\tilde{\tau} = \tau + t$$

which yields

$$\frac{1}{T^2}\left|\int_{-T/2}^{T/2} dt\, e^{-i4\pi ft}\int_{-T/2}^{T/2} d\tilde{\tau}\, e^{-i2\pi f[\tilde{\tau}-t]}B(\tilde{\tau})\right|^2$$

$$= \frac{1}{T^2}\left|\int_{-T/2}^{T/2} dt\, e^{-i2\pi ft}\underbrace{\int_{-T/2}^{T/2} d\tilde{\tau}\, e^{-i2\pi f\tilde{\tau}}B(\tilde{\tau})}_{=S_T(f)}\right|^2$$

$$= \left|\frac{\sin(\pi fT)}{\pi fT}S_T(f)\right|^2$$

which in the limit of $T \to \infty$ goes to zero.

In this limit, the variance of the spectral estimator thus becomes

$$\lim_{T\to\infty} \mathrm{var}\{S_T(f)\} = \overline{[S(f)]^2} \tag{B7}$$

which ultimately result in the variability of (B1) being equal to unity in the limit of infinite record length.

$$\lim_{T\to\infty} \varepsilon^2_{S_T} = \frac{\overline{[S(f)]^2}}{\overline{[S(f)]^2}} = 1 \tag{B8}$$

# Appendix C

# Derivation of the relations for the sampling function

Assume the existence of a randomly sampled signal with a sampling function $h_{\Delta t}(t)$ consisting of a distribution of Heaviside step function finite pulses

$$H(t_i) = \theta(t - t_i) - \theta(t - t_i - \Delta t), \quad i = 1, 2, ..., \infty \tag{C1}$$

of width $\Delta t$ and height $1/\Delta t$. The sampling function could then be expressed as the sum of the individual sampling functions.

$$h_{\Delta t}(t) = \sum_{i=1}^{\infty} H(t_i) \tag{C2}$$

A short time record of the sampling signal could look like the one displayed in figure C.1. The time average of the sampling function is given by

$$\overline{h_{\Delta t}(t)} = \lim_{T\to\infty} \frac{1}{T} \int_0^T h_{\Delta t}(t)\, dt = \lim_{T, N_T \to \infty} \frac{N_T}{T} = \nu \tag{C3}$$

where $N_T$ is the expected number of samples in time $T$, which is the record length and $\nu$ is the average sampling rate.

The two-time correlation, $\overline{h_{\Delta t}(t) h_{\Delta t}(t+\tau)}$, can also be computed using

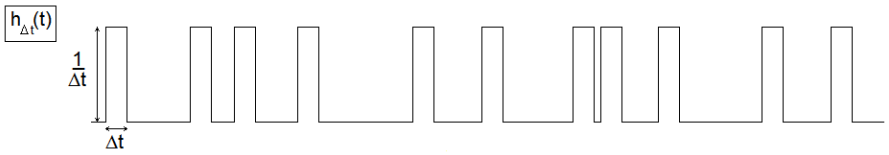


Figure C.1: Sketch of random sampling signal

the sequence of traces shown in Figure C.2 and

$$\overline{h_{\Delta t}(t)h_{\Delta t}(t+\tau)} = \lim_{T\to\infty}\frac{1}{T}\int_0^T h_{\Delta t}(t)h_{\Delta t}(t+\tau)\,dt. \tag{C4}$$

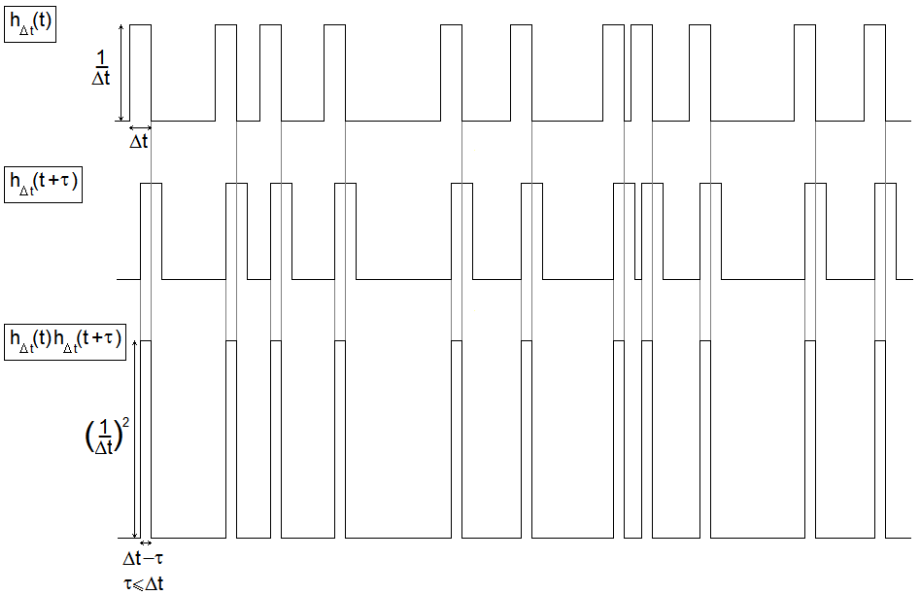


Figure C.2: Sketch of the random sampling signals $h(t)$ and $h(t+\tau)$. The lowermost figure shows the correlation of the sampling function for time lag $\tau \leq \Delta t$.

For time lags $\tau \leq \Delta t$ the product $h_{\Delta t}(t)h_{\Delta t}(t+\tau)$ yields a distribution of Heaviside step function finite pulses of width $\Delta t - \tau$ and height $1/\Delta t^2$, see figure C.2.

Thus for $\tau \leq \Delta t$ only the self-products are of interest; i.e., the correlation of the individual realization with itself. The solution is simply the average area of $h_{\Delta t}(t)h_{\Delta t}(t+\tau)$ times the number of samples per unit time.

$$\overline{h_{\Delta t}(t)h_{\Delta t}(t+\tau)} = \lim_{N_T,T\to\infty}\frac{N_T}{T}\frac{|\Delta t-\tau|}{\Delta t^2} = \nu\frac{|\Delta t-\tau|}{\Delta t^2}, \quad \tau \leq \Delta t. \tag{C5}$$

When $\tau > \Delta t$, the self-products are zero, but we must account for the random overlap of the sampling functions. The probability of two pulses randomly overlapping can be computed as follows. First assume there is a pulse already at time t. Now ask, for time $\tau > \Delta t$, what is the probability that a second pulse overlaps it? Since the pulses are statistically independent of each other, this is simply the probability that there is another pulse in the interval $t+\tau \pm \Delta t/2$, which is just $\nu\Delta t$. But this is the same as the probability that the first pulse is turned on in the interval $(t-\Delta t/2, t+\Delta t/2)$. Thus

$$\overline{h_{\Delta t}(t)h_{\Delta t}(t+\tau)}|_{\tau>\Delta t} = \frac{1}{\Delta t^2}(\nu\Delta t)^2 = \nu^2 \tag{C6}$$

Summarizing the results, one therefore obtains the following;

$$\overline{h_{\Delta t}(t)h_{\Delta t}(t+\tau)} = \begin{cases} \nu\frac{|\Delta t-\tau|}{\Delta t^2} & \tau \leq \Delta t \\ \\ \nu^2 & \tau > \Delta t \end{cases} \tag{C7}$$

It is easy to see that the first term satisfies the condition to be a $\delta$-function in the limit as $\Delta t \to 0$, see figure C.3. Thus

$$\lim_{\Delta t\to 0} \overline{h_{\Delta t}(t)h_{\Delta t}(t+\tau)} = \overline{h(t)h(t+\tau)} = \nu\delta(\tau) + \nu^2. \tag{C8}$$

Since $\overline{h(t)} = \nu$, the autocorrelation of $h(t)$ can be computed as

$$\overline{\Big[h(t) - \overline{h(t)}\Big]\Big[h(t+\tau) - \overline{h(t+\tau)}\Big]} = \overline{h(t)h(t+\tau)} - \nu^2 = \nu\delta(\tau) \tag{C9}$$

Thus as expected, the pulses are uncorrelated (at least in the limit as $\Delta t \to 0$).

This sampling function is not dimensionless, which can simply be remedied by normalizing by $\nu$. Let's call the normalized sampling function $g(t)$.

$$\overline{g(t)} = 1 \tag{C10}$$

$$\overline{g(t)g(t+\tau)} = \frac{\delta(\tau)}{\nu} + 1 \tag{C11}$$

$$\overline{\Big[g(t) - \overline{g(t)}\Big]\Big[g(t+\tau) - \overline{g(t+\tau)}\Big]} = \frac{\delta(\tau)}{\nu} \tag{C12}$$

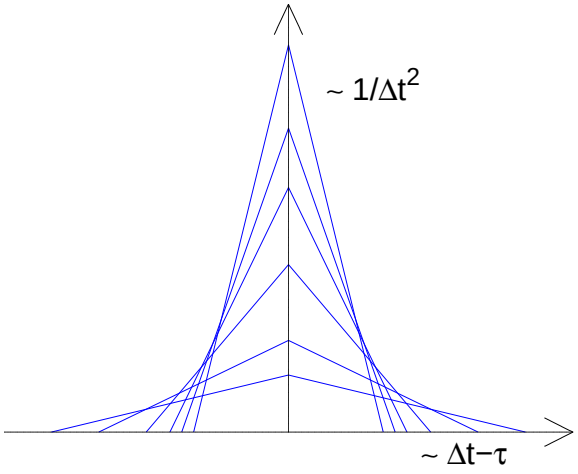


Figure C.3: Sketch of $\nu|\Delta t - \tau|/\Delta t^2$ for different values of $\Delta t \geq \tau$. As $\Delta t$ approaches zero, the function becomes increasingly narrow and steep, becoming a $\delta$-function in the limit.

# Appendix D

# Variability of spectral estimator for random sampling

In the same manner as in Appendix B, we seek for the variance of the spectral estimator to obtain its variability. Appendix B treats the case of regular sampling, whilst this appendix is concerned with the randomly sampled case. The fourth order moment of the random sampling function

$$\overline{gg'g''g'''} = 1+$$

$$\frac{1}{\nu}\left[\delta(t'-t)+\delta(t''-t)+\delta(t'''-t)+\delta(t''-t')+\delta(t'''-t')+\delta(t'''-t'')\right]+$$

$$\frac{1}{\nu^2}\left[\delta(t'-t)\delta(t''-t)+\delta(t'-t)\delta(t'''-t)+\delta(t'''-t)\delta(t''-t)+\delta(t'''-t')\delta(t''-t')\right]+$$

$$\frac{1}{\nu^3}\delta(t'-t)\delta(t''-t)\delta(t'''-t) \tag{D1}$$

is incorporated into the variance of the spectral estimator. This quantity can be derived by assuming that $g$, $g'$, $g''$ and $g'''$ are uncorrelated, for which the following must hold true:

$$\overline{(g-\nu)(g'-\nu)(g''-\nu)(g'''-\nu)} = \frac{1}{\nu^3}\delta(t'-t)\delta(t''-t)\delta(t'''-t) \tag{D2}$$

$$\begin{cases} \overline{(g-\nu)(g'-\nu)(g''-\nu)} &= \frac{1}{\nu^2}\delta(t'-t)\delta(t''-t) \\ \overline{(g-\nu)(g'-\nu)(g'''-\nu)} &= \frac{1}{\nu^2}\delta(t'-t)\delta(t'''-t) \\ \overline{(g-\nu)(g''-\nu)(g'''-\nu)} &= \frac{1}{\nu^2}\delta(t''-t)\delta(t'''-t) \\ \overline{(g'-\nu)(g''-\nu)(g'''-\nu)} &= \frac{1}{\nu^2}\delta(t''-t')\delta(t'''-t') \end{cases} \tag{D3}$$

$$\begin{cases} \overline{(g-\nu)(g'-\nu)} &= \frac{1}{\nu}\delta(t'-t) \\ \overline{(g-\nu)(g''-\nu)} &= \frac{1}{\nu}\delta(t''-t) \\ \overline{(g-\nu)(g'''-\nu)} &= \frac{1}{\nu}\delta(t'''-t) \\ \overline{(g'-\nu)(g''-\nu)} &= \frac{1}{\nu}\delta(t''-t') \\ \overline{(g'-\nu)(g'''-\nu)} &= \frac{1}{\nu}\delta(t'''-t') \\ \overline{(g''-\nu)(g'''-\nu)} &= \frac{1}{\nu}\delta(t'''-t'') \end{cases} \tag{D4}$$

Expanding equation (D2), one can solve for $\overline{gg'g''g'''}$. Similarly expanding (D3) and (D4) and substituting these into (D2), one obtains (D1).

Assuming that the sampling process is independent of the process being sampled and that the fourth order moments of the velocities are jointly Gaussian (i.e. $\overline{uu'u''u'''} = \overline{uu'}\ \overline{u''u'''} + \overline{uu''}\ \overline{u'u'''} + \overline{uu'''}\ \overline{u'u''}$);

$$\mathrm{var}\{S_T^R(f)\} =$$

$$\left\langle \frac{1}{T^2} \int_{-T/2}^{T/2}\int_{-T/2}^{T/2}\int_{-T/2}^{T/2}\int_{-T/2}^{T/2} e^{-i2\pi f[(t-t')+(t''-t''')]} uu'u''u'''gg'g''g'''\,dt\,dt'\,dt''\,dt''' \right\rangle =$$

$$\frac{1}{T^2} \int_{-T/2}^{T/2}\int_{-T/2}^{T/2}\int_{-T/2}^{T/2}\int_{-T/2}^{T/2} e^{-i2\pi f[(t-t')+(t''-t''')]} \overline{uu'u''u'''}\ \overline{gg'g''g'''}\,dt\,dt'\,dt''\,dt''' =$$

$$\frac{1}{T^2} \int_{-T/2}^{T/2}\int_{-T/2}^{T/2}\int_{-T/2}^{T/2}\int_{-T/2}^{T/2} e^{-i2\pi f[(t-t')+(t''-t''')]} \left[\overline{uu'}\ \overline{u''u'''} + \overline{uu''}\ \overline{u'u'''} + \overline{uu'''}\ \overline{u'u''}\right] \times$$

$$\Bigg[ \underbrace{1}_{A} + \frac{1}{\nu}\Big[ \underbrace{\delta(t'-t)}_{B} + \underbrace{\delta(t''-t)}_{C} + \underbrace{\delta(t'''-t)}_{D} + \underbrace{\delta(t''-t')}_{E} + \underbrace{\delta(t'''-t')}_{F} + \underbrace{\delta(t'''-t'')}_{G} \Big] +$$

$$\frac{1}{\nu^2}\Big[ \underbrace{\delta(t'-t)\delta(t''-t)}_{H} + \underbrace{\delta(t'-t)\delta(t'''-t)}_{I} +$$

$$\underbrace{\delta(t''-t)\delta(t'''-t)}_{J} + \underbrace{\delta(t''-t')\delta(t'''-t')}_{K} \Big] +$$

$$\frac{1}{\nu^3}\underbrace{\delta(t'-t)\delta(t''-t)\delta(t'''-t)}_{L} \Bigg]\, dt\,dt'\,dt''\,dt''' \tag{D5}$$

## Properties of the delta function

In the following, some fundamental properties of the generalized Dirac delta function are used. The first condition is that it integrates to unity across the infinite time span:

$$\int_{-\infty}^{\infty} \delta(t - t_0)\, dt = 1 \tag{D6}$$

which is true for any real value $t_0$. Furthermore,

$$\delta(t) = 0, \quad t \neq 0 \tag{D7}$$

In addition, the delta function can impose a time delay on a function, commonly called the shifting property, which is also fundamental to the impulse function.

$$\int_{-\infty}^{\infty} f(t)\delta(t - t_0)\, dt = f(t_0) \tag{D8}$$

## Non-overlapping time intervals (Term A)

The integral of only term A for non-overlapping intervals was evaluated in Appendix B and approaches $\overline{[S(f)]^2}$ in the limit $T \to \infty$.

## Two time intervals overlapping (Terms B-G)

The argument of the integral using only term B where dt and dt′ overlap yields;

$$\delta(t' - t)\overline{uu'u''u'''} = \delta(t' - t)\left[\underbrace{\overline{uu'}\ \overline{u''u'''}}_{B1} + \underbrace{\overline{uu''}\ \overline{u'u'''}}_{B2} + \underbrace{\overline{uu'''}\ \overline{u'u''}}_{B3}\right]$$

For **term B1**, let

$\tau = t' - t, \quad -T/2 - t \leq \tau \leq T/2 - t$

so that

$$\frac{1}{\nu T^2} \underbrace{\int_{-T/2}^{T/2} dt}_{=T} \underbrace{\int_{-T/2-t}^{T/2-t} d\tau\, e^{i2\pi f\tau} B(\tau)\delta(\tau)}_{=B(0)\text{ using S.P. (D8)}} \underbrace{\int_{-T/2}^{T/2} dt'' \int_{-T/2}^{T/2} dt'''\, e^{-i2\pi f(t''-t''')} B(t''' - t'')}_{=T\cdot S_T(f)}$$

$$= \boxed{\frac{1}{\nu} B(0) S_T(f)}$$

For **term B2**, let

$$\begin{cases} \tau &= t'' - t \\ \tilde{\tau} &= t''' - t' \end{cases}$$

Noting that the limits on the last two integrals merely introduce a phase shift, term B2 becomes

$$\frac{1}{\nu T^2} \underbrace{\int_{-T/2}^{T/2} dt}_{=T} \underbrace{\int_{-T/2}^{T/2} dt'\, \delta(t'-t) e^{-i4\pi f[t-t']}}_{e^0=1,\,\text{S.P. (D8)}} \underbrace{\int_{-T/2-t}^{T/2-t} d\tau\, e^{-i2\pi f\tau} B(\tau)}_{=S_T(f)} \underbrace{\int_{-T/2-t'}^{T/2-t'} d\tilde{\tau} e^{i2\pi f\tilde{\tau}} B(\tilde{\tau})}_{=S_T(f)}$$

$$= [S_T(f)]^2 \frac{1}{\nu T}$$

$$\boxed{\to 0 \text{ as } T \to \infty}$$

For **term B3**, let

$$\begin{cases} \tau &= t''' - t \\ \tilde{\tau} &= t'' - t' \end{cases}$$

$$\frac{1}{\nu T^2} \underbrace{\int_{-T/2}^{T/2} dt}_{=T} \underbrace{\int_{-T/2}^{T/2} dt'\, \delta(t'-t)}_{\equiv 1\ \forall t,\ T\to\infty \text{ by defn.}} \underbrace{\int_{-T/2-t}^{T/2-t} d\tau\, e^{i2\pi f\tau} B(\tau)}_{=S_T(f)} \underbrace{\int_{-T/2-t'}^{T/2-t'} d\tilde{\tau}\, e^{-i2\pi f\tilde{\tau}} B(\tilde{\tau})}_{=S_T(f)}$$

$$= [S_T(f)]^2 \frac{1}{\nu T}$$

$$\boxed{\to 0 \text{ as } T \to \infty}$$

The contributions for terms C to G are found in a similar manner, yielding a total contribution of $4B(0)S_T(f)/\nu$ as $T \to \infty$.

# Three time intervals overlapping (Terms H-K)

From the argument in the integral where dt overlaps dt′ and dt″, one obtains

$$\delta(t'-t)\delta(t''-t)\overline{uu'u''u'''} = \delta(t''-t)\delta(t'''-t)\left[\underbrace{\overline{uu'}\;\overline{u''u'''}}_{H1} + \underbrace{\overline{uu''}\;\overline{u'u'''}}_{H2} + \underbrace{\overline{uu'''}\;\overline{u'u''}}_{H3}\right]$$

For **term H1**:

$$\frac{1}{\nu^2T^2}\int_{-T/2}^{T/2} dt\, e^{-i2\pi ft} \underbrace{\int_{-T/2}^{T/2} dt'\, e^{i2\pi ft'} B(t'-t)\delta(t'-t)}_{=e^{i2\pi ft}B(0),\, S.P.\,(D8)} \times$$

$$\int_{-T/2}^{T/2} dt'''\int_{-T/2}^{T/2} dt''\, e^{-i2\pi f[t''-t''']} B(t'''-t'')\delta(t''-t)$$

$$= \frac{B(0)}{\nu^2T^2}\int_{-T/2}^{T/2} dt \int_{-T/2}^{T/2} dt''' \underbrace{\int_{-T/2}^{T/2} dt''\, e^{-i2\pi f[t''-t''']} B(t'''-t'')\delta(t''-t)}_{=e^{-i2\pi f[t-t''']}B(t'''-t),\, S.P.\,(D8)}$$

$$= \frac{B(0)}{\nu^2T^2}\int_{-T/2}^{T/2} dt \int_{-T/2}^{T/2} dt''' e^{-i2\pi f[t-t''']} B(t'''-t)$$

$$= \frac{1}{\nu^2T} B(0) S_T(f)$$

$$\boxed{\to 0 \text{ as } T\to\infty}$$

For **term H2** we want to take the Fourier transform of

$$\delta(t'-t)\delta(t''-t)\overline{uu''}\;\overline{u'u'''}$$

reducing the integral to

$$\frac{1}{\nu^2T^2}\int_{-T/2}^{T/2} dt\, e^{-i2\pi ft} \underbrace{\int_{-T/2}^{T/2} dt''\, e^{-i2\pi ft''} B(t''-t)\delta(t''-t)}_{=e^{-i2\pi ft}B(0),\, S.P.\,(D8)} \times$$

$$\int_{-T/2}^{T/2} dt'''\, e^{i2\pi f t'''} \underbrace{\int_{-T/2}^{T/2} dt'\, e^{i2\pi f t'} B(t''' - t')\delta(t' - t)}_{= e^{i2\pi f t} B(t'''-t),\, S.P.\,(D8)}$$

$$= \frac{B(0)}{\nu^2 T^2} \underbrace{\int_{-T/2}^{T/2} dt\, e^{-i2\pi f t} \int_{-T/2}^{T/2} dt'''\, e^{i2\pi f t'''} B(t''' - t)}_{= T \cdot S_T(f)}$$

$$= \frac{1}{\nu^2 T} B(0) S_T(f)$$

$$\boxed{\to 0 \text{ as } T \to \infty}$$

For **term H3**:

$$\frac{1}{\nu^2 T^2} \int_{-T/2}^{T/2}\int_{-T/2}^{T/2}\int_{-T/2}^{T/2}\int_{-T/2}^{T/2} e^{-i2\pi f[(t-t')+(t''-t''')]} B(t''' - t) B(t'' - t') \times$$

$$\delta(t' - t)\delta(t'' - t)\, dt\, dt'\, dt''\, dt'''$$

$$= \frac{1}{\nu^2 T^2} \underbrace{\int_{-T/2}^{T/2} dt\, e^{-i2\pi f t} \int_{-T/2}^{T/2} dt'''\, e^{i2\pi f t'''} B(t''' - t) \times}_{= T \cdot S_T(f)}$$

$$\int_{-T/2}^{T/2} dt'\, e^{i2\pi f t'} \delta(t' - t) \underbrace{\int_{-T/2}^{T/2} dt''\, e^{-i2\pi f t''} B(t'' - t')\delta(t'' - t)}_{= e^{-i2\pi f t} B(t-t'),\, S.P.\,(D8)}$$

$$= \frac{1}{\nu^2 T} S_T(f) \underbrace{\int_{-T/2}^{T/2} dt'\, e^{-i2\pi f[t-t']} B(t - t')\delta(t' - t)}_{= B(0),\, S.P.\,(D8)}$$

$$= \frac{1}{\nu^2 T} B(0) S_T(f)$$

$$\boxed{\to 0 \text{ as } T \to \infty}$$

The contributions from all terms (H-K), found in a similar manner as above, reduce to zero in the limit as $T \to \infty$.

## Four time intervals overlapping (Term L)

From the argument in the integral where dt overlaps dt′, dt″ and dt‴ one obtains

$$\delta(t'-t)\delta(t''-t)\delta(t'''-t)\overline{uu'u''u'''}$$

$$= \delta(t'-t)\delta(t''-t)\delta(t'''-t)\left[\underbrace{\overline{uu'}\;\overline{u''u'''}}_{L1} + \underbrace{\overline{uu''}\;\overline{u'u'''}}_{L2} + \underbrace{\overline{uu'''}\;\overline{u'u''}}_{L3}\right]$$

For **term L1**

$$\frac{1}{\nu^3 T^2}\int_{-T/2}^{T/2} dt\, e^{-i2\pi ft}\int_{-T/2}^{T/2} dt'\, e^{i2\pi ft'}\delta(t'-t)B(t'-t)\times$$

$$\int_{-T/2}^{T/2} dt''\, e^{-i2\pi ft''}\delta(t''-t)\underbrace{\int_{-T/2}^{T/2} dt'''\, e^{i2\pi ft'''}\delta(t'''-t)B(t'''-t'')}_{=e^{i2\pi ft}B(t-t''),\,S.P.\,(D8)}$$

$$= \frac{1}{\nu^3 T^2}\int_{-T/2}^{T/2} dt\, e^{-i2\pi ft}\underbrace{\int_{-T/2}^{T/2} dt'\, e^{i2\pi ft'}\delta(t'-t)B(t'-t)}_{=e^{i2\pi ft}B(0),\,S.P.\,(D8)}\times$$

$$\underbrace{\int_{-T/2}^{T/2} dt''\, e^{-i2\pi f(t''-t)}\delta(t''-t)B(t-t'')}_{=e^{0}B(0)=B(0),\,S.P.\,(D8)}$$

$$= \frac{1}{\nu^3 T^2}\left[B(0)\right]^2\int_{-T/2}^{T/2} dt$$

$$= \frac{1}{\nu^3 T}\left[B(0)\right]^2$$

$$\boxed{\to 0 \text{ as } T\to\infty}$$

Similarly for **term L2**

$$\frac{1}{\nu^3 T^2} \int_{-T/2}^{T/2} dt\, e^{-i2\pi ft} \int_{-T/2}^{T/2} dt''\, e^{-i2\pi ft''} \delta(t''-t) B(t''-t) \times$$

$$\int_{-T/2}^{T/2} dt'\, e^{i2\pi ft'} \delta(t'-t) \underbrace{\int_{-T/2}^{T/2} dt'''\, e^{i2\pi ft'''} \delta(t'''-t) B(t'''-t')}_{= e^{i2\pi ft} B(t-t'),\, S.P.\,(D8)}$$

$$= \frac{1}{\nu^3 T^2} \int_{-T/2}^{T/2} dt\, e^{-i2\pi ft} \int_{-T/2}^{T/2} dt''\, e^{-i2\pi ft''} \delta(t''-t) B(t''-t) \times$$

$$\underbrace{\int_{-T/2}^{T/2} dt'\, e^{i2\pi f[t+t']} \delta(t'-t) B(t-t')}_{= e^{i2\pi f[2t]} B(0),\, S.P.\,(D8)}$$

$$= \frac{B(0)}{\nu^3 T^2} \int_{-T/2}^{T/2} dt\, e^{-i2\pi ft} \underbrace{\int_{-T/2}^{T/2} dt''\, e^{-i2\pi f[t''-2t]} \delta(t''-t) B(t''-t)}_{= e^{i2\pi ft} B(0),\, S.P.\,(D8)}$$

$$= \frac{1}{\nu^3 T^2} [B(0)]^2$$

$$\boxed{\to 0 \text{ as } T \to \infty}$$

Finally, for **term L3**

$$\frac{1}{\nu^3 T^2}\int_{-T/2}^{T/2} dt\, e^{-i2\pi ft}\underbrace{\int_{-T/2}^{T/2} dt'''\, e^{i2\pi ft'''}\delta(t'''-t)B(t'''-t)}_{e^{i2\pi ft}B(0),\, S.P.\,(D8)}\times$$

$$\underbrace{\int_{-T/2}^{T/2} dt'\, e^{i2\pi ft'}\delta(t'-t)\int_{-T/2}^{T/2} dt''\, e^{-i2\pi ft''}\delta(t''-t)B(t''-t')}_{=e^{-i2\pi ft}B(0),\, S.P.\,(D8)}$$

$$=\frac{1}{\nu^3 T^2}\left[B(0)\right]^2\underbrace{\int_{-T/2}^{T/2} dt}_{=T}\underbrace{\int_{-T/2}^{T/2} dt'\, e^{i2\pi f[t'-t]}\delta(t'-t)}_{=e^0=1,\, S.P.\,(D8)}$$

$$=\frac{1}{\nu^3 T}\left[B(0)\right]^2$$

$$\boxed{\to 0 \text{ as } T\to\infty}$$

## Sum of contributions

In summary, the terms add up to yield the variance of the spectral estimator for randomly sampled data;

$$\lim_{T\to\infty}\operatorname{var}\left\{S_T^R(f)\right\}=\left[S(f)\right]^2+\frac{4}{\nu}B(0)S(f)$$

Ultimately the variability of the spectral estimator based on randomly sampled data in the limit $T\to\infty$ is given by:

$$\lim_{T\to\infty}\varepsilon^2_{S_T^R}=\frac{\left[S(f)\right]^2+\frac{4}{\nu}B(0)S(f)}{\left[S(f)\right]^2}=1+\frac{4}{\nu}\frac{B(0)}{S(f)}$$